

**IMPROVING THE DETECTABILITY OF GRAVITATIONAL  
WAVE COUNTERPARTS OF SHORT-HARD  
GAMMA RAY BURSTS**

By

**SHAON GHOSH**

A dissertation submitted in partial fulfillment  
of the requirements for the degree of

**DOCTOR OF PHILOSOPHY**

**WASHINGTON STATE UNIVERSITY**  
Department of Physics and Astronomy

**DECEMBER 2013**

To the Faculty of Washington State University:

The members of the Committee appointed to examine the dissertation of SHAON GHOSH find it satisfactory and recommend that it be accepted.

---

Sukanta Bose, Ph.D., Chair

---

Matthew Duez, Ph.D.

---

Guy Worthey, Ph.D.

IMPROVING THE DETECTABILITY OF GRAVITATIONAL  
WAVE COUNTERPARTS OF SHORT-HARD  
GAMMA RAY BURSTS

Abstract

by Shaon Ghosh, Ph.D.  
Washington State University  
December 2013

Chair: Sukanta Bose

With multiple observatories and missions being planned for detecting orphaned afterglows associated with gamma-ray bursts (GRBs) we emphasize the importance of developing data analysis strategies for searching their possible counterpart signals in the data of gravitational wave detectors in the advanced detector era. This is especially attractive since short hard gamma-ray bursts (SGRBs) may have compact binary coalescences involving neutron stars (CBCNS) as their progenitors, which emit gravitational waves. Joint electromagnetic and gravitational wave observations of these objects will enrich our understanding of their beaming, energetics, galactic environment, and shed light on a host of other outstanding questions related to them. We recognize some of the astrophysical factors that determine what fraction of these sources can generate orphaned afterglows. We developed a search pipeline by modifying the existing blind hierarchical coherent search pipeline, targeting their sky-position and time of occurrence known from EM observations to enable it to search for counterparts of SGRB and SGRB afterglows in gravitational wave detector data. The modifications allow it to analyze extended periods of time in the gravitational wave data in the past of the afterglow detection epoch, while targeting its known sky-position, to search for gravitational

waves from the common progenitor. We assess the improvement in gravitational wave detectability to be had from utilizing the sky-position information. We also propose a method for mitigating the effects on the detection efficiency of targeted searches of gravitational wave signals from the putative CBCNS sources of afterglows and short gamma-ray bursts arising from the presence of errors in detector calibration or CBCNS waveform models used in the search.

# Acknowledgement

This work, that spans over six years of my life, would not have been possible in the absence of numerous key personalities. Some have contributed academically, some through inspirations and motivations. A word of gratitude towards them is the least I can offer, and in my humble opinion, the person that deserves the most is my adviser Sukanta Bose. It is through him I educated myself in the subject of gravitational waves physics and data analysis. He had been a source of inspiration. His scrupulous and fastidious attention to details sharpened my skills necessary for quality scientific work.

It is impossible to overstate the assistance I received from my fellow LIGO scientific collaborators (LSC). Valuable feedback I got from them on my work eventually rendered robustness to my thesis. Special mention of course must be made of Ian Harry, with whom I worked the most. He meticulously went through my results and gave extremely useful comments. Ian's expertise in the same field of research as mine meant he invariably became an invaluable natural critique of my work. He provided me infrastructures necessary for my analysis, in absence of which much of the success of this work would have been extremely difficult to emulate.

Special note of thanks are in order for Nickolas Fotopoulos, Alexander Dietz, Jordi Burguet Castell, Valeriu Predoi and Stephen Fairhurst. All of them have from time to time provided me with feedback on my work.

As a member of the Washington State University Relativity Group (WSURG), I would like to take this opportunity to thank Michael Allen, Sukanta Bose, Carl Brannen, Thilina Dayanga, Brett Deaton, Matthew Duez, Nikolay Frik, Ryan Magee, Fatemeh Nouri, Violet Pool, Szymon Steplewski, Dipongkar Talukder, Baitian Tang and Guy Worthey. All the discussions we had over the years in our weekly Astro-News Hour enriched my knowledge and invigorated my interest in astronomy and astrophysics. Special thanks here must go to our LIGO group members in WSU like Thilina Dayanga and Dipongkar Talukder with whom I have worked closely and I learned a lot on data analysis from. I would like to

thank Matt Duez specially for a numerical relativity project that I did with him. It was a truly enriching experience, something that has kindled in me interests to study numerical relativity in greater details. I would also like to thank Guy Worthey and Sukanta Bose for teaching me graduate level courses on astronomy and general relativity respectively. Both Matt and Guy were also my thesis committee members. I would like to thank them for their efforts in going through my thesis and providing me with their valuable comments.

With Fred Raab and Gregory Mendell I spent every week an hour discussing ongoing projects in LIGO and my own projects. This used to be one of the most productive discussions I had, and I would like to thank both Fred and Greg for that. Both of them were extremely eloquent and critical commentators of my work. In particular, Greg's comments and suggestions were indispensable for my work. Parts of this thesis benefit immensely from his inputs and insights.

I deeply acknowledge Bruce Allen for hosting me in Albert Einstein Institute (AEI) in Hannover, Germany for five months. Time spent in the intellectually stimulating environment of AEI served me as a great launchpad for the performance and training as a scientist. Discussions with Bruce Allen, Drew Keppel, Reinhard Prix, Christian Röver, and Francesco Salemi helped me in my understanding of the subject. During my visit I also made some great friends with whom I continue to stay in touch.

I also thank Ajit K. Kembhavi for hosting me at Inter University center of Astronomy and Astrophysics (IUCAA) in Pune, India for a total of 9 months during the final year of my Ph.D. I came in touch with some of the best astronomers and Physicists in the field during my stay there. Discussions with Sanjeev Dhurandhar, Sanjit Mitra, Tarun Souradeep and frequent visitors to IUCAA like Bala Iyer and Rajesh Nayak were very productive. Discussions with scientists like Naresh Dadhich and Dipankar Bhattacharya helped me broaden the spectrum of my research interests. I whole heartedly thank all of them.

None of the work I did would have been possible if I was not financially supported by National Science Foundation of United States. I am grateful for NSF grants PHY-0855679

and PHY-1206108 for the support I recieved for the major part of my doctoral work. I was also supported by the Department of Physics and Astronomy by the Millenium Fellowship in the first year of my graduate studies and College of Science research assistantship during the fall semester of 2009, for which I am thankful to the Washington State University College of Science and Department of Physics and Astronomy.

Finally I must express my deepest gratitude to my family for supporting me through out the years of my graduate studies. To my Ma, who has become to me the very embodiment of everything that is good in the world. Today her absence is missed more than ever. To my Baba, who has motivated me from my childhood to dream big. To my sister Tuli, who patiently listened to my rants about how tough life is at grad school and last but never the least, my wife Anuradha, whose love, patience and faith in me gave me the strength and courage required at the harshest of times.

# Table of Contents

|          |   |           |
|----------|---|-----------|
| <b>1</b> | <b>Introduction</b>   | <b>1</b>  |
| <b>2</b> | <b>A brief survey of gravitational wave physics, experiment and techniques of data analysis</b> | <b>6</b>  |
| 2.1      | Gravitational waves . . . . .   | 8         |
| 2.2      | Gravitational wave sources . . . . .  | 12        |
| 2.2.1    | Gravitational waves from compact binary inspiral - weak field limit . . . . .                   | 13        |
| 2.3      | Laser interferometric techniques to detect gravitational waves . . . . .                        | 19        |
| 2.3.1    | Basic interferometric principle . . . . .   | 19        |
| 2.3.2    | Noises in interferometric gravitational wave detectors . . . . .                                | 22        |
| 2.4      | Basic data analysis techniques . . . . .  | 25        |
| 2.4.1    | Data segmentation . . . . .   | 26        |
| 2.4.2    | Template bank . . . . .   | 27        |
| 2.4.3    | Matched filtering and detection statistic . . . . .   | 27        |
| 2.4.4    | $\chi^2$ test . . . . .   | 29        |
| 2.4.5    | Coincidence test and background estimation . . . . .  | 30        |
| 2.5      | Search for gravitational waves from progenitors of short GRBs . . . . .                         | 31        |
| 2.5.1    | Short duration gamma ray bursts . . . . .   | 32        |
| 2.5.2    | External trigger pipeline . . . . .   | 34        |
| <b>3</b> | <b>Searching for gravitational waves in a network of detectors</b>                              | <b>37</b> |

|          |  |           |
|----------|--|-----------|
| 3.1      | Introduction . . . . .   | 37        |
| 3.2      | Signal at a single detector . . . . .  | 40        |
| 3.2.1    | Circular polarization basis . . . . .  | 41        |
| 3.3      | A network of detectors . . . . .   | 45        |
| 3.3.1    | Construction of network detection statistic using physical parameters                                    | 46        |
| 3.3.2    | Construction of network detection statistic using symmetrized parameters . . . . .                       | 50        |
| 3.3.3    | Maximization of detection statistic over time of arrival . . . . .                                       | 62        |
| 3.3.4    | The null stream statistic . . . . .  | 65        |
| 3.4      | Coherent search pipeline for all-time, all-sky search . . . . .  | 69        |
| 3.4.1    | The coherent bank . . . . .  | 69        |
| 3.4.2    | The coherent trigger bank and filtering with it . . . . .  | 71        |
| 3.4.3    | The coherent inspiral analysis - CHIA . . . . .  | 71        |
| 3.5      | An example of blind hierarchical coherent search . . . . .   | 72        |
| 3.6      | Discussion . . . . .   | 74        |
| <b>4</b> | <b>Short hard gamma-ray bursts and orphaned afterglows as external triggers to gravitational waves</b>   | <b>79</b> |
| 4.1      | Introduction . . . . .   | 79        |
| 4.2      | SGRBs, orphaned afterglows, and their prospects as GW candidates . . . . .                               | 85        |
| 4.2.1    | Comparing the detectabilities of GW counterparts of SGRBs and orphaned afterglows . . . . .              | 87        |
| 4.2.2    | The fraction of compact binary coalescences detectable as GW events                                      | 89        |
| 4.2.3    | Fraction of SGRBs with orphaned afterglows . . . . .   | 96        |
| 4.2.4    | Probability of detecting an orphaned afterglow in conjunction with a gravitational wave signal . . . . . | 97        |
| 4.3      | Externally triggered search for GW signals from poorly localized CBC sources                             | 105       |

|          |   |            |
|----------|---|------------|
| 4.3.1    | Effect of GRB sky-position error on the detection efficiency of a targeted GW search: Searching at a single inaccurate position . . . . . | 107        |
| 4.3.2    | Effect of GRB sky-position error on the detection efficiency of a targeted GW search: Searching at multiple sky positions . . . . .       | 109        |
| 4.4      | Searching all-sky, all-time CBC triggers in LIGO's S5 data for GW candidates concurrent with GRBs . . . . .                               | 112        |
| 4.5      | Improving the performance of targeted GW searches . . . . .   | 117        |
| 4.5.1    | Targeted GW search over a finite sky patch even for accurately known GRB sky position . . . . .   | 118        |
| 4.5.2    | Targeted search for GW sources using inaccurate templates: Masses .   | 120        |
| 4.5.3    | Targeted search for GW sources using inaccurate templates: Spin . .   | 121        |
| 4.6      | Discussion . . . . .  | 123        |
| <b>5</b> | <b>Waveform inaccuracy and its effects on parameter estimation and detection</b>  | <b>138</b> |
| 5.1      | Introduction . . . . .  | 138        |
| 5.2      | BBH waveforms used for parameter estimation . . . . .   | 140        |
| 5.3      | Parameter measurement errors . . . . .  | 142        |
| 5.3.1    | Numerical simulations . . . . .   | 147        |
| 5.3.2    | Analytic results using leading order approximation of the waveform discrepancies . . . . .  | 154        |
| 5.4      | Waveform inaccuracy and its effect on detection of gravitational waves from progenitors of short GRBs . . . . .                           | 156        |
| 5.4.1    | Detection efficiency . . . . .  | 162        |
| 5.5      | Discussion . . . . .  | 164        |
| <b>6</b> | <b>Conclusion</b>   | <b>178</b> |

|          |  |            |
|----------|--|------------|
| <b>A</b> | <b>A brief discussion of Einstein's General relativity</b>                 | <b>181</b> |
| A.1      | Introduction . . . . .   | 181        |
| A.2      | Distance formula in flat space . . . . .                                   | 182        |
| A.3      | Distance formula in flat spacetime . . . . .                               | 184        |
| A.4      | Distance formula in curved space . . . . .                                 | 187        |
| A.5      | Observer in uniformly accelerated frame moving in flat spacetime . . . . . | 189        |
| A.6      | Principle of equivalence . . . . .   | 191        |
| A.7      | Metric in curved spacetime, vectors and geodesics . . . . .                | 195        |
| A.8      | Covariant derivatives, parallel transport and curvature tensors . . . . .  | 203        |
| A.9      | Einstein tensor and Einstein field equations . . . . .                     | 208        |
| <b>B</b> | <b>Linearized gravity and gravitational waves</b>                          | <b>210</b> |
| B.1      | Linearized gravity . . . . .   | 210        |
| B.2      | Transverse traceless gauge . . . . .                                       | 212        |
| B.3      | Gravitational wave emitted from a source . . . . .                         | 215        |
|          | <b>Bibliography</b>  | <b>227</b> |

# List of Figures

|     |  |    |
|-----|--|----|
| 2.1 | Figure obtained from Weisberg et al. (2010). . . . .   | 7  |
| 2.2 | Compact binary system of masses $m_1$ and $m_2$ in the $x^1 - x^2$ plane. . . . .  | 14 |
| 2.3 | The above figure shows the two frames, source frame shown with red axes and axes labeled by subscript $s$ , and the wave frame shown with blue axes. The $z$ axis in the wave frame denotes the direction of propagation of the wave. The inclination angle $\iota$ is the angle between the $z_s$ axis of the source frame and the $z$ axis of the wave frame. The polarization angle $\psi$ is the angle between the $x_s$ axis of the source frame and the $x$ axis of the wave frame projected on to the source frame. . . . . | 16 |
| 2.4 | A schematic diagram of a power recycled Fabry-Perot Michelson interferometer.  | 20 |
| 2.5 | LIGO noise curve depiction from Ref. wikimedia commons. Above Fig. shows contributions from the different noise elements. . . . .  | 25 |
| 2.6 | Actual LIGO noise curve (courtesy: LIGO Scientific Collaboration). Figure shows how the sensitivity of the detector progressively improved over time. By S6, the sensitivity outperformed the design sensitivity. . . . .  | 26 |
| 2.7 | Short duration GRB firing from compact binary coalescence. . . . .   | 33 |
| 2.8 | Schematic representation of the external trigger search analysis segment. The grey region indicates the offsource segments. There are a total of 340 offsource segments. The red central region is the 6 second onsource segment. The black regions are the discarded parts of the data for reasons explained in the text.   | 35 |

|     |  |    |
|-----|--|----|
| 3.1 | The knowledge of time delay between signals in two detectors arising from the same source helps one in locating it in the sky. . . . .   | 39 |
| 3.2 | Evolution of chirp frequency with time. The cut-off frequency is taken to be 10 Hz. Note that the $x$ -axis denotes the value of $a$ which at the end of the chirp is zero. . . . .  | 41 |
| 3.3 | The source frame (depicted in green-colored axes) is transformed into the wave frame in red. The wave frame is then projected on the detector frame labeled with axes subscript $d$ . . . . .  | 43 |
| 3.4 | A schematic representation of the hierarchical coherent search pipeline. . . .   | 70 |
| 3.5 | These are scatter plots of the combined and coherent SNRs of injection triggers, represented by red plus symbols, and background (or “slide”) triggers, represented by the black crosses. The coherent SNR was used to cluster the triggers, from both injections and slides. The coherent SNR performs noticeably better than the combined effective SNR in discriminating signals from background: In the left plot, at a detection threshold of a little above 6 in the coherent SNR all the injections found in the coincident stage are recovered with a vanishing false-alarm probability. For the same false-alarm probability, the combined effective SNR detects a lesser number of injected signals. . . . | 77 |

|     |   |    |
|-----|---|----|
| 3.6 | <p>The receiver operating characteristic (ROC) curves of three CBC searches are compared above. The ROC of the search with the coincident stage alone is plotted in solid red line, and has the weakest performance owing to the 13 found injections that are weaker than the loudest background trigger in that search. On the other hand, the ROC curve for the hierarchical pipeline, with coherent stage included, is shown in black dash-dotted line and has the best performance. It has a constant detection probability because all found injections are louder than the loudest background trigger for this pipeline. Finally, the third ROC curve, shown as a blue dashed line is the coincident stage, with the null-stream veto applied. This veto improves the performance of the coincident pipeline, so much so that for low detection-thresholds (or high false-alarm probability) its ROC curve rises to match that of the pipeline with the coherent stage. The average error in the detection probabilities plotted here is less than <math>3 \times 10^{-4}</math>.</p> | 78 |
| 4.1 | <p>The design noise amplitude spectral densities (ASDs) of LIGO-I, Advanced LIGO (aLIGO), and Advanced Virgo (AdV) detectors obtained from LIGO Algorithms Library.</p>   | 87 |

- 4.2 The blue (solid) curve shows the percentage of sky inaccessible to interferometric detectors for the detection of GW signals from CBC sources (with all possible orientations), plotted as a function of the source distance. For comparison, if all sources were oriented face-on (i.e., with  $\iota = 0$  or  $\pi$ ) and if the detector had  $\mathcal{P}(\theta, \phi) = 1$  everywhere on the sky, then all of those sources would be detectable in that hypothetical detector at all distances obeying  $r \leq r_H$ . On the other hand, if all sources were oriented edge-on (i.e., with  $\iota = \pi/2$ ), then Eq. (4.5) shows that, hypothetically, for  $\mathcal{P}(\theta, \phi) = 1$  everywhere on the sky, all of those sources would be inaccessible for  $r > r_H/2\sqrt{2}$  but accessible when closer. The red (dashed) step function represents those sources in that imaginary detector. . . . . 92
- 4.3 Probability of detecting a CBC source at a distance  $r$  (given in units of the horizon distance  $r_H$ ) assuming that the sources are distributed uniformly in the volume of interest. The four different plots are for four different values of  $\mathcal{P}(\theta, \phi)$ . The blue curve shows the probability of a system that is overhead. For a given  $\mathcal{P}(\theta, \phi)$ , the largest distance at which the probability reaches unity is when a CBC is detectable for all possible values of its inclination angle. For an overhead source (i.e., with  $\theta = 0$ ) this distance is  $r = r_H/2\sqrt{2}$ . For other sky positions, it is  $r = r_H\sqrt{\mathcal{P}(\theta, \phi)}/2\sqrt{2}$ . . . . . 93

4.4 **Left:** Mean density of detectable sources on the two sphere at a distance  $r$ . **Middle:** Maximum density of detectable sources on the two sphere at a distance  $r$ . **Right:** The cumulative fraction of detectable CBC sources in a spherical volume of radius  $r$  plotted as a function of  $r$ . The sources are distributed uniformly in volume and are oriented randomly. It attains a maximum value of 8.65% when  $r$  reaches the horizon distance. **Bottom** Comparison between the cumulative fraction of detectable CBC sources in a spherical volume of radius  $r$  for a single detector and for various network of detectors plotted as a function of  $r$ . . . . . 95

4.5 Fraction of neutron star - black hole binary sources that give rise to a gamma-ray burst, which may or may not be beamed at us, for the special case of  $p_\eta(\eta) = \delta(\eta - 0.25)$ ,  $p_\chi(\chi) = \delta(\chi - 1.0)$ , and  $p_\kappa(\kappa) = \delta(\kappa - 1.0)$ . The minimum mass of the neutron star required for the emission, and for these choices of the probability densities, is plotted on the  $x$ -axis. . . . . 102

4.6 Comparison of the detection efficiencies of (from left to right) low chirp-mass, medium chirp-mass and high chirp-mass CBCNS systems with accurately known sky positions (blue or upper curves) and those with a sky-position error of  $20^\circ$  (red or lower curves). . . . . 125

4.7 Detection efficiency comparison for injections with a sky-position error of  $20^\circ$  (from left to right) in low chirp-mass, medium chirp-mass and high chirp-mass bins. . . . . 126

- 4.8 **Left:** Plots of the false-alarm probability of a sky-patch search as a function of the number of the sky position templates or points in the patch, for SNR values 6.0 - 7.5. The  $x$ -axis displays the number of sky points in the patch, which includes the true sky-position. An increase in the number of sky points in a search causes a monotonic increase in the false-alarm probability, for any given SNR, and it asymptotes to the all-sky FAP value at that SNR. **Right:** False-alarm probability plotted as a function of SNR for sky-patches with a varying number of sky points. Here the false-alarm probability at a given SNR, plotted on the  $x$ -axis, is defined as the number of background triggers that are found louder than that SNR divided by the total number of background triggers of any SNR found in the search with that sky-patch. . . . . 127
- 4.9 **Left plot:** The  $\log_{10}$  of the percentage change in the H1L1V1 network SNR owing to a  $20^\circ$  error in the Declination of the source is mapped as a function of the true source sky position. **Right plot:** Same as the left plot except that here the error in the sky position of the source is taken to be 4 square-degrees of solid angle. For both plots the detector noise PSD is taken to be LIGO-I LIGO Algorithms Library for all three detectors. The source is a non-spinning CBCNS with component masses  $2.5M_\odot$  and  $40M_\odot$ , optimally oriented and located at a distance of 17Mpc. . . . . 128

4.10 **Top left:** Network response across the sky; the quantity  $\sqrt{\sum_I (F_+^I)^2 + (F_\times^I)^2}$ , normalized to have a maximum value of unity, plotted as a function of the sky for the H1L1V1 network. The four white asterisks in this plot are located at the two most sensitive and two least sensitive sky positions. Their RA and dec, in degrees, are  $(300.0^\circ, -40.0^\circ)$ ,  $(120.0^\circ, 40.0^\circ)$  and  $(245.0^\circ, 20.0^\circ)$ ,  $(65.0^\circ, -18.0^\circ)$ , respectively. These locations were chosen for our study of the variation of detection efficiency across the sky. **Top right:** LIGO-Hanford sensitivity; the two white stars give the locations of greatest H1 response. At these two spots L1 and V1 have a relatively weak response. Thus, injections in these locations provide a good measure of how much the detection efficiency suffers when only one interferometer in the H1L1V1 network has a good response. Their RA and dec (in degrees) are  $(330.0^\circ, -46.0^\circ)$ ,  $(145.0^\circ, 45.0^\circ)$ . **Bottom row:** Same as the top right plot but for L1's best response (bottom left), at  $(115.0^\circ, 30.0^\circ)$  and  $(295.0^\circ, -32.0^\circ)$ , and V1's best response (bottom right), at  $(195.0^\circ, -45.0^\circ)$  and  $(17.0^\circ, 42.0^\circ)$ . . . . . 129

- 4.11 The  $y$ -axis above denotes the detection efficiency of injections in the ten sky positions shown in Fig. 4.10. The source is the same as the one used in Fig. 4.9. The ten different sky positions where injections were made to study the variation of detection efficiency as a function of the source sky position are listed on the  $x$ -axis. Their RA and dec (in degrees) are **1**:  $(245.0^\circ, 20.0^\circ)$ , **2**:  $(300.0^\circ, -40.0^\circ)$ , **3**:  $(120.0^\circ, 40.0^\circ)$ , **4**:  $(65.0^\circ, -18.0^\circ)$ , **5**:  $(330.0^\circ, -46.0^\circ)$ , **6**:  $(145.0^\circ, 45.0^\circ)$ , **7**:  $(30.0^\circ, 115.0^\circ)$ , **8**:  $(295.0^\circ, -32^\circ)$ , **9**:  $(195.0^\circ, -45.0^\circ)$ , and **10**:  $(17.0^\circ, 42.0^\circ)$ . The color code of the indices is as follows: Red-colored indices are points where the network response is the highest, as shown in Fig. 4.10. Blue indices are points of lowest network response, and green indices are points where one of the interferometers in the H1L1V1 network has a high response and the other two have a low response. Note that for the first sky position the fractional loss in SNR of the loudest injection is negative. This is because there the SNR of the injection trigger happens to be smaller than that of the loudest background trigger. . . . . 130
- 4.12 The above plots of SNRs of triggers in two detectors show the region where a coincident search with individual detector SNR thresholds of 5.5 will not find any triggers with a network combined SNR, shown in the colorbar, that is greater than 9 but a search with no individual detector thresholds will. Thresholding at an individual detector level rejects all coincidences that have a low SNR in one of the detectors. The three-detector case is easy to understand from this study: If the SNRs of a signal are less than the threshold in two of the three detectors but greater than that in the third, the combined SNR can still have an appreciable value (with a low FAP). . . . . 131
- 4.13 Detection efficiency comparison (from left to right) for the low chirp-mass, medium chirp-mass and high chirp-mass bins for four sky modes. Unlike in Fig. 4.7 there is no sky-position error here. . . . . 134

|      |   |     |
|------|---|-----|
| 4.14 | <p>In these plots we study the combined distribution of the SNRs of the 3000 injections from all three sky-mode searches. For every injection we compute the mean of its network SNRs found by the known-sky, sky-patch, and all-sky modes of the search. We next compile the list of the 3000 mean SNRs. This is the reference list with which we compare the SNRs of injections from any of the search modes. Pairwise comparisons of distributions of injection SNRs from the different sky-mode searches are shown in these plots. In the first plot we find that 253 of the injections had all-sky SNRs greater than 90% of the mean SNRs. The corresponding number of injections (189) was smaller for known-sky SNRs. At the other end, more known-sky SNRs are less loud than all-sky SNRs: While 552 injections had known-sky SNRs weaker than 90% of the mean SNRs, the corresponding number of injections was 171 for all-sky SNRs. One finds qualitatively similar improvement in the SNR values of the same injections in the sky-patch mode compared to the known-sky mode of the search. . . . .</p> | 135 |
| 4.15 | <p>Similar plot as in Fig. 4.14 with only those injections were considered whose SNR is less than 20. We note that the performance of the all-sky and sky-patch modes are even better for weaker SNR triggers compared to the known-sky mode in the region where 90% or more triggers were found louder than the mean SNR. . . . .</p>  | 136 |

|      |   |     |
|------|---|-----|
| 4.16 | Plot of ratio of SNR of the injection trigger when the search was conducted over a patch of 21 points to that of the SNR of the same injection found in a search conducted in one point in the sky. The top plot with red bars is for the case of non-spinning injections, and the bottom plot is the same for the spinning injections. This study was conducted on 100 injections in the low-mass region of the template bank. For the spinning case, the spin was chosen to be very high, i.e., with the spin parameter greater than 0.75, so that the effect of spin is prominent. . . . . | 137 |
| 5.1  | In the vector space defined by the data, the exact and the approximate waveforms exist in different manifolds. Here we show it with an example where the data has three time points and hence is three dimensional. These three time points forms the three axes in the figure. Note that in general the two waveforms will exist in different planes, as shown in this example. Thus it is not possible to rotate any one of the waveforms in its own manifold and align it with a waveform in the other manifold. . . . .   | 143 |
| 5.2  | For the true parameters the approximate waveform will not give the best fit. This is the systematic error in the parameter that we incur due to the inaccuracy in the templates. . . . .  | 145 |
| 5.3  | The fitting factor obtained from numerical simulations of matched filtering with a bank of 3.5PN TaylorT1 templates of (complete) inspiral-merger-ringdown waveforms as target signals in AdvLIGO PSD. The target waveforms are parameterized by the BBH component masses $m_1$ and $m_2$ , each ranging from 13 - 104 $M_\odot$ . . . . .  | 149 |

|      |   |     |
|------|---|-----|
| 5.4  | The fractional error in total-mass (in %) obtained from numerical simulations of the same template bank and target signals, in AdvLIGO PSD, as shown in Fig. 5.3. Target signals with $\eta = 0.25$ are represented by points along the equal-mass line (not shown) extending from the left-bottom corner to the top-right corner of the plot. . . . .  | 151 |
| 5.5  | The fractional error in total-mass (in %) given by the analytic expression Eq. (5.14) for AdvLIGO PSD. Above, $m_1$ and $m_2$ represent the true parameters. . . . .  | 152 |
| 5.6  | The fractional error in the symmetric mass-ratio (in %) obtained from numerical simulations for the same template bank and target signals, in AdvLIGO PSD, as shown in Fig. 5.3. . . . .  | 154 |
| 5.7  | The fractional error in the symmetric mass-ratio in AdvLIGO PSD (in %). The figure on the left is obtained from numerical simulations, and that on the right is computed from the analytic expression in Eq. (5.13). . . . .  | 155 |
| 5.8  | Coherent $\chi^2$ values for weakly spinning sources that were found by searching with non-spinning templates tend to be lower than those for strongly spinning sources. The red pluses are spinning sources that have $a \leq 0.01$ . The blue pluses have larger spin values. When searched with non-spinning templates, the signal mismatch is increasing the coherent $\chi^2$ values. The extent of the deterioration is less when the mismatch is lower in the case of low spin system. . . . . | 158 |
| 5.9  | Coherent $\chi^2$ vs coherent SNR plots comparing the spinning and the non-spinning template searches. The black crosses are the background triggers, and the red pluses are the found injection triggers. Both the studies were done on the same set of spin aligned BNS sources. Performance of the non-spinning templates suffers due to the waveform mismatch between them and the injection. . . . .   | 166 |
| 5.10 | Flowchart depicting the method of increasing analysis time for better estimate of the background. Above, $n$ is an integer. . . . .   | 167 |

|      |   |     |
|------|---|-----|
| 5.11 | Coherent $\chi^2$ vs coherent SNR plots for spinning BNS injections that were searched with non-spinning templates(left plot) and spinning templates (right plot). The background was estimated using the additional time technique illustrated in Fig. 5.10. . . . .                                 | 168 |
| 5.12 | Coherent $\chi^2$ vs coherent SNR plots for spinning NSBH injections that were searched with non-spinning templates(Left) and spinning templates (Right). Background was estimated using the additional time technique illustrated in Fig. 5.10. . . . .  | 169 |
| 5.13 | Coherent $\chi^2$ vs coherent SNR plots for weak spinning BNS (top panel) injections that were searched with non-spinning templates(Left) and spinning templates (Right). Note the blue contours of zero-FAP new_SNR contour in all the four cases misses out majority of the injections. . . . .     | 170 |
| 5.14 | Coherent $\chi^2$ vs coherent SNR plots for weak spinning NSBH (bottom panel) injections that were searched with non-spinning templates(Left) and spinning templates (Right). Note the blue contours of zero-FAP new_SNR contour in all the four cases misses out majority of the injections. . . . . | 171 |
| 5.15 | Comparison of test_stat (green contour) with new_SNR (blue dashed contour) for BNS injections. We note that the test_stat in these cases are performing better in finding signals with zero FAP. . . . .  | 172 |
| 5.16 | Comparison of test-stat (green contour) with new-NR (blue dashed contour) for NSBH injections. We note that the test_stat in these cases performing better in finding signals with zero FAP. . . . .  | 173 |

|      |   |     |
|------|---|-----|
| 5.17 | The fractional error in estimation of total mass is plotted in the top panel. The one on the top left was obtained when the templates used were spin-aligned and hence the search is devoid of systematic error, the one on the top right was obtained in a search where non-spinning templates were used and therefore, suffers from systematic effect of waveform inaccuracies. The differences are so minute that they are not reflected in the plot colors, so in the lower panel we show the differential of these two sets of errors (error for spin-aligned templates - error for non-spinning templates). . . . . . | 174 |
| 5.18 | The fractional error in estimation of total mass is plotted for weaker BNS injections. The one on the top left was obtained when the templates used were spin-aligned, the one on the right was obtained in a search where non-spinning templates were used. Note that in the later search there was substantial loss of detection. The title of the plots define the color bars. . . . . .   | 175 |
| 5.19 | Detection efficiency curves for BNS and NSBH sources. Note that in the BNS case the search based on non-spinning template bank performed consistently worse than the search with spin-aligned templates. This is the direct consequence of waveform inaccuracy hurt detectability. In the NSBH case the improvement is not that remarkable because the detection statistics used here is new-SNR which was losing a lot sources as shown in Fig. 5.14. . . . . .  | 176 |
| 5.20 | Detection efficiency curves for NSBH sources. Here we show the detection efficiency plots for the weaker NSBH sources. Same study for weaker BNS sources gave detection efficiency at all distance bins to be zero as no found injections were louder than the loudest background from that study . . . . .   | 177 |

|      |  |     |
|------|--|-----|
| 5.21 | ROC curves for weak NSBH systems with high spin, searched with spinning templates (red curves) and non-spinning templates (blue curves). Dashed curves indicate ROC curves with plotted with new-SNR as detection statistic, while solid curves indicate the ROC curves plotted with test-stat as detection statistic. . . . . | 177 |
| A.1  | Distance between two points in three dimensional cartesian coordinate system.  | 183 |
| A.2  | Path followed by a free particle is given by the path for which the action is an extremum. . . . .   | 185 |
| A.3  | Distance between two points on the surface of a sphere. . . . .  | 188 |
| A.4  | An accelerated frame in a gravity-less environment is indistinguishable from an inertial frame under gravity. . . . .  | 192 |
| A.5  | Definition of basis vectors at the tangent space of a manifold. . . . .  | 197 |

# List of Tables

|     |  |     |
|-----|--|-----|
| 4.1 | Fermi SGRBs with large sky-position uncertainties that were concurrent with LIGO's S5 run. . . . . | 132 |
| 4.2 | Short IPN GRBs with large sky position errors. . . . .   | 133 |

Dedicated to the memory of my mother.

## Related Publications

1. S. Bose, S. Ghosh, P. Ajith, “Systematic errors in measuring parameters of non-spinning compact binary coalescences with post-Newtonian templates,” 2010 Class. Quantum Grav. **27**, 114001.
2. S. Bose, T. Dayanga, S. Ghosh, D. Talukder, “A blind hierarchical coherent search for gravitational-wave signals from coalescing compact binaries in a network of interferometric detectors,” 2011 Class. Quantum Grav. **28**, 134009
3. S. Ghosh, S. Bose, “Toward finding gravitational-wave signals from progenitors of short hard gamma-ray bursts and orphaned afterglows,” 2013, Submitted to Phys. Rev. D, (LIGO DCC : P1200169-v2)
4. S. Ghosh, S. Bose, I. Harry, “Waveform inaccuracy and its effect on detection of gravitational waves from progenitors of GRBs,” 2014, in preparation (LIGO DCC : T1300597-v2)

# Chapter 1

## Introduction

Among the four fundamental forces in nature, gravity and electromagnetism are the only two that operate over long range, and directly manifest their effects in our macroscopic world. Even though the strength of gravity is thirty six orders of magnitude weaker than electromagnetism, they exhibit some basic similarities. For instance, both follow the inverse square law, both are central forces and as a result both are conservative. Maxwell's theory of electromagnetism explains the origin of electromagnetic radiation. In gravity too, one can expect similar long range radiation. Ironically, to understand this, one has to forgo the idea of gravity being a force.

Einstein's general relativity, which discards the picture of gravity as an action at a distance, predicts the existence of gravitational radiation. According to general relativity, matter curves spacetime around it and a free particle in the presence of this curvature follows the shortest path in this spacetime called a geodesic. The resulting motion of the particles in this curved spacetime is what we identify as motion under the force of gravity in the Newtonian sense. Gravitational radiation is the wave of disturbance of the spacetime that travels at a speed of light (Hartle (2003)).

Unlike some of the other general relativistic predictions, like the gravitational bending of light, precession of perihelion of Mercury, etc., gravitational wave is one of the results of

strong field regime of gravity. Indirect evidence of the existence of gravitational waves was obtained from the observation of the binary pulsar system PSR B1913 + 16 discovered in 1974, commonly known as the Hulse and Taylor binary pulsar after its discoverers, Russell A. Hulse and Joseph H. Taylor in 1974. Study of orbital time period decay helped in establishing the indirect detection of gravitational wave in 1978. However, a direct detection of gravitational waves have eluded scientists for more than half a century, ever since Joseph Weber began his observations using bar detectors, which commonly came to be known as the ‘Weber bars’ (Weber (1969)). Modern era of astronomy witnessed the advent of the interferometric detectors like Laser Interferometer Gravitational wave Observatory (LIGO) at Hanford, Washington and Livingston, Louisiana, in the United States and Virgo gravitational wave detector near Pisa, Italy, that are sensitive enough to detect gravitational waves from extragalactic coalescing binary systems. With more such detectors on the horizon, like LIGO India and KAGRA in Japan, expectations are high that a direct detection of gravitational waves by the end of this decade is imminent.

But detection of gravitational waves, though immensely important, is not the ultimate goal of these detectors. Advanced technology available today has made it possible to envision a new age of multi-messenger astronomy in the coming decades where electromagnetic, gravitational wave and neutrino observatories around the world (and beyond) will work as a network to unravel a plethora of information about the cosmos from black holes to the big bang. In this changing landscape of astronomy, this thesis aims at providing some insights about the prospects of gravitational wave astronomy. Here we provide an outline of the contents of the remaining part of the thesis.

- **Chapter 2** gives a brief introduction to the physics of gravitational waves. We discuss how we arrive at the wave solution of general relativity in linearized gravity. We also discuss about the sources of gravitational waves. Our main focus among these sources is the compact binary coalescing (CBC) source. We then proceed to a discussion of the interferometric detector itself, how it is used to detect gravitational waves, what

are the sources of noise in such detectors and how we deal with them.

Finally we talk about the basic data analysis techniques incorporated in the search for gravitational waves from coalescing binaries, known as the coincident search. We end this chapter with a discussion of detection of gravitational waves from short duration gamma ray bursts (SGRB). We discuss very briefly the physics of SGRB and introduce the reader to the standard external trigger pipeline that is used for the detection of gravitational waves from the progenitors of such events.

- **Chapter 3** discusses the development of a detection statistic for a network of interferometric detectors. We motivate the discussion with the arguments in favor of a network search. We establish why a network of multiple interferometric detectors is indispensable for gravitational wave detection and astronomy. At the single detector level we introduce the reader to the circular polarization basis of gravitational waves and how it is used in conjunction with the antenna pattern function of the source sky position to construct the gravitational wave strain at a particular detector. Then we demonstrate how to extend this formalism to a network of multiple detectors by considering the data at different detectors as a data vector with dimension of the number of detectors.

Once the formalism is established, we use it to construct the detection statistic for the network by maximization of the logarithmic likelihood ratio. From the network analysis a natural tool for vetoing non-astrophysical signals evolves. This is called the null stream, which we briefly discuss next.

We have developed a detection pipeline that is called the hierarchical coherent search pipeline which uses this network search technique. We elaborate upon the details of this pipeline and finish the chapter with an example run that was conducted on simulated Gaussian noise, where we established the performance improvement upon using the hierarchical coherent search over the coincident search. We quantified this

improvement using receiver operator characteristic curves. This chapter is based in part from Ref. Bose et al. (2011).

- **Chapter 4** addresses the prospects of detection of gravitational waves from progenitors of short duration GRBs. CBC systems involving at least one of the binary components as a neutron star are widely considered to be one of the best progenitor models for short duration GRBs (Nakar (2007)). Currently multiple observatories and missions are being planned for detecting orphaned afterglows associated with short GRBs. We motivated a simple calculation using geometry and CBC progenitor model of SGRB to estimate the improvement in the detection rate of gravitational waves using LIGO (and other interferometric observatories) if orphaned afterglow triggers are incorporated as external triggers. We also studied the effect of sky position uncertainty of the GRB in the detection efficiency of gravitational wave signals from these sources. We also studied the mass-sky position parameter error covariance and showed that in presence of accurate sky position information the detection efficiency still remains sub-optimal for a targeted search compared to a search that does not use any sky position information and searches for the gravitational wave in the sky, despite the greater false alarm probability from increased trials factor in the later. We invented a new sky-patch model for search that allows for some relaxation in the sky position, yet constraining the search to a patch on the sky, thereby reducing the false alarm probability. We showed that there are parts of the parameter space where the sky-patch mode of search performs better than the standard targeted search. We carried out an analysis on spinning injections where the search was conducted with non-spinning templates. We found that incorporating multiple sky points tends to increase SNR of some of the found injection triggers. This hints at the possible presence of parameter covariance between spin and sky position errors. The discussions in this chapter is based on the work we presented in Ref. Ghosh and Bose (2013).

- **Chapter 5** focuses on the effect of waveform inaccuracy on parameter estimation and detection of gravitational wave signals. One way gravitational wave astronomy can contribute to multi-messenger astronomy is by providing information that is complementary to the findings of the electromagnetic observatories. This includes the estimation of parameter that can be measured directly using gravitational wave observations, like component masses in the case of CBC sources and distances. Prompt emissions from a GRB source, that is not beamed at us, will missed by electromagnetic observatories. However, gravitational waves detected from these sources may help one locate them in patches on the sky that can be followed up using X-ray and optical telescopes to search for afterglows. However, all these pursuits understandably requires precision parameter estimation ability. We study how the waveform inaccuracy in our modeled searches hurt chirp mass and symmetric mass ratio estimation and how those errors vary over the mass parameter space.

We then studied the effect of the waveform inaccuracy from the perspective of detection in an external trigger search. Here we considered the effect of using non-spinning templates in order to search spinning waveform. We contrasted the results with the case where we used spin-aligned templates to search for spin-aligned signals and quantified the performance improvement using receiver operator characteristic curves.

We explored the implementation of the coherent  $\chi^2$  statistic to construct a detection statistic that is better suited to deal with non-stationary noise artifacts. Incorporating this new detections statistic in conjunction with the spinning template bank, we were able to enhance the detection probability of the pipeline. The studies presented in this chapter is based on the work we presented in Refs. Bose et al. (2010) and Ghosh et al. (2013).

# Chapter 2

## A brief survey of gravitational wave physics, experiment and techniques of data analysis

The endeavor for the detection of gravitational waves presently undertaken by the Laser Interferometer Gravitational wave Observatory (LIGO) in the United States and its counterparts around the world like Virgo in Italy, etc., will soon reach its climax within the end of this decade. Among many interesting astrophysical targets, one the most prominent one is a compact binary coalescing (CBC) system. These are some of the most violent events in the universe that, unfortunately in most of the cases, go unnoticed since only a tiny fraction of their energy gets emitted in electromagnetic waves. Bulk of the energy radiated by such systems is in the form of gravitational waves. With the advent of gravitational wave astronomy our knowledge about such systems will be enriched.

Prediction of gravitational radiation was already made by Einstein in 1916 (Einstein (1916)). Its existence was verified in 1978 by the observations conducted by Russell Alan Hulse and Joseph Hooton Taylor when they observed the binary pulsar system PSR B1913+16 (Weisberg et al. (2010)). The orbital period of the pulsar was found to be decreasing at a

rate predicted by Einstein’s relativity (see Fig. 2.1). The ratio of the observed decay rate of

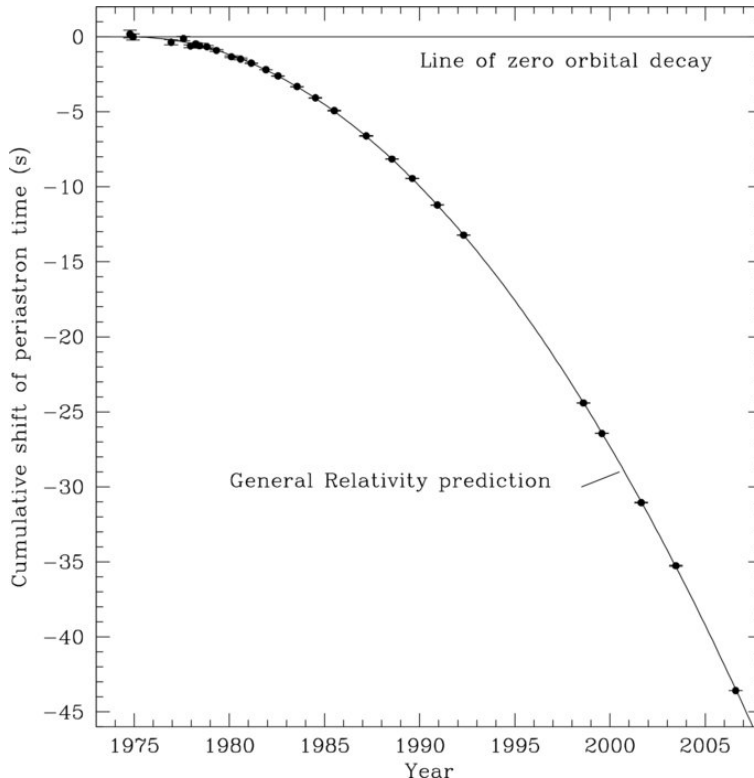


Figure 2.1: Figure obtained from Weisberg et al. (2010).

the orbital period to the predicted rate was calculated to be  $0.997 \pm 0.002$  in Ref. Weisberg et al. (2010). This discovery helped Hulse and Taylor win the 1993 Nobel prize in Physics. This however was an indirect verification of the existence of gravitational waves. Detection of gravitational waves in interferometric detectors may become the first direct detection of gravitational waves.

However not all sources of gravitational waves are electromagnetically weak. One notable exception is the short duration gamma ray burst (SGRB). It is conjectured that a short duration gamma ray burst has a CBC progenitor. However there are other alternative hypotheses for SGRB progenitors. A direct detection of gravitational waves in coincidence with a short GRB will prove decisive about the question of the right progenitor model of SGRB. Presence of *a priori* knowledge about the sky position and time of occurrence of these coalescing events from the GRB alerts will allow us to perform a targeted search, thus,

improving this chances of GW detections. We will discuss more about targeted searching in chapter 4.

In the rest of this chapter we will first develop the mathematical framework of gravitational radiation and thereafter will discuss briefly about LIGO detectors. We will conclude this chapter with some discussion about the data analysis techniques that are used in a CBC search.

## 2.1 Gravitational waves

In Newtonian theory gravity acts instantaneously. What it means is that if the source of the gravitational potential were to change, a test particle placed at infinity will immediately react to that. A crude, but useful example that is often cited supposes that if the sun instantaneously disappears from the center of the solar system, should the planets immediately deviate from their elliptical orbits and start moving tangentially away? If this was to be true then the planets will come to ‘know’ of the sun’s non-existence much before the light from the sun ceases to reach the planets. This breaks a fundamental principle of the Special Relativity by allowing the sun send signal (of its absence) faster than light. General Relativity (GR) helps us formulate the problem in such a way that the solution naturally shows that gravity too should conform with the ultimate speed limit of light. In GR gravity is no longer considered a force in itself. Instead the presence of massive objects curves the spacetime around them, and, gravity is the spacetime curvature. Here we will simply delineate the quantities that are essential for us to develop the theory of gravitational waves. For a more detailed discussion on these quantities the reader can refer to Appendix A. We will follow the following convention unless otherwise specified. Repeated indices (also called ‘dummy’ indices) are summed over and  $x^0 = ct$ ,  $x^1 = x$ ,  $x^2 = y$ ,  $x^3 = z$ . The Greek indices like  $\mu, \nu$  run from (0, 3) and Latin indices like  $i, j$  run from (1, 3).

For given spacetime metric  $g_{\mu\nu}$ , we define a quantity, called the Christoffel symbols, as

follows

$$\Gamma_{\mu\nu}^{\delta} = \frac{1}{2}g^{\alpha\delta} \left[ \frac{\partial g_{\alpha\mu}}{\partial x^{\nu}} + \frac{\partial g_{\alpha\nu}}{\partial x^{\mu}} - \frac{\partial g_{\mu\nu}}{\partial x^{\alpha}} \right]. \quad (2.1)$$

The curvature of the spacetime, characterized by a quantity called the Riemann curvature tensor, is defined using the derivatives and products of the Christoffel symbols

$$R_{\nu\alpha\delta}^{\mu} = \partial_{\alpha}\Gamma_{\nu\delta}^{\mu} - \partial_{\delta}\Gamma_{\nu\alpha}^{\mu} + \Gamma_{\gamma\alpha}^{\mu}\Gamma_{\nu\delta}^{\gamma} - \Gamma_{\gamma\delta}^{\mu}\Gamma_{\nu\alpha}^{\gamma}, \quad (2.2)$$

where  $\partial_{\mu} \equiv \partial/\partial x^{\mu}$ . A quantity related to the Riemann curvature tensor is the Ricci tensor, which is obtained by contracting two indices of the Riemann tensor using the metric tensor as follows

$$R_{\nu\delta} = g^{\mu\alpha} R_{\mu\nu\alpha\delta}. \quad (2.3)$$

$R_{\nu\delta}$  is symmetric second rank tensor. Contracting once more gives us a scalar called the Ricci scalar

$$R = g^{\nu\delta} R_{\nu\delta}. \quad (2.4)$$

From the Ricci tensor and the Ricci scalar it is possible to construct a tensor that is divergenceless,

$$G_{\mu\nu} = R_{\mu\nu} - \frac{1}{2}g_{\mu\nu}R, \quad (2.5)$$

this is called the Einstein tensor. Finally the Einstein field equations that connect the spacetime curvature to matter is given by

$$G_{\mu\nu} = \frac{8\pi G}{c^4} T_{\mu\nu}, \quad (2.6)$$

where  $T_{\mu\nu}$  in the right hand side is called the stress-energy tensor. The  $T^{00}$  term in the stress-energy tensor is the energy density (divided by  $c^2$ ),  $T^{0i}$  is the momentum density,  $T^{ii}$  terms are the pressure along three spatial axes, and other  $T^{ij}$  terms corresponds to the momentum fluxes through planes described by the  $x^i - x^j$  planes.

## Linearized gravity

The theory of linearized gravity lies at the foundation of gravitational wave physics. For a detailed discussion on this subject the reader can refer to Appendix B. We present the final results here.

In the weak field limit we can express the curvature as a perturbation on the flat space-time. This assumption lets us write the metric in weak field regime as

$$g_{\mu\nu} = \eta_{\mu\nu} + h_{\mu\nu}, \quad (2.7)$$

where  $|h_{\mu\nu}| \ll 1$ . Thus from Eq. (2.1) we can write

$$\Gamma_{\alpha\beta}^{\gamma} = \frac{1}{2}\eta^{\gamma\delta} \left( \frac{\partial h_{\beta\delta}}{\partial x^{\alpha}} + \frac{\partial h_{\alpha\delta}}{\partial x^{\beta}} - \frac{\partial h_{\alpha\beta}}{\partial x^{\delta}} \right). \quad (2.8)$$

Knowing the form of the Cristoffel symbols, one can now proceed to calculate the components of the Riemann curvature tensor from Eq. (2.2), the Ricci tensor using Eq. (2.3), the Ricci scalar using Eq. (2.4) and finally the Einstein tensor for weak field as

$$G_{\alpha\beta} = \frac{1}{2} \left[ \frac{\partial^2 h_{\alpha}{}^{\mu}}{\partial x^{\mu} \partial x^{\beta}} - \eta^{\mu\delta} \frac{\partial^2 h_{\alpha\beta}}{\partial x^{\mu} \partial x^{\delta}} - \frac{\partial^2 h}{\partial x^{\alpha} \partial x^{\beta}} + \frac{\partial^2 h^{\mu}{}_{\beta}}{\partial x^{\alpha} \partial x^{\mu}} \right] - \frac{1}{2} \eta_{\alpha\beta} \left[ \frac{\partial^2 h^{\mu\nu}}{\partial x^{\mu} \partial x^{\nu}} - \eta^{\mu\nu} \frac{\partial^2 h}{\partial x^{\mu} \partial x^{\nu}} \right]. \quad (2.9)$$

The trace-reversed metric perturbation can be written as,  $\bar{h}_{\alpha\beta} = h_{\alpha\beta} - \frac{1}{2}\eta_{\alpha\beta} h$ , where  $h$  is the trace of the metric perturbation. Using these expressions and applying the Lorenz gauge condition ( $\partial^{\bar{h}}{}^{\mu\alpha}/\partial x^{\mu} = 0$ ), one can write

$$\square \bar{h}_{\alpha\beta} = -\frac{16\pi G}{c^4} T_{\alpha\beta}, \quad (2.10)$$

which is the Einstein's field equation in the linearized gravity. Thus in free space this becomes

the wave equation

$$\square \bar{h}_{\alpha\beta} = 0. \quad (2.11)$$

One of the solutions of the above equation is the plane wave solution.

$$\bar{h}_{\alpha\beta} = A_{\alpha\beta} e^{ik_\gamma x^\gamma}, \quad (2.12)$$

where the quantity  $A_{\alpha\beta}$  is the amplitude of the gravitational wave. Note that this is a second rank symmetric tensor. Thus the number of independent components of  $A_{\alpha\beta}$  is 10. Choosing a gauge conditions where the time components of the amplitude terms are zero and the perturbation is transverse and traceless helps us to reduce the number of independent components in the amplitude to 2. Which we write as follows

$$A_{\alpha\beta}^{\text{TT}} = \begin{pmatrix} 0 & 0 & 0 & 0 \\ 0 & h_+ & h_\times & 0 \\ 0 & h_\times & -h_+ & 0 \\ 0 & 0 & 0 & 0 \end{pmatrix}. \quad (2.13)$$

This is the amplitude of the gravitational wave propagating through free space in the transverse traceless gauge (symbolically represented by the superscript TT). In this gauge the solution of the linearized Einstein's equations in Eq. (B.13) is given by

$$h_{ab}^{\text{TT}}(t) = \frac{2G}{c^4 r} \ddot{Q}_{ab}^{\text{TT}}(t - r/c), \quad (2.14)$$

where  $Q^{ab}$  is the mass quadrupole moment tensor defined for a system with density profile  $\rho(x^\mu)$  as

$$Q^{ab} = \int x^a x^b \rho(t - r/c, r) dV. \quad (2.15)$$

where  $dV$  is a volume element, and  $r^2 = x_i x^i$ .

## 2.2 Gravitational wave sources

In the last section we developed the theory of the gravitational wave, how it can be characterized using matrix perturbation and how it is generated given a mass distribution. Note that in Eq. (B.24) the presence of double derivative on the mass quadrupole moment indicates that finite gravitational wave radiation is only possible from some specific types of systems. For instance, a stationary system will not generate gravitational waves. Similarly a system moving with uniform velocity will not generate any gravitational waves. In general any constant spherically symmetric motion is incapable of generating gravitational waves. We will here discuss some of the most important sources of gravitational sources in nature.

The gravitational collapse of the core of an evolved massive star emanates an enormous quantity of energy. A fraction of this energy is emitted in the form of gravitational waves. There are two mechanism through which the gravitational core collapse of a star can emit gravitational waves. In one model, when a star collapses under its own gravity, it spins up (conserving the angular momentum). Eventually this core forms a neutron star, but prior to the formation of the neutron star, dynamical instabilities of this highly spinning core can emit gravitational waves.

The other model incorporates r-mode instabilities in neutron stars. However, as we have discussed, the system cannot be spherically symmetric for gravitational wave emission to be possible. Thus, it is essential that the collapse is not perfectly spherically symmetric. Since, at the present, there does not exist any realistic solution of an asymmetric core collapse in three dimension. Thus the search for gravitational waves from stellar collapses has to be performed without the aid of any model.

A rapidly rotating imperfectly spherical neutron star is another interesting source for gravitational waves. such a star will loose energy through gravitational wave radiation slowly. This is an example of continuous wave emission. Even though the radiated power is smaller compared to a core collapse, integrated over long duration (months), it can be good candidate for detection.

A binary system composed of compact objects like neutron stars and black holes are arguably the candidates best suited for detection of gravitational waves. These are some of the strongest emitters known. Additionally, we also know fairly accurately the analytical expressions of the gravitational waveforms that are emitted from these systems. The knowledge of the waveform for a compact binary systems allows us to search for these signals in noisy detector data, giving us an edge in discovery over all other prospective detection candidates. In a compact binary system the gravitational wave emitted lowers the energy of the system. This results in shrinking of the distance of separation between the objects. The resulting motion is called an inspiral, where the two objects comes closer to each other thereby increasing the mass quadrupole moment and hence the amplitude of the radiation. In the next section we will derive the expression of these waveforms in the weak field limit. There are more accurate compact binary coalescence (CBC) waveforms at stronger limits of gravity that are available in the literature where various degrees of approximations and numerical methods are used (discussions about these will be presented in later chapters). But the calculation in the weak field limit is still useful to give us an idea of the fundamental structure of the CBC waveform.

### **2.2.1 Gravitational waves from compact binary inspiral - weak field limit**

For the rest of the work we will be concerned with the compact binary coalescing (CBC) systems. So it is good place to build some insight on it. Here we will derive an expression of the gravitational waveform using weak field approximation that was developed in Sec. 2.1.

Let us assume that the compact binary components are point objects, each having a mass denoted by  $m_1$  and  $m_2$ . Let us further assume that the motion is confined to  $x^1 - x^2$  plane. We depict that in Fig. 2.2. We choose the coordinate system at the center of mass frame of reference. The line joining the two components makes an angle  $\varphi$  with the  $x^1$  axis. The distance between the two masses at any given moment of time is given by

$l = r_1 + r_2$  such that  $r_1 = rm_2/(m_1 + m_2) = l\mu/m_1$  and  $r_2 = rm_1/(m_1 + m_2) = l\mu/m_2$ , where  $\mu = m_1m_2/(m_1 + m_2)$  is the reduced mass of the system. The calculation of the components of the mass quadrupole moment becomes trivial in this scenario.

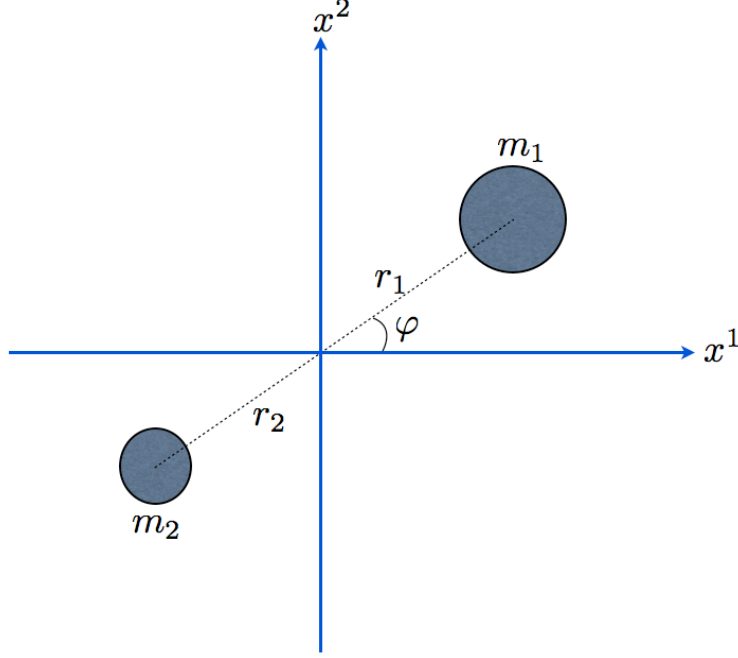


Figure 2.2: Compact binary system of masses  $m_1$  and  $m_2$  in the  $x^1 - x^2$  plane.

Let the  $x^i$  component of the position vector of mass  $m_{1,2}$  be given by  $x_{1,2}^i$ , thus from Fig. 2.2 we note that

$$\begin{aligned} x_1^1 &= r_1 \cos \varphi, & x_1^2 &= r_1 \sin \varphi, & x_1^3 &= 0, \\ x_2^1 &= -r_2 \cos \varphi, & x_2^2 &= -r_2 \sin \varphi, & x_2^3 &= 0. \end{aligned} \tag{2.16}$$

Thus the components of the mass quadrupole moments calculated using Eq. (B.23) are

$$\begin{aligned} \mathcal{Q}_{11} &= m_1(r_1 \cos \varphi)^2 + m_2(-r_2 \cos \varphi)^2 = \left( m_1 \frac{l^2 \mu^2}{m_1^2} + m_2 \frac{l^2 \mu^2}{m_2^2} \right) \cos^2 \varphi = \frac{1}{2} \mu l^2 (1 + \cos 2\varphi), \\ \mathcal{Q}_{12} &= I_{21} = m_1 r_1^2 \sin \varphi \cos \varphi + m_2 r_2^2 \sin \varphi \cos \varphi = l^2 \mu^2 \left( \frac{1}{m_1} + \frac{1}{m_2} \right) \sin \varphi \cos \varphi = \frac{1}{2} \mu l^2 \sin 2\varphi \\ \mathcal{Q}_{22} &= m_1(r_1 \sin \varphi)^2 + m_2(-r_2 \sin \varphi)^2 = \left( m_1 \frac{l^2 \mu^2}{m_1^2} + m_2 \frac{l^2 \mu^2}{m_2^2} \right) \sin^2 \varphi = \frac{1}{2} \mu l^2 (1 - \cos 2\varphi). \end{aligned} \tag{2.17}$$

If we assume that the angular velocity of the system is  $\omega$  then  $\varphi = \omega t$ . Thus double time

derivatives of the components of the mass quadrupole moment can be written as

$$\begin{aligned}
\ddot{Q}_{11} &= \frac{1}{2}\mu l^2 \frac{d}{dt}(1 + \cos 2\omega t) = -2\mu l^2 \omega^2 \cos 2\varphi, \\
\ddot{Q}_{12} &= \frac{1}{2}\mu l^2 \frac{d}{dt} \sin 2\omega t = -2\mu l^2 \omega^2 \sin 2\varphi, \\
\ddot{Q}_{22} &= \frac{1}{2}\mu l^2 \frac{d}{dt}(1 - \cos 2\omega t) = 2\mu l^2 \omega^2 \cos 2\varphi.
\end{aligned} \tag{2.18}$$

Note that the trace of the  $\ddot{Q}_{ij}$  is zero and the matrix is symmetric, which means that in the chosen geometry the double time derivative of the mass quadrupole moment is already in the symmetric traceless coordinates. Therefore we can use Eq. (B.24) directly to obtain the gravitational waveform for a compact binary system.

$$h_{ab}^{\text{TT}}(t) = \frac{2G}{c^4 r} \ddot{Q}_{ab}^{\text{TT}}(t - r/c) = -\frac{4G\mu l^2 \omega^2}{c^4 r} \begin{pmatrix} \cos 2\varphi(t - \frac{r}{c}) & \sin 2\varphi(t - \frac{r}{c}) & 0 \\ \sin 2\varphi(t - \frac{r}{c}) & -\cos 2\varphi(t - \frac{r}{c}) & 0 \\ 0 & 0 & 0 \end{pmatrix}. \tag{2.19}$$

If the plane of the binary is not perpendicular to the observer's line of sight, then we need to use Eulerian rotation matrix to transform the waveform tensor from the frame of the binary to the frame of the observer. This is depicted in Fig. 2.3.

Transformation from the source frame to the wave frame involves two eulerian rotations. The first rotation is performed by rotating  $x_s$  axis about the source frame  $z_s$  axis to align itself to the projected  $x$  axis of the wave frame (dashed arrow in the source frame in Fig. 2.3) by an angle  $\psi$ . The next transformation involves rotation of the  $z_s$  axis about the new  $x_s$  axis by an angle  $\iota$ . Thus mathematically the two frames are related by a rotation matrix

$$\mathcal{R}(\psi, \iota) = \begin{pmatrix} 1 & 0 & 0 \\ 0 & \cos \iota & \sin \iota \\ 0 & -\sin \iota & \cos \iota \end{pmatrix} \begin{pmatrix} \cos \psi & \sin \psi & 0 \\ -\sin \psi & \cos \psi & 0 \\ 0 & 0 & 1 \end{pmatrix}, \tag{2.20}$$

Thus the transformation of the metric perturbation from the source frame to the wave frame

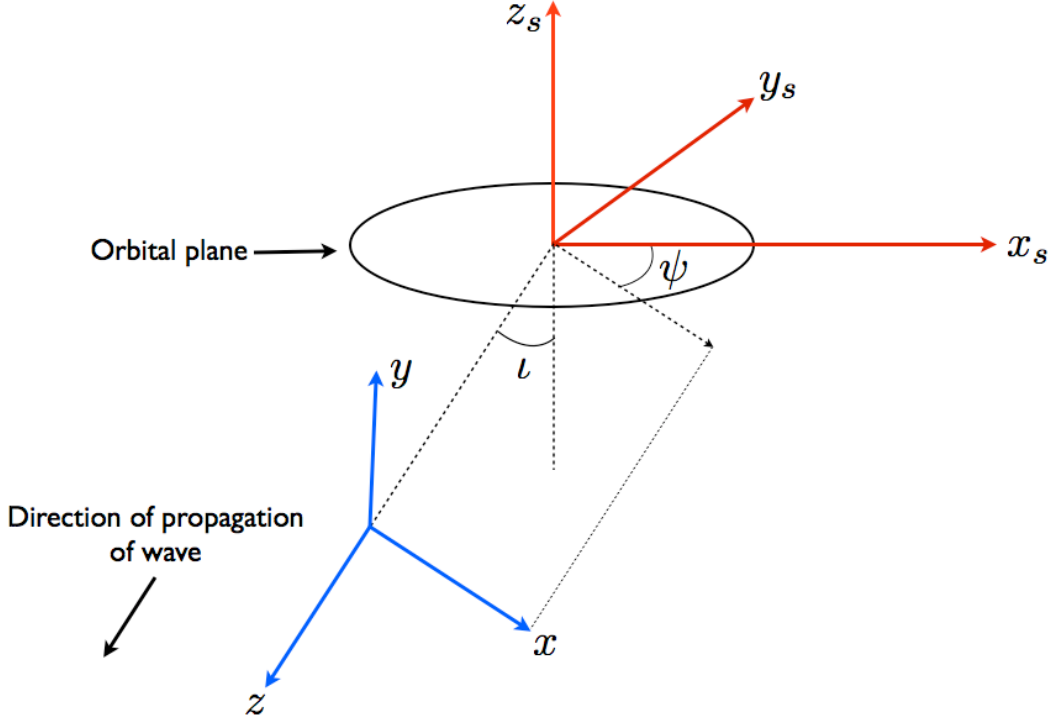


Figure 2.3: The above figure shows the two frames, source frame shown with red axes and axes labeled by subscript  $s$ , and the wave frame shown with blue axes. The  $z$  axis in the wave frame denotes the direction of propagation of the wave. The inclination angle  $\iota$  is the angle between the  $z_s$  axis of the source frame and the  $z$  axis of the wave frame. The polarization angle  $\psi$  is the angle between the  $x_s$  axis of the source frame and the  $x$  axis of the wave frame projected on to the source frame.

is given by

$$\mathbf{h}'(t) = \mathcal{R}\mathbf{h}^{\text{TT}}(t)\mathcal{R}^{\text{T}}, \quad (2.21)$$

where the  $\mathbf{h}'(t)$  denotes the transformed metric perturbation tensor in matrix notation and  $\mathbf{h}$  is the source frame transverse traceless metric perturbation tensor. Note that the transformation to the new coordinate will not preserve the transverse traceless state of the source metric. Thus we will need to re-convert it to this form after the transformation. Therefore we get

$$\mathbf{h}'(t) = -\frac{4G\mu l^2 \omega^2}{c^4 r} \mathcal{R} \begin{pmatrix} \cos 2\varphi & \sin 2\varphi & 0 \\ \sin 2\varphi & -\cos 2\varphi & 0 \\ 0 & 0 & 0 \end{pmatrix} \mathcal{R}^{\text{T}}. \quad (2.22)$$

After calculating the above product of three matrices we get

$$\mathbf{h}'(t) = -\frac{4G\mu l^2 \omega^2}{c^4 r} \begin{pmatrix} \cos \epsilon & \sin \epsilon \cos \iota & -\sin \epsilon \sin \iota \\ \sin \epsilon \cos \iota & -\cos \epsilon \cos^2 \iota & \cos \epsilon \cos \iota \sin \iota \\ -\sin \epsilon \sin \iota & \cos \epsilon \cos \iota \sin \iota & \cos \epsilon \sin^2 \iota \end{pmatrix}, \quad (2.23)$$

where  $\epsilon = 2\varphi - 2\psi$ . Clearly this is not transverse traceless anymore. Taking the transverse projection along the  $z$  axis of this matrix is equivalent to substituting all the  $(i, 3)$  and  $(3, i)$  elements by zero. Thus we get the transverse component to be

$$\mathbf{h}'(t) = -\frac{4G\mu l^2 \omega^2}{c^4 r} \begin{pmatrix} \cos \epsilon & \sin \epsilon \cos \iota & 0 \\ \sin \epsilon \cos \iota & -\cos \epsilon \cos^2 \iota & 0 \\ 0 & 0 & 0 \end{pmatrix}. \quad (2.24)$$

The trace of the above quantity is given by

$$h' = -\frac{4G\mu l^2 \omega^2}{c^4 r} (\cos \epsilon - \cos \epsilon \cos^2 \iota), \quad (2.25)$$

from which we find the transverse traceless metric perturbation in the wave frame to be

$$\begin{aligned} \mathbf{h}'^{\text{TT}}(t) &= \mathbf{h}'(t) - h' \begin{pmatrix} 1 & 0 & 0 \\ 0 & 1 & 0 \\ 0 & 0 & 0 \end{pmatrix}, \\ &= \frac{4G\mu l^2 \omega^2}{c^4 r} \begin{pmatrix} -\frac{1}{2} \cos(2\varphi - 2\psi)(1 + \cos^2 \iota) & \sin(2\varphi - 2\psi) \cos \iota & 0 \\ \sin(2\varphi - 2\psi) \cos \iota & \frac{1}{2} \cos(2\varphi - 2\psi)(1 + \cos^2 \iota) & 0 \\ 0 & 0 & 0 \end{pmatrix}, \end{aligned} \quad (2.26)$$

where we have substituted back  $\epsilon$ . Thus the two polarizations of the gravitational waves, commonly called the *cross* polarization and the *plus* polarization in the wave frame are given

by

$$\begin{aligned} h_+(t) &= -\frac{4G\mu l^2 \omega^2}{c^4 r} \frac{(1 + \cos^2 \iota)}{2} \cos(2\varphi - 2\psi), \\ h_\times(t) &= -\frac{4G\mu l^2 \omega^2}{c^4 r} \cos \iota \sin(2\varphi - 2\psi). \end{aligned} \quad (2.27)$$

Thus we have derived the mathematical expression of the gravitational waveform emitted from a compact binary system in the weak field limit. Note that the amplitude of both the plus and the cross polarizations are proportional to the newtonian potential. More accurate waveform is obtained by using post newtonian approximations, which is essentially an expansion of the general relativistic equation of motion in orders of  $v^2/c^2$ . We show here the gravitational waveform in the restricted post newtonian approximation obtained from Ref. Pai et al. (2001). In chapter 4 we will use this waveform to derive an expression for the detection statistic in a network of detectors.

$$\begin{aligned} h_+(t; r, \iota, \delta_c, t_c, \xi, ) &= \frac{2\mathcal{N}}{r} a^{-1/4}(t; t_c, \xi) \frac{1 + \cos^2 \iota}{2} \cos[\varphi(t; t_c, \xi) + \delta_c], \\ h_\times(t; r, \iota, \delta_c, t_c, \xi, ) &= \frac{2\mathcal{N}}{r} a^{-1/4}(t; t_c, \xi) \cos \iota \sin[\varphi(t; t_c, \xi) + \delta_c], \end{aligned} \quad (2.28)$$

where the factor  $\mathcal{N}$  is given by,

$$\mathcal{N} = \frac{2G^{5/3} \mathcal{M}^{5/3} (\pi f_s)^{2/3}}{c^4}, \quad (2.29)$$

and,

$$a(t; t_c, \xi) = \frac{t_c - t}{\xi}. \quad (2.30)$$

$\delta_c$  is the coalescence phase of the binary orbit,  $r$  is the distance to the source, and  $\mathcal{M}$  is the chirp mass defined as,

$$\mathcal{M} = \frac{(m_1 m_2)^{3/5}}{(m_1 + m_2)^{1/5}}, \quad (2.31)$$

and  $\xi$  is the chirp time given by

$$\xi = 1390 \left( \frac{\mathcal{M}}{M_\odot} \right)^{-5/3} \left( \frac{f_s}{10 \text{ Hz}} \right)^{-8/3} \text{ sec}. \quad (2.32)$$

The  $\psi$  dependence in Eq. (2.27) is generally separated from the waveform (which is possible because  $\psi$  is introduced in the expression of the waveform at the wave frame through the operation of a rotation matrices involving  $\psi$ ). This rotation is performed about the propagation axis of the wave. Thus, it is possible to include it in a function, called the antenna pattern function that we will discuss in the next chapter.

## 2.3 Laser interferometric techniques to detect gravitational waves

In this section we will discuss briefly about the technique of detection of gravitational waves using laser interferometry. The principle of Michelson interferometer is the fundamental idea behind the construction of the LIGO detectors. The detector consists of two arms of equal lengths that are perpendicular to each other. The mirrors of the interferometer at the end of these arms act as the test masses for the incoming gravitational waves. The phase of the laser beam in the interferometer is modulated in the presence of a gravitational wave. The optical path lengths of the interferometer arms are set in such a way that in absence of a gravitational wave the light interferes destructively at the photo diode shown in Fig. 2.4, where we show a schematic diagram of the basic construction of a LIGO interferometer.

The partially transmitting input mirrors between the highly reflecting end mirrors and the beam splitter in both the arms reflect the beam of laser multiple times increasing the power in the cavities. In LIGO this method increases the power up to a factor of 100 at about 100 Hz. The partially reflecting mirror between the beam splitter and the laser recycles the power building up optical cavity. It uses the phenomenon of optical resonance to amplify the power that is being lost in the Michelson interferometer.

### 2.3.1 Basic interferometric principle

We will now consider a very special case, following what was done in Ref. Saulson (1994),

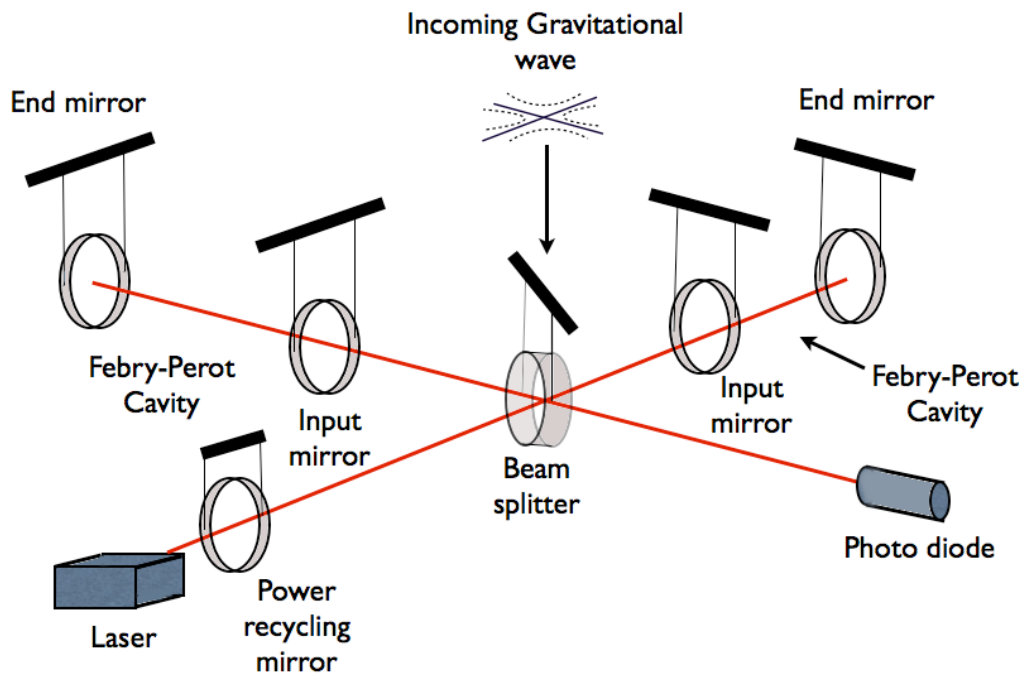


Figure 2.4: A schematic diagram of a power recycled Fabry-Perot Michelson interferometer.

to show how the interferometer can interact with an incoming gravitational wave. Let us first align the coordinate system such that the arms of the interferometer form the  $x$  and  $y$  axes and the origin is at the point of the beam splitter. Also let us assume that the incoming gravitational wave is traveling along the negative  $z$  axis. Since the light in the arms of the interferometer is confined to move along either the  $x$  or the  $y$  axis, an interval between any two points will depend only on  $dx$  or  $dy$  depending on which arm we are calculating. Thus this choice of coordinates helps us in having to deal with only the  $h_{11}$  and the  $h_{22}$  components of the metric perturbation that we developed in Eq. (2.19). From special relativity we recall that a beam of light always travels along a null geodesic ( $ds = 0$ ). Thus, we can write

$$g_{\mu\nu} dx^\mu dx^\nu = 0, \tag{2.33}$$

$$(\eta_{\mu\nu} + h_{\mu\nu}) dx^\mu dx^\nu = 0.$$

Now we are going to assume that the arms of the interferometer are sufficiently small such

that the light travel time within the interferometer is much smaller than the time period of oscillation of the gravitational wave. This ensures that while calculating the difference in time taken by a beam of light, that is split at  $t = 0$  at the beam splitter, we do not have to worry about time varying  $h_{11}$  and  $h_{22}$ . For a beam of light along the  $x$  axis, the time  $t_+$  taken by it to travel from the beam splitter to the end test mass (distance  $L$ ) is given by

$$\begin{aligned} (\eta_{\mu\nu} + h_{\mu\nu})dx^\mu dx^\nu &= 0, \\ -c^2 dt^2 + [1 + h_{11}(\omega t)]dx^2 &= 0, \\ t_+ &= \frac{1}{c} \int_0^L [1 + h_{11}(\omega t)]^{1/2} dx, \end{aligned} \tag{2.34}$$

The time taken by the returning beam of light after reflecting from the end mirror can be found similarly and in this approximation where  $h_{11}(\omega t)$  does not change appreciably during that time, the amount of time taken by the beam can be calculated to be the same

$$t_- = \frac{1}{c} \int_0^L [1 + h_{11}(\omega t)]^{1/2} dx. \tag{2.35}$$

Since the metric perturbation terms are taken to be very small  $|h_{11}| \ll 1$  we can approximate the total time  $T_x$  taken for the beam of light in the  $x$  arm to return back to the beam splitter as

$$T_x = \frac{2}{c} \int_0^L \left[ 1 + \frac{1}{2} h_{11}(\omega t) \right] dx, \tag{2.36}$$

and the total time taken for the beam of light in  $y$  arm to return is given by

$$T_y = \frac{2}{c} \int_0^L \left[ 1 + \frac{1}{2} h_{22}(\omega t) \right] dy, \tag{2.37}$$

where we know from Eq. (2.19) that  $h_{11}(\omega t) = -h_{22}(\omega t) = h$ . Therefore the difference in time taken by the beams of light in the  $x$  and the  $y$  arm, to return to the beam splitter is

given by

$$\begin{aligned}\Delta T &= \frac{2}{c} \int_0^L \left[ 1 + \frac{1}{2} h(\omega t) \right] dx - \frac{2}{c} \int_0^L \left[ 1 + \frac{1}{2} h(\omega t) \right] dy, \\ \Delta T &= \frac{2}{c} \int_0^L h(\omega t) dx = h(\omega t) \frac{2L}{c},\end{aligned}\tag{2.38}$$

from which we get the shift in phase due to the gravitational wave to be

$$\Delta\phi_{\text{laser}} = h(\omega t) \frac{2L}{c} \frac{2\pi c}{\lambda},\tag{2.39}$$

where  $\lambda$  is the wavelength of the laser used. One key thing to note here is that the change in phase, which is responsible for the shifting of the interference fringes, is directly proportional to the length of the interferometers and that is why these interferometers are built in such large scales.

### 2.3.2 Noises in interferometric gravitational wave detectors

The strains in the interferometer arms due to gravitational wave, from a CBC source, that is typically coming to us from an extra galactic distance, are smaller than nuclear dimension. Measuring such weak signals presents serious obstacles due to ambient and instrumental noises. There are multiple sources of noises that affect the performance of the interferometer. Significant effort in the LIGO Scientific Collaboration (LSC) is spent to address this issue. Reduction of noise is key to science outcome of the experiment. Thus a brief discussion of the different types of noises in interferometers is presented next.

#### Thermal noise

Detection of gravitational waves in an interferometer involves precise measurement of motion in the end mirrors. This motion is smaller than the scale of nuclear diameters. The mean square thermal vibrations in a system is proportional to the temperature. If some sort of thermal noise reduction is not implemented, this can effectively dominate the motion of the end mirrors. The energy of the thermal noise tends to be concentrated near the resonance

frequencies of the mirrors. Thus the most obvious and simplest step one could take would be to construct mirrors whose resonant frequencies lie away from the frequency band that is of astrophysical interest. Thermal noise is further reduced by reducing the cross section area of the pendulum wire as the elastic energy in the flexing regions of the wires is proportional to the fourth power of the radius of the cross section as given in Ref. Abbott and et. al (2009). Mechanical damping in the test mass mirrors cause thermal noise through dissipation. This constitutes the dominant thermal noise through dissipation.

### Photon shot noise and radiation pressure noise

As we have discussed before the detection of a gravitational wave requires the ability to differentiate between a dark and a bright fringe at the photo diode. However the definition of a ‘dark’ or a ‘bright’ fringe depends on the number of photons present at any given time. Light that interferes after being reflected from the end mirrors arrives as a stream of photons. The power  $P$  of a laser is related to the average number of photons that it emits per second. Following Ref. Saulson (1994) we can write, this rate of photons emitted per second, or the photon flux as

$$\bar{n}_\gamma = \frac{\lambda}{h_p c} P, \quad (2.40)$$

where  $h_p$  is the Planck’s constant and  $\lambda$  is the wavelength of the laser. However, for any given rate, if one estimates the probability distribution of the number of photons that are actually forming the fringe, which is being observed over a fixed duration of time, then this turns out to be Poisson distribution. Over a fixed time interval of  $t_{\text{obs}}$  if one makes a measurement of the number of photons that are forming the fringe, then over an ensemble of such intervals the average number of photon count will be  $\bar{n}_\gamma t_{\text{obs}}$ . However for a single interval the fluctuation is given by

$$\text{fluctuation} = \frac{\sqrt{\bar{n}_\gamma t_{\text{obs}}}}{\bar{n}_\gamma t_{\text{obs}}} = \frac{1}{\sqrt{\bar{n}_\gamma t_{\text{obs}}}} = \sqrt{\frac{h_p c}{\lambda P t_{\text{obs}}}}, \quad (2.41)$$

from which we immediately see that the fluctuation can be reduced by increasing the power of the laser.

However, increasing the power of the laser indefinitely will not be the solution addressing the photon shot noise, since that increases the radiation pressure in the mirrors. Every photon that hits the mirrors imparts a finite amount of momentum and increasing the power results in the increasing the number of photons hitting per second on the mirrors. This will result in the increase of the radiation pressure noise.

### Seismic noise

Finally the vibration on the surface of the earth contributes to the random motion of the mirrors. This noise is called the seismic noise. Seismic noise is not characterized by any fundamental constants like  $k_B$  in the case of thermal noise or  $h_p$  in the case of photon shot noise or radiation pressure noise. The solution to mitigating the seismic noise is vibration isolators. A simple vibration isolator would be a spring that, for a given value of its stiffness constant, will resonate when an external periodic force of frequency

$$f_{\text{res}} = \frac{1}{2\pi} \sqrt{\frac{k}{m}}, \quad (2.42)$$

is applied. At very large frequencies ( $f \gg f_{\text{res}}$ ), the inertia of the mass attached to the spring will not permit the mass to vibrate. Thus the mass has been isolated with the help of the spring from any external vibrations that have a high enough frequency. In LIGO advanced isolation techniques are implemented that essentially use this principle at the fundamental level to reduce seismic noises.

There are other sources of noises. But in this work we will not go into these details. It suffices here to outline the noises in the system that fundamentally put constraints on the operating point of the interferometers. Fig. 2.5 shows a cartoon with all these noises put together. The region shaded in orange is where we aim to detect signals from coalescing

binaries. In Fig. 2.6 we present the actual LIGO sensitivity curves.

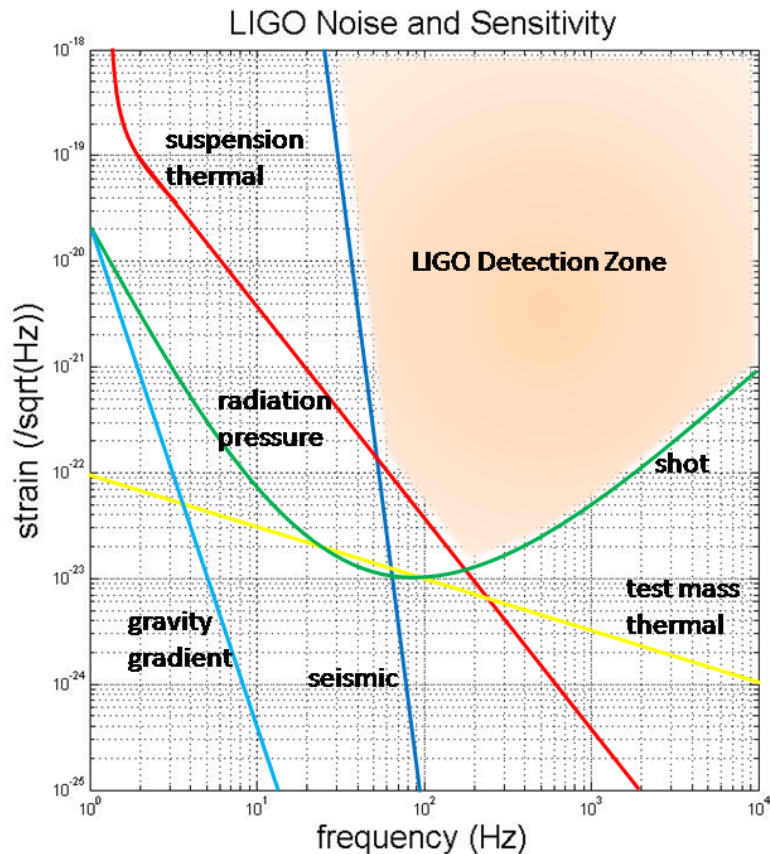


Figure 2.5: LIGO noise curve depiction from Ref. wikipedia commons. Above Fig. shows contributions from the different noise elements.

## 2.4 Basic data analysis techniques

Building of interferometers that are sensitive enough for a science experiment alone does not ensure a detection. Fundamental physical constraints, discussed in the previous section, does not allow us to reduce the noise to such an extent the gravitational wave signals are louder than the noise. As a consequence data analysis techniques are incorporated to search for these signals. Different types of sources have different genre of techniques. Here we will discuss the one that is relevant to this work, namely, data analysis techniques used for compact binary coalescences.

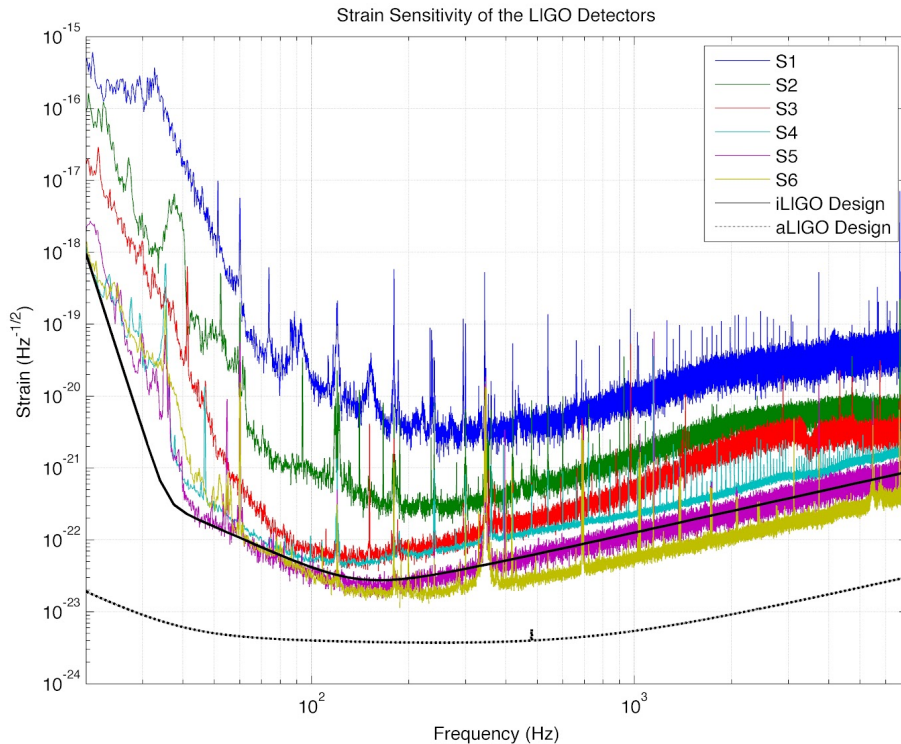


Figure 2.6: Actual LIGO noise curve (courtesy: LIGO Scientific Collaboration). Figure shows how the sensitivity of the detector progressively improved over time. By S6, the sensitivity outperformed the design sensitivity.

### 2.4.1 Data segmentation

A nice description of data segmentation in LIGO CBC search is given in Refs. Brown, Duncan (2004) and Allen et al. (2012). Here we briefly summarize the data segmentation procedure. A continuous stretch of calibrated data obtained from the interferometer that is more than 2048 seconds long is called a science segment. Each science segment is then divided into chunks of data that are 2048 seconds long. These chunks are chosen in the science segment in such a way that they have an overlap of 128 seconds with the previous chunk. Each chunk is then further divided into analysis segments, each of which 256 seconds long. Sixty four seconds of data at the start and an equal duration of data at the end of each analysis segment are discarded. The subsequent analysis segment is chosen in such a way that there is an overlap with the previous analysis segment by 64 seconds. Continuing this

process we analyze the entire 2048 seconds chunk except the first and the last 64 seconds. The noise power spectral density (PSD) of the data is calculated for every analysis segment.

### 2.4.2 Template bank

As we have discussed earlier, in data analysis of CBC signals we take advantage of the fact that we have good prior understanding of the signal. This knowledge of gravitational waveforms allows us to construct templates that we can use to match filter the data to search for signals. A template is essentially a gravitational waveform weighted by the noise power spectral density (PSD) of the detector. As we have discussed the noise PSD is estimated for every analysis segment. The noise PSD for a chunk is calculated by taking the average of the noise PSD for all the analysis segment in the chunk. This ensures that presence of any anomaly, like some non-stationary artifact or a real gravitational wave only minimally biases the PSD. Then using a theoretical waveform family, templates are generated for different values of mass pairs in such way that the maximum loss in signal to noise ratio (SNR) for a signal that falls in between two templates in the template bank is 3%.

For the search of gravitational waves from progenitors of short GRBs, the templates typically used are in the mass range  $[1, 3]M_{\odot}$  for a neutron star and  $[3, 15]M_{\odot}$  for a black hole. One can now generate spin-aligned templates for such externally triggered searches as well. It was shown in Ref. Brown et al. (2012), that it is possible to reduce the effective dimensionality of the template bank for an aligned spin system to 2. Results of such a search will be presented in chapter 5.

### 2.4.3 Matched filtering and detection statistic

At the heart of the search of gravitational waves in noisy data lies the technique of matched filtering. Here we will briefly discuss it. Let us define the inner product between

two time series  $h$  and  $s$  as

$$\langle s|h \rangle = 2\Re \int_{-\infty}^{\infty} \frac{\tilde{s}(f)\tilde{h}^*(f)}{S_n(f)} df, \quad (2.43)$$

where,  $S_n(f)$  is the noise power spectral density. The ratio between the likelihoods of, obtaining a data when a given signal is present, and, obtaining the same same data in the absence of the signal, is called the likelihood ratio. This is given by (see for example in Ref. Capano, Collin D. (2011))

$$\lambda = \frac{\exp \left[ -\frac{1}{2} \langle s-h|s-h \rangle \right]}{\exp \left[ -\frac{1}{2} \langle s|s \rangle \right]} = \exp \left[ \langle s|h \rangle - \frac{1}{2} \langle h|h \rangle \right], \quad (2.44)$$

where  $s$  represents the data and  $h$  represents the gravitational waveform that is used to construct the template. From this definition of the likelihood ratio and the gravitational waveform for compact binary coalescence given in Eq. (2.28) it was shown in Ref. Capano, Collin D. (2011) (and the references therein), that the optimal detection statistic  $\rho$  is given by

$$\rho^2 = \frac{|z|^2}{\sigma^2}, \quad (2.45)$$

where  $\sigma$  is the template norm  $\langle h|h \rangle$ , and  $z$  is the *matched filter output* defined as quadrature sum of the inner products between the data and the two polarization components of the template waveform.

$$\begin{aligned} z^2 &= x^2 + y^2, \\ x &= \langle s|h_+ \rangle, \\ y &= \langle s|h_\times \rangle. \end{aligned} \quad (2.46)$$

Thus for a given time series of strain data and template one can construct the detection statistic using the matched filter output  $z$ . One can then construct a time series of this detection statistic called the SNR time series using Fourier transform as shown in Ref. Capano, Collin D. (2011). The maximum value in the time series is stored whenever it crosses a preset threshold and is called a trigger.

#### 2.4.4 $\chi^2$ test

The detection statistic we discussed in the last section is optimal in Gaussian noise. Unfortunately, real detector noise can have non-stationary noise components. As a result there will be triggers with loud SNR values, after filtering the data with the templates, due to features in the data that look nothing like a gravitational wave signal. In other words we do not have an optimal detection statistic for non-stationary noise exhibited by the interferometers. Thus it is necessary to develop statistical tools that can distinguish between a trigger that is obtained from the matched filter output of a true signal and a trigger due to non-stationarity in the data. The latter type of triggers are called *glitches*. One such test that is used in the CBC pipeline is the  $\chi^2$  test.

The fundamental idea behind this test is that if we split a template into multiples frequency bins that give equal energy in each bin if filtered with the template waveform, then a true signal in the data will give equal contribution to the match filter output in each of these bins. However, for a non-stationary feature in the data the matched filter output might not necessarily be same across all the bins. Details about this test can be found in Ref. Allen (2005). Here we summarize the main points.

Suppose we split the template into  $p$  bins denoted by  $\Delta f_i$  where  $i$  ranges from 1 to  $p$ . We will call each of these a sub-template. Each bin gives equal energy on the average when the data has a signal corresponding to the same template. We can define a match filter between these sub-templates as follows

$$z_i = 2\Re \int_{(-\Delta f_i) \cup (\Delta f_i)} \frac{\tilde{s}(f)\tilde{h}^*(f)}{S_n(f)} df, \quad (2.47)$$

where the range of integration is over negative and positive values of frequencies in the bin defined by  $\Delta f_i$ . It is obvious then that the total match filter output  $z$  is simply given by

$$z = \sum_{i=1}^p z_i. \quad (2.48)$$

From this we can define the  $\chi^2$  statistic as

$$\chi^2 = p \sum_{i=1}^p \left( z_i - \frac{z}{p} \right)^2, \quad (2.49)$$

The mean value of  $\chi^2$  is  $p - 1$  if there is no non-stationarity in the data. However for glitches typically this value will be larger. This gives us a tool to discriminate between glitches and real signals. One can construct a detection statistic using this  $\chi^2$  information and the SNR. One such detection statistic that is commonly used in the LSC for the external trigger search is called *new SNR* (Harry and Fairhurst (2011))

$$\rho_{\text{new}} = \begin{cases} \frac{\rho}{\left[ \left( 1 + \left( \frac{\chi^2}{p} \right)^{4/3} \right) / 2 \right]^{1/4}} & \text{if } \chi^2 > p, \\ \rho & \text{if } \chi^2 \leq p. \end{cases} \quad (2.50)$$

The  $\chi^2$  statistic is however more useful when there is good match between the signal and the template and its value scales quadratically with the mismatch between signal and template as was shown in Ref. Allen (2005). We will see the effect of signal mismatch on  $\chi^2$  in chapter 5.

### 2.4.5 Coincidence test and background estimation

For claiming detection it is very important that a signal is being detected in coincidence in multiple detectors. Thus we repeat the matched filtering and  $\chi^2$  steps discussed above in all the detectors in a network. A list of triggers is obtained for all the detectors. The next step in the CBC pipeline is the coincidence stage. The idea behind the coincidence stage of the pipeline is that any trigger that is of astrophysical origin should be observed in multiple detectors with time delays consistent with its sky position, provided those detectors are all favorably oriented to that sky position. Furthermore, the triggers that are obtained in different detectors should also be of masses that are commensurate with each other. The

coincidence test is performed by forming error ellipsoids around each trigger that takes into account the covariances between trigger time and template masses. These ellipsoids are defined by the covariance matrices in the parameter space. Details of this method are given in Ref. Robinson et al. (2008). The reason one does not demand exact coincidence of parameters is because detector noise can cause the measured parameter values to differ in different detectors. Thus it is very unlikely that real triggers of astrophysical origin in different detectors will show up with the exact same masses and at time delays exactly characterized by the light travel time between the two detectors.

Since there is no way to shield the interferometers from incoming gravitational waves, an estimation of background is obtained by time slides. In a time slide experiment the trigger list in one detector is slid in time w.r.t the trigger list of another detector by amounts much larger than light travel time between the detectors (known as unphysical slide time) and accidental coincidences of such triggers are looked for. A background estimation is performed with the help of a total of 100 time slides per pair of detectors.

However, this method of finding background is implemented for a blind search, where the sky location and time of occurrence of coalescence are not known *a priori* and the search is conducted over large temporal stretches of the data. In an external trigger search, where the time of the occurrence of the event is known, a different approach is implemented. This we will discuss in the next section where we outline the search methodology of the external trigger search.

## 2.5 Search for gravitational waves from progenitors of short GRBs

The search for gravitational waves from a progenitor of a short duration GRB is among one of the most interesting research investigations conducted by LIGO. It is of special significance because it combines information of both electromagnetic and gravitational wave

astronomy. As a CBC search, it leverages the prior knowledge of gravitational waveforms of the progenitors. Additionally the knowledge of the time of the event helps in reducing the amount of data one needs to search. Especially, this helps in reducing the search time for estimating the background. It also helps us to reduce the threshold of detection, thereby helping us in improving the probability of detecting weaker signals. We will discuss the prospects of such a targeted search in chapter 4. In this section we will talk about some of the technical details about the external trigger search, which we will refer to, whenever required, in the later chapters. For more details please refer to Refs. Abadie and et. al (2010) and Abadie and et. al (2012b). Before we discuss the basic features of the targeted search (also known as the external trigger search), we will invest some time to understand the basic physics behind the short GRB emission. For details refer to Ref. Piran (1999).

### **2.5.1 Short duration gamma ray bursts**

The process of a short GRB triggering is depicted in Fig. 2.7. The mechanism of short GRB using a CBC model can be explained as follows (Vedrenne, Gilbert and Atteia, Jean-Luc (2009)). The primary requirement for this is an accretion disk; therefore, a short duration GRB progenitor must have a neutron star as one of the binary components (the other one can be a neutron star or a black hole). The time scales of these events are short. Typically they must be less than 2 seconds long to be categorized as a short GRB. The following discussion will give us an idea about the relevance of this time scale.

Let us assume that a neutron star is in a binary system with a black hole, the case of the binary neutron star can also be explained by the same model, but a neutron star black hole binary is chosen here for convenience as we know that the accretion disk will be formed by the neutron star alone. As the neutron star comes closer to the black hole, strong tidal forces from the black hole disrupt its structural integrity and begin to rip it apart. Matter that is being ripped out of the neutron star begins to form a disk around the black hole and accretes into the latter. It is not necessary for the entire neutron star to be disrupted before

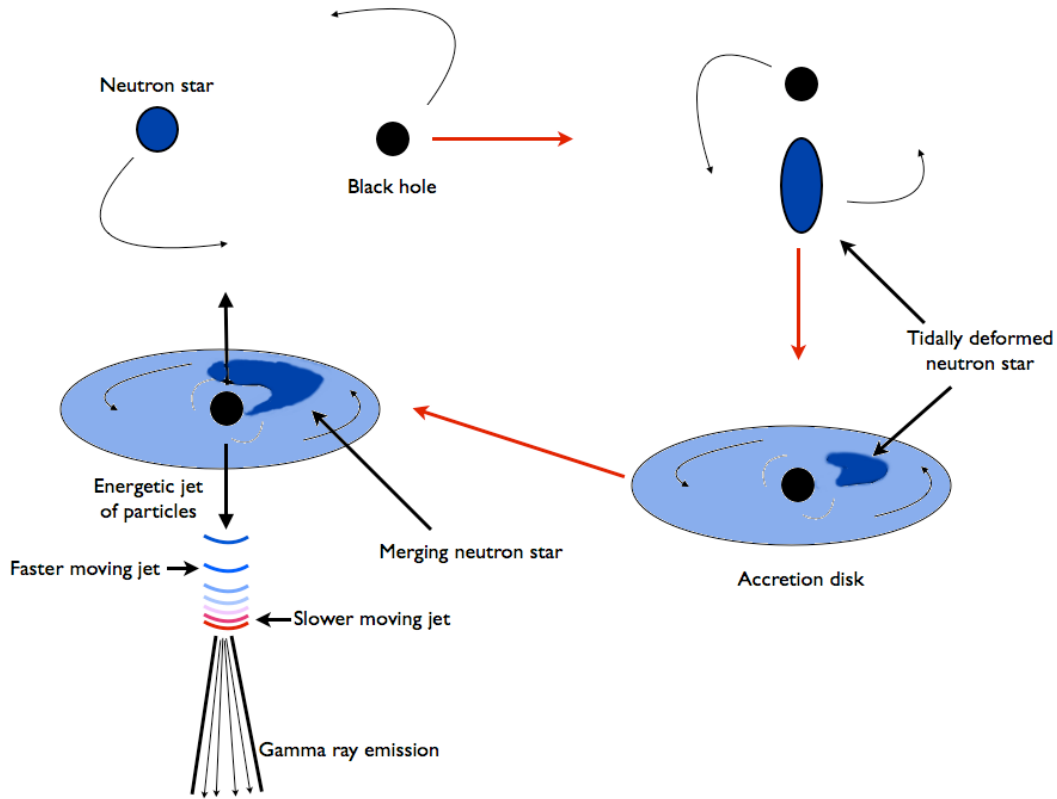


Figure 2.7: Short duration GRB firing from compact binary coalescence.

the GRB is launched.

The catastrophic compressional heating and dissipation in the accretion disk supplies huge amount of energy to the axial jet emanated out of the accretion disk. If the energy is higher than the pair production energy then a fireball of  $e^+ - e^-$  and photons is created. This fireball will stop the photons from escaping due to its high opacity arising from the presence of the electron-positron pairs, much like what we observe in the the early universe. The heating from the accretion disk will continue to supply pressure, resulting in a rapid expansion of the fireball as a jet with a Lorentz factor of  $\sim 100$ . As the fireball jet expands, it cools down, and when the energy drops below the pair production energy, the electron-positron pairs begin to recombine and annihilate, thereby creating streams of photons that are now able to escape to infinity due to reduced opacity of the fireball. These photons are, however, radiated in the jet's frame and, therefore, in the observer's frame they are

strongly blue shifted due to the large Lorentz factor associated with the jet. This shifts typical photons into the gamma ray spectrum for these events. Thus it is imperative that the accretion disk powering the fireball must generate enough heat for the fireball to be expanding at such ultra-relativistic speed to ensure that the photons that we observe are in the gamma ray frequency range. This puts a lower bound on the mass accretion rate and as was shown in Ref. Kiuchi et al. (2010b) an accretion rate of  $\sim 0.1M_{\odot}$  per second is required for a GRB to be initiated. Typically this magnitude of accretion rate can be achieved if  $\sim 0.01M_{\odot}$  of matter is present in the accretion disk. Such an accretion disk will trigger a fireball lasting for  $\sim 0.1$  second resulting in a GRB that lasts for  $\sim 0.1$  second. Higher accretion rates can be achieved if more mass is present in the disk. This sets the time scale of a short GRB to be in the range of a few tenths of a second to a few seconds long.

## 2.5.2 External trigger pipeline

The matter from the neutron star will continue to contribute to the accretion disk formation until the merger of the binary system. Thus, the generation of the GRB coincides with the merger event within a window of about few seconds. The external trigger pipeline chooses this window, also known as the *onsource* window, to be 6 seconds long (Abadie and et. al (2010)) based on the physical models and tolerances towards the uncertainties in these models. This window is chosen from one second before the GRB trigger alert time to 5 seconds after the GRB alert time. During the match filtering any trigger that is found in this onsource window is called an onsource trigger. Measurement of background is done by analyzing similar 6 second windows away from the GRB onsource window. These are called *offsource* windows. A total of 340 such offsource windows are chosen that builds up an offsource analysis segment. To prevent biasing of the background estimation by any possible gravitational wave triggers in the onsource window, 48 seconds worth of data on both sides of the onsource window are discarded from the analysis. The choice of the 48 seconds is based on the fact that the longest template used in the search is 48 seconds long. From both

the ends of the offsource analysis region 72 seconds of data are not analyzed that might be susceptible to presence of filter transients. This is shown schematically in Fig. 2.8.

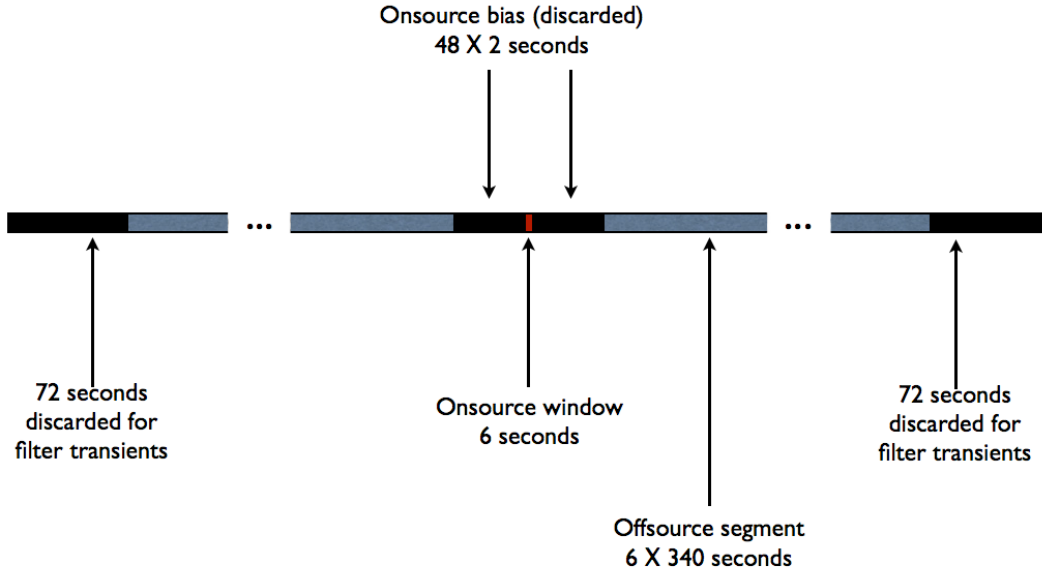


Figure 2.8: Schematic representation of the external trigger search analysis segment. The grey region indicates the offsource segments. There are a total of 340 offsource segments. The red central region is the 6 second onsource segment. The black regions are the discarded parts of the data for reasons explained in the text.

Less computational power is required in the background estimation of the external trigger search compared to time slides in the conventional blind search. This allows us to search for gravitational waves coherently in the sky, which is computationally more expensive than the conventional coincidence search described in Sec. 2.4. In coincidence search one combines the contribution from the two gravitational wave polarizations in quadratures as given in Eq. (2.46). However one must bear in mind that these inner products are actually complex numbers and when taking their magnitudes, we are discarding the phase information from the search. In a coherent search one combines the matched filter outputs in a way that helps us use the phase information. Detailed discussions about constructing a coherent search will

be presented in the next chapter. The coherent analysis used in external trigger search is discussed in Ref. Harry and Fairhurst (2011).

As opposed to the triggered search, in the conventional blind search we have developed a hierarchical coherent search technique where the coherent analysis runs as a follow-up on the coincidence search. We will describe the complete methodology in the next chapter and present the results of searches that were done using the that technique. We have also developed a hierarchical coherent search pipeline for the external trigger search. This is especially helpful in studying performances of searches of gravitational waves from GRBs that have large sky position errors. The hierarchical coherent search also has the potential to be extended to other types of external trigger searches, for instance, a search for gravitational waves from progenitors of orphaned afterglows. All these we will discuss in chapter 4.

We also studied the effect of parameter covariance between mass and sky position using hierarchical coherent search. Upon increasing the size of the grid, over which the search was conducted, from one point (targeted search) to a patch on the sky, a performance enhancement in terms of detection efficiency was recorded. This seemingly counterintuitive point can be understood through study of parameter error covariance. We discuss this in details in chapter 4.

# Chapter 3

## Searching for gravitational waves in a network of detectors

### 3.1 Introduction

In the previous chapter we discussed the data analysis techniques that are used for detection of gravitational waves (GW) from compact binary coalescing (CBC) sources. GW detectors however do not continuously operate. Interferometers can go out of operation multiple times in a given day. This happens when lock is lost in an interferometer, e.g., due to external disturbances (Saulson (1994)). It takes time and effort to bring them back online. This means that there are possibilities that one might miss out on potential detections when the detectors are not in lock. Gravitational wave interferometer sensitivity is not completely isotropic either, being more sensitive to overhead locations in the sky than at points on the sky that lie on the plane described by the arms of the detectors. Thus the farthest observable distance for a given detector varies as a function of the RA and Dec values of the direction in the sky. Finally, a single gravitational wave detector is incapable of locating a source in the sky. All one can do with data from one detector is to infer the presence of gravitational wave at a given time, estimate the mass pair of the source based on the templates that gave

the maximum signal to noise ratio (SNR) and the sources effective distance based on the strength of the signal. Not only are we ‘blind’ about the direction of the source we can not say anything about the intrinsic (pertaining to the binary systems geometry and physical properties) parameters (other than the component masses of course) of the source like the polarization angle of the incoming wave and the inclination angle of the binary orbit.

With these in mind, one realizes multiple detector sites will indeed address a number of these issues. Firstly, with multiple detectors the live time of the network increases. If one of the detectors of the network goes out of lock, the other detectors might still be actively taking science data thus improving our chance of catching an astrophysical event. As the number of detectors in a network increases, the probability of all the detectors simultaneously going out of lock gets remote.

Secondly, since all the detectors will not be in the same plane and will not have identical orientations, therefore the network will to be more isotropic in sensitivity. Specifically the lower sensitivity near the blind spots of detector A can be compensated by the higher sensitivity to that direction of the sky for detector B if the two detectors A and B are not oriented identically. This increases the detection volume by increasing the sky coverage.

Thirdly, with detectors at multiple sites, we get multiple baselines. Two detectors give us one baseline, allowing us to estimate the time delay between the arrival of the signal at the individual detectors. This allows us to locate the source on a ring in the sky as shown in Fig. 3.2 where the two detectors,  $D1$  and  $D2$ , are located in two different sites. The time of arrival of a signal at a particular detector can be different from the other detector depending upon the distance between the two detectors  $l$ , also known as the baseline, and the position of the source in the sky. The source being infinitely far away from the detectors, subtends the same angle  $\theta$  w.r.t the baseline at both the sites. Therefore from Fig. 3.2 we note that,

$$\cos \theta = \frac{c(t_1 - t_2)}{l} = \frac{c\Delta t}{l}. \quad (3.1)$$

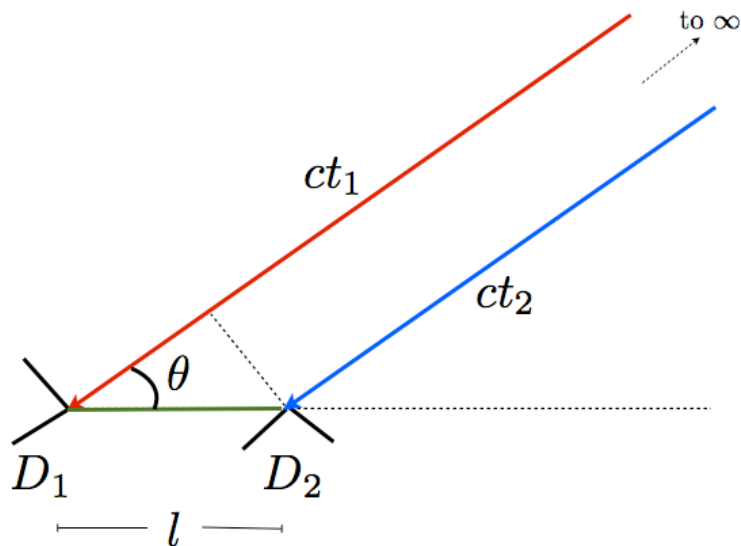


Figure 3.1: The knowledge of time delay between signals in two detectors arising from the same source helps one in locating it in the sky.

Thus, knowing  $\Delta t$ , one can estimate  $\theta$ , which confines the location of the source on a ring in the sky defined by the cone half angle  $\theta$ . Adding a third detector at a different site in the network allows us to locate the source at the points of crossing of the two rings corresponding to the two time delays. Thus we see that with detectors at multiple sites, we are able to estimate the sky position of a source, this is not possible with a single detector. As we shall see later in this chapter, three detectors at different sites with different orientations also allow us to estimate other parameters like the polarization angle of the gravitational wave, the inclination angle of the binary's orbit and the luminosity distance of the source. Finally, it is worth remembering that a trigger in a single interferometer is not enough to claim detection. To increase our confidence we need detections in coincidence with other detectors, thus making network of detectors indispensable for claiming the detection of gravitational waves. So for defining the problem of detection and parameter estimation, it is essential to understand the geometry and sensitivity of a network of detectors.

## 3.2 Signal at a single detector

Let us begin our discussion with the signal at a single detector. We have worked out the mathematics of the gravitational waves emitted by a compact binary coalescing source in Chapter 2. There we presented the form of the restricted post-Newtonian approximation, the two polarizations determining the gravitational waveform, as in Eq. (2.28), that was obtained from in Ref. Pai et al. (2001) are as follows,

$$\begin{aligned} h_+(t; r, \iota, \delta_c, t_c, \xi, ) &= \frac{2\mathcal{N}}{r} a^{-1/4}(t; t_c, \xi) \frac{1 + \cos^2 \iota}{2} \cos [\varphi(t; t_c, \xi) + \delta_c], \\ h_\times(t; r, \iota, \delta_c, t_c, \xi, ) &= \frac{2\mathcal{N}}{r} a^{-1/4}(t; t_c, \xi) \cos \iota \sin [\varphi(t; t_c, \xi) + \delta_c], \end{aligned} \quad (3.2)$$

where the factor  $\mathcal{N}$  is given by

$$\mathcal{N} = \frac{2G^{5/3} \mathcal{M}^{5/3} (\pi f_s)^{2/3}}{c^4}, \quad (3.3)$$

and we have defined

$$a(t; t_c, \xi) = \frac{t_c - t}{\xi}. \quad (3.4)$$

In the above equations  $\iota$  is the inclination angle of the binary orbit,  $r$  is the distance to the source, and  $\mathcal{M}$  is the chirp mass defined as,

$$\mathcal{M} = \frac{(m_1 m_2)^{3/5}}{(m_1 + m_2)^{1/5}}, \quad (3.5)$$

where  $m_1$  and  $m_2$  are the individual binary component masses. For a given cut-off frequency  $f_s$  in a detector, the length of the chirp is quantified by the chirp time which is given by,

$$\xi = 1390 \left( \frac{\mathcal{M}}{M_\odot} \right)^{-5/3} \left( \frac{f_s}{10 \text{ Hz}} \right)^{-8/3} \text{ sec}. \quad (3.6)$$

Thus, at a particular time  $t$ ,  $a(t; t_c, \xi)$  denotes the fraction of time left for the coalescence. At the time of arrival this factor is 1 and at  $t_c$  it becomes zero. By time of arrival of the signal

at the detector one means the time at which the instantaneous frequency of the waveform is given by  $f_s$ . The phase of the waveform at which the coalescence occurs is called the coalescence phase  $\delta_c$  and the corresponding time is  $t_c$ . At any given moment of time the instantaneous frequency is given by

$$f(t; f_s, t_c, \xi) = f_s a^{-3/8}(t; t_c, \xi). \quad (3.7)$$

Figure. 3.4 shows the evolution of the instantaneous frequency with time Note that the in

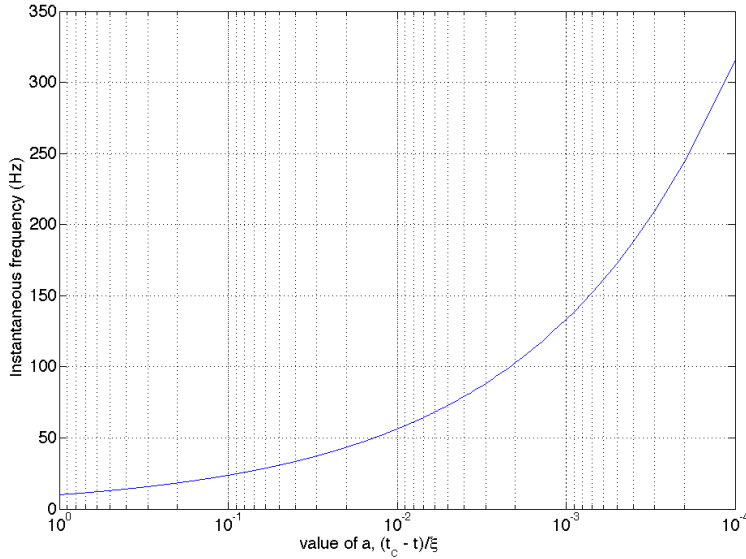


Figure 3.2: Evolution of chirp frequency with time. The cut-off frequency is taken to be 10 Hz. Note that the  $x$ -axis denotes the value of  $a$  which at the end of the chirp is zero.

this approximation frequency diverges at coalescence time  $t_c$ .

### 3.2.1 Circular polarization basis

Having defined the mathematical structure of the CBC gravitational waveform, let us now define two mutually orthogonal normalized waveforms  $s_0$  and  $s_{\pi/2}$ , as done in Ref. Pai et al. (2001), such that, they combine to form the complex waveform at a particular detector,

$$S(t; t_c, \xi) = s_0 + i s_{\pi/2}. \quad (3.8)$$

Constructing these orthonormal waveforms  $s_0$  and  $s_{\pi/2}$  as shown in Eq. (3.9), allows us to encapsulate all the time dependent pieces in the Eq. (3.2) in to the complex signal  $S(t; t_c, \xi)$

$$\begin{aligned} s_0 &= \frac{1}{g} [(t_c - t)\xi]^{-1/4} \cos \varphi(t) = \frac{a^{1/4}(t)}{g\sqrt{\xi}} \cos \varphi(t), \\ s_{\pi/2} &= \frac{1}{g} [(t_c - t)\xi]^{-1/4} \sin \varphi(t) = \frac{a^{1/4}(t)}{g\sqrt{\xi}} \sin \varphi(t), \end{aligned} \quad (3.9)$$

such that

$$S(t; t_c, \xi) = \frac{1}{g} [(t_c - t)\xi]^{-1/4} e^{i\varphi(t)} = \frac{a^{-1/4}(t)}{g\sqrt{\xi}} e^{i\varphi(t)}, \quad (3.10)$$

where  $g$  is a normalization factor that is constructed in such a way that the norm of the complex strain at a given detector is<sup>1</sup>.

$$\langle S(t; t_c, \xi) | S(t; t_c, \xi) \rangle = 2. \quad (3.11)$$

The inner product  $\langle x|y \rangle$  is defined as

$$\langle x|y \rangle = \int_{-\infty}^{\infty} \frac{\tilde{x}^*(f)\tilde{y}(f) + \tilde{x}(f)\tilde{y}^*(f)}{S_n(|f|)} df. \quad (3.12)$$

The gravitational wave strain at a particular detector is obtained by projecting the incoming gravitational wave, expressed in the wave frame (see Fig. 2.3), on the detectors frame, whose axes are defined as follows. If we choose the detector X arm as the  $x$ -axis and upward directions as the  $z$ -axis then the  $y$ -axis is constructed in such a way that the detector frame is a right handed cartesian coordinate system. We extend Fig. 2.3 by bringing in the detector frame and show this explicitly in Fig. 3.3.

$$s(t) = h_+(t)F_+ + h_{\times}(t)F_{\times}, \quad (3.13)$$

---

<sup>1</sup>Ref. Bose et al. (2011) uses the convention that chooses  $g$  such that  $\langle S(t; t_c, \xi) | S(t; t_c, \xi) \rangle = 1$  thus there will be a difference of a factor of 2 between the results we develop here and the results of the referenced paper. The choice we are adopting in this chapter is from the Ref. Pai et al. (2001) which is motivated by the fact that if  $s_0$  and  $s_{\pi/2}$  are to be normalized to 1 then the value of the inner product of  $S$  with itself will be 2. Keeping it normalized to 2 gives a much symmetric look as we will see in Eq. (3.70).

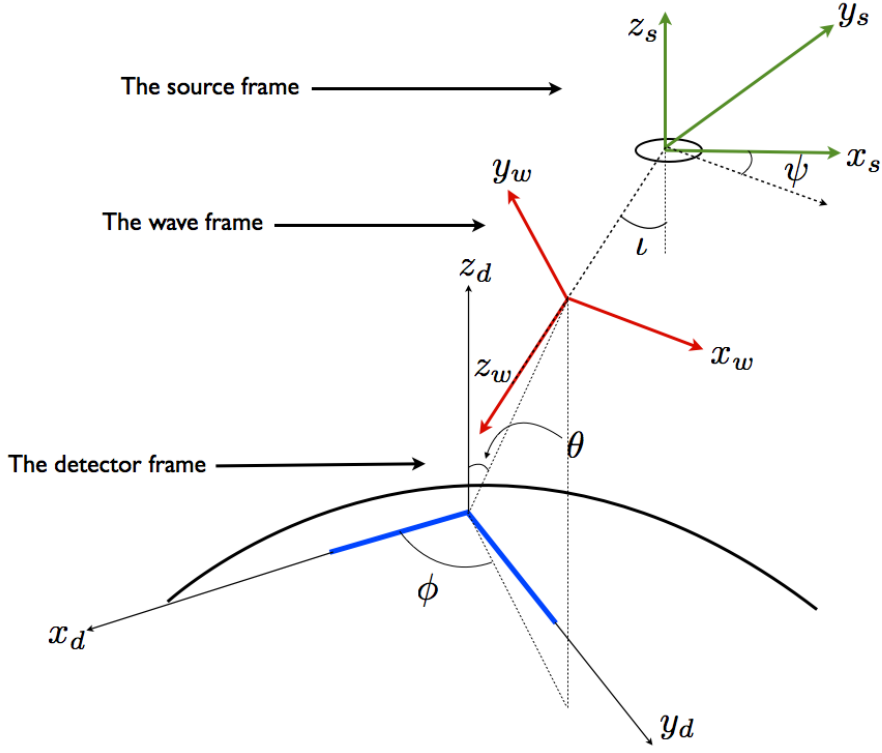


Figure 3.3: The source frame (depicted in green-colored axes) is transformed into the wave frame in red. The wave frame is then projected on the detector frame labeled with axes subscript  $d$ .

where the antenna pattern functions are given as

$$\begin{aligned}
 F_+(\theta, \phi, \psi) &= -\frac{1}{2}(1 + \cos^2 \theta) \cos 2\phi \cos 2\psi - \cos \theta \sin 2\phi \sin 2\psi, \\
 F_\times(\theta, \phi, \psi) &= \frac{1}{2}(1 + \cos^2 \theta) \cos 2\phi \sin 2\psi - \cos \theta \sin 2\phi \cos 2\psi.
 \end{aligned}
 \tag{3.14}$$

Using the complex notation,  $F = F_+ + iF_\times$ , we get

$$s(t) = h_+(t)\Re(F) + h_\times(t)\Im(F).
 \tag{3.15}$$

Thus, we can write, using Eq. (3.2)

$$\begin{aligned} s(t) &= \frac{2\mathcal{N}}{r} a^{-1/4} \left[ \frac{1 + \cos^2 \iota}{2} \cos(\varphi + \delta_c) \Re(F) + \cos \iota \sin(\varphi + \delta_c) \Im(F) \right] \\ &= \frac{2\mathcal{N}}{r} a^{-1/4} \Re \left[ \left( \frac{1 + \cos^2 \iota}{2} \Re(F) - i \cos \iota \Im(F) \right) e^{i(\varphi(t) + \delta_c)} \right]. \end{aligned} \quad (3.16)$$

Let us define an extended antenna pattern function

$$E(\theta, \phi, \psi, \iota) \equiv g \left( \frac{1 + \cos^2 \iota}{2} \Re(F) + i \cos \iota \Im(F) \right). \quad (3.17)$$

Using this definition, we get the gravitational wave strain at a given detector to be

$$s(t) = \frac{2\mathcal{N}}{r} \frac{a^{-1/4}}{g} \Re \left( E^* e^{i(\varphi(t) + \delta_c)} \right) = \frac{2\mathcal{N}\sqrt{\xi}}{r} \Re \left[ \left( E^* \frac{a^{-1/4}}{g\sqrt{\xi}} e^{i\varphi(t)} \right) e^{i\delta_c} \right]. \quad (3.18)$$

Using Eq. (3.10) we can write the signal to be

$$s(t) = \frac{2\mathcal{N}\sqrt{\xi}}{r} \Re \left[ (E^* S) e^{i\delta_c} \right], \quad (3.19)$$

from which we immediately evaluate the normalization factor

$$\langle s|s \rangle = \frac{4\mathcal{N}^2}{r^2} \xi \langle (E^* S) e^{i\delta_c} | (E^* S) e^{i\delta_c} \rangle = \frac{4\mathcal{N}^2}{r^2} \xi (E^* E) = \sigma_s^2, \quad (3.20)$$

where  $\sigma_s^2$  is the norm of the strain at a given detector.

Note that the  $\theta, \phi, \psi$  and  $\iota$  dependence in the strain  $s(t)$  comes purely from the extended antenna pattern function  $E$ . From Eq. (3.19) we see that both the phase and the amplitude part of  $E$  contributes to the strain  $s(t)$  in such a way that it is not possible to combine the amplitude part of  $E$  with the overall amplitude of the strain and isolate it from the phase part of  $E$  combined with an overall phase part. Thus for a single detector, one is only able to estimate those parameters that are related to the overall amplitude of the wave, for example, the effective distance, chirp mass  $\mathcal{M}$  and mass ratio. This is an important point.

This degeneracy will be solved using multiple detectors. This brings us to the discussion of network of detectors.

### 3.3 A network of detectors

Having constructed the precise structure of the signal at a single detector, we are now in a position to discuss about the network signal constructed out of it. In order to do so, let us define the network strain vector  $\mathbf{s}(t)$  of dimension  $M$  constructed out of the individual detector strains

$$\mathbf{s}(t) = \{s_1(t), s_2(t), \dots, s_M(t)\} = s^I(t), \quad (3.21)$$

where  $I$  is the detector index. From Eq. (3.10) we can construct the  $I$ th detector complex waveform

$$S^I(t; t_c, \xi) = \frac{1}{g_I} [(t_c - t_I)\xi]^{-1/4} e^{i\varphi(t_I)} = \frac{a^{-1/4}(t)}{g_I \sqrt{\xi}} e^{i\varphi(t_I)}. \quad (3.22)$$

Similarly, the extended antenna pattern can also be computed at the  $I$ th detector to be,

$$E^I(\theta, \phi, \psi, \iota) = g_I \left( \frac{1 + \cos^2 \iota}{2} \Re(F^I) + i \cos \iota \Im(F^I) \right). \quad (3.23)$$

Using Eqs. (3.20), (3.21), (3.22) and (3.23) we write the network strain vectors as

$$\mathbf{s}(t) = \frac{2\mathcal{N}\sqrt{\xi}}{r} \left( \Re [(E_1^* S^1) e^{i\delta_c}], \Re [(E_2^* S^2) e^{i\delta_c}], \dots, \Re [(E_M^* S^M) e^{i\delta_c}] \right), \quad (3.24)$$

and the norm of the network strain vector can be written as

$$\langle \mathbf{s} | \mathbf{s} \rangle = \frac{4\mathcal{N}^2}{r^2} \xi \sum_{I=1}^M \langle (E_I^* S) e^{i\delta_c} | (E_I^* S) e^{i\delta_c} \rangle = \frac{4\mathcal{N}^2}{r^2} \xi \sum_{I=1}^M (E^* E) = \boldsymbol{\sigma}_s^2, \quad (3.25)$$

where  $\boldsymbol{\sigma}_s$  is the network strain vector norm. Using the network strain vector norm we can

define the network strain unit vector

$$\hat{\mathbf{s}}(\mathbf{t}) = \mathbf{s}(\mathbf{t})/\boldsymbol{\sigma}_s, \quad (3.26)$$

such that

$$\hat{\mathbf{s}}(\mathbf{t}) = (\Re [(Q_1^* S^1) e^{i\delta_c}], \Re [(Q_2^* S^2) e^{i\delta_c}], \dots, \Re [(Q_M^* S^M) e^{i\delta_c}]), \quad (3.27)$$

where  $\mathbf{Q}$  is the network vector, defined as

$$\mathbf{Q} = \left( \frac{E^1}{\sqrt{E_1^* E^1}}, \frac{E^2}{\sqrt{E_2^* E^2}}, \dots, \frac{E^M}{\sqrt{E_M^* E^M}} \right). \quad (3.28)$$

### 3.3.1 Construction of network detection statistic using physical parameters

Now that we have constructed the network strain, we will embark upon the construction of a network detection statistic. However, we will first develop the idea for a single detector, for which we gave the strain in absence of any noise given in Eq. (3.19). In presence of background noise this strain will be augmented with a random strain  $n(t)$ . Thus the resultant effective strain that we will measure in the detector we call data  $x$ ;

$$x(t) = n(t) + s(t), \quad (3.29)$$

where the  $s(t)$  is the strain purely due to the gravitational waveform in absence of any noise. Note that the strength of the gravitational wave signal arriving at a particular detector is extremely weak. Typically the noise at the detector tends to be much greater in amplitude than that. Therefore our best chance of finding the gravitational wave signal is if we know what we are searching for. Specifically, if we know the waveform that we expect from CBC systems, we can match filter the strain at a particular detector with a bank of gravitational wave templates to construct the matched filter outputs. Let us define the probability of

obtaining a strain of  $s(t)$  at a particular detector as

$$P(x) = P(x|s)P(s) + P(x|0)P(0), \quad (3.30)$$

where,  $P(x|s)$  denotes the probability that a strain data of  $x(t)$  was obtained in the detector when a real gravitational wave signal is present in the detector data i.e,  $x(t) = n(t) + s(t)$ , while  $P(x|0)$  denotes the same when no gravitational wave signal is present i.e,  $x(t) = n(t)$ . Using the same notation we can denote the probability that for a given strain data  $s(t)$  at our disposal a gravitational signal is present as  $P(s|x)$ . Bayes theorem states that this probability is related to the likelihood that a given signal  $s(t)$  will generate a strain data  $x(t)$ , denoted by  $P(x|s)$ , as

$$P(s|x) = \frac{P(s)P(x|s)}{P(x)} = \frac{P(s)P(x|s)}{P(x|s)P(s) + P(x|0)P(0)}. \quad (3.31)$$

Dividing the numerator and the denominator by  $P(s)P(x|0)$  and defining the ratio of two likelihoods,  $P(x|s)$  and  $P(x|0)$  as  $\lambda$ , where  $P(x|0)$  is the likelihood that the data with strain  $x(t)$  was obtained from the detector when no gravitational wave signal is present, we get

$$P(s|x) = \frac{\lambda}{\lambda + P(0)/P(s)}; \quad \lambda = \frac{P(x|s)}{P(x|0)}. \quad (3.32)$$

One can write the likelihood ratio in terms of probability densities as

$$\lambda = \frac{p(x|s)}{p(x|0)}. \quad (3.33)$$

From Ref. Finn (1992), we note that if the noise of the detector is assumed to be Gaussian then, the probability that the measurement of the strain in the detector yields an instance of noise  $n(t)$ , is given by

$$p(n) = N_n \exp \left[ -\frac{1}{2} \langle n|n \rangle \right], \quad (3.34)$$

$N_n$  being a normalization factor. In absence of any signal i.e,  $x = n$ , the probability that a strain of  $x(t)$  is measured in the detector must be equal to

$$p(x)|_{h=0} = N_n \exp \left[ -\frac{1}{2} \langle n|n \rangle \right] = N_n \exp \left[ -\frac{1}{2} \langle x|x \rangle \right]. \quad (3.35)$$

Since this measurement was obtained in absence of any signal, thus the conditional probability

$$p(x|0) = p(x)|_{h=0} = N_n \exp \left[ -\frac{1}{2} \langle x|x \rangle \right], \quad (3.36)$$

in presence of signal the noise can be written as  $n = x - s$  therefore

$$p(x|s) = N_n \exp \left[ -\frac{1}{2} \langle n|n \rangle \right] = N_n \exp \left[ -\frac{1}{2} \langle x - s|x - s \rangle \right]. \quad (3.37)$$

From Eqs. (3.33), (3.36) and (3.37) we get

$$\lambda = \frac{\exp \left[ -\frac{1}{2} \langle x - s|x - s \rangle \right]}{\exp \left[ -\frac{1}{2} \langle x|x \rangle \right]} = \exp \left[ \langle x|s \rangle - \frac{1}{2} \langle s|s \rangle \right]. \quad (3.38)$$

Let us now consider the case of a network of detectors. Recall that in Eq. (3.21) we have defined as network strain vector which we will be using as the template vector. We can construct a similar network data vector

$$\mathbf{x}(\mathbf{t}) = \{x_1(t), x_2(t), \dots, x_M(t)\} = x^I(t). \quad (3.39)$$

Thus for every single detector in a network we can define a likelihood ratio of the form given in Eq. (3.38)

$$\lambda^I = \exp \left[ \langle x^I|s^I \rangle - \frac{1}{2} \langle s^I|s^I \rangle \right]. \quad (3.40)$$

Since both the numerator and the denominator of the likelihood ratio are probabilities and if we assume that the noise in the detectors are independent of each other, therefore we can

construct a network likelihood ratio as follow

$$\boldsymbol{\lambda} = \prod_{I=1}^M \lambda^I = \prod_{I=1}^M \exp \left[ \langle x^I | s^I \rangle - \frac{1}{2} \langle s^I | s^I \rangle \right]. \quad (3.41)$$

Thus we can define the logarithmic likelihood ratio for a network of detectors as

$$\ln \boldsymbol{\lambda} = \sum_{I=1}^M \left( \langle x^I | s^I \rangle - \frac{1}{2} \langle s^I | s^I \rangle \right) = \langle \mathbf{x} | \mathbf{s} \rangle - \frac{1}{2} \langle \mathbf{s} | \mathbf{s} \rangle, \quad (3.42)$$

where we have used definitions of  $\mathbf{s}$  and  $\mathbf{x}$  from Eqs. (3.21) and (3.39). Using Eq. (3.20) we can write the above equation as

$$\begin{aligned} \ln \boldsymbol{\lambda} &= \langle \mathbf{x} | \mathbf{s} \rangle - \frac{1}{2} \boldsymbol{\sigma}_s^2 \\ &= \boldsymbol{\sigma}_s \sum_{I=1}^M \langle x^I | \hat{s}^I \rangle - \frac{1}{2} \boldsymbol{\sigma}_s^2. \end{aligned} \quad (3.43)$$

It was shown in Ref. Pai et al. (2001) that the log likelihood ratio defined above can be analytically maximized over four parameters namely, luminosity distance  $r$ , coalescence phase  $\delta_c$ , inclination angle  $\iota$  and polarization angle  $\psi$ . Using the values of the above four parameters at which the log likelihood is maximized, we can create an analytically maximized log likelihood ratio

$$\Lambda = 2 \ln \lambda \Big|_{\hat{\boldsymbol{\sigma}}_s, \hat{\delta}_c, \hat{\psi}, \hat{\iota}} = \|C_H\|^2 = |C^+|^2 + |C^-|^2 = (c_0^+)^2 + (c_{\pi/2}^+)^2 + (c_0^-)^2 + (c_{\pi/2}^-)^2, \quad (3.44)$$

where the quantities  $C^\pm$  are defined in Ref. Pai et al. (2001) as

$$C^\pm = \hat{\mathbf{v}}^\pm \cdot \mathbf{C} = c_0^\pm + i c_{\pi/2}^\pm, \quad (3.45)$$

which are the projection of  $\mathbf{C}$  on  $\hat{\mathbf{v}}^\pm$ , and

$$\begin{aligned} \mathbf{C} &= (\langle x^1 | S^1 \rangle, \langle x^2 | S^2 \rangle, \dots, \langle x^M | S^M \rangle) , \\ C^I &= c_0^I + ic_{\pi/2}^I , \end{aligned} \tag{3.46}$$

$\hat{\mathbf{v}}^\pm$  constitutes a real orthonormal basis on the helicity plane defined by the plane formed by the network vector  $\mathbf{Q}$ .

We still need to maximize the log likelihood over the  $\mathcal{M}, \eta, \theta, \phi$  and  $t_c$ , which is done numerically during the search. Note, now that the parameters  $(r, \delta_c, \psi, \iota)$  can be maximized analytically, and upon maximization the log likelihood ratio will look like the sums of quadratures as given in Eq. (3.44). The maximization of  $\mathbf{C} \cdot \mathbf{Q}$  over these variables however required some geometrical insights. This gives us the hint that there must exist a set of parameters in which, these quantities over which the maximization was done analytically, can be separated out from the rest of the parameters. We are now going to transform the strain variables into a set of new parameters that will make the  $(r, \delta_c, \psi, \iota)$  dependence of the strain manifestly evident. Upon doing so the structure of maximized log likelihood ratio in Eq. (3.44) will emerge naturally. Recognizing these symmetries in the structure of the log likelihood ratio of a network of detector will aid us in constructing the network detection statistic in a way that is easy to implement in the search pipeline.

### 3.3.2 Construction of network detection statistic using symmetrized parameters

In this section we will work out the details of a new parameter set that will help us constructing the maximized log likelihood ratio with the symmetric look of Eq. (3.44).

We begin by noting in Eq. (3.44) that, the final detection statistic is the sum of four

squares which we explicitly write here

$$\Lambda = |C^+|^2 + |C^-|^2 = (\hat{\mathbf{v}}^+ \cdot \mathbf{c}_0)^2 + (\hat{\mathbf{v}}^+ \cdot \mathbf{c}_{\pi/2})^2 + (\hat{\mathbf{v}}^- \cdot \mathbf{c}_0)^2 + (\hat{\mathbf{v}}^- \cdot \mathbf{c}_{\pi/2})^2, \quad (3.47)$$

where we define  $\mathbf{c}_0$  and  $\mathbf{c}_{\pi/2}$  using  $\mathbf{C} = \mathbf{c}_0 + i\mathbf{c}_{\pi/2}$ , which is the network version of Eq. (3.46).

Thus the detection statistic can be written as

$$\begin{aligned} \Lambda &= (\hat{\mathbf{v}}^+ \cdot \langle \mathbf{x} | \mathbf{s}_0 \rangle)^2 + (\hat{\mathbf{v}}^+ \cdot \langle \mathbf{x} | \mathbf{s}_{\pi/2} \rangle)^2 + (\hat{\mathbf{v}}^- \cdot \langle \mathbf{x} | \mathbf{s}_0 \rangle)^2 + (\hat{\mathbf{v}}^- \cdot \langle \mathbf{x} | \mathbf{s}_{\pi/2} \rangle)^2 \\ &= (\langle \mathbf{x} | \hat{\mathbf{v}}^+ \cdot \mathbf{s}_0 \rangle)^2 + (\langle \mathbf{x} | \hat{\mathbf{v}}^+ \cdot \mathbf{s}_{\pi/2} \rangle)^2 + (\langle \mathbf{x} | \hat{\mathbf{v}}^- \cdot \mathbf{s}_0 \rangle)^2 + (\langle \mathbf{x} | \hat{\mathbf{v}}^- \cdot \mathbf{s}_{\pi/2} \rangle)^2 \\ &= (\langle \mathbf{x} | \mathbf{s}_0^+ \rangle)^2 + (\langle \mathbf{x} | \mathbf{s}_{\pi/2}^+ \rangle)^2 + (\langle \mathbf{x} | \mathbf{s}_0^- \rangle)^2 + (\langle \mathbf{x} | \mathbf{s}_{\pi/2}^- \rangle)^2, \end{aligned} \quad (3.48)$$

where  $\mathbf{S} = \mathbf{s}_0 + i\mathbf{s}_{\pi/2}$ . The  $\langle \mathbf{x} | \mathbf{s}_{0,\pi/2}^\pm \rangle$  term can be interpreted as the inner product between the data  $\mathbf{x}$  and the waveform polarization  $\mathbf{s}_{0,\pi/2}^\pm$ . Thus the network template can be decomposed into four polarization basis. Equation (3.9) shows us that the vector  $\mathbf{s}_0^\pm$  will have a  $\cos \varphi(t^I)$  associated with all its components and the vector  $\mathbf{s}_{\pi/2}^\pm$  will have a  $\sin \varphi(t^I)$  associated with its components. Thus we note that among the four polarization components of the network template, two will have  $\cos \varphi(t)$  dependence and two will have a  $\sin \varphi(t)$  dependence. These dependencies are what we will look to isolate so that we can write,

$$s(t) = \sum_{k=1}^4 a^{(k)} h^{(k)}(t), \quad (3.49)$$

where,  $h^{(k)}(t)$  is the  $k$ -th polarization of the network template and  $a^{(k)}$  are the new set of parameters. The terms  $h^{(k)}(t)$  have the following forms

$$\begin{aligned} h^{(1)}(t) &\propto u(\theta, \phi) \cos[\varphi(t; t_c, \xi) + \delta_c], \\ h^{(2)}(t) &\propto v(\theta, \phi) \cos[\varphi(t; t_c, \xi) + \delta_c], \\ h^{(3)}(t) &\propto u(\theta, \phi) \sin[\varphi(t; t_c, \xi) + \delta_c], \\ h^{(4)}(t) &\propto v(\theta, \phi) \sin[\varphi(t; t_c, \xi) + \delta_c]. \end{aligned} \quad (3.50)$$

We start from the expression of gravitational strain at a particular detector. From Eq. (3.14) we can write

$$\begin{aligned} F_+(\theta, \phi, \psi) &= u(\theta, \phi) \cos 2\psi + v(\theta, \phi) \sin 2\psi, \\ F_\times(\theta, \phi, \psi) &= -u(\theta, \phi) \sin 2\psi + v(\theta, \phi) \cos 2\psi, \end{aligned} \quad (3.51)$$

where the functions  $u(\theta, \phi)$  and  $v(\theta, \phi)$  are given by

$$\begin{aligned} u(\theta, \phi) &= -\frac{1}{2}(1 + \cos^2 \theta) \cos 2\phi, \\ v(\theta, \phi) &= -\cos \theta \sin 2\phi. \end{aligned} \quad (3.52)$$

Thus, using these definition of  $F_+$  and  $F_\times$ , we can now write the strain at the detector as

$$s(t) = [u(\theta, \phi) \cos 2\psi + v(\theta, \phi) \sin 2\psi] h_+ + [-u(\theta, \phi) \sin 2\psi + v(\theta, \phi) \cos 2\psi] h_\times. \quad (3.53)$$

Substituting the expressions of the  $h_+$  and  $h_\times$  from Eq. (3.2) in the above equation, we get

$$\begin{aligned} s(t) &= [u(\theta, \phi) \cos 2\psi + v(\theta, \phi) \sin 2\psi] \frac{2\mathcal{N}}{r} a^{-1/4}(t; t_c, \xi) \frac{1 + \cos^2 \iota}{2} \cos [\varphi(t; t_c, \xi) + \delta_c] + \\ & \quad [-u(\theta, \phi) \sin 2\psi + v(\theta, \phi) \cos 2\psi] \frac{2\mathcal{N}}{r} a^{-1/4}(t; t_c, \xi) \cos \iota \sin [\varphi(t; t_c, \xi) + \delta_c]. \end{aligned} \quad (3.54)$$

Expanding the  $\cos [\varphi(t; t_c, \xi) + \delta_c]$  and  $\sin [\varphi(t; t_c, \xi) + \delta_c]$  terms we get

$$\begin{aligned} s(t) &= \frac{2\mathcal{N}}{r} a^{-1/4}(t; t_c, \xi) \left( \cos 2\psi \cos \delta_c \frac{1 + \cos^2 \iota}{2} - \sin 2\psi \sin \delta_c \cos \iota \right) \cos \varphi(t; t_c, \xi) + \\ & \quad \frac{2\mathcal{N}}{r} a^{-1/4}(t; t_c, \xi) \left( \sin 2\psi \cos \delta_c \frac{1 + \cos^2 \iota}{2} + \cos 2\psi \sin \delta_c \cos \iota \right) \cos \varphi(t; t_c, \xi) + \\ & \quad - \frac{2\mathcal{N}}{r} a^{-1/4}(t; t_c, \xi) \left( \cos 2\psi \sin \delta_c \frac{1 + \cos^2 \iota}{2} + \sin 2\psi \cos \delta_c \cos \iota \right) \sin \varphi(t; t_c, \xi) + \\ & \quad - \frac{2\mathcal{N}}{r} a^{-1/4}(t; t_c, \xi) \left( \sin 2\psi \sin \delta_c \frac{1 + \cos^2 \iota}{2} - \cos 2\psi \cos \delta_c \cos \iota \right) \sin \varphi(t; t_c, \xi). \end{aligned} \quad (3.55)$$

Comparing the above equation to the desired form of Eq. (3.50) we find

$$\begin{aligned}
a^{(1)} &= \frac{1}{r} \left( \cos 2\psi \cos \delta_c \frac{1 + \cos^2 \iota}{2} - \sin 2\psi \sin \delta_c \cos \iota \right), \\
a^{(2)} &= \frac{1}{r} \left( \sin 2\psi \cos \delta_c \frac{1 + \cos^2 \iota}{2} + \cos 2\psi \sin \delta_c \cos \iota \right), \\
a^{(3)} &= -\frac{1}{r} \left( \cos 2\psi \sin \delta_c \frac{1 + \cos^2 \iota}{2} + \sin 2\psi \cos \delta_c \cos \iota \right), \\
a^{(4)} &= -\frac{1}{r} \left( \sin 2\psi \sin \delta_c \frac{1 + \cos^2 \iota}{2} - \cos 2\psi \cos \delta_c \cos \iota \right).
\end{aligned} \tag{3.56}$$

Thus we note that the new parameters  $a^{(1)}, a^{(2)}, a^{(3)}, a^{(4)}$  exclusively absorbed the information of the gravitational waveform parameters that can be analytically maximized, namely  $r, \delta_c, \psi, \iota$ . We call them the symmetrized parameters since all of them have the same dimension of length inverse. This choice of new parameters makes tackling of the problem much simpler as we will see below. The various polarizations of the network strain  $s(t)$  are again found by comparing Eq. (3.55) with Eq. (3.50) as follows

$$\begin{aligned}
h^{(1)}(t) &= 2\mathcal{N}a^{-1/4}(t; t_c, \xi)u(\theta, \phi) \cos [\varphi(t; t_c, \xi) + \delta_c], \\
h^{(2)}(t) &= 2\mathcal{N}a^{-1/4}(t; t_c, \xi)v(\theta, \phi) \cos [\varphi(t; t_c, \xi) + \delta_c], \\
h^{(3)}(t) &= 2\mathcal{N}a^{-1/4}(t; t_c, \xi)u(\theta, \phi) \sin [\varphi(t; t_c, \xi) + \delta_c], \\
h^{(4)}(t) &= 2\mathcal{N}a^{-1/4}(t; t_c, \xi)v(\theta, \phi) \sin [\varphi(t; t_c, \xi) + \delta_c].
\end{aligned} \tag{3.57}$$

Using Eq. (3.10), we can write the 4 polarization components of the network strain as

$$\begin{aligned}
h^{(1)}(t) &= \mathcal{N}g\sqrt{\xi}u(\theta, \phi)(S + S^*), \\
h^{(2)}(t) &= \mathcal{N}g\sqrt{\xi}v(\theta, \phi)(S + S^*), \\
h^{(3)}(t) &= \frac{1}{i}\mathcal{N}g\sqrt{\xi}u(\theta, \phi)(S - S^*), \\
h^{(4)}(t) &= \frac{1}{i}\mathcal{N}g\sqrt{\xi}v(\theta, \phi)(S - S^*).
\end{aligned} \tag{3.58}$$

As we have seen in Eq. (3.42), the log likelihood ratio for the network can be written as

$$\begin{aligned}
\ln \boldsymbol{\lambda} &= \sum_{I=1}^M \left( \langle x^I | s^I \rangle - \frac{1}{2} \langle s^I | s^I \rangle \right) \\
&= \sum_{I=1}^M \left( \left\langle x^I \left| \sum_{j=1}^4 a^{(j)} h_I^{(j)} \right. \right\rangle - \frac{1}{2} \left\langle \sum_{j=1}^4 a^{(j)} h_I^{(j)} \left| \sum_{k=1}^4 a^{(k)} h_I^{(k)} \right. \right\rangle \right) \\
&= \sum_{I=1}^M \left( \sum_{j=1}^4 a^{(j)} \langle x^I | h_I^{(j)} \rangle - \frac{1}{2} \sum_{j=1}^4 \sum_{k=1}^4 a^{(j)} a^{(k)} \langle h_I^{(j)} | h_I^{(k)} \rangle \right) \\
&= \sum_{I=1}^M \left( \sum_{j=1}^4 a^{(j)} N_I^j - \frac{1}{2} \sum_{j=1}^4 \sum_{k=1}^4 a^{(j)} a^{(k)} M_I^{jk} \right),
\end{aligned} \tag{3.59}$$

where we have defined

$$\begin{aligned}
N_I^j &= \langle x^I | h_I^{(j)} \rangle, \\
M_I^{jk} &= \langle h_I^{(j)} | h_I^{(k)} \rangle.
\end{aligned} \tag{3.60}$$

The quantity  $a_I^{(j)} N_I^j$  can be interpreted as the  $j$ th polarization contribution to the inner product  $\langle x^I | s^I \rangle$ . Now we calculate  $N_I^j$  using Eqs. (3.58) (3.60).

$$\begin{aligned}
N_I^1 &= \mathcal{N} g_I \sqrt{\xi} u_I(\theta, \phi) \langle x^I | (S^I + S_I^*) \rangle = \mathcal{N} g_I \sqrt{\xi} u_I(\theta, \phi) (C^I + C_I^*) = 2\mathcal{N} g_I \sqrt{\xi} u_I(\theta, \phi) c_0^I, \\
N_I^2 &= \mathcal{N} g_I \sqrt{\xi} v_I(\theta, \phi) \langle x^I | (S^I + S_I^*) \rangle = \mathcal{N} g_I \sqrt{\xi} v_I(\theta, \phi) (C^I + C_I^*) = 2\mathcal{N} g_I \sqrt{\xi} v_I(\theta, \phi) c_0^I, \\
N_I^3 &= \frac{1}{i} \mathcal{N} g_I \sqrt{\xi} u_I(\theta, \phi) \langle x^I | (S^I - S_I^*) \rangle = \frac{1}{i} \mathcal{N} g_I \sqrt{\xi} u_I(\theta, \phi) (C^I - C_I^*) = 2\mathcal{N} g_I \sqrt{\xi} u_I(\theta, \phi) c_{\pi/2}^I, \\
N_I^4 &= \frac{1}{i} \mathcal{N} g_I \sqrt{\xi} v_I(\theta, \phi) \langle x^I | (S^I - S_I^*) \rangle = \frac{1}{i} \mathcal{N} g_I \sqrt{\xi} v_I(\theta, \phi) (C^I - C_I^*) = 2\mathcal{N} g_I \sqrt{\xi} v_I(\theta, \phi) c_{\pi/2}^I,
\end{aligned} \tag{3.61}$$

which for the network of detectors can be written as

$$\mathbf{N} = \begin{pmatrix} N_1 \\ N_2 \\ N_3 \\ N_4 \end{pmatrix} = \chi \begin{pmatrix} \sum_{I=1}^M g_I u_I c_0^I \\ \sum_{I=1}^M g_I v_I c_0^I \\ \sum_{I=1}^M g_I u_I c_{\pi/2}^I \\ \sum_{I=1}^M g_I v_I c_{\pi/2}^I \end{pmatrix} = \chi \begin{pmatrix} \mathbf{u}_g \cdot \mathbf{c}_+ \\ \mathbf{v}_g \cdot \mathbf{c}_+ \\ \mathbf{u}_g \cdot \mathbf{c}_- \\ \mathbf{v}_g \cdot \mathbf{c}_- \end{pmatrix}, \tag{3.62}$$

where, the quantity  $\chi$  is given by

$$\chi = 2\mathcal{N}\sqrt{\xi}, \quad (3.63)$$

$\mathbf{u}_g$  and  $\mathbf{v}_g$  are the network vectors given by

$$\begin{aligned} \mathbf{u}_g &= g_I u^I(\theta, \phi), \\ \mathbf{v}_g &= g_I v^I(\theta, \phi), \end{aligned} \quad (3.64)$$

where the repeated indices are not summed over in the above equations. Now we will construct the matrix represented by  $M_I^{jk} = \langle h_I^{(j)} | h_I^{(k)} \rangle$ . Thus

$$\begin{aligned} M_I^{11} &= \langle h_I^{(1)} | h_I^{(1)} \rangle = \mathcal{N}^2 g_I^2 \xi u_I^2(\theta, \phi) \langle S^I + S_I^* | S^I + S_I^* \rangle, \\ &= \mathcal{N}^2 g_I^2 \xi u_I^2(\theta, \phi) [\langle S^I | S^I \rangle + \langle S^I | S_I^* \rangle + \langle S_I^* | S^I \rangle + \langle S_I^* | S_I^* \rangle]. \end{aligned} \quad (3.65)$$

Note that  $S^I = s_0^I + i s_{\pi/2}^I$ , where  $s_0^I$  and  $s_{\pi/2}^I$  are orthonormal waveforms. We already know from Eq. (3.11) that  $\langle S^I | S^I \rangle = 2$ , which implies that  $\langle S_I^* | S_I^* \rangle = 2$  too. The inner product  $\langle S^I | S_I^* \rangle$  can be shown to be 0 as follows

$$\begin{aligned} \langle S^I | S_I^* \rangle &= \langle s_0^I + i s_{\pi/2}^I | s_0^I - i s_{\pi/2}^I \rangle = \langle s_0^I | s_0^I \rangle - \langle i s_{\pi/2}^I | i s_{\pi/2}^I \rangle, \\ &= \langle s_0^I | s_0^I \rangle - (-i)(i) \langle s_{\pi/2}^I | s_{\pi/2}^I \rangle = \langle s_0^I | s_0^I \rangle - \langle s_{\pi/2}^I | s_{\pi/2}^I \rangle = 0. \end{aligned} \quad (3.66)$$

Thus we can write

$$M_I^{11} = 4\mathcal{N}^2 g_I^2 \xi u_I^2(\theta, \phi). \quad (3.67)$$

Similarly we calculate all the other components of  $M_I^{jk}$ ,

$$\begin{aligned}
M_I^{12} &= M_I^{21} = \langle h_I^{(1)} | h_I^{(2)} \rangle = \mathcal{N}^2 g_I^2 \xi u_I(\theta, \phi) v_I(\theta, \phi) \langle S^I + S_I^* | S^I + S_I^* \rangle = 4\mathcal{N}^2 g_I^2 \xi u_I(\theta, \phi) v(\theta, \phi), \\
M_I^{13} &= M_I^{31} = \langle h_I^{(1)} | h_I^{(3)} \rangle = \frac{1}{i} \mathcal{N}^2 g_I^2 \xi u_I^2(\theta, \phi) \langle S^I + S_I^* | S^I - S_I^* \rangle = 0, \\
M_I^{14} &= M_I^{41} = \langle h_I^{(1)} | h_I^{(4)} \rangle = \frac{1}{i} \mathcal{N}^2 g_I^2 \xi u_I(\theta, \phi) v_I(\theta, \phi) \langle S^I + S_I^* | S^I - S_I^* \rangle = 0, \\
M_I^{22} &= \langle h_I^{(2)} | h_I^{(2)} \rangle = 4\mathcal{N}^2 g_I^2 \xi v_I^2(\theta, \phi), \\
M_I^{23} &= M_I^{32} = \langle h_I^{(2)} | h_I^{(3)} \rangle = \frac{1}{i} \mathcal{N}^2 g_I^2 \xi u_I(\theta, \phi) v_I(\theta, \phi) \langle S^I + S_I^* | S^I - S_I^* \rangle = 0, \\
M_I^{24} &= M_I^{42} = \langle h_I^{(2)} | h_I^{(4)} \rangle = \frac{1}{i} \mathcal{N}^2 g_I^2 \xi u_I^2(\theta, \phi) \langle S^I + S_I^* | S^I - S_I^* \rangle = 0, \\
M_I^{33} &= \langle h_I^{(3)} | h_I^{(3)} \rangle = \mathcal{N}^2 g_I^2 \xi u_I^2(\theta, \phi) \left( \frac{1}{i} \right) \left( \frac{1}{-i} \right) \langle S^I - S_I^* | S^I - S_I^* \rangle = 4\mathcal{N}^2 g_I^2 \xi u_I^2(\theta, \phi), \\
M_I^{34} &= M_I^{43} = \mathcal{N}^2 g_I^2 \xi u_I(\theta, \phi) v_I(\theta, \phi) \left( \frac{1}{i} \right) \left( \frac{1}{-i} \right) \langle S^I - S_I^* | S^I - S_I^* \rangle = 4\mathcal{N}^2 g_I^2 \xi u_I(\theta, \phi) v_I(\theta, \phi).
\end{aligned} \tag{3.68}$$

Thus the network  $\mathbf{M}$  matrix is given by

$$\mathbf{M} = \begin{pmatrix} A & B & 0 & 0 \\ B & C & 0 & 0 \\ 0 & 0 & A & B \\ 0 & 0 & B & C \end{pmatrix}. \tag{3.69}$$

where, the values of  $A, B$  and  $C$  is given by

$$\begin{aligned}
A &= 4\mathcal{N}^2 \xi \sum_{I=1}^M (g_I u_I(\theta, \phi))^2 = \chi^2 \mathbf{u}_g \cdot \mathbf{u}_g, \\
B &= 4\mathcal{N}^2 \xi \sum_{I=1}^M g_I u_I(\theta, \phi) g_I v_I(\theta, \phi) = \chi^2 \mathbf{u}_g \cdot \mathbf{v}_g, \\
C &= 4\mathcal{N}^2 \xi \sum_{I=1}^M (g_I v_I(\theta, \phi))^2 = \chi^2 \mathbf{v}_g \cdot \mathbf{v}_g,
\end{aligned} \tag{3.70}$$

where we have used Eq. (3.64)<sup>2</sup> and

$$\begin{aligned}
\sum_{I=1}^M (g_I u_I(\theta, \phi))^2 &= (g_1 u_1(\theta, \phi))^2 + (g_2 u_2(\theta, \phi))^2 + \dots + (g_M u_M(\theta, \phi))^2 = \mathbf{u}_g \cdot \mathbf{u}_g, \\
\sum_{I=1}^M (g_I v_I(\theta, \phi))^2 &= (g_1 v_1(\theta, \phi))^2 + (g_2 v_2(\theta, \phi))^2 + \dots + (g_M v_M(\theta, \phi))^2 = \mathbf{v}_g \cdot \mathbf{v}_g, \\
\sum_{I=1}^M (g_I u_I(\theta, \phi))(g_I v_I(\theta, \phi)) &= \mathbf{u}_g \cdot \mathbf{v}_g.
\end{aligned} \tag{3.71}$$

Defining a vector  $\mathbf{a} = (a^{(1)}, a^{(2)}, a^{(3)}, a^{(4)})$ , the network log likelihood in Eq. (3.59) can be written as

$$\ln \boldsymbol{\lambda} = \mathbf{a}^T \cdot \mathbf{N} - \frac{1}{2} \mathbf{a}^T \cdot \mathbf{M} \cdot \mathbf{a}. \tag{3.72}$$

This clearly shows the advantage of using the parameters  $(a^{(1)}, a^{(2)}, a^{(3)}, a^{(4)})$ . All the parameters that we can analytically maximize are in the vector  $\mathbf{a}$  and the log likelihood itself is dependent on this vector through products. In the form we got in Eq. (3.42) the log likelihood has dependencies on the parameters  $r, \delta_c, \psi$  and  $\iota$ , some of which are in the amplitude term of the RHS, some in the phase and some can only be obtained after taking special transformations into a helical plane defined by complex vectors, and analytic maximization provided some geometric insights. But, here, we see that the problem of analytic maximization has been reduced to a straight forward problem of linear algebra. Thus, we proceed to maximize Eq. (3.72) as follows. Let the parameters  $\mathbf{a}$  at which the log likelihood is maximized are given by the maximized vector,  $\hat{\mathbf{a}}$

$$\begin{aligned}
\left. \frac{\partial \ln \lambda}{\partial \mathbf{a}} \right|_{\hat{\mathbf{a}}} &= \mathbf{N} - \hat{\mathbf{a}} \cdot \mathbf{M}, \\
\implies \hat{\mathbf{a}} &= \mathbf{N} \cdot \mathbf{M}^{-1} \quad \text{and,} \quad \hat{\mathbf{a}}^T = \mathbf{M}^{-1} \cdot \mathbf{N}^T = \mathbf{N}^T \cdot \mathbf{M}^{-1},
\end{aligned} \tag{3.73}$$

where we have used the fact that  $\mathbf{M}$  is an symmetric block diagonal matrix and hence its

---

<sup>2</sup>Note that the choice of  $\langle S|S \rangle = 2$  has resulted in to making the constant terms in  $\mathbf{N}$  as  $\chi$  and that in  $\mathbf{M}$  as  $\chi^2$ . If we chose a convention of  $\langle S|S \rangle = 1$ , then the constant term for  $\mathbf{M}$  would have become  $\chi^2/2$ , giving us a factor of 2 in every expression involving components of  $\mathbf{M}$  and  $\mathbf{N}$ .

inverse must be symmetric block diagonal too. Therefore the maximized log likelihood ratio is given by

$$\begin{aligned}
\ln \boldsymbol{\lambda} \Big|_{\hat{\mathbf{a}}} &= \mathbf{N}^T \cdot \mathbf{M}^{-1} \cdot \mathbf{N} - \frac{1}{2} \mathbf{N}^T \cdot \mathbf{M}^{-1} \cdot \mathbf{M} \cdot \mathbf{N} \cdot \mathbf{M}^{-1} \\
&= \mathbf{N}^T \cdot \mathbf{M}^{-1} \cdot \mathbf{N} - \frac{1}{2} \mathbf{N}^T \cdot \mathbf{M}^{-1} \cdot \mathbf{N} \\
&= \frac{1}{2} \mathbf{N}^T \cdot \mathbf{M}^{-1} \cdot \mathbf{N}.
\end{aligned} \tag{3.74}$$

From which we construct an expression of the previously defined detection statistic in Eq. (3.44)

$$\boxed{\Lambda = 2 \ln \boldsymbol{\lambda} \Big|_{\hat{\mathbf{a}}} = \mathbf{N}^T \cdot \mathbf{M}^{-1} \cdot \mathbf{N}}, \tag{3.75}$$

writing it out explicitly we get

$$\Lambda = \frac{1}{\Delta^2} \begin{pmatrix} N_1 & N_2 & N_3 & N_4 \end{pmatrix} \begin{pmatrix} C & -B & 0 & 0 \\ -B & A & 0 & 0 \\ 0 & 0 & C & -B \\ 0 & 0 & -B & A \end{pmatrix} \begin{pmatrix} N_1 \\ N_2 \\ N_3 \\ N_4 \end{pmatrix}, \tag{3.76}$$

where  $\Delta = |\mathbf{M}| = AC - B^2$ . To get the sum of squares form of the log likelihood ratio that was obtained after taking several projections in the helicity plane in Eq. (3.44), all we need to do here is diagonalize the  $4 \times 4$  square matrix in the above equation. Let us call this the  $\bar{\mathbf{m}}$  matrix. let us assume that the orthogonal matrix  $\mathbf{O}$  diagonalizes the  $\bar{\mathbf{m}}$ . Therefore we can write

$$\mathbf{N}^T \cdot \bar{\mathbf{m}} \cdot \mathbf{N} = \mathbf{N}^T \cdot \mathbf{O} \cdot \mathbf{O}^T \cdot \bar{\mathbf{m}} \cdot \mathbf{O} \cdot \mathbf{O}^T \cdot \mathbf{N}. \tag{3.77}$$

In order to find this matrix  $\mathbf{O}$  that diagonalizes  $\bar{\mathbf{m}}$ , we first calculate the eigenvalues of  $\mathbf{M}$ . Since  $\bar{\mathbf{m}}$  is block diagonal and the individual blocks are identical, thus the eigenvalues will be of the form  $\zeta_1, \zeta_2, \zeta_1, \zeta_2$ . We obtain the values of  $\zeta_1$  and  $\zeta_2$  from the secular determinant of the block matrix

$$\begin{pmatrix} C & -B \\ -B & A \end{pmatrix} \tag{3.78}$$

which gives us

$$\begin{vmatrix} C - \zeta & -B \\ -B & A - \zeta \end{vmatrix} = 0, \quad (3.79)$$

which upon solving gives us the eigenvalues as follows

$$\begin{aligned} \zeta_1 &= \frac{1}{2}(A + C + D), \\ \zeta_2 &= \frac{1}{2}(A + C - D), \end{aligned} \quad (3.80)$$

where  $D = \sqrt{(A - C)^2 + 4B^2}$ . Therefore, the eigenvectors of  $\bar{\mathbf{m}}$  can be calculated using the eigenvalue equations

$$\begin{aligned} \bar{\mathbf{m}}|\mathbf{e}_1\rangle &= \zeta_1|\mathbf{e}\rangle, \\ \bar{\mathbf{m}}|\mathbf{e}_2\rangle &= \zeta_2|\mathbf{e}\rangle, \end{aligned} \quad (3.81)$$

where  $|\mathbf{e}_{1,2}\rangle$  are the eigenvector of  $\bar{\mathbf{m}}$ . Thus we calculate the eigenvectors from

$$\begin{pmatrix} C & -B \\ -B & A \end{pmatrix} \begin{pmatrix} e_{1,2}^{(1)} \\ e_{1,2}^{(2)} \end{pmatrix} = \zeta_{1,2} \begin{pmatrix} e_{1,2}^{(1)} \\ e_{1,2}^{(2)} \end{pmatrix}. \quad (3.82)$$

Solving the above equations we get the eigenvectors to be

$$\mathbf{e}_1 = \begin{pmatrix} \frac{1}{G_1} \\ \frac{C-A-D}{2BG_1} \end{pmatrix}, \quad \mathbf{e}_2 = \begin{pmatrix} \frac{1}{G_2} \\ \frac{C-A+D}{2BG_2} \end{pmatrix}, \quad (3.83)$$

where  $G_1$  and  $G_2$  are the eigenvector normalization factors

$$\begin{aligned} G_1 &= \frac{\sqrt{(C - A - D)^2 + 4B^2}}{2B}, \\ G_2 &= \frac{\sqrt{(C - A + D)^2 + 4B^2}}{2B}. \end{aligned} \quad (3.84)$$

Thus we have now constructed the orthogonal diagonalizing matrix  $\mathbf{O}$

$$\mathbf{O} = \begin{pmatrix} 1/G_1 & 1/G_2 & 0 & 0 \\ \frac{C-A-D}{2BG_1} & \frac{C-A+D}{2BG_2} & 0 & 0 \\ 0 & 0 & 1/G_1 & 1/G_2 \\ 0 & 0 & \frac{C-A-D}{2BG_1} & \frac{C-A+D}{2BG_2} \end{pmatrix}. \quad (3.85)$$

From Eq. (3.77), we can write

$$\mathbf{N}^T \cdot \bar{\mathbf{m}} \cdot \mathbf{N} = \mathbf{N}_{\mathbf{O}}^T \cdot \bar{\mathbf{m}}_{\text{diag}} \cdot \mathbf{N}_{\mathbf{O}}, \quad (3.86)$$

where

$$\begin{aligned} \mathbf{N}_{\mathbf{O}} &= \mathbf{N}^T \cdot \mathbf{O}, \\ \bar{\mathbf{m}}_{\text{diag}} &= \mathbf{O}^T \cdot \bar{\mathbf{m}} \cdot \mathbf{O}, \end{aligned} \quad (3.87)$$

we now determine these matrices after diagonalization

$$\mathbf{N}_{\mathbf{O}} = \begin{pmatrix} 1/G_1 & \frac{C-A-D}{2BG_1} & 0 & 0 \\ 1/G_2 & \frac{C-A+D}{2BG_2} & 0 & 0 \\ 0 & 0 & 1/G_1 & \frac{C-A-D}{2BG_1} \\ 0 & 0 & 1/G_2 & \frac{C-A+D}{2BG_2} \end{pmatrix} \begin{pmatrix} N_1 \\ N_2 \\ N_3 \\ N_4 \end{pmatrix}, \quad (3.88)$$

from the above equation and Eq. (3.62), we get

$$\mathbf{N}_{\mathbf{O}} = \begin{pmatrix} \frac{N_1}{G_1} + \frac{C-A-D}{2BG_1} N_2 \\ \frac{N_1}{G_2} + \frac{C-A+D}{2BG_2} N_2 \\ \frac{N_3}{G_1} + \frac{C-A-D}{2BG_1} N_4 \\ \frac{N_3}{G_2} + \frac{C-A+D}{2BG_2} N_4 \end{pmatrix} = \begin{pmatrix} \frac{\chi}{G_1} \mathbf{u}_g \cdot \mathbf{c}_+ + \chi \frac{C-A-D}{2BG_1} \mathbf{v}_g \cdot \mathbf{c}_+ \\ \frac{\chi}{G_2} \mathbf{u}_g \cdot \mathbf{c}_+ + \chi \frac{C-A+D}{2BG_2} \mathbf{v}_g \cdot \mathbf{c}_+ \\ \frac{\chi}{G_1} \mathbf{u}_g \cdot \mathbf{c}_- + \chi \frac{C-A-D}{2BG_1} \mathbf{v}_g \cdot \mathbf{c}_- \\ \frac{\chi}{G_2} \mathbf{u}_g \cdot \mathbf{c}_- + \chi \frac{C-A+D}{2BG_2} \mathbf{v}_g \cdot \mathbf{c}_- \end{pmatrix}. \quad (3.89)$$

The diagonalized matrix  $\bar{\mathbf{m}}$  is of course simply  $\mathbf{diag}(\zeta_1, \zeta_2, \zeta_1, \zeta_2)$ . Using this and Eqs. (3.76)

(3.77), (3.80), (3.85) and (3.89), we get

$$\begin{aligned}
\Lambda = \frac{1}{\Delta^2} & \left[ \left( \frac{\chi}{G_1} \mathbf{u}_g \cdot \mathbf{c}_+ + \chi \frac{C - A - D}{2BG_1} \mathbf{v}_g \cdot \mathbf{c}_+ \right)^2 \frac{1}{2} (A + C + D) + \right. \\
& \left( \frac{\chi}{G_2} \mathbf{u}_g \cdot \mathbf{c}_+ + \chi \frac{C - A + D}{2BG_2} \mathbf{v}_g \cdot \mathbf{c}_+ \right)^2 \frac{1}{2} (A + C - D) + \\
& \left( \frac{\chi}{G_1} \mathbf{u}_g \cdot \mathbf{c}_- + \chi \frac{C - A - D}{2BG_1} \mathbf{v}_g \cdot \mathbf{c}_- \right)^2 \frac{1}{2} (A + C + D) + \\
& \left. \left( \frac{\chi}{G_2} \mathbf{u}_g \cdot \mathbf{c}_- + \chi \frac{C - A + D}{2BG_2} \mathbf{v}_g \cdot \mathbf{c}_- \right)^2 \frac{1}{2} (A + C - D) \right]. \tag{3.90}
\end{aligned}$$

Let us now define the following vectors

$$\begin{aligned}
\mathbf{w}_+ &= \frac{\chi}{\Delta^2 G_1} \sqrt{\frac{A + C + D}{2}} \mathbf{u}_g + \chi \frac{C - A - D}{2B\Delta^2 G_1} \sqrt{\frac{A + C + D}{2}} \mathbf{v}_g, \\
\mathbf{w}_- &= \frac{\chi}{\Delta^2 G_2} \sqrt{\frac{A + C - D}{2}} \mathbf{u}_g + \chi \frac{C - A + D}{2B\Delta^2 G_2} \sqrt{\frac{A + C - D}{2}} \mathbf{v}_g, \tag{3.91}
\end{aligned}$$

using these newly defined basis  $(\mathbf{w}_+, \mathbf{w}_-)$ , we can define the log likelihood ratio as

$$\boxed{\Lambda = 2 \ln \boldsymbol{\lambda} \Big|_{\hat{\mathbf{a}}} = (\mathbf{w}_+ \cdot \mathbf{c}_+)^2 + (\mathbf{w}_- \cdot \mathbf{c}_+)^2 + (\mathbf{w}_+ \cdot \mathbf{c}_-)^2 + (\mathbf{w}_- \cdot \mathbf{c}_-)^2}. \tag{3.92}$$

Finally, we have constructed back the maximized log likelihood ratio using the symmetrized parameters  $(a^{(1)}, a^{(2)}, a^{(3)}, a^{(4)}, )$ , that we previously obtained using physical parameters  $(r, \delta_c, \psi, \iota)$  in Eq. (3.44). Note that in Eq. (3.91), the quantities  $\Delta, G_1$  and  $G_2$  are constructed out of  $A, B$  and  $C$ . The quantities  $A, B$  and  $C$  themselves are constructed from  $\mathbf{u}_g, \mathbf{v}_g$  and  $\chi$  as shown in Eq. (3.70). The values of  $\mathbf{u}_g$  and  $\mathbf{v}_g$  are given in terms of the  $u^I(\theta, \phi)$  and  $v^I(\theta, \phi)$  and  $g_I$  as shown in Eq. (3.64). Finally Eq. (3.52) shows the precise expression of the dependences of  $u^I(\theta, \phi)$  and  $v^I(\theta, \phi)$  on the sky coordinates  $\theta$  and  $\phi$ . Thus the vectors  $\mathbf{w}_+$  and  $\mathbf{w}_-$  are completely specified in terms of the geometry and we have developed the

explicit expressions of them here. The  $\mathbf{c}_+$  and  $\mathbf{c}_-$  are expressed below

$$\begin{aligned}\mathbf{c}_+ &= (c_0^1, c_0^2, \dots, c_0^M), \\ \mathbf{c}_- &= (c_{\pi/2}^1, c_{\pi/2}^2, \dots, c_{\pi/2}^M),\end{aligned}\tag{3.93}$$

comes directly from the inner product between the data  $x^I$  with the template  $s_0^I$  and  $s_{\pi/2}^I$ , respectively (as shown in Eq. (3.46)). So the quantity in Eq. (3.92) is fully defined now and can be computed very easily for given values of sky positions and masses. Thus if we construct a template bank of mass parameters. Then for every mass pair in the template bank, it will be possible for us to construct a  $\Lambda(\theta, \phi)|_{m_1, m_2}$ . Calculating this quantity over a grid set on sky we can find the maximum. This lets us maximize the  $\Lambda$  for that mass pair. Repeating this same analysis for all the pairs of masses in the template bank we will construct  $\Lambda(m_1, m_2)$ . Maximizing over all the mass pairs will now give us  $\mathbf{\Lambda}$ , which we call the *coherent statistic*

$$\boxed{\mathbf{\Lambda} = \max_{m_1, m_2, \theta, \phi} \Lambda}.\tag{3.94}$$

### 3.3.3 Maximization of detection statistic over time of arrival

We have discussed the maximization of the log likelihood ratio for all the 8 parameters in the previous sections, however we left out one important parameter, the time of arrival of the signal which we will deal with now. The first thing we note about the time of arrival of the signal is that this will be different at different sites in a network of detectors. Thus we need to set a reference detector w.r.t which we can measure the time of arrival at other detectors through time delays. The second thing we note is that for different values of  $(\theta, \phi)$  the time delays will be different for the same choice of the network of the detectors. Keeping these in mind let us write the complex waveform in Eq. (3.10) at detector  $I$  as follows

$$S^{(I)}(t - \tau_{(I)}; t_c, \xi) = \frac{a^{-1/4}(t - \tau_{(I)})}{g\sqrt{\xi}} e^{i\varphi(t - \tau_{(I)})},\tag{3.95}$$

where,  $\tau_{(I)} = \tau_{(I)}(\theta, \phi)$  is the time delay between detector  $I$  and some reference detectors. Two things to note here are, firstly the reference detector does not need to be an *actual* detector. It could very well be the center of the earth, and secondly, the time delay  $\tau_{(I)}$  could be either positive or negative. If the reference detector in the network is one of the detectors on the earth, then the maximum time delay one could have for all possible sky positions of a source is about 40 ms (time taken by light to travel the distance of the diameter of the earth). In a search one does not know *a priori* at what time the signal is arriving at a particular detector. Thus one needs to construct the log likelihood ratio for all possible values of time of arrivals. This is done by taking cross-correlation between  $x^I(t)$  and  $S^{(I)}(t - \tau_{(I)}; t_c, \xi)$  whose output will be  $C^I(\tau_{(I)}) = c_0^I(\tau_{(I)}) + ic_{\pi/2}^I(\tau_{(I)})$ . This implies we need to find the time dependent orthonormal components of the complex waveform. This we do as follows. Let us drop the detector index  $I$  in the following calculation for brevity. The Fourier transform of  $s_0(t - \tau)$  is given by

$$\begin{aligned}\tilde{s}_{0,\pi/2}(f) &= \int_{-\infty}^{\infty} s_{0,\pi/2}(t - \tau)e^{-2\pi ift} dt = \int_{-\infty}^{\infty} s_{0,\pi/2}(t')e^{-2\pi if(t'+\tau)} dt', \\ \tilde{s}_{0,\pi/2}(f) &= e^{-2\pi if\tau} \tilde{s}_{0,\pi/2}(f'), \\ \tilde{s}_{0,\pi/2}(f') &= e^{+2\pi if\tau} \tilde{s}_{0,\pi/2}(f),\end{aligned}\tag{3.96}$$

where  $\tilde{s}_{0,\pi/2}(f)$  is the Fourier transform of the coalescence time independent orthonormal components of the complex waveform. Recall that the cross-correlation components  $c_{0,\pi/2}(\tau)$  were defined by the definition of the inner products

$$\begin{aligned}c_{0,\pi/2}(\tau) &= \int_{-\infty}^{\infty} \frac{\tilde{x}^*(f)\tilde{s}_{0,\pi/2}(f') + \tilde{x}(f)\tilde{s}_{0,\pi/2}^*(f')}{S_n(|f'|)} df', \\ &= \int_{-\infty}^{\infty} \frac{\tilde{x}^*(f)\tilde{s}_{0,\pi/2}(f) + \tilde{x}(f)\tilde{s}_{0,\pi/2}^*(f)}{S_n(|f'|)} e^{+2\pi if\tau} df' .\end{aligned}\tag{3.97}$$

Thus computing  $c_{0,\pi/2}(\tau)$  for all values of  $\tau$  we will have a time series of  $C(\tau)$  at each detector. However to construct the detection statistic in Eq. (3.92), one needs to compute the  $c_{0,\pi/2}(\tau)$

for all the  $M$  detectors in the network. If the detectors are not co-located, then one needs to take into account for the time delay between them. This is precisely why the  $\tau_{(I)}$  term is present in the expression of  $S^{(I)}(t - \tau_{(I)}; t_c, \xi)$  in Eq. (3.95). In all the detectors the  $C^I(\tau)$  values will peak when the values of  $(m_1, m_2, \theta, \phi)$  matches that of the chirp signal in the data and when  $t - \tau - \tau_{(I)}(\theta, \phi) = t'_c - t_c$ , where  $t_c$  is the coalescence time of the chirp signal in the data and  $t'_c$  is the coalescence time of the chirp signal of the template waveform. Thus the detection statistic is maximized over the time of arrival.

However, in the search pipeline we employ an alternative strategy to maximize the likelihood over arrival time. This is a little easier to implement as an algorithm. Instead of calculating the values of  $\mathbf{C}$  of all possible time delays permissible between pairs of detectors for every single point in the grid laid out on the sky, we compute the  $C^I(\tau)$  for every single detector in the network with the time of arrival as that of the reference detector. Thus we will generate  $M$  streams of complex time series. Now for a particular time of arrival at the reference detector  $t_a$ , and particular choice of sky coordinates  $\theta$  and  $\phi$  one can construct back all the time delays in all the other detectors in the network. Thus the network correlation vector can be written as

$$\mathbf{C}(\tau) = [C^1(\tau + \tau_{(1)}(\theta', \phi')), C^2(\tau + \tau_{(2)}(\theta', \phi')), \dots, C^M(\tau + \tau_{(M)}(\theta', \phi'))] . \quad (3.98)$$

Thus by just shifting the complex time series with appropriate time lags between the individual detectors we can construct the network correlation vector as a function of the time of arrival. The real and imaginary parts of this vector, ( $\Re[\mathbf{C}(\tau)] = \mathbf{c}_+(\tau)$  and ( $\Im[\mathbf{C}(\tau)] = \mathbf{c}_-(\tau)$ ), constructs the maximized log likelihood ratio in Eq. (3.92) as a function of arrival time in the reference detector. In presence of a chirp this log likelihood ratio will maximize when the appropriate time of arrival is chosen at the reference detector and when the time delays owing to the choice of the sky position are commensurate.

### 3.3.4 The null stream statistic

The network coherent search also provides another statistic called the *null stream statistic* or simply *null statistic*. This is particular helpful in discerning between actual astrophysical signals and other non-stationary artifacts of environmental and instrumental origin, masquerading as legitimate signals, called *glitches*. The single detector  $\chi^2$  test that we discussed briefly in the previous chapter combined with the null statistic forms a potent signal discriminator in CBC search. In this section we will motivate the basic idea of this statistic <sup>3</sup>.

Consider a case of a three detector (Note that this statistic is not useful for network with less than three detectors) network. The gravitational wave strain in the individual detectors  $s_1, s_2$  and  $s_3$  in the network in absence of any noise is given by

$$\begin{aligned} s_1 &= F_+^1 h_+ + F_\times^1 h_\times, \\ s_2 &= F_+^2 h_+ + F_\times^2 h_\times, \\ s_3 &= F_+^3 h_+ + F_\times^3 h_\times, \end{aligned} \tag{3.99}$$

where  $F_{+,\times}^I$  denote the antenna pattern functions in the  $I$ th detector. From the last two equations of Eq. (3.99), we can find the two polarizations of the gravitational waveform as follows

$$\begin{pmatrix} h_+ \\ h_\times \end{pmatrix} = \begin{pmatrix} F_+^2 & F_\times^2 \\ F_+^3 & F_\times^3 \end{pmatrix}^{-1} \begin{pmatrix} s_2 \\ s_3 \end{pmatrix}, \tag{3.100}$$

Thus

$$\begin{aligned} h_+ &= \frac{F_\times^3 s_2 - F_\times^2 s_3}{F_+^2 F_\times^3 - F_\times^2 F_+^3}, \\ h_\times &= \frac{F_+^2 s_3 - F_+^3 s_2}{F_+^2 F_\times^3 - F_\times^2 F_+^3}. \end{aligned} \tag{3.101}$$

---

<sup>3</sup>For details about this statistic one may find Ref. Gürsel and Tinto (1989) useful.

Substituting the expressions of  $h_+$  and  $h_\times$  in Eq. (3.99), we get

$$\begin{aligned}
s_1 &= F_+^1 \frac{F_\times^3 s_2 - F_\times^2 s_3}{F_+^2 F_\times^3 - F_\times^2 F_+^3} + F_\times^1 \frac{F_+^2 s_3 - F_+^3 s_2}{F_+^2 F_\times^3 - F_\times^2 F_+^3}, \\
&= \left( \frac{F_+^1 F_\times^3 - F_\times^1 F_+^3}{F_+^2 F_\times^3 - F_\times^2 F_+^3} \right) s_2 + \left( \frac{F_\times^1 F_+^2 - F_+^1 F_\times^2}{F_+^2 F_\times^3 - F_\times^2 F_+^3} \right) s_3.
\end{aligned} \tag{3.102}$$

Let us now define the quantities

$$\begin{aligned}
K_1 &= F_+^2 F_\times^3 - F_\times^2 F_+^3, \\
K_2 &= - (F_+^1 F_\times^3 - F_\times^1 F_+^3), \\
K_3 &= - (F_\times^1 F_+^2 - F_+^1 F_\times^2).
\end{aligned} \tag{3.103}$$

Substituting the above expressions of  $K_1, K_2$  and  $K_3$  in Eq. (3.102) we get

$$s_1 = -\frac{K_2}{K_1} s_2 - \frac{K_3}{K_1} s_3. \tag{3.104}$$

Thus from the strains in two detectors in a network for an astrophysical signal it is possible to predict the strain in the third detector by simple geometry. This has two uses. Firstly, in a search for gravitational waves from a source whose location is unknown to us, this can be used to locate the object if three detectors have been taking data at that time. Since in a coherent search one will be searching in the sky over a grid, at every point in the grid we can perform this test where we predict the strain in one of the detectors using the strains in the other two detectors and then comparing that with the actual recorded strain in that detector. Secondly, if we assume that the noise across the detectors in a network is un-correlated, then the predicted strain in one of the detectors from the other two detectors need not follow Eq. (3.104) for noise artifacts or glitches. This can be used to discriminate between astrophysical signals and glitches. From Eq. (3.104) we can form a quantity

$$\kappa = K_1 s_1 + K_2 s_2 + K_3 s_3, \tag{3.105}$$

that vanishes when there is no noise in the detector. But as we know

$$s_I(t) = \frac{2\mathcal{N}\sqrt{\xi}}{r} \Re [(E_I^* S^I) e^{i\delta_c}] , \quad (3.106)$$

therefore

$$\kappa = \frac{2\mathcal{N}\sqrt{\xi}}{r} \sum_{I=1}^3 K_I \Re [(E_I^* S^I) e^{i\delta_c}] = \frac{2\mathcal{N}\sqrt{\xi}}{r} \Re \left[ \sum_{I=1}^3 K_I (E_I^* S^I) \right] e^{i\delta_c} . \quad (3.107)$$

In absence of any noise this quantity will be equal to zero. Thus this quantity is identically canceling the contribution of signal from all the detectors in the network. However it is the sum over the  $I$  that is causing the signal contribution to vanish. Thus we can redefine the quantity  $\kappa$  as

$$\kappa = \sum_{I=1}^3 K_I g_I S^I , \quad (3.108)$$

which should also identically cancel the signal contribution from all the detectors. Note that the factor  $g_I$  comes from  $E_I^*$  as given in Eq. (3.23). Fourier transforming the above equation yields

$$\kappa = \sum_{I=1}^3 K_I E_I^* \tilde{S}^I(f) , \quad (3.109)$$

which in absence of any noise should also vanish, satisfying the condition of nullity

$$\sum_{I=1}^3 K_I E_I^* \tilde{S}^I(f) = \sum_{I=1}^3 K_I g_I \tilde{S}^I(f) = 0 , \quad (3.110)$$

where we have used Eq. (3.23) and divided by all terms that are independent of the detector index  $I$ . Recall that  $C = \langle x|S \rangle$ . Thus the correlation time series can be written as

$$C(\tau) = 2 \int_{-\infty}^{\infty} \frac{\tilde{x}^*(f) \tilde{S}(f)}{S_n(|f|)} e^{2\pi i f \tau} df , \quad (3.111)$$

whose Fourier transform is given by

$$\begin{aligned}
\tilde{C}(f') &= \int_{-\infty}^{\infty} \left[ 2 \int_{-\infty}^{\infty} \frac{\tilde{x}^*(f)\tilde{S}(f)}{S_n(|f|)} e^{2\pi i f \tau} df \right] e^{-2\pi i f' \tau} d\tau \\
&= 2 \int_{-\infty}^{\infty} \frac{\tilde{x}^*(f)\tilde{S}(f)}{S_n(|f|)} \left[ \int_{-\infty}^{\infty} e^{2\pi i (f-f')\tau} d\tau \right] df \\
&= 2 \int_{-\infty}^{\infty} \frac{\tilde{x}^*(f)\tilde{S}(f)}{S_n(|f|)} \delta(f-f') df \\
&= 2 \frac{\tilde{x}^*(f')\tilde{S}(f')}{S_n(|f'|)},
\end{aligned} \tag{3.112}$$

which gives us

$$\tilde{S}(f) = \frac{S_n(|f|)\tilde{C}(f)}{2\tilde{x}^*(f)}. \tag{3.113}$$

Substituting this back to Eq. (3.110), we get

$$\sum_{I=1}^3 K_I \frac{S_{n(I)}(|f|)\tilde{C}_I(f)}{\tilde{x}_I^*(f)/g_I} = 0. \tag{3.114}$$

From the above equation one can write, generalizing for  $M$  detectors

$$\kappa = \sum_{I=1}^M K_I S_{n(I)}(|f|)\tilde{C}_I(f) = 0, \tag{3.115}$$

which is a vanishing quantity in presence of stationary noise. However if there is non-stationarity in the data, it will not vanish, which motivates us to construct the statistic

$$\rho_{\text{null}} = \frac{\langle |\kappa| \rangle}{\sqrt{\text{Var}(|\kappa|)}}, \tag{3.116}$$

which is called the null SNR. The null SNR time series is called the null stream. A larger value of the null SNR for a particular trigger implies less chance of it to be a signal of astrophysical origin. This is analogous to single detector  $\chi^2$  test in the coincidence pipeline. Note that since the signal contribution is identically cancelled in quantity defined above, the

null SNR is independent of the signal strength. However, if there is a mismatch between the template and the signal then the matched filter output  $C^I(t)$  will scale linearly with the mismatch. This implies that the null SNR  $\rho_{\text{null}}$  too will scale linearly with the mismatch in the signal. since the coherent SNR is related quadratically to the matched filter output (see for example Eqs. (3.44) and (3.92) ), thus one can conclude that the null stream scales quadratically with coherent SNR in presence of mismatch. This feature is analogous to single detector  $\chi^2$  test in coincident search as well.

### 3.4 Coherent search pipeline for all-time, all-sky search

Pursuing a complete coherent search requires an enormous amount of computational power, especially for background construction. Unlike the coincident search where, in the absence of spin, a two dimensional mass template bank suffices, a coherent search requires that one uses the same template bank to compute the detection statistic for every point in a grid on the sky and then maximize it. This is equivalent to searching the data using a four dimensional template bank, characterized by the two masses and the two sky positions. Such an endeavor is currently beyond the capabilities of the gravitational waves scientific community. Thus we are left with the alternative of employing a hierarchical search technique. We will explain the technical details of this search strategy, called the *hierarchical coherent search pipeline* in this section, a schematic diagram of which is presented in Fig. 3.4.

#### 3.4.1 The coherent bank

Recall, from the previous chapter, that the coincident search pipeline outputs gravitational waves triggers at the end of the search that were obtained by matched filtering the data with a bank of templates. The triggers that were thus obtained at the end of the search correspond to the mass pairs that were a subset of the original template bank. In a hierar-

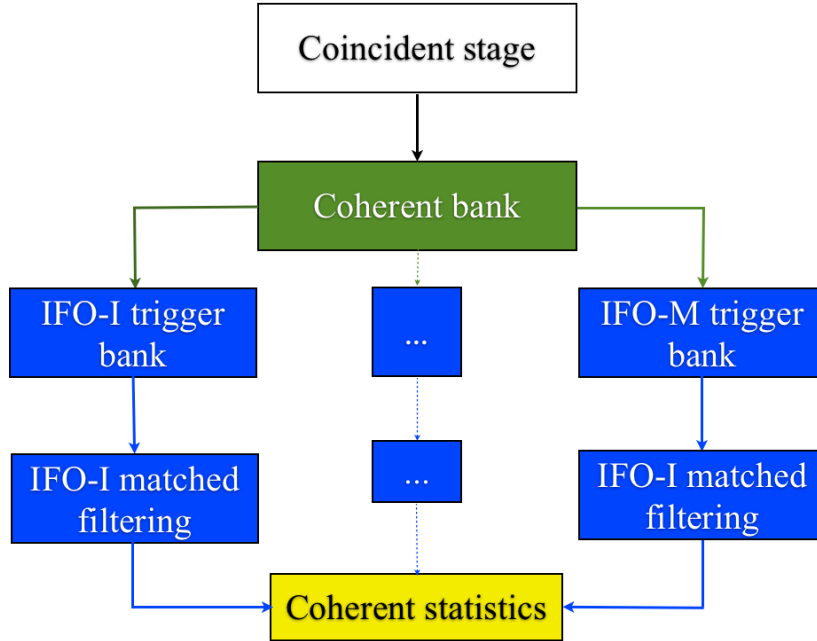


Figure 3.4: A schematic representation of the hierarchical coherent search pipeline.

chical coherent search pipeline, the mass pairs of these triggers are used as template bank for the coherent stage of the pipeline. This is named the *coherent bank*, which is the first step of the hierarchical coherent search pipeline. However, one should note that the final triggers obtained from the coincidence pipeline are triggers that were found in coincidence in more than one detectors. Triggers in different detectors that are coincident and arise from the same GW source can have different mass pairs owing to the possibility that the noise PSDs of the detectors they arise in are somewhat different and because of the random nature of noise. For every coincident trigger, we construct a network template with a single mass pair, namely the one corresponding to the loudest SNR among all the detectors, to search coherently around the end-time of that putative signal. Thus, for a double coincident trigger (triggers in two detectors that were found in coincidence in time of coalescence and masses) if ‘detector A’ had a trigger with an SNR of  $\rho_A$  obtained from a template with mass pairs  $(m_1^A, m_2^A)$  and ‘detector B’ had a trigger with an SNR of  $\rho_B$  from a template of masses  $(m_1^B, m_2^B)$ , and if with  $\rho_A < \rho_B$  then we will store  $(m_1^B, m_2^B)$  as component masses for the

network template bank.

### 3.4.2 The coherent trigger bank and filtering with it

The second step in the coherent stage is the construction of trigger banks, whereby the coherent-bank template for every coincident trigger is copied as a single-detector templates as depicted in Fig. 3.4. These are called the *coherent trigbanks*. The fundamental structures of the coherent trigbanks are identical to that of the template banks except that they are a subset of the template banks. Next, the match filtered output of the data and the coherent trigbank templates are obtained. Note from Sec. 3.3.3 that for the computation of the  $\mathbf{C}$  vector for a network of detector for a particular sky position, the knowledge of the time lag between pairs of detectors in the network is required, and this was implemented in a nice way by shifting the complex data time series of one detector w.r.t another in time. However, the standard match filtering, that is implemented in the coincidence search pipeline, do not output this complex data time series. It simply outputs the parameters of the trigger that crosses a preset threshold. This is changed in the coherent stage of the pipeline. Since it increases the computational burden to output the complex time series of the entire matched filter, we store 125 msec snippets of it around the coincident trigger times. Additionally, the coherent matched filtering step computes the template normalization factors  $g^I$  and  $\chi^2$  values for the maximum SNR mass pair across all detectors per coincident trigger.

### 3.4.3 The coherent inspiral analysis - CHIA

The final step of the coherent stage is the coherent-statistic step, which matches the parameters of each triple-coincident trigger to the complex time series data output by the matched filtering step and uses them, the corresponding template-norms, and the  $\chi^2$  values in the respective detectors to compute the coherent detection statistic and the null stream statistic as given in Eqs. (3.92) and (3.116). This step maximizes the log likelihood ratio over all the parameters as explained in Sec. 3.3.2. The triggers that are obtained, which

we call the coherent triggers, upon maximization over the 4 parameters  $(r, \delta_c, \psi, \iota)$  in the form of the symmetrized parameters  $(a^{(1)}, a^{(2)}, a^{(3)}, a^{(4)})$ , and time of arrival for every sky points in the grid are maximized for every mass pair in the template. The maximization is then done over all the masses and one coherent detection statistic is obtained for that particular time of arrival. Thus we will obtain multiple triggers characterized by a time (corresponding to the signal arrival time) called the trigger end time. Not all these triggers are independent, since a single signal can triggers multiple threshold crossing responses in the parameter space. To solve for this degeneracy a clustering is done over time in which we keep one trigger (which has the loudest coherent SNR) per window (which is pre-specified) of end times. This concludes the hierarchical coherent search analysis, and we are left with a list of clustered triggers with end times, their coherent SNR, null SNR and recovered gravitational wave parameters. Based on the coherent SNR and the null stream one can then rank these triggers according to their significance in a search.

### 3.5 An example of blind hierarchical coherent search

To study the performance gain arising from using the coherent stage, we ran the CBC search pipeline, after modifications to run the hierarchical coherent stage at the end of the coincidence stage, with and without that stage on simulated Gaussian noise, with LIGO-I noise PSD in the 4 km LIGO detectors in Hanford (H1), Livingston (L1), and in the Virgo detector (V1), for the duration of approximately a month. Specifically, this search pipeline was run once with signal injections and again without injections but with time-slid data so that the background could be estimated. The estimation of background with time slides in coherent search is done by just following up on the background triggers obtained from the coincident search stage with the same technique illustrated in the previous section. One advantage of this study is that we can compare the performance improvement due to the coherent search directly w.r.t the previous stage of coincident analysis. The disadvantage

of this study is, as we will see in the results, that it does not reflect the true potential of a fully coherent search as we are using the result of the coincident stage as the input. This makes our analysis somewhat constrained by the performance of the coincident pipeline. The left plot in Fig. 3.5 compares the performance of the coherent statistic and the combined effective SNR. The right plot in the same plot compares the coherent SNR and null-stream statistic. For these simulations, 1051 signals were injected in software in all three detectors. The source distances of all injections were between 100-500 Mpc. The total masses of these sources were chosen to be in the range 25-100  $M_{\odot}$ , and component masses between 1-99  $M_{\odot}$ . A total of 55 of those injections were found, above the single-interferometer detection thresholds of 5.0 and coherent SNR threshold of 3.75. The latter threshold was intentionally chosen to be lower since we anticipated that some coincident background triggers will have negative cross-terms owing to incoherent phases, thereby, yielding lower coherent SNRs.

All injections recovered by the coincident stage were also found by the coherent stage, and are symbolized by red pluses. The background triggers that are found by the coincident stage and survive the coherent stage are depicted by the black crosses. The blue circles, on the other hand, denote background triggers in the coincident stage that got vetoed by the choice of the threshold on the coherent SNR in the coherent stage. To include them in the left plot, we arbitrarily assign all of them  $\rho_{\text{coh}} = 3.0$ . Comparing the sets of black crosses and blue circles reveals that the coherent stage not only reduces the number of background triggers but, in this case, also vetoes some of the loudest ones (in combined-effective SNR). Furthermore, whereas all found injections have coherent SNR greater than that of the loudest background trigger, 13 of them have combined-effective-SNR weaker than that of the loudest background trigger (shown in blue circles). When compared to the loudest black cross, that number drops to 7. It drops further when some of the background triggers with the loudest null-stream (as shown in the right plot) are vetoed. The resulting performance improvement is depicted in the blue dash-dotted Receiver-Operating-Characteristic (ROC) curve in Fig. 3.6; its performance is better than that of the coincident stage (shown in red), without the

null-stream vetoes. The former asymptotes to the ROC curve of the coherent stage (shown in black dashes) for higher false-alarm probabilities.

Finally, Fig. 3.5 reveals the existence of a gap between the loudest background and the weakest injection  $\rho_{\text{coh}}$  values. One might argue that this is owing to the lack of a sufficient number of weak signal injections made into the data. We have verified that, indeed, one can get some injection triggers to show up in that gap by making multiple weak injections (say, with source distances between 500-750 Mpc) in the data. Those studies also reveal that the detection efficiency in that region is very low (i.e., less than 1 in 250). We believe that this low efficiency is partly caused by the coincident stage, in the way it has been designed and tuned, turning it into the chief constraining factor for the performance of the coherent stage.

## 3.6 Discussion

In this chapter we studied from the basic principles how to construct a detection statistic for searching gravitational waves in a network of detectors. Use of a network for detection of gravitational wave is of paramount importance. Searching with a single detector poses multiple problems. Firstly, interferometers can go out of lock multiple times in a given day giving rise to the possibility that one might miss out on a potential detection when the detectors are not operating in science mode. Secondly, gravitational wave detectors are not completely isotropic, making parts of the sky less sensitive to detection and thereby reducing the volume of detection than an isotropic detector. Thirdly, a single gravitational wave detector is incapable of locating a source in the sky and all we can do is infer upon the time of arrival of a particular signal. Finally a trigger in a single detector is not considered to be detection as the confidence associated with such an event is not very high. All these problems are addressed when we use multiple detectors in different sites. Thus devising a detection strategy for multiple detectors is very pertinent to the cause of gravitational wave astronomy.

We first developed the detection statistic for a network of interferometers using the maximum log likelihood ratio. The likelihood ratio was expressed in terms of the ratio of probability that an output was obtained given there was signal present in the data and the probability that an output was obtained when no signal was present in the data. We then generalized it for multiple detectors. Finally we analytically maximized this log likelihood ratio.

We then discussed about another statistic that one can obtain from multiple detectors, called the null stream. In presence of three detectors the null stream combines the strain from two detectors to construct the strain in the third and compares it with the actual observed strain in the third detector. In absence of any noise, strain in the third detector caused by a real astrophysical signal will be reproduced exactly by the knowledge of the strain in the two other detectors and thus the difference between the observed strain and the estimated strain (the null stream) must vanish. In presence of Gaussian noise the mean of this difference should vanish, however in presence of noise artifacts, known as glitches, this null stream will contain a remnant from the glitch. Thus the null stream is an excellent tool to distinguish between a real astrophysical signal and a noise glitch.

Finally, we outlined the CBC coherent search pipeline that is used in the all-time, all-sky search (or blind). We then followed up with an example where we searched in one month long CBC data in simulated Gaussian noise. We noted the performance improvement upon implementation of the coherent stage through receiver operator characteristic curves. We observed an improvement of  $\sim 22\%$  at the zero false alarm rate region when one switches from a coincident search to a hierarchical coherent search. Upon using null stream for vetoing glitches an improvement of up to  $\sim 57\%$  was recorded.

The performance improvement that we noted in our study was despite the fact that the search was constrained by the performance of the coincident stage. A full fledged coherent study is expected to yield a much better result. The current performance enhancement occurs primarily because the SNR of the background triggers are significantly lowered by

the coherent stage and some of the loudest ones are vetoed by the null stream. We will however recover more injection triggers upon using the full coherent search. With improving computational powers it is expected that in the near future we will be able to implement a fully coherent search, at least in some restricted cases.

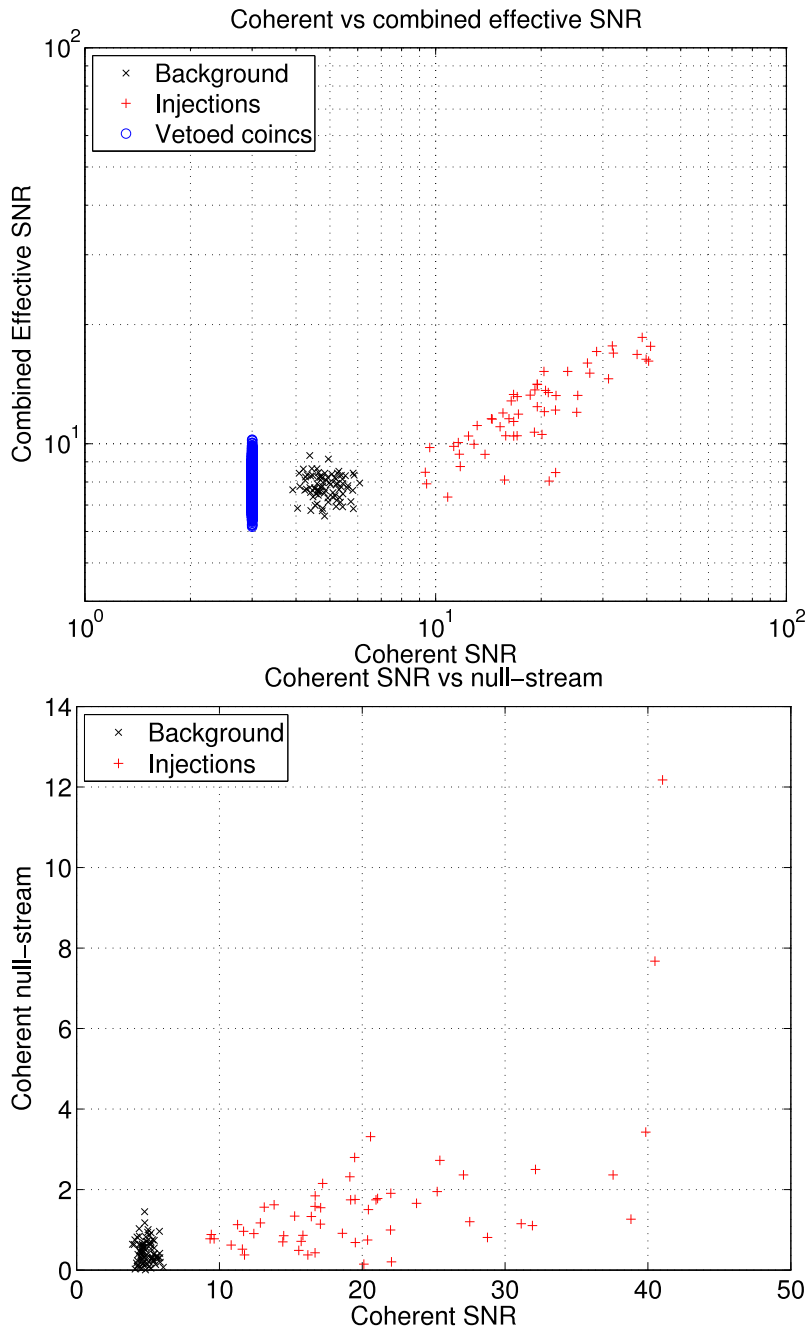


Figure 3.5: These are scatter plots of the combined and coherent SNRs of injection triggers, represented by red plus symbols, and background (or “slide”) triggers, represented by the black crosses. The coherent SNR was used to cluster the triggers, from both injections and slides. The coherent SNR performs noticeably better than the combined effective SNR in discriminating signals from background: In the left plot, at a detection threshold of a little above 6 in the coherent SNR all the injections found in the coincident stage are recovered with a vanishing false-alarm probability. For the same false-alarm probability, the combined effective SNR detects a lesser number of injected signals.

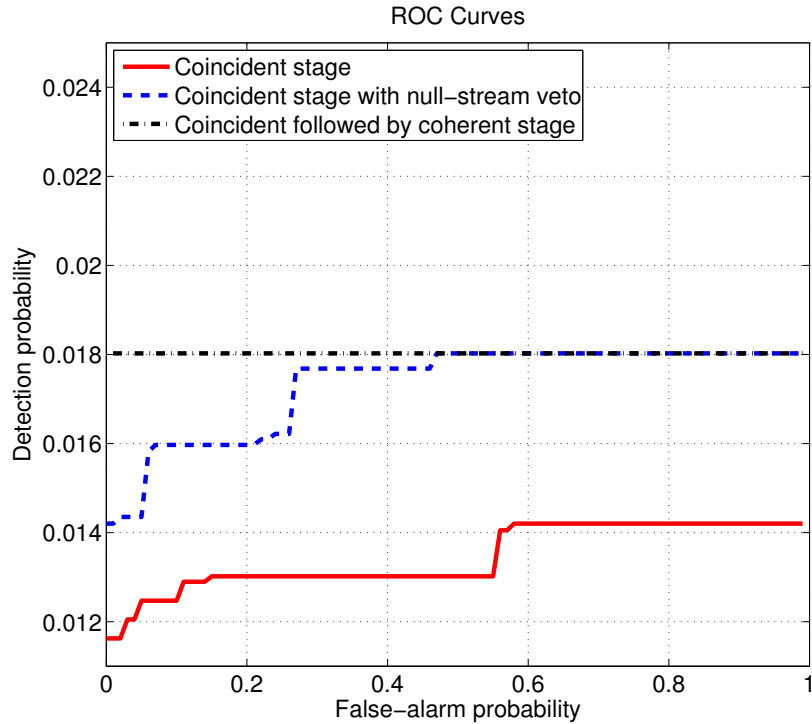


Figure 3.6: The receiver operating characteristic (ROC) curves of three CBC searches are compared above. The ROC of the search with the coincident stage alone is plotted in solid red line, and has the weakest performance owing to the 13 found injections that are weaker than the loudest background trigger in that search. On the other hand, the ROC curve for the hierarchical pipeline, with coherent stage included, is shown in black dash-dotted line and has the best performance. It has a constant detection probability because all found injections are louder than the loudest background trigger for this pipeline. Finally, the third ROC curve, shown as a blue dashed line is the coincident stage, with the null-stream veto applied. This veto improves the performance of the coincident pipeline, so much so that for low detection-thresholds (or high false-alarm probability) its ROC curve rises to match that of the pipeline with the coherent stage. The average error in the detection probabilities plotted here is less than  $3 \times 10^{-4}$ .

# Chapter 4

## Short hard gamma-ray bursts and orphaned afterglows as external triggers to gravitational waves

### 4.1 Introduction

Short duration gamma-ray bursts (SGRBs) are less of an enigma now than when the extraterrestrial nature of the first gamma-ray bursts (GRBs) was established in the seventies Klebesadel et al. (1973). Since then we have learned a lot about their characteristics and how they differ from their long duration counterparts, the long GRBs or LGRBs. This knowledge includes the nature of their host galaxies, including their redshift, star formation rate, age, metallicity, distances of separation from the host galaxy, and distinguishing features in their light-curves compared to those of LGRBs Nysewander et al. (2009); Nakar (2007); Gehrels et al. (2009); Metzger and Berger (2012). Some critical aspects are still unknown or need unequivocal observational confirmation. While there is some evidence that the progenitor of a SGRB might be the compact binary coalescence (CBC) of a black hole (BH) and a neutron star (NS) or two neutron stars (see, e.g., the review in Ref. Nakar (2007)), the

observation of gravitational waves (GWs) from them can provide direct confirmation of that hypothesis Nissanke et al. (2010); Metzger and Berger (2012); Harry and Fairhurst (2011); Kelley et al. (2012); Dietz et al. (2012); Nissanke et al. (2012); Bartos et al. (2012). Heretofore, such CBCs, which include at least one neutron star, will be termed as “CBCNS” sources. Once GW observations are occurring regularly in the advanced detector era (ADE), GW associations with SGRBs can provide additional astrophysical information about these objects.

It is well established that gamma-ray bursts are transient events of gamma-ray flashes occurring at cosmological distances. These events are different from soft gamma repeaters specifically in being extremely intense, of short duration, and in being non-repeating. On the basis of spectral hardness, these events broadly divide into two categories, those of a short duration spanning less than 2 sec and with a harder gamma-ray spectrum and those of a duration longer than 2 sec and with a softer gamma-ray spectrum. The first one is called the short duration gamma-ray burst and the second is called the long duration gamma-ray burst. Because of the dichotomy in the time scales of these events and the fact that they systematically fall in different regions in spectral hardness, it can be conjectured that different physics is involved in their occurrence. The most likely progenitor of the long duration gamma-ray burst is a core collapse supernova of a massive star MacFadyen and Woosley (1999) and that of a short duration one is the merger of the two objects in a compact binary system involving at least one neutron star as a component Eichler et al. (1989). The physical time scales of a collapsar and the coalescence of the remnants of neutron star and black holes are commensurate with the time scales of the long duration and short duration gamma-ray bursts, respectively. A gravitational wave (GW) discovery coincident with a short gamma-ray burst observation will provide the strongest evidence to date of the merger model. The time delay between the gravitational wave signal and the GRB will provide clues to the burst mechanism and additional information in the form of GW polarization will help us determine the source geometry. Coincident GW-GRB discovery will also enable

us to measure the source distance independently of the cosmological distance ladder and, therefore, provide a test for it.

Gravitational wave observations can complement electromagnetic (EM) studies to better understand the SGRB sources and even resolve some anomalies. In fact it is known that some SGRB light-curves last for quite a bit more than 2 sec and some LGRB light-curves resemble those of SGRBs. This has led to a recent proposal of categorizing GRBs based not on their light-curves but on their progenitor type: In this classification scheme, Type I GRBs are associated with CBCNS and Type II with a collapsar Zhang (2006). It is to be seen if this scheme will stand the scrutiny of GW observations. Additionally, multi-baseline network of GW detectors can resolve the inclination of those sources accurately enough to constrain the beaming angle of the GRBs Nissanke et al. (2010). This is a nice alternative to the method based on electromagnetic afterglows proposed by Rhoads in 1997 Rhoads (1997). An accurate determination of the beaming angle will resolve how energetic SGRBs really are and, thereby, unravel if SGRBs have a narrow or wide range of energy output and what the possible reasons for it might be. Rhoads' method depends upon the presence of an afterglow that presents clear evidence for breaks in the power-law in the emission spectrum of the putative GRB jet Rhoads (1997). It can work even when the gamma-ray emission from the GRB itself goes unobserved, such as when the afterglow is an "orphan". On the other hand, an afterglow may not reveal the sought spectral breaks because it may not extend over a wide enough frequency range. (See Refs. Neal Dalal and Kim Griest and Jason Pruet (2002) for additional problems with this method.) Such afterglows, e.g., in X-ray, optical, or radio, may still provide spectroscopic redshift Yu et al. (2011); Zafar et al. (2011); Kruhler et al. (2011), and distance to the source. Joint EM and GW observations can determine both the distance and the inclination angle of the CBCNS more accurately than either one of them.

It is obvious that this type of joint observation will also aid in improving theoretical models of SGRB afterglows. If indeed it is established that they are associated with CBCNS, then a host of outstanding questions can be answered. For example, how much later can

afterglows in different bands of the EM spectrum occur after the CBCNS merger? How isotropic are the afterglows? How varied can the afterglow energetics be? How strongly beamed SGRBs are can be resolved by joint GW-EM observations, which in turn can shed light on afterglow energetics, as noted above. Is the source model rich enough to explain that observed variety? What strong gravity physics can be probed with joint GW-EM observations? On the other hand, if no GW signals are observed from multiple SGRBs within a distance of about 500Mpc, then it would disprove the hypothesis that CBCNS are the progenitors of SGRBs.

While most studies in the past have focused on targeted searches of GW counterparts of SGRBs here we broaden the category of EM triggers by including orphaned afterglows of SGRBs. By a targeted GW search we mean a search for GWs from a part of the sky where an EM or a neutrino signal was detected from a source that may also emit GWs. The EM or neutrino signal is then termed as an external trigger whose sky-position, time, or other characteristics, deemed relevant, are used to define the GW search. In this paper, we highlight the astrophysical factors that are required to estimate how many GW signals will be detected from SGRBs and orphaned afterglows in the ADE. The Laser Interferometer Gravitational-wave Observatory (LIGO) and the Virgo detector, have demonstrated successfully that large scale interferometers can be used to detect GWs that change their arm-lengths at sub-nuclear scales. With the advent of the next generation gravitational wave interferometers in the next few to several years, with roughly ten times increased strain sensitivity, we increase the event rate thousandfold. These interferometers include the advanced LIGO (aLIGO) AdL and the advanced Virgo (AdV) detectors, the Japanese detector KAGRA Kuroda and LCGT Collaboration (2010) and a LIGO detector in India. Collaboration with the gamma-ray astronomy community has helped us understand and use GRBs to trigger searches in the data of GW detectors Abbott et al. (2008). Prior information about the sky position and time of the EM event improves GW detection confidence and significantly reduces the data analysis computational cost of the search. It also helps us reduce the threshold for detection of possible

candidates and false alarm probability, as we discuss here. The sensitivity of such a targeted GW search depends strongly on the accuracy of the GRB sky position. A substantial fraction of GRBs detected by some observatories, e.g., Fermi Abdo et al. (2009), can have error radii in the sky that are several degrees wide. The interplanetary network (IPN) Hurley is a group of satellites with onboard gamma-ray detectors that are used to locate gamma-ray bursts in the sky through triangulation. Given the number of satellites detecting a particular GRB and also the uncertainty in the relative location of the satellites and clock synchronization, the sky positions of a good fraction of GRBs detected by them can have errors of several degrees or worse. In this paper we study the effect of the error in the SGRB sky position on the detectability of GW from its progenitor. In such cases, one needs to search over a wider patch in the sky for GW signals. Note that when there is ambiguity about the short or long nature of a GRB from studying its light-curve, it makes sense to allow for the possibility of it being a SGRB and, therefore, search for a GW counterpart.

On the other hand, when the sky-position of a GRB is accurately known, searching for a GW counterpart only at that location and close to the GRB time would seem to be the best strategy to detect GWs. This is true unless there exists a significant mismatch between the modeled GW waveform and the CBCNS signal or if the detector calibration is erroneous. It turns out that each of these sources of error can cause a non-negligible drop in the signal-to-noise ratio (SNR). In such a case of systematic error, searching in a larger patch of the sky than just a single sky position can reduce the extent of that drop and improve the detection confidence. More importantly, when the SNR is close to the detection threshold it can make all the difference between a detection and a non-detection.

The layout of the paper is as follows. In Sec. 4.2 we show how the detectability of a GW signal from an orphaned afterglow improves owing to the localization of the source in the sky. Unless noted otherwise, the working assumption in the rest of the paper is that CBCNS sources are the progenitors of SGRBs. In that vein, we show how the possible beaming of the SGRB influences the fraction of CBCNS sources that will be detected as orphaned afterglows

of SGRBs. The framework used for this calculation is broadened to enquire what fraction of all CBCs in a given volume will be detectable as GW events. For that general case of CBC sources we reproduce the well known result that GW strain of a detected source, when averaged over its sky position and orientation, is less than the maximum strain from an optimally oriented and located source of the same kind, by a factor of 2.26. In Sec. 4.3, we study the effect of poor sky localization of SGRBs on the detectability of GWs from them. These results emphasize the importance of performing GW searches over a sky-grid involving multiple sky-positions covering the error regions of the SGRBs. In Sec. 4.4, we study CBC triggers from previously analyzed LIGO data to check if any of them was concurrent with a GRB. In Sec. 4.5, we study other causes of systematic errors, e.g., detector calibration errors and the mismatch between a GW signal and the waveform model used to search for it. Here we find that searching in a wider patch of the sky for the GW counterpart of a SGRB or an orphaned afterglow, even when the sky-position of the latter is known accurately through EM observations, can improve the detectability of the signal owing to the possible covariance of the errors in the waveform or calibration with the error in the source sky-position. We end with a discussion in Sec. 4.6 of some unresolved issues related to GW-EM targeted searches that should be explored in the near future.

A note on conventions and terminology used in this paper is in order. Unless otherwise specified, a detector in this paper means a GW detector and should be distinguished from non-GW detectors, such as gamma-ray detectors. Similarly, a GW search refers to a targeted GW search unless it is explicitly stated that the search in question is of an un-targeted type where the sky position or timing information of an EM or neutrino observation is not used to search in GW detector data. Finally, the LIGO detectors, with 4km arm-lengths, in Hanford and Livingston (US) are labelled H1 and L1, respectively, while the Virgo detector in Cascina (Italy) is denoted as V1. These three detectors form three single baseline networks, H1L1, L1V1, H1V1, and one multi-baseline network H1L1V1. A second LIGO detector in Hanford, which participated in the first five LIGO science runs, had 2km long arms and is labelled

H2.

## 4.2 SGRBs, orphaned afterglows, and their prospects as GW candidates

In this section, we show how the rate of CBC detections would improve if GW counterparts of orphaned afterglows are sought in data of ADE detectors. Currently, SGRBs are the only targeted searches for GWs from CBCs. As we conclude below, the improvement in rates can be modest enough that orphaned afterglows should be added to the list of targeted GW searches.

The first afterglow of a SGRB was observed in 2005 Berger et al. (2005). Afterglow emissions of short GRBs are similar to that of long GRBs, but are less luminous. While it is not confirmed yet what the progenitor of a SGRB is, it is widely believed that it might be the merger of a NS with another NS or a stellar mass BH. Alternative sources, e.g., long-lived magnetars Bernardini et al. (2012), have been proposed too. It is not clear if in the alternative model the magnetar is in itself the product of a CBCNS progenitor. GW observations will provide direct confirmation of the SGRB model or help rule it out. If the SGRB model is correct, then the GRB is powered by an accretion disk that is formed after the tidal disruption of a NS by its other compact companion. Matter falling into the central spinning object from the accretion disk can form bipolar jets via the Blandford-Znajek mechanism. Numerical relativistic simulations suggest this as a likely scenario, especially, if the central object is a highly spinning black hole and the NS equation of state (EOS) is relatively stiff, which allow for large enough accretion disks Foucart et al. (2012). Strong magnetic fields are also believed to play an important role in powering GRBs. The gamma-ray burst is generated by the shock-accelerated electrons in the relativistic jet. This is the so-called fireball model (see, e.g., the review Piran (1999)). A GRB afterglow is produced when the jet interacts with medium surrounding the burst. In the process it can produce

radiation over a wide range of frequencies, from X-Rays to radio, as the jet slows while ploughing through that medium.

A kilonova could be another EM manifestation of a CBCNS progenitor. The ejecta from NS-NS merger is neutron rich. This results in the formation of heavier elements due to r-process neutron captures. These heavy elements undergo nuclear fission and beta decays on time scales of the order of a day. These are also interesting candidates for external trigger study. The data analysis pipeline that is constructed for detecting GW counterparts to orphaned afterglows in archived data can also be applied to kilonovae because in both cases the sky position will be known accurately enough to launch a search in GW archived data for the time of arrival of the signal.

There are existing missions, like Swift and Fermi, that are expected to overlap with aLIGO observations from 2015-2018 and, perhaps, even beyond. There are a handful of planned observatories that will target GRB afterglows and orphaned afterglows in the next several years with expected concurrent observations with aLIGO and, possibly, AdV detectors. The Australian Square Kilometer Array Pathfinder (ASKAP) is currently under construction at the Murchison Radio-astronomy Observatory in Western Australia and is expected to start early operations in 2013 Murphy et al. (2012). Its initial five-years operation period will overlap with aLIGO science runs. Among proposed observatories, Lobster is a NASA mission that will have a wide-field X-ray imager, which will be more sensitive than Swift's BAT but will have a smaller 0.5sr field of view, and a narrow-field followup IR telescope and slewing apparatus. The French-Chinese Space-based multi-band astronomical Variable Objects Monitor (SVOM) and the broad spectral band Indian Astronomy Satellite ASTROSAT are a couple of other missions that will have capabilities of detecting GRB afterglows and will likely overlap with aLIGO observations. Furthermore, the South Korean-led Ultra-fast Flash Observatory Pathfinder (UFFO-P) mission intends to catch the rise of GRBs Grossan et al. (2012).

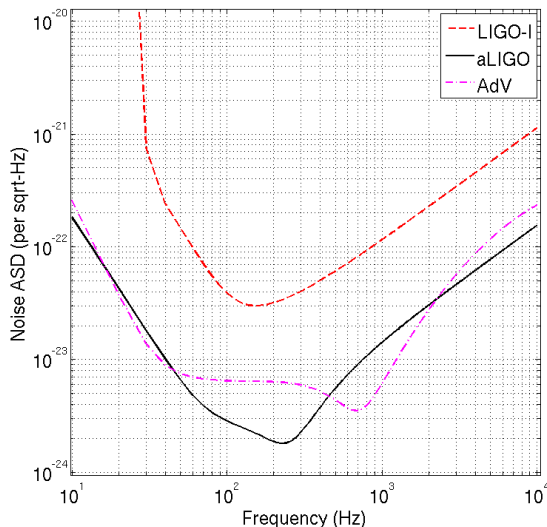


Figure 4.1: The design noise amplitude spectral densities (ASDs) of LIGO-I, Advanced LIGO (aLIGO), and Advanced Virgo (AdV) detectors obtained from LIGO Algorithms Library.

#### 4.2.1 Comparing the detectabilities of GW counterparts of SGRBs and orphaned afterglows

We would like to estimate how much the detection probability improves when the sky-position of a GW source is accurately known but its time of occurrence has a window of uncertainty,  $T_{\text{OAG}}$ . Following Ref. Dietz et al. (2012), let the desired FAP of a GW search be  $10^{-4}$ . Reference Dietz et al. (2012) estimated that when the time of occurrence is known accurately, the GW SNR threshold at that FAP is  $\rho_{\text{th}}^{\text{GRB}} = 9.0$ , dropping from  $\rho_{\text{th}}^{\text{LM}} = 11.3$  at the same FAP for an all-sky, all-time (i.e., a blind) GW search of low-mass (LM) CBC signals in a period of  $T_{\text{LM}} = 3$  months, from sources with total mass of  $\leq 25M_{\odot}$  and each component mass between  $1M_{\odot}$  and  $25M_{\odot}$ . For an X-ray afterglow the putative CBCNS coalescence can occur an hour to a day in the past. For  $T_{\text{OAG}} = 10^5$  sec, the FAP at a SNR threshold  $\rho_{\text{th}}$  obeys

$$\frac{\text{FAP}_{\text{OAG}}(\rho_{\text{th}})}{\text{FAP}_{\text{LM}}(\rho_{\text{th}})} = \frac{T_{\text{OAG}}}{T_{\text{LM}}} \approx \frac{10^5}{10^7} = 10^{-2}. \quad (4.1)$$

We would like to find  $\rho_{\text{th}} = \rho_{\text{th}}^{\text{OAG}}$  such that  $\text{FAP}_{\text{OAG}} = 10^{-4}$ . Equivalently, we ask what is  $\rho_{\text{th}}^{\text{OAG}}$  for  $\text{FAR}_{\text{OAG}} = 10^{-2}\text{yr}^{-1}$ ? The answer, based on real data from the sixth science

run (S6) of the LIGO H1 and L1 detectors, can be obtained from the data plotted in Fig. 3 of Ref. Abadie et al. (2012b), namely,  $\rho_{\text{th}}^{\text{OAG}} = 10.5$ . In comparison, at a FAP of  $10^{-4}$ , the false-alarm rate (FAR) of a year-long low-mass CBC search at threshold  $\rho_{\text{th}}^{\text{LM}} = 11.3$  is  $\text{FAR}_{\text{LM}}(\rho_{\text{th}}^{\text{LM}} = 11.3) = 10^{-4}\text{yr}^{-1}$ , as shown in Refs. Abadie et al. (2012b); Dietz et al. (2012). The threshold  $\rho_{\text{th}}^{\text{OAG}}$  is about 17% higher than the threshold for targeted GW searches of SGRBs with known sky position and time of occurrence but 8% lower than that of all-sky, all-time searches.

There is an additional improvement that arises when one considers the fact that accurate information about the sky-position will further lower the FAR of a targeted GW search. With that information in hand, one need not search in the sky or the time-delays of the signals from the same source in different GW detectors. This reduces the FAR by a factor of a few to hundred depending on how big or small the duration of the noise artifacts are compared to the time-delays across the detector baselines. For instance, consider the single baseline H1L1, which has a light-travel time of  $\pm 10$  msec. Let the FAP in each detector be  $P_i$ , where  $i = 1, 2$  denotes the two detectors. Also, for every trigger in H1 let  $N_2$  be the number of independent experiments of L1 coincidences one can perform in twice the light-travel time across the baseline. Then the joint FAP of H1L1 is

$$P = P_1 [1 - (1 - P_2)^{N_2}]. \quad (4.2)$$

The filter response to noise artifacts in the data that masquerade as signals is similar to that on real signals, as expected. Studies of software injections of simulated signals in GW detector data show that the timescale of such a response is about 2 msec, which is roughly the inverse of the frequency where GW signals from binary neutron stars (BNSs) contribute maximally to the signal-to-noise ratio. Thus,  $N_2$  is 10 for a 20 msec window. This means that if  $P_1 \approx P_2$ , then each one of them is about  $3.2 \times 10^{-3}$  when  $P = 10^{-4}$ . However, when the SGRB's sky position and time of occurrence are known and, therefore, the time-

delays of its signals in the network detectors are known, the joint FAP is  $10^{-5}$ , which is, of course, 10 times smaller. With three baselines, a further reduction in FAP is possible. This will lower the thresholds discussed earlier somewhat. In this paper, we will assume that the FAP discussed in this section remains valid up to a total mass of about  $43M_{\odot}$ , which is the maximum total mass used in targeted GW searches in LIGO-Virgo data. It is worth emphasizing that  $P_{1,2}$  and, therefore,  $P$  depend on the SNR. Results of Monte Carlo simulations discussed in Sec. 4.3 bear out this property.

### 4.2.2 The fraction of compact binary coalescences detectable as GW events

Here we calculate the fraction of all compact binary coalescences occurring in the Universe that are detectable as GW events in a single detector. For this calculation, we assume the CBCs to be distributed uniformly in the volume accessible to ADE detectors. Let  $r_H$  be the horizon distance or the maximum distance to which an optimally oriented and optimally located source can be detected, for given component masses and spins. Let these parameters constitute the components of a vector  $\boldsymbol{\vartheta}_{\text{in}}$ . Then the horizon distance  $r_H(\boldsymbol{\vartheta}_{\text{in}})$  depends on the values of these parameters. Directions directly overhead or underneath of the plane containing the arms of an interferometric detector are optimal source locations. On the other hand, the optimal orientation of a CBC source is one where its inclination angle  $\iota$ , i.e., the angle between its orbital angular momentum vector and the negative of the line of sight vector, is zero. If  $\mathcal{P}(\theta, \phi)$  is the antenna power pattern of a single interferometer,

$$\mathcal{P}(\theta, \phi) = F_+(\theta, \phi, \psi)^2 + F_{\times}(\theta, \phi, \psi)^2 = \frac{1}{4}(1 + \cos^2 \theta)^2 \cos^2 2\phi + \cos^2 \theta \sin^2 2\phi, \quad (4.3)$$

then  $r_H \sqrt{\mathcal{P}(\theta, \phi)}$  is the greatest distance to which a CBC source is detectable in the  $(\theta, \phi)$  direction, where  $\mathcal{P}(\theta, \phi) \leq 1$ . For the rest of this section, we will take the binary component to be non-spinning unless mentioned otherwise. At the greatest detectable distance the

binary will have a face-on orientation, i.e., the orbital inclination angle  $\iota$  will be zero or  $\pi$  radians. As one decreases the distance, binaries with a wider variety of inclinations become detectable. So much so that for favorable directions the closest binaries will be detectable with any value of  $\iota$ , with the maximum possible value being  $\pi/2$ , namely, the edge-on orientation. By accounting for all allowed inclinations, at every  $r \leq r_H \sqrt{\mathcal{P}(\theta, \phi)}$ , we find the fraction of CBCs that will be detectable as GW events.

The gravitational wave power received at a detector on earth depends on the sky position of the source  $(\theta, \phi)$  and the orbital inclination angle  $\iota$  as follows:

$$P_{\text{rad}}(\iota, \theta, \phi) = \mathcal{P}(\theta, \phi) P_{\text{rad}}(\iota = 0, \theta = 0) \frac{(1 + 6 \cos^2 \iota + \cos^4 \iota)}{8}, \quad (4.4)$$

where  $P_{\text{rad}}(\iota = 0, \theta = 0)$  is the GW power of a source that is optimally oriented and located in the sky. The GW strain signal strength at a detector is measured in terms of the SNR Bose et al. (2011). The SNR is inversely proportional to the source distance  $r$ . By the definition of the horizon distance  $r_H$  an optimally oriented ( $\iota = 0$ ) and located ( $\theta = 0$  or  $\theta = \pi$ ) source at that distance will be found with a SNR at the threshold of detection,  $\rho_{\text{th}}$ . Of course, this distance will vary for sources of different mass combinations. Thus we can write the SNR with above dependencies on distance and power

$$\rho(r, \iota, \theta, \phi) = \rho_{\text{th}} \frac{\sqrt{\mathcal{P}(\theta, \phi)} r_H}{r} \sqrt{\frac{1}{8} (1 + 6 \cos^2 \iota + \cos^4 \iota)}. \quad (4.5)$$

Whether a particular source of component masses  $(m_1, m_2)$ , at a distance  $r \leq r_H$  will be detectable or not is determined by the inclination angle of the binary.

For every source at a particular distance and sky position there is a limiting inclination angle,  $\iota_{\text{max}}$ , beyond which the signal from the source falls below the detection threshold. Thus, the probability that a source is detectable or not is the probability that the source has an inclination angle at most equal to  $\iota_{\text{max}}$ . The probability distribution of the inclination angle  $p(\iota) = \sin \iota$ . Thus, the probability of detecting a source at a distance  $r$  and sky position

$(\theta, \phi)$  is given by,

$$P(0 \leq \iota \leq \iota_{\max}(r, \theta, \phi)) = \frac{2 \int_0^{\iota_{\max}(r, \theta, \phi)} p(\iota) d\iota}{\int_0^\pi p(\iota) d\iota} = 1 - \cos \iota_{\max}(r, \theta, \phi). \quad (4.6)$$

Since the SNR at this limiting inclination angle must be at the threshold of detection, one can use Eq. (4.5) to find it as a function of  $r, \theta$  and  $\phi$ :

$$\cos^2 \iota_{\max} = -3 \pm \sqrt{8 + \frac{8r^2}{\mathcal{P}(\theta, \phi)r_H^2}}, \quad (4.7)$$

which has the following real solution:

$$\cos \iota_{\max}(r, \theta, \phi) = \begin{cases} \left[ \sqrt{8 + \frac{8r^2}{\mathcal{P}(\theta, \phi)r_H^2}} - 3 \right]^{1/2}, & \text{if } \frac{1}{2\sqrt{2}} \leq \frac{r}{r_H \sqrt{\mathcal{P}(\theta, \phi)}} \leq 1. \\ 0, & \text{if } \frac{r}{r_H \sqrt{\mathcal{P}(\theta, \phi)}} < \frac{1}{2\sqrt{2}}. \end{cases} \quad (4.8)$$

Above we used the fact that since  $\cos^2 \iota_{\max}(r, \theta, \phi)$  must be in the interval  $[0, 1]$ , the source distance must obey

$$\frac{r}{r_H \sqrt{\mathcal{P}(\theta, \phi)}} \leq 1. \quad (4.9)$$

The detection volume is defined by the bounding surface that satisfies the above inequality. The bound in Eq. (4.9) is used in Fig. 4.2, to show the percentage of the sky or  $4\pi$  steradians that is inaccessible for detection as a function of the distance to the source.

The probability of detecting a CBC source is

$$P(0 \leq \iota \leq \iota_{\max}(r, \theta, \phi)) = \begin{cases} 1 - \left[ \sqrt{8 + \frac{8r^2}{\mathcal{P}(\theta, \phi)r_H^2}} - 3 \right]^{1/2}, & \text{if } \frac{1}{2\sqrt{2}} \leq \frac{r}{r_H \sqrt{\mathcal{P}(\theta, \phi)}} \leq 1, \\ 1, & \text{if } \frac{r}{r_H \sqrt{\mathcal{P}(\theta, \phi)}} < \frac{1}{2\sqrt{2}}, \end{cases} \quad (4.10)$$

where Eq. (4.6) was used along with the constraint in Eq. (4.9). At  $r = r_H$  the only value

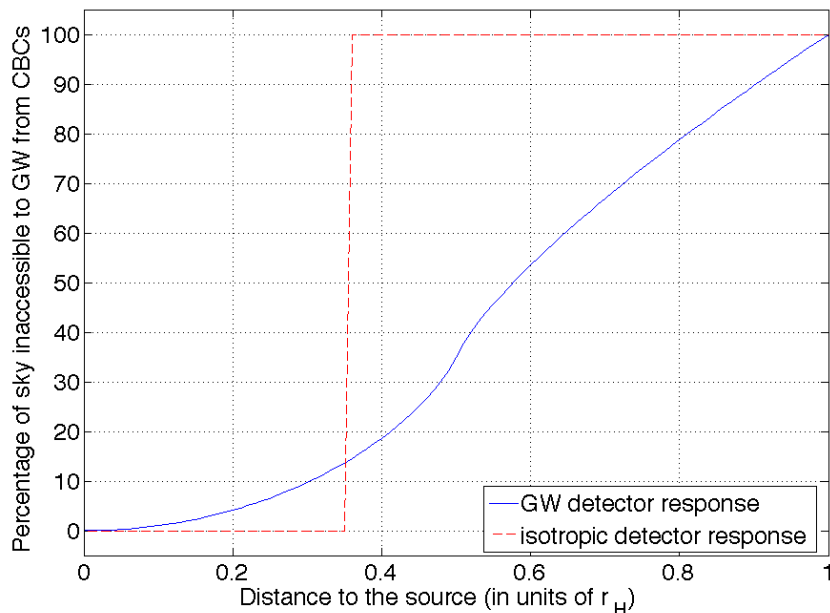


Figure 4.2: The blue (solid) curve shows the percentage of sky inaccessible to interferometric detectors for the detection of GW signals from CBC sources (with all possible orientations), plotted as a function of the source distance. For comparison, if all sources were oriented face-on (i.e., with  $\iota = 0$  or  $\pi$ ) and if the detector had  $\mathcal{P}(\theta, \phi) = 1$  everywhere on the sky, then all of those sources would be detectable in that hypothetical detector at all distances obeying  $r \leq r_H$ . On the other hand, if all sources were oriented edge-on (i.e., with  $\iota = \pi/2$ ), then Eq. (4.5) shows that, hypothetically, for  $\mathcal{P}(\theta, \phi) = 1$  everywhere on the sky, all of those sources would be inaccessible for  $r > r_H/2\sqrt{2}$  but accessible when closer. The red (dashed) step function represents those sources in that imaginary detector.

of  $\mathcal{P}(\theta, \phi)$  possible is 1.0 (see Eq. (4.9)). Thus, the probability of detecting a source at the horizon distance is vanishingly small. As one reduces the source distance the probability increases monotonically till it reaches unity at a distance of  $r_H\sqrt{\mathcal{P}(\theta, \phi)}/(2\sqrt{2})$ . This is shown in Fig. 4.3 for five different lines of sight, namely, overhead (i.e,  $\theta = 0$ ), corresponding to  $\mathcal{P}(\theta, \phi) = 1.0$ , and four other directions, corresponding to  $\mathcal{P}(\theta, \phi) = 0.7, 0.5, 0.2$  and  $0.01$ , respectively.

Suppose all CBC sources are distributed uniformly throughout the Universe. As discussed in Ref. Abadie et al. (2010a), this is a good approximation to the true distribution for most of the volume that will be accessible to ADE detectors except for sources within 20Mpc. If the total number of sources that exist in a spherical volume of radius  $r_H$  is  $N$ , then the total

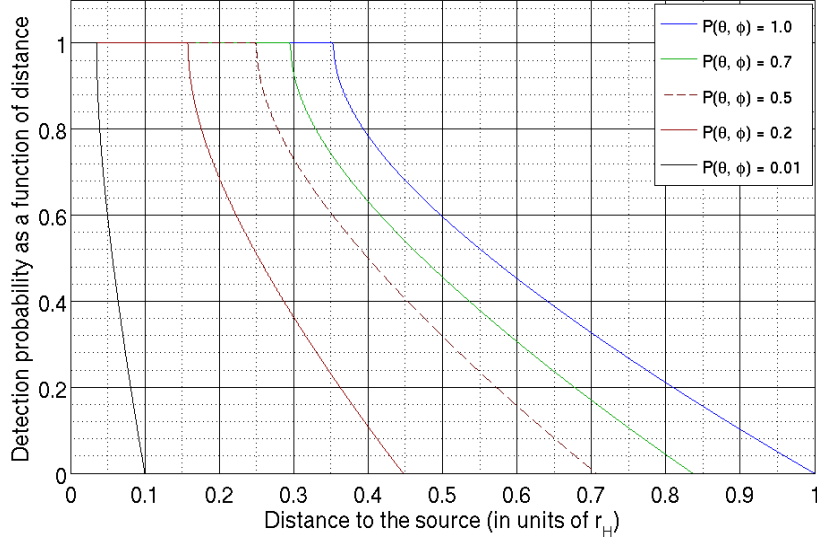


Figure 4.3: Probability of detecting a CBC source at a distance  $r$  (given in units of the horizon distance  $r_H$ ) assuming that the sources are distributed uniformly in the volume of interest. The four different plots are for four different values of  $\mathcal{P}(\theta, \phi)$ . The blue curve shows the probability of a system that is overhead. For a given  $\mathcal{P}(\theta, \phi)$ , the largest distance at which the probability reaches unity is when a CBC is detectable for all possible values of its inclination angle. For an overhead source (i.e., with  $\theta = 0$ ) this distance is  $r = r_H/2\sqrt{2}$ . For other sky positions, it is  $r = r_H\sqrt{\mathcal{P}(\theta, \phi)}/2\sqrt{2}$ .

number of sources detectable in a volume element  $dV = r^2 \sin \theta dr d\theta d\phi$  is

$$dN_{det}(r, \theta, \phi) = \mathcal{D}(r, \theta, \phi) r^2 \sin \theta dr d\theta d\phi, \quad (4.11)$$

where

$$\mathcal{D}(r, \theta, \phi) \equiv \begin{cases} \frac{3N}{4\pi r_H^3} \left[ 1 - \left( \sqrt{8 + \frac{8r^2}{\mathcal{P}(\theta, \phi)r_H^2}} - 3 \right)^{1/2} \right], & \text{if } \frac{r_H\sqrt{\mathcal{P}(\theta, \phi)}}{2\sqrt{2}} \leq r \leq r_H\sqrt{\mathcal{P}(\theta, \phi)}, \\ \frac{3N}{4\pi r_H^3}, & \text{if } r < \frac{r_H\sqrt{\mathcal{P}(\theta, \phi)}}{2\sqrt{2}}, \end{cases} \quad (4.12)$$

is the density of sources detectable at a particular point  $(r, \theta, \phi)$  in space. For nearby distances the density of detectable sources is higher than that at greater distances. Let

us define the mean density of detectable sources at a distance  $r$  as

$$\mathcal{D}_{\text{mean}}(r) = \frac{1}{4\pi} \int_0^{2\pi} d\phi \int_0^\pi d\theta \mathcal{D}(r, \theta, \phi) \sin \theta. \quad (4.13)$$

In the left plot of Fig. 4.4 we show how  $\mathcal{D}_{\text{mean}}(r)$  depends on the distance. Note that at small distances  $\mathcal{D}_{\text{mean}}(r)$  approaches the density of all CBC sources. As we go away from the detector, we begin to lose sources that are sub-optimally oriented and located in the sky. Eventually  $\mathcal{D}_{\text{mean}}(r)$  gets vanishingly small at the horizon distance where only those sources that are located overhead and have a face-on orientation are detectable.

The maximum density of detectable sources at a given distance is always overhead or underneath the detector. One can also see from the middle plot of Fig. 4.4 that the maximum density of detectable sources up to the distance of  $r_H/2\sqrt{2}$ , is equal to the density of all CBC sources. Beyond  $r = r_H/2\sqrt{2}$  the signal falls below threshold for sub-optimally oriented sources and hence the density of detectable sources decreases. Eventually, at  $r = r_H$  the density of detectable sources overhead or underneath gets vanishingly small, with only the face-on sources being detectable. The fraction of CBC sources that are detectable in gravitational waves is

$$f_{\text{CBC}} = \frac{1}{N} \int_{V_H} \mathcal{D}(r, \theta, \phi) dV, \quad (4.14)$$

where  $V_H$  is the volume of a sphere of radius  $r_H$ . Note that the effect of source redshift on this fraction is negligible for distances accessible to ADE detectors Abadie et al. (2010a). Numerically integrating Eq. (4.14) we find  $f_{\text{CBC}} = 0.0865$ , i.e, 8.65% of CBC sources within the detection volume are detectable with an SNR louder than the threshold  $\rho_{\text{th}}$ . In the right plot of Fig. 4.4 we show how the ratio of the number of detectable sources up to a distance  $r$  to the total number of CBC sources within the volume  $V_H$  varies as a function of  $r$ . Since this fraction scales as the cube of the average GW signal amplitude of a detectable source, the ratio of the signal amplitude of a CBC source at a distance  $r < r_H$ , when averaged over

the location and orientation angles, is  $(1/0.0865)^{1/3} = 2.26$  times smaller than that from the same source optimally located and oriented at the same distance. This is the same factor that is used to compute the rate of CBC sources Abadie et al. (2010a); Finn and Chernoff (1993). We conducted similar studies for multiple detectors. We combined the antenna power pattern  $\mathcal{P}(\theta, \phi)$  for the individual detectors numerically and solve for the integration in Eq. (4.14). We get  $f_{\text{CBC}}^{\text{HL}} = 0.0917$ ,  $f_{\text{CBC}}^{\text{HLV}} = 0.1350$ ,  $f_{\text{CBC}}^{\text{HLI}} = 0.1298$ ,  $f_{\text{CBC}}^{\text{HLVI}} = 0.1541$  and  $f_{\text{CBC}}^{\text{HLVIK}} = 0.1811$ , where ‘HLV’ stands for the usual Hanford-Livingston-Virgo network. ‘I’ stands for LIGO-India and ‘K’ stands for KAGRA.

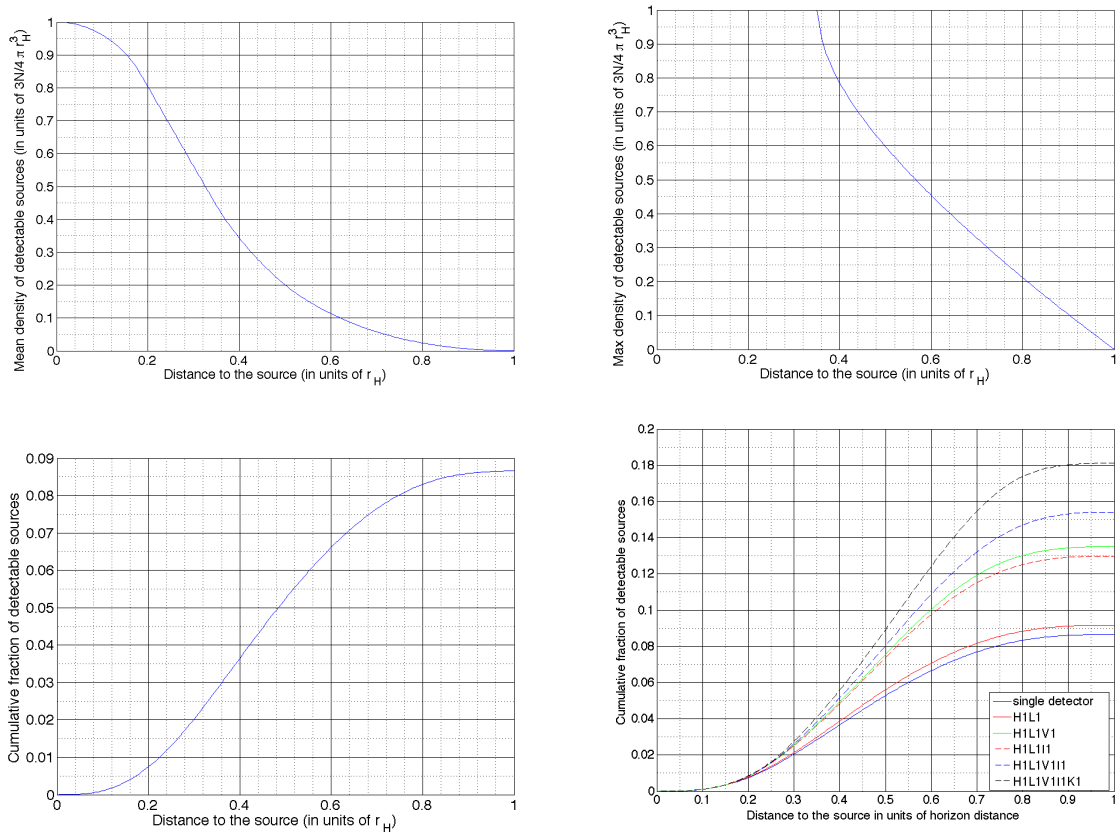


Figure 4.4: **Left:** Mean density of detectable sources on the two sphere at a distance  $r$ . **Middle:** Maximum density of detectable sources on the two sphere at a distance  $r$ . **Right:** The cumulative fraction of detectable CBC sources in a spherical volume of radius  $r$  plotted as a function of  $r$ . The sources are distributed uniformly in volume and are oriented randomly. It attains a maximum value of 8.65% when  $r$  reaches the horizon distance. **Bottom** Comparison between the cumulative fraction of detectable CBC sources in a spherical volume of radius  $r$  for a single detector and for various network of detectors plotted as a function of  $r$ .

### 4.2.3 Fraction of SGRBs with orphaned afterglows

In the remainder of this section we will assume that CBCNS sources are the only progenitors of SGRBs and their afterglows. We first recognize the various factors that determine the number of SGRBs associated with CBCNS progenitors that are detectable by GW observations:

$$\begin{aligned}
 &\text{Number of SGRBs associated with CBCNS GW detections} = \\
 &\text{Number of CBCNS sources detectable by us} \times \\
 &\text{fraction of CBCNS sources that emit gamma rays} \times \\
 &\text{fraction of CBCNS gamma-ray emitters beamed toward us and detected as SGRBs.}
 \end{aligned}
 \tag{4.15}$$

The above equation, factor for factor, can be symbolically expressed as

$$N_{\gamma,\text{GW}} = N_{\text{GW}} \times P(\gamma|\text{CBCNS}) \times P(\text{SGRB}|\gamma, \text{CBCNS}). \tag{4.16}$$

When the CBC population is limited to include only BNS and NSBH sources, the  $N_{det}$  derived from Eq. (4.11) reduces to  $N_{\text{GW}}$ . Also, by a CBCNS gamma-ray emitter we mean a CBCNS source that would be detectable in gamma-rays by us provided the rays were beamed at us. Let the gamma-ray emission of SGRBs be strongly beamed, with a beaming half-angle of  $\beta_{\text{B}}$ . Then the fraction of CBCNS gamma-ray emitters that will be observable to us as SGRBs is

$$P(\text{SGRB}|\gamma, \text{CBCNS}) = \frac{2\pi \int_0^{\beta_{\text{B}}} \sin \theta d\theta}{4\pi} = \sin^2 \frac{\beta_{\text{B}}}{2}. \tag{4.17}$$

If SGRBs were beamed isotropically,  $\beta_{\text{B}} = \pi$  and the above fraction is unity. Therefore, the fraction of CBCNS gamma-ray emitters that will beam their gamma rays away from us is

$$1 - \sin^2 \frac{\beta_{\text{B}}}{2}. \tag{4.18}$$

Let  $f_{AG}$  be the fraction of CBCNS gamma-ray emitters that produce afterglows that are bright enough to be detectable by our observatories. Then the fraction of CBCNS gamma-ray emitters with an orphaned afterglow is

$$f_{OAG} \equiv f_{AG} \left( 1 - \sin^2 \frac{\beta_B}{2} \right). \quad (4.19)$$

The fraction  $f_{AG}$  depends on the environment of SGRBs, which is not well understood Metzger and Berger (2012). Note that some afterglows may be beamed (e.g., some X-ray afterglows), some others may be more isotropic (e.g., radio afterglows), and a fraction of them may be too weak to detect. On the other hand, the way  $f_{OAG}$  is defined, it does not include CBCNS gamma-ray emitters that beam at us but we fail to detect them as SGRBs. Moreover, a subset of orphaned afterglows may arise from CBCNS sources that do not produce a GRB, e.g., due to baryon loading Rhoads (2003). Including these last two types of systems will only increase the number of orphaned afterglows associated with CBCNS sources.

#### 4.2.4 Probability of detecting an orphaned afterglow in conjunction with a gravitational wave signal

Let  $P(\gamma|\text{BNS})$  and  $P(\gamma|\text{NSBH})$  denote the fractions of binary neutron star and neutron star - black hole binary coalescences, respectively, that emit gamma rays. Thus, the fraction of CBCNS sources that emit gamma rays can be written as

$$P(\gamma|\text{CBCNS}) = P(\gamma|\text{NSBH}) + P(\gamma|\text{BNS}). \quad (4.20)$$

Below, we first study the factors that influence  $P(\gamma|\text{NSBH})$  followed by those that affect  $P(\gamma|\text{BNS})$ .

The central engine of a SGRB is the accretion disk that is created by the tidal disruption

of an inspiraling neutron star. Some studies predict that an accretion disk of mass  $m_{\text{disk}} \gtrsim 0.01M_{\odot}$  can provide sufficient energy to launch a jet for a duration of around 100 msec by neutrino radiation Kiuchi et al. (2010a). Thus, whether a system emits a gamma-ray burst or not will depend foremost on whether the neutron star can transfer  $0.01M_{\odot}$  in to the accretion disk. A massive NS with low compactness is more likely to transfer the required mass to an accretion disk massive enough to launch a jet than a low-mass neutron star with high compactness. Let us assume that the smallest mass of an accretion disk that is required to fire the GRB engine is  $m_*$ . If we further assume that the neutron star mass is distributed normally from a lower limit  $m_{\text{min}}$  to an upper limit  $m_{\text{max}}$ , and that the mean neutron star mass is  $\bar{m}$ , then we can write the probability density of neutron star mass as,<sup>1</sup>

$$p_{\text{NS}}(m) = \begin{cases} \frac{1}{I} e^{-(m-\bar{m})^2/2\sigma^2}, & \text{if } m_{\text{min}} \leq m \leq m_{\text{max}}, \\ 0, & \text{otherwise,} \end{cases} \quad (4.21)$$

where,

$$I = \int_{m_{\text{min}}}^{m_{\text{max}}} e^{-(m-\bar{m})^2/2\sigma^2} dm = \sigma \sqrt{\frac{\pi}{2}} \left[ \text{erfc} \left( \frac{m_{\text{min}} - \bar{m}}{\sigma\sqrt{2}} \right) - \text{erfc} \left( \frac{m_{\text{max}} - \bar{m}}{\sigma\sqrt{2}} \right) \right]. \quad (4.22)$$

We follow Ref. Strobel and Weigel (2001) in setting  $m_{\text{min}} = 0.88M_{\odot}$ . The values of all other parameters that define the above distribution are obtained from the empirical study given in Ref. zel et al. (2012), namely,  $\bar{m} = 1.28M_{\odot}$ ,  $m_{\text{max}} = 3.2M_{\odot}$ , and the standard deviation  $\sigma = 0.24M_{\odot}$ . The normalization factor is then deduced to be  $I = 0.5729M_{\odot}$ .

Low-mass neutron stars are less likely to form a massive enough accretion disk that can launch an ultrarelativistic jet. If  $m_*$  is the lower limit on the mass of a neutron stars forming

---

<sup>1</sup>The formalism developed here can be applied to a different set of parameter values, as and when it is refined with new observations.

SGRBs, then the fraction of all neutron stars with  $m > m_*$  is:

$$P(m_*) = \int_{m_*}^{\infty} p_{\text{NS}}(m) dm = \frac{1}{I} \int_{m_*}^{m_{\text{max}}} e^{-(m-\bar{m})^2/2\sigma^2} dm. \quad (4.23)$$

If one assumes that the neutron stars in binaries are a good representation of all neutron stars from the same volume of the universe, then  $P(m_*)$  is also the fraction of neutron stars in any CBCNS system in that volume that can form SGRBs. Below, we argue that  $m_*$  must be related to other CBCNS parameters that are relevant to the formation of a SGRB. These are the compressibility  $\kappa$  of the neutron star, the spin parameter  $\chi$  of the companion black hole and the symmetrized mass-ratio  $\eta = m_1 m_2 / (m_1 + m_2)^2$  of the binary, with component masses  $m_1$  and  $m_2$ .

Let  $P(\text{NS}|m_*, \kappa_{\text{min}}, \kappa_{\text{max}})$  be the fraction of neutron stars that have mass greater than  $m_*$  and compressibility in the range  $(\kappa_{\text{min}}, \kappa_{\text{max}})$ . Let  $p(m, \kappa)$  be the joint probability density of neutron stars in  $m$  and  $\kappa$ . Also, let the probability densities of stellar mass black holes in their spin parameter  $\chi$  be  $p_\chi(\chi)$  and of NSBH binary systems in their symmetrized mass-ratio  $\eta$  be  $p_\eta(\eta)$ . Next let us assume that NSBH binaries are constituted of components drawn randomly from neutron star and stellar mass black hole populations.<sup>2</sup> If so, the fraction of NSBH systems that can form an accretion disk capable of generating a GRB is

$$\begin{aligned} & P(\text{NSBH}|m_*, \kappa_{\text{min}}, \kappa_{\text{max}}) \\ &= P(\text{NS}|m_*, \kappa_{\text{min}}, \kappa_{\text{max}}) \int_0^{0.25} d\eta p_\eta(\eta) \int_0^1 d\chi p_\chi(\chi) \\ &= \int_0^{0.25} d\eta p_\eta(\eta) \int_0^1 d\chi p_\chi(\chi) \int_{\kappa_{\text{min}}}^{\kappa_{\text{max}}} d\kappa \int_{m_*}^{m_{\text{max}}} dm p(\kappa, m). \end{aligned} \quad (4.24)$$

If there is no correlation between neutron star masses and compressibility, and  $p(m, \kappa) \equiv$

---

<sup>2</sup>This assumption may not be completely valid and, therefore, the resulting simplified probability expression is only approximate.

$p_\kappa(\kappa)p_{\text{NS}}(m)$ , then

$$P(\text{NSBH}|m_*, \kappa_{\min}, \kappa_{\max}) = \int_0^{0.25} d\eta p_\eta(\eta) \int_0^1 d\chi p_\chi(\chi) \int_{\kappa_{\min}}^{\kappa_{\max}} d\kappa p_\kappa(\kappa) \int_{m_*}^{m_{\max}} dm p_{\text{NS}}(m). \quad (4.25)$$

A more general formula, which allows  $m_*$  to vary with  $\eta$ ,  $\chi$  and  $\kappa$  of a CBCNS system that is capable of emitting gamma rays, is:

$$P(\text{NSBH}|m_*, \kappa_{\min}, \kappa_{\max}) = \int_0^{0.25} d\eta p_\eta(\eta) \int_0^1 d\chi p_\chi(\chi) \int_{\kappa_{\min}}^{\kappa_{\max}} d\kappa p_\kappa(\kappa) \int_{m_*(\kappa, \chi, \eta)}^{m_{\max}} dm p_{\text{NS}}(m), \quad (4.26)$$

where the integrals are now coupled due to the dependence of  $m_*$  on  $\eta$ ,  $\chi$  and  $\kappa$  in the lower limit of the NS mass integral. As argued below, we speculate that the above probability is more applicable in nature than the one given in Eq. (4.25).

The likelihood of forming a large accretion disk depends on the equation of state (EOS) of the neutron star, in addition to its mass. For a given mass, a neutron star with a stiffer EOS is more likely to give a large accretion disk: A neutron star that is more compact is less likely to get ripped apart by the tidal force of its binary companion before it reaches the last stable orbit (LSO). If the companion is a black hole, then such a neutron star will cross the LSO and plunge into the companion without any GRB arising from such a system. However, if the black hole has a large spin component along the orbital angular momentum of the binary, then the LSO is smaller. In the test particle limit, the LSO around a non-spinning black hole of mass  $M_{\text{BH}}$  is at a distance of  $R = 6GM_{\text{BH}}/c^2$ , whereas around a maximally spinning black hole of the same mass it is at the horizon,  $R = GM_{\text{BH}}/c^2$ , for prograde orbits. For binary systems of interest, the location of such an orbit is less sharply defined. In lieu of it one uses the distance at which a slowly inspiraling system makes its transition into a rapid plunge. In any case, a neutron star is more likely to inspiral closer to the companion black hole if the latter has a large spin component along the direction of the orbital angular momentum. This makes it more likely for a neutron star to get tidally

deformed and ripped apart into an accretion disk and, consequently, trigger the central GRB engine through accretion of neutron star matter into the companion. Furthermore, a smaller black hole has a larger tidal radius and is more likely to shred the neutron star before it reaches the LSO than a larger black hole. This implies that the GRB is more likely to be triggered from a binary source with a low mass-ratio. Thus, the threshold mass  $m_*$  of the neutron star that is necessary, but not sufficient, to form a GRB triggering accretion disk is a function of the compactness of the neutron star, the companion spin and the mass-ratio of the binary. Hence, Eq. (4.23) can be reexpressed as

$$\begin{aligned}
P(m_*(\kappa, \chi, \eta)) &= \frac{1}{I} \int_{m_*(\kappa, \chi, \eta)}^{m_{\max}} e^{-(m-\bar{m})^2/2\sigma^2} dm \\
&= \frac{\sigma}{I} \sqrt{\frac{\pi}{2}} \left[ \operatorname{erfc} \left( \frac{m_*(\kappa, \chi, \eta) - \bar{m}}{\sigma\sqrt{2}} \right) - \operatorname{erfc} \left( \frac{m_{\max} - \bar{m}}{\sigma\sqrt{2}} \right) \right].
\end{aligned} \tag{4.27}$$

Eq. (4.26) then gives the fraction of all NSBH sources that can form an accretion disk capable of generating a GRB to be

$$\begin{aligned}
P(\gamma|\text{NSBH}) &= \epsilon_1 P(\text{NSBH}|m_*, \kappa_{\min}, \kappa_{\max}) \\
&= \epsilon_1 \int_0^{0.25} d\eta p_\eta(\eta) \int_0^1 d\chi p_\chi(\chi) \int_{\kappa_{\min}}^{\kappa_{\max}} d\kappa p_\kappa(\kappa) P(m_*(\kappa, \chi, \eta)),
\end{aligned} \tag{4.28}$$

where we included the factor  $\epsilon_1$ , which is the efficiency of the NSBH systems in Eq. (4.26), with the values of the parameters  $(m, \kappa, \chi, \eta)$  in their appropriate ranges, in producing a GRB. That efficiency may depend on the strength of the NS magnetic field, precession of the system, and other factors that might be unraveled through future numerical simulations. It is important to clarify that the true dependence of  $P(\gamma|\text{NSBH})$  on NSBH parameters may be more complex than the one given above, the primary purpose of which is to recognize those parameters and to explain their physical relevance.

For the special case, where the aforementioned probability density functions are single

valued, with

$$p_\eta(\eta) = \delta(\eta - 0.25), \quad p_\chi(\chi) = \delta(\chi - 1.0), \quad p_\kappa(\kappa) = \delta(\kappa - 1.0), \quad (4.29)$$

and if one takes  $\epsilon_1 = 1.0$ , one finds that

$$\begin{aligned} P(\gamma|\text{NSBH}) &= \frac{\sigma}{I} \sqrt{\frac{\pi}{2}} \left[ \text{erfc} \left( \frac{m_0 - \bar{m}}{\sigma\sqrt{2}} \right) - \text{erfc} \left( \frac{m_{\text{max}} - \bar{m}}{\sigma\sqrt{2}} \right) \right] \\ &= 0.53 \times \left[ \text{erfc} \left( \frac{m_0 - 1.28}{0.34} \right) - 1.23 \times 10^{-15} \right], \end{aligned} \quad (4.30)$$

where  $m_0 = m_*(\kappa = 1, \chi = 1, \eta = 0.25)$ . The value of the minimum mass  $m_0$  is constrained to lie between  $m_{\text{min}}$  and  $m_{\text{max}}$ ; its distribution for the densities in Eq. (4.29) is shown in Fig. 4.5.

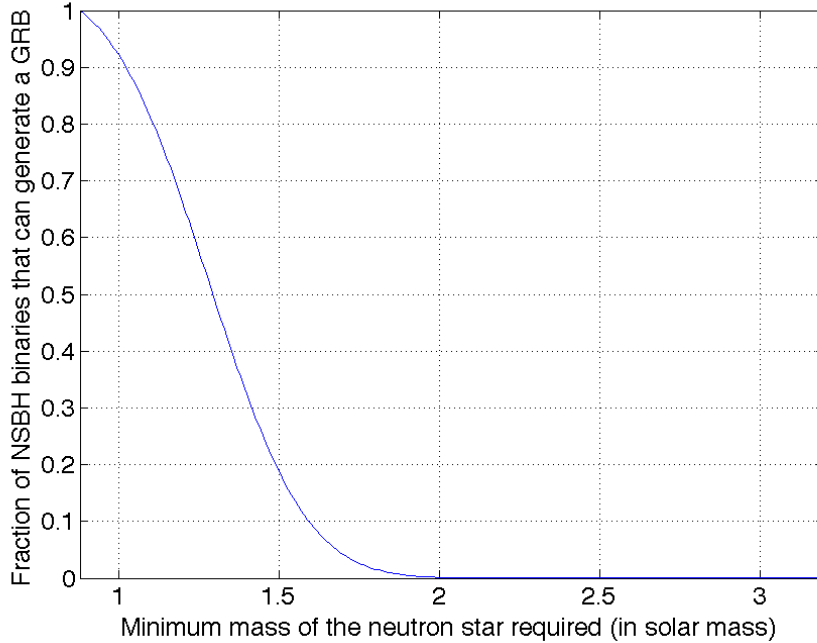


Figure 4.5: Fraction of neutron star - black hole binary sources that give rise to a gamma-ray burst, which may or may not be beamed at us, for the special case of  $p_\eta(\eta) = \delta(\eta - 0.25)$ ,  $p_\chi(\chi) = \delta(\chi - 1.0)$ , and  $p_\kappa(\kappa) = \delta(\kappa - 1.0)$ . The minimum mass of the neutron star required for the emission, and for these choices of the probability densities, is plotted on the  $x$ -axis.

Next consider the fraction  $P(\gamma|\text{BNS})$ . For a coalescing binary neutron star system to be

a progenitor of a gamma-ray burst, it first needs to result in the formation of a black hole with an accretion disk around it. Some studies indicate that there can be two paths for that to happen (see, e.g., Ref. Bartos et al. (2012) and the references therein):

- The mass of the binary system ( $m_1 + m_2$ ) is greater than  $3M_\odot$  and the individual neutron star masses are unequal ( $m_1 \neq m_2$ ). Let the probability of BNS systems that satisfy these criteria be  $P_A$ .
- The condition  $m_{\text{max}} < (m_1 + m_2) < 3M_\odot$  is satisfied, but  $(m_1 + m_2)$  is not so large that the hypermassive neutron star resulting from the merger promptly collapses to a black hole. Let the probability of these binaries be  $P_B$ .

Assuming this hypothesis to be true, the joint probability of a binary neutron star system coalescing to form an accretion disk around a central black hole can be written as,

$$P_{\text{BNS, disk}} = P_A + P_B \quad (4.31)$$

Note, however, that merely the creation of an accretion disk is not enough for triggering the GRB engine. For that to happen one needs an accretion disk that is massive enough to generate the accretion rate required for triggering a GRB. Whether such an accretion disk can be formed depends on multiple factors: Nuclear matter from both neutron stars can contribute to the accretion disk in varying amounts. Low compactness of a neutron star improves the chances of formation of a massive accretion disk. The component masses, spins and the orbital eccentricity also play a role. A precise determination of their influence is beyond the scope of this paper. To make progress we introduce a second efficiency factor,  $\epsilon_2$ , that determines how likely it is for a BNS system to form an accretion disk massive enough to trigger a GRB. Then the fraction of BNS coalescences associated with GRBs is

$$P(\gamma|\text{BNS}) = \epsilon_2 P_{\text{BNS,disk}} \cdot \quad (4.32)$$

Thus, the probability of observing an orphaned afterglow in conjunction with a gravitational wave signal from its CBCNS progenitor can be obtained using Eqs. (4.14) and (4.18) to be:

$$\begin{aligned}
 P(\text{OAG, GW}) &= f_{\text{CBC}} f_{\text{OAG}} P(\gamma|\text{CBCNS}) \\
 &= 0.0865 \left(1 - \sin^2 \frac{\beta_{\text{B}}}{2}\right) f_{\text{AG}} P(\gamma|\text{CBCNS}), \quad (4.33)
 \end{aligned}$$

where  $P(\gamma|\text{CBCNS})$  is obtained by using  $P(\gamma|\text{NSBH})$  from Eq. (4.28) and  $P(\gamma|\text{BNS})$  from Eq. (4.32) in Eq. (4.20). The first two factors are purely geometric, with one arising from GW beaming and the other from SGRB beaming. The last two factors are based on the microphysics of the medium surrounding SGRBs and of neutron star matter. The last three factors will probably have to wait for joint EM-GW observations before their values are finally known.

If GRBs are used to trigger GW searches, then the detection threshold is lowered by at least  $11.3/9.0 = 1.25$ , which increases the GW rate by  $1.25^3 = 1.95$ . So 50 CBCNS per year (which is the likely rate of BNS and NSBH detections in aLIGO Abadie et al. (2010a)) increases to 98. However, recall that  $N_{\gamma,\text{GW}}/N_{\text{GW}}$  is the fraction of CBCNS GW detections that are expected to be associated with SGRBs. Thus, if that fraction is 3%, one can expect 3 GW detections due to GRBs in one year.

Afterglows at smaller energies or longer wavelengths than gamma rays will be observable more isotropically. All detected GWs will have observable afterglows provided they all are 100% efficient in triggering bursts that encounter a dense enough surrounding medium to produce a strong afterglow. But the efficiency will most likely be far less than 100%. The detected GWs will give us a sense of the likelihood of afterglows, orphaned or not, occurring with GWs. Recall that  $f_{\text{OAG}}$  is the fraction of CBCNS with afterglows that are observed by us as orphans. An afterglow will improve GW detectability by reducing the detection threshold by 8% of the all-sky, all-time GW search, as shown below Eq. (4.1). Thus, the realistic estimate of 50 detected CBCNS per year will increase to about  $1.08^3 \times 50 = 63$  per

year, and  $63f_{\text{OAG}}$  additional GW events can be expected due to follow-up of EM transients, some of which will be orphaned afterglows. If  $f_{\text{OAG}}$  is 3%, then a couple of additional GW events can be detected every year due to an orphaned afterglow. Note that our choice of a few percent as example values of  $f_{\text{OAG}}$  and  $N_{\gamma,\text{GW}}/N_{\text{GW}}$  is conservative and is, e.g., smaller or similar to values obtained in Ref. Kelley et al. (2012), which conducted a comprehensive study of expected rates of EM emissions observed in coincidence with GW events. While the absolute number of expected EM-GW associations may be small, the astrophysical insights these events will provide, as noted in Sec. 4.1, highlights the importance of pursuing their joint detection.

The above analysis makes the case for pursuing a two-pronged approach to finding CBCNS GW sources associated with orphaned afterglows. One approach is to use a GW detection to trigger an afterglow search in EM observatories. This requires the computationally expensive GW detections to be fast so that they can have a shot at detecting even prompt emissions. This is realizable (see, e.g., Cannon et al. (2012) and the references therein). A more fundamental challenge in this approach arises from the fact that the sky localization error of GW searches can be several square-degrees, when at least 3 sites have tracked the GW event, or worse, with a smaller number of sites tracking the event. Therefore, sky-localization demands a high duty factor of the GW detectors. The second approach is to use EM observatories to find afterglow candidates and then search GW data, which may even be archived, for GW events. This is easier to implement but can be equally rewarding in terms of accessing new knowledge about these most energetic events in the Universe.

### **4.3 Externally triggered search for GW signals from poorly localized CBC sources**

A sizable fraction of GRBs do not have accurately known sky positions. A selected list of such GRBs that occurred during LIGO's S5 run is presented in tables 4.1 and 4.2. The

error in the sky position can arise from constraints inherent to the triangulation method, used by gamma-ray burst detectors. Typically, electromagnetic observatories have good sky localization. However, for a transient phenomenon like a GRB, the primary objective is detection rather than source localization, and a large fraction of GRBs are found with inaccurate sky positions. Detection of an afterglow in conjunction with a GRB can provide that information with a better accuracy since an afterglow can improve the localization of the associated GRB Rhoads (2000); Vanden Berk et al. (2002); Neal Dalal and Kim Griest and Jason Pruet (2002). The observation of a significant fraction of GRBs with error radii of tens of degrees, however, motivated us to study the effect of poor sky localization on the detectability of the CBCNS progenitor in GW searches externally triggered by GRBs. For this analysis, any localization with an error radius of more than a few degrees is termed as poor.

Currently, externally triggered searches for gravitational waves are conducted exclusively in archived data, in a 6 sec time-window around the epoch of a short duration GRB Abadie et al. (2010b, 2012a); Predoi and Hurley (2012). When the sky position of the GRB is known accurately from EM observations, a GW search is launched for that sky position. If the CBCNS progenitor model of SGRBs is correct, and if the source is within a detector’s range, one expects to observe a GW signal from it. The knowledge of the time of the event helps to reduce the false-alarm probability at a given SNR, as discussed in Sec. 4.2.1. There we also showed that a further reduction of false-alarm probability, by an order of magnitude, can be achieved by searching for GWs from a single direction in the sky. This allows for setting a lower detection threshold, which in turn helps target more distant SGRBs and increases their GW detection rate. While this process is optimal for a source with an accurately known sky position, e.g., from EM observations, it is not so when the sky position is unknown or has a large error radius.

In Fig. 4.6, we show how the detection efficiency suffers when a SGRB’s true location is  $20^\circ$  away from the reported sky position. We selected the time and the sky-position of

GRB090709B for this study. This GRB occurred on 09 Jul 2009 at 15:07:42 (UTC), i.e., at a GPS time of 931187277 sec, and at a Right Ascension (RA) of  $93.5^\circ$  and a Declination (dec) of  $64.1^\circ$ . In a 2190 sec observation window centered at this GRB time, but after dropping 246 sec immediately around that instant, we injected 3000 CBCNS signals. The CBCNS masses ranged from  $m_1 = 1 - 3M_\odot$  for the neutron star and  $m_2 = 1 - 40M_\odot$  for the black hole. For this study the binary components were taken to be non-spinning. The signals were injected in Gaussian noise with LIGO-I LIGO Algorithms Library power spectral density (PSD) (Helstrom (1995)) simulated for the H1L1V1 network. The results are grouped into three categories based on the chirp-mass  $\mathcal{M}_c = (m_1 m_2)^{3/5} / (m_1 + m_2)^{1/5}$  of the triggers arising from injections and background. These are the low chirp-mass, with range  $(0.0, 3.48]M_\odot$ , the medium chirp-mass  $(3.48, 6.0]M_\odot$  and the high chirp-mass  $(6.0, 20.0]M_\odot$  systems. The reason for using the chirp mass for categorizing triggers is that the duration of the signal in the detector band is primarily determined by it. The characteristics of the noise artifacts that trigger the search pipeline also depend on the chirp masses of the search templates used.

### **4.3.1 Effect of GRB sky-position error on the detection efficiency of a targeted GW search: Searching at a single inaccurate position**

To quantitatively assess the effect of inaccurate GRB sky position on CBCNS searches, we study the detection efficiency of the search conducted as a function of the source distance for two cases, one with  $20^\circ$  sky position error and another with no sky position error. The detection efficiency in a given distance bin and mass bin is the fraction of the injected triggers in that distance and mass bin found louder than the loudest background trigger in the same mass bin. Measurement of the distance to a GW source depends on a network's ability to resolve the signal's polarization (Ajith and Bose (2009a)). Such a resolution is not possible for every network or every sky position. For injections, the distances used to simulate the

signals are used to bin them. The calculation of the detection efficiency in any distance bin uses the loudness of the loudest background trigger, in the mass bin of interest, regardless of whether it was possible to estimate its distance or not.

The results of this simulation study are shown in Fig. 4.6. As expected, the detection efficiency deteriorates due to the systematic error in the sky position of the GRB used in the search for its GW signal. Compared to the case of no sky-position error, it drops in the low chirp-mass bin by 22% and 24% at injected distances of 40 Mpc and 50 Mpc, respectively, in the medium chirp-mass bin by 12.5% at an injected distance of 50 Mpc, and in the high chirp-mass bin by 15.7% and 20.5% at injected distances of 40 Mpc and 50 Mpc, respectively.

One way to tackle the problem of loss of GW detection efficiency due to an inaccurately known sky position from EM observations is to search in a wider region in the sky. This improves the chances of targeting the true sky position of the source. But it can also reduce the confidence in a detection candidate. This is because searching in multiple sky positions, or signal time-delays across the GW detector baselines, makes the noise background worse. Specifically, it increases the false-alarm probability at a given SNR, thereby reducing the significance of a signal. To assess what the trade off is between improvement in detectability and the deterioration in FAP, we performed a search of the same set of simulated injections as studied above except that (a) their sky position is now erroneous by  $20^\circ$ , in declination only, and (b) we use a larger set of sky-position templates. These templates were chosen to be distributed isotropically in a patch of sky around the reported GRB sky coordinates, with one template per pixel, which is four square-degrees in size.<sup>3</sup>

The triggers output by the search were clustered in sky position by maximizing their SNR over the patch. We named this the *sky-patch* mode of search, as opposed to the *known-sky* mode, where the search was confined to a single point in the sky, as discussed above. For the limiting case, we also conducted experiments where the sky-patch was extended to cover the whole sky. Results from the known-sky, sky-patch and all-sky searches are presented in Fig.

---

<sup>3</sup>The reason for this choice is explained below.

4.7. Three sky-patches were used, with  $5 \times 5$ ,  $10 \times 10$ , and  $20 \times 20$  pixels. The improvement in the detection efficiency is up to about 20% in any of the sky-patch modes or the all-sky mode compared to the known-sky mode. However, the detection efficiencies of the sky-patch and all-sky modes are smaller in many distance bins compared to that of the known-sky mode with no sky-position error (see the top curves in Fig. 4.6). This proves that while a wide-area sky search performs worse, due to an increased FAP, than the known-sky search with no sky-position error, nevertheless it performs better than a known-sky search with a  $20^\circ$  error in the GRB sky position.

Figure 4.8 shows how the false-alarm probability (FAP) increases as one widens the size of the sky patch. The first (left-hand side) plot depicts how the FAP at a given SNR increases with the number of sky points. Note how the FAP climbs sharply in increasing from one point in the sky to two points in the sky, before asymptotically approaching the all-sky FAP value at that SNR. On the other hand, as shown in the second (right-hand side) plot in that figure the FAP has the expected fall-off behavior with increasing SNR for any given sky-mode search. It also shows that at any given SNR the FAP increases as the sky-patch area is widened.

### **4.3.2 Effect of GRB sky-position error on the detection efficiency of a targeted GW search: Searching at multiple sky positions**

Here we enquire how the above results transform as one varies the sky-position of a GRB. Although a GW detector is much less directional, as shown in Fig. 4.10, than, say, an optical telescope (Saulson (1994); Creighton and Anderson (2011)), the variation of its response across the sky cannot be neglected in determining the efficiency of a GW search. While the integrated response of a network of detectors is smoother across the sky than the response of any single detector, there are patches in the sky where its minima are nearly zero and

maxima are nearly unity.<sup>4</sup> How sensitive a network is to a sky-position does not depend on the detector antenna-patterns alone but also on how their noise PSDs compare in the band where the signal is present. If the latter are identical, the network SNR has the same variation in the sky as shown in Fig. 4.10, which is computed for a face-on binary. On the other hand, the fractional drop in SNR of a signal owing to a systematic error in the sky position used in the search template can have a different variation in the sky than that shown in Fig. 4.10. This is because that drop is determined by how fast the network response and the time-delays across the baselines in the network change with  $(\theta, \phi)$  at a sky-position, which, in turn, can be estimated by the network Fisher matrix of the CBC signal as a function of the two sky-position angles (see Refs. Helstrom (1995); Ajith and Bose (2009a); Keppel (2012)). That fractional loss in SNR is plotted in Fig. 4.9 as a function of sky for a couple of cases, namely, when the error in the sky-position of the source is (a)  $20^\circ$  in Declination and (b) 4 square-degrees of solid angle. Inferring the effect of that loss on the detection efficiency is non-trivial since the latter also depends on the change in FAR due to the error. We next assess their combined effect through Monte Carlo simulations across a set of different sky positions.

To check the inferences drawn from the Fisher matrix calculations above on the variation of detection efficiency across the sky, we conducted a set of Monte Carlo simulations, the results of which are summarized in Fig. 4.11. In this experiment, we ran a targeted coincident detection search (Abbott et al. (2008)) with the H1L1V1 network in simulated Gaussian data with LIGO-I noise PSD. The noise background for each of the ten different sky positions, depicted in Fig. 4.10 as white stars, was obtained. We also injected in each of those ten positions a non-spinning CBCNS source, with component masses  $(2.5M_\odot, 40.0M_\odot)$  and optimal orientation at a distance of 17Mpc, and ran the same search pipeline with the correct sky template and the incorrect one (with  $20^\circ$  error) to assess the effect of that systematic

---

<sup>4</sup>The response in Eq. (4.3) when summed over the number detectors can attain a maximum value equal to the number of detectors. However, the network response plotted in Fig. 4.10 is normalized to have a maximum value of unity.

error on the recovered SNR. These experiments output the SNRs of the injections at the different sky positions, with and without the sky-template error.

Ideally, the same number of injections should have been made at each of the ten sky positions as in the study in Sec. 4.3.1, namely, 3000, but that requires an order of magnitude more computational resources. Instead, we use the SNR of the single optimally oriented injection at each sky position to infer the detection efficiency. We do so by noting that the detection efficiencies presented in the previous section are for injections distributed uniformly in distance. Thus, the detection efficiency at any sky-position can be approximated by comparing the SNR of the loudest (optimally oriented) injection with that of the loudest background trigger at that sky position, as follows: Consider  $N + 1$  injections of GW signals from the same type of CBCNS source at a single sky position, but uniformly distributed in distance. Then, the SNRs of these injections will be uniformly distributed such that their sorted list forms an arithmetic progression  $\{\rho_0, \rho_1, \rho_2, \dots, \rho_N\}$ , where  $\rho_{i+1} - \rho_i \equiv \Delta\rho$  is a constant for  $0 \leq i \leq N$ . Let  $\rho_B$  be the loudest background SNR. If  $\rho_0 < \rho_B < \rho_N$  and  $\Delta\rho \rightarrow 0$ , one will always find a  $\rho_i$  that is equal to  $\rho_B$ , say, for  $i = k$ . Therefore, all the triggers in the range  $[\rho_0, \rho_{k-1}]$  have SNRs below that of the loudest background trigger. One can then define the ratio

$$D = \frac{\rho_N - \rho_B}{\rho_N} = \frac{N\Delta\rho - k\Delta\rho}{N\Delta\rho} = \frac{N - k}{N}, \quad (4.34)$$

where we took  $\rho_0 = 0$ . The final expression shows that  $D$  is the ratio of the total number of injections louder than the loudest background to the total number of injections, which is just the detection efficiency. Thus,  $D$  can be approximated by the first expression, i.e., by comparing the SNRs of the optimally oriented injection and the loudest background trigger. This is what we have plotted on the vertical axis in Fig. 4.11. There the sky positions are indexed from one to ten on the horizontal axis.

A comment is in order about the choice of an *isotropic* grid of sky-position templates

in the sky-patch search modes: A better method of distributing templates in the sky is to require that the maximum fractional drop in SNR due to the mismatch in the sky position of the signal and the template be constant (Ajith and Bose (2009a); Keppel (2012)). However, as shown in Figs. 4.9 and 4.10 in the neighborhoods of all ten injection sky positions a template spacing of 4 square-degrees will contribute less than 10% to the overall SNR drop, which will be dominated by the systematic error in the sky-position of the injections. The latter causes a drop of about 100% or more across much of the sky. Reducing the pixel size increases the number of pixels needed to cover the same sky-patch, thereby, increasing the computational cost (which is the number of floating-point operations required per unit time) of the search.

To summarize, the above studies show that the effect of a systematic error in sky position is to reduce the detection efficiency of a known-sky search by a significant amount. The detection efficiency is less affected when a sky-patch is used to search for the GW counterpart.

## 4.4 Searching all-sky, all-time CBC triggers in LIGO's S5 data for GW candidates concurrent with GRBs

In this section we develop the motivation for conducting a search of coincident all-sky, all-time (Babak et al. (2012)) CBC triggers in LIGO's S5 data (Abbott et al. (2009b,a); Abadie et al. (2010c, 2011)) for GW candidates concurrent with GRBs. No GW detections were reported in CBC searches of any kind in LIGO's S5 data because no triggers had a low enough FAP. However, as explained in Sec. 4.2 the FAP of a blind search is higher than that of a targeted search, at the same SNR. Thus, an all-sky, all-time CBC trigger that is concurrent with a GRB can have a lower FAP in a targeted GW search and can lead to a GW detection. Indeed, a fully coherent targeted search has been performed to look for GW signals coincident with GRBs (Harry and Fairhurst (2011)). However, that search, which is computationally more expensive than a coincident search, was limited to GRBs

with accurate sky-position information as external triggers (Babak et al. (2012)). The other feature of the all-sky, all-time coincident GW triggers is that their FAP is computed over a duration of data that spans weeks as opposed to 2190 sec for data sets used in targeted searches. Therefore, here we focus on GRBs with poor sky-position information that were not used to trigger GW searches. If a GRB was found to be concurrent with a GW trigger that was not significant enough in the all-sky, all-time coincident search, it might still be interesting to invest the computational resources to perform a targeted fully coherent or hierarchical coherent search (Bose et al. (2011)) around that GRB time. This is because the concurrent GW trigger can gain in significance in the latter types of search owing to their lower noise background.

We next show why the choice of SNR thresholds in the coincident search allows for the possibility of finding interesting GW triggers concurrent with GRBs. We argue that it is possible for some of these triggers to have a low enough FAP in a targeted search to constitute a detection. As discussed earlier, the detection threshold in a targeted search in H1L1 is a network SNR of 9.0, for a FAP of  $10^{-4}$ . If all detectors are equally sensitive to a source, then the SNR in each detector of a signal at the threshold of detection is 6.4, which is 9.0 divided by the square root of the number of detectors (see Refs. Helstrom (1995); Pai et al. (2001)). During the fifth science run in LIGO (S5) three detectors were taking data. These were H1, H2, and L1. A fourth detector, Virgo (V1), joined them in the last several months of S5, where it shared its data from the first Virgo Science Run (VSR1) with LIGO. Although the sensitivities of H2 and V1 were about half or worse than those of H1 and L1, triggers from all five detectors were analyzed for this GRB coincidence study.

Specifically, an H1L1 coincident candidate with a SNR of 6.4 in each of H1 and L1 will have a FAP of  $10^{-4}$  or less in a targeted search. It is therefore important to enquire if any coincident GW candidates were found in an all-sky, all-time (i.e., un-triggered) search that were concurrent or near concurrent with a GRB (Predoi and Hurley (2012)). Note that even if an H1L1 candidate is found with a FAP higher than  $10^{-4}$  in the all-sky, all-time search,

it can have a FAP of  $10^{-4}$  or less in the targeted search, i.e., when found concurrent with a GRB. With this in mind we examined H1L1 candidates found by the un-triggered low- and high-mass searches to check for coincidences with GRBs.

Next consider what the inclusion of H2 does to a search. The weakest signal that can produce a triggered H1L1 candidate with a FAP of  $10^{-4}$  (or H1L1 SNR of 9.0) will have a SNR of 6.4 in each of the two detectors, as mentioned above. As one increases the number of detectors,  $N$ , a network SNR that is lower by a factor of  $N^{1/2}$  would have the same FAP, assuming that the detectors are similar in their noise and antenna profiles. Thus, a network SNR of  $9.0/\sqrt{(3/2)} = 7.3$  in H1H2L1 would have a FAP of  $10^{-4}$  if H2 had the same sensitivity as H1 and L1. Since H2 actually has a lower sensitivity, the H1H2L1 SNR at the same FAP is closer to 8.0. So the H2 SNR at which a signal can contribute to a H1H2L1 un-triggered coincident candidate at the same FAP is 2.7. This signal will have a SNR of 5.4 in H1 and L1, which is close to the SNR threshold placed on H1 and L1 in the un-triggered searches, namely, 5.5. (Note that the orientations of H1 and L1, while not identical, are very similar, as borne out by their responses displayed in Fig. 4.10. Higher values of the SNR in H2 reduce the H1H2L1 FAP and lower values increase the FAP. So, between an H1 (and L1) SNR of 5.5 and 6.4, contribution of H2's SNR helps keep the network FAP at or below  $10^{-4}$ . Therefore, it makes sense to examine lists of H1H2L1 triggers from the coincident low-mass and high-mass searches that have SNRs in H1, L1, and H2, greater than or equal to 5.5, 5.5, and 2.7, respectively. This was the main motivation behind the experiment reported in this section. As an aside, note that since the all-sky, all-time searches had a SNR threshold of 5.5 in all detectors, it makes sense to do targeted searches to detect, especially, those signals in H1H2L1 that would have an H2 SNR in the range (2.7, 5.5). This point is illustrated in the plots in Fig. 4.12. In the left-hand side plot we show the case where no SNR threshold is set in any detector. Thus, every trigger from a detector is retained and the thresholding (which is at a network SNR of 9.0 in this example) is done on the combined SNR, which is just the square-root of the sum of squares of the individual detector SNRs. The right-hand

side plot in the same figure depicts the case where triggers from a detector are retained in the coincident network analysis only when their SNR is above 5.5.

This also provides an important motivation for the hierarchical coherent search (Bose et al. (2011)). The idea behind the hierarchical coherent search is that for all coincident candidates in H1 or L1, which have a SNR above 5.5 in each detector, include the data from H2 in the H1H2L1 analysis, as long as H2 was active, even if H2 did not contribute a threshold-crossing trigger to a candidate found by the coincident pipeline. In other words, the hierarchical coherent pipeline is expected to have the most impact on the detectability of those signals that have a SNR of (5.5, 6.4). While this is a narrow range, note that the first detections will likely happen at SNRs close to the upper limit of that range. (As shown in Ref. Schutz (2011), the most likely detected SNR is 1.26 times greater than the SNR threshold. For a threshold of 5.5, it is 6.9.) This keeps the computational costs at a minimum, while taking full advantage of the signal’s phase coherence across the network detectors in improving its detectability. Also when H1 (L1) is not active, H2L1 (H1H2) triggers can be detections. In practice, the hierarchical coherent pipeline searches with SNR thresholds of  $\{\rho_{\text{th}}^{\text{H1}} = 4.0, \rho_{\text{th}}^{\text{L1}} = 4.0, \rho_{\text{th}}^{\text{H2}} = 3.0\}$ . Ideally, the H2 threshold should be lower, at 2.7, as discussed above, but it is still in the range of interesting SNR values. Note, however, that we do not analyze H1H2 triggers because our background estimation of those triggers is not robust owing to cross-correlated noise at the same site.

GRB alerts issued by gamma-ray observatories can have large sky-position errors. It is counterproductive to search using the known-sky mode for GWs from such GRBs, as discussed in Sec. 4.3. Indeed, fully coherent pipelines are in use (Predoi and Hurley (2012)) to search over sky-patches with multiple sky positions for GWs from these objects. Typically, a GRB alert provides the source sky-position along with an error box or error radius associated with it. Those errors for some GRBs are tabulated in tables 4.1 and 4.2.

## **List of SGRBs detected with large sky-position errors by the Fermi gamma-ray satellite**

While the gamma-ray burst monitor (GBM) on-board the Fermi satellite has an excellent sky coverage, its sky resolution can be poor on occasion. In the first two years of Fermi's observation time, 491 GRBs were detected by GBM (Paciesas et al. (2012)). Of these, we found that 40 GRBs with  $T_{90} \leq 2.0$  sec have a large sky-position uncertainty (i.e., the error radius is greater than  $10^\circ$ ). (Here,  $T_{90}$  is the duration over which a burst emits between 5% to 95% of its total measured photon counts after the background has been subtracted.) Given the large error radii of these GRBs in table 4.1, we expect a significant drop in detection efficiency of these GRBs if one employs a known-sky targeted search. Therefore, these GRBs make good candidates for GW searches of the sky-patch or all-sky type.

## **List of short GRBs, detected with large sky position error, by IPN satellites**

IPN is a network of spatially separated gamma-ray burst detectors on several satellites. It uses delays in the time of arrival of gamma-ray signals at these detectors to triangulate the GRB sky positions. IPN has been detecting GRBs since the 1970s. At its peak it involved 10 satellites located at various distances from the Sun, between the orbits of Venus and Mars. Currently, IPN uses four spacecraft, namely, the NASA/ESA Ulysses mission, WIND, HETE-II and 2001 Mars Odyssey. The sky position determination by triangulation across the network can be erroneous when a smaller number of spacecraft detect the signals. The following factors contribute to IPN sky position errors:

- Inaccuracy in the synchronization of clocks in the gamma-ray detectors and in the calibration of those clocks contribute to errors in timing the arrival of signals and, hence, the GRB sky position.
- Uncertainty in the spatial location of the spacecraft leads to errors in the lengths of the baselines and, therefore, errors in estimating the signal time-delays across the baselines.

- The number of satellites detecting a particular GRB can be less than 3 in some cases. Two detectors form a single baseline, which can do no better than localize the GRB on a ring in the sky. The two types of errors discussed above broaden that ring to an annulus.

In the conventional targeted GW search, IPN GRBs with error boxes larger than 100 square degrees were dropped from the initial set of GRBs. After all, the computational requirement posed by a fully coherent GW search in a wide sky region are very high (Pai et al. (2001); Predoi and Hurley (2012)). A list of a subset of such short GRBs that occurred during LIGO’s S5 is given in Table 4.2. Triggers from the coincident all-sky, all-time CBC search pipeline, as studied in Refs. Babak et al. (2012); Abadie et al. (2011); Abbott et al. (2009b), can be checked for GW candidates concurrent with the GRBs listed in that table. While such an exercise is not carried out here, the analysis given above can be used by detector networks to motivate such a search in their data.

## 4.5 Improving the performance of targeted GW searches

If the sky position of a GW source is accurately known from EM observations, such as of an associated SGRB or afterglow, then one might naively suspect that the search for its GW signal should employ only that single position. A search that uses multiple sky-position “templates” is computationally more expensive. More importantly it will also incur a higher false-alarm probability, as we estimated below Eq. (4.2). In spite of these drawbacks, a case can be made to also search away from the true sky-position provided it increases the detection efficiency, which, at a given FAP, is the number of signals detected louder than a background trigger at that FAP. Such an anomaly can occur, e.g., when there is a mismatch between the signal and the template owing to (a) inaccurate modeling of the signal (as discussed in Ref. Bose et al. (2010)) or (b) detector calibration errors (as discussed in Allen (1996); Bose (2005)).

Detectors have calibration errors of about 5-10% in the strain amplitude and up to several degrees in the strain phase. The error can vary from one detector to another and in time. While the temporal variation is expected to be slow and minimally affect targeted GW detectability of transients, the detector dependence can affect the signal’s amplitude and time-delay differently in the network detectors, thereby, partially mimicking an error in the sky-position. Note that calibration errors have been shown to affect estimation of signal parameters, such as CBC masses, strongly (in fact, linearly) Allen (1996); Bose (2005). As we show below, the covariance of the error in sky-position angles with that in other source parameters suggests that searching in a wider patch can sometimes mitigate the adverse effect on signal SNR and detectability.

Furthermore, the BH spin can be very high in SGRB sources that include a black hole. However, GW template banks for NSBH systems with high BH spin have not been applied in GW searches yet. Searching those systems with inaccurate templates, either with non-spinning ones, as is done in Refs. Abadie et al. (2010b, 2012c), or with effective template families can severely diminish their detectability. These searches can also benefit from a somewhat expanded search in the sky, again owing to the covariance of the sky position angles with other source parameters, even if the sky-position is known accurately.

#### **4.5.1 Targeted GW search over a finite sky patch even for accurately known GRB sky position**

A mismatch between a signal and a template can lead to a drop in the SNR and, therefore, affect the detection probability. However, for some types of errors that probability can be partially salvaged by allowing the template sky-position to be different from the true one. Essentially, if there exists a non-vanishing covariance between the errors in sky-position and other CBC parameters, then it can be exploited to mitigate the SNR loss. The nine parameters that characterize the non-spinning CBC signals are the total mass  $M$ , the symmetrized mass-ratio  $\eta$ , the sky-position angles  $(\theta, \phi)$ , the polarization angle  $\psi$ , the orbital inclination

angle  $\iota$ , the luminosity distance  $d_L$ , the initial (or some reference) phase  $\varphi_0$ , the time of arrival (or some reference time)  $t_0$ , and the overall signal amplitude  $\mathcal{A}$ . We group these as components of the parameter vector,  $\boldsymbol{\vartheta} \equiv \{\mathcal{A}, t_0, \varphi_0, M, \eta, \theta, \phi, \psi, \iota\}$ . Owing to noise, their estimates,  $\hat{\boldsymbol{\vartheta}}$ , may differ from the true values, i.e.,  $\hat{\boldsymbol{\vartheta}} = \boldsymbol{\vartheta} + \Delta\boldsymbol{\vartheta}$ , where  $\Delta\vartheta^a$  is the random error in estimating the parameter  $\vartheta^a$ . The magnitude of these errors can be estimated from the elements of the variance-covariance matrix,  $g^{\mu\nu} = \overline{\Delta\vartheta^\mu \Delta\vartheta^\nu}$  Helstrom (1995). The mismatch between a template and a signal is

$$\mathcal{M}(\boldsymbol{\vartheta}^\sigma) = g_{\mu\nu} \Delta\vartheta^\mu \Delta\vartheta^\nu, \quad (4.35)$$

where we have used the Einstein summation convention for the repeated indices  $\mu$  and  $\nu$ . For simplicity, consider a template that matches a signal in all its parameters except  $M$  and the two sky-position angles. Assume that an observer has no control on changing  $\Delta M$  but can vary the template sky-position angles. Then the above mismatch  $\mathcal{M}$  is minimum when

$$\Delta\theta = \Delta\tilde{\theta} \equiv \frac{C_{M\theta}}{C_{MM}} \Delta M, \quad (4.36)$$

$$\Delta\phi = \Delta\tilde{\phi} \equiv \frac{C_{M\phi}}{C_{MM}} \Delta M, \quad (4.37)$$

where a tilde denotes the parameter value that minimizes the mismatch and  $C_{\mu\nu}$  is the cofactor of the metric  $g_{\mu\nu}$ . The minimized mismatch is

$$\mathcal{M}(\boldsymbol{\vartheta}^\sigma) \Big|_{\Delta\tilde{\theta}, \Delta\tilde{\phi}} = \frac{g(\boldsymbol{\vartheta}^\sigma)}{C_{MM}(\boldsymbol{\vartheta}^\sigma)} \Delta M^2, \quad (4.38)$$

where  $g$  is the determinant of  $g_{\mu\nu}$ . The above expression can be vanishingly small, even for a finite  $\Delta M$ , if  $g(\boldsymbol{\vartheta}^\sigma)$  is so. The same idea can work over a larger parameter space that includes  $\eta$ , spin parameters (for spinning waveforms), and calibration errors. Indeed, in Ref. Bose et al. (2008) it was demonstrated that allowing  $\eta$  to exceed somewhat beyond its physically

permitted upper limit of 0.25 (which is its value for binaries with mass-ratio of unity) in a mass template bank can improve the detection efficiency of a CBC search.

In CBC searches, one typically uses a bank of templates, derived from a waveform model, that are discretely spaced in the template parameters. Searches in LIGO and Virgo data have used template banks in the component masses that keep the separation of templates close enough to suffer at most a 3% loss in the SNR in any detector. The simulations studied in this paper have used the same type of mass template banks. As suggested by Eq. (4.38) above and proved in signal injection studies below, that SNR drop can be mitigated by using a sky-patch instead of a single sky position in targeted GW searches.

#### **4.5.2 Targeted search for GW sources using inaccurate templates: Masses**

To test the implications of the analytic calculations of Sec. 4.5.1, we carried out a Monte Carlo simulation with 3000 non-spinning injections, identical to the ones used for the systematic sky-position error study in Sec. 4.3. We conducted four types of sky-position template searches, namely, one in the known-sky search mode, two with different sky-patch sizes, and one in the all-sky search mode. The detection efficiencies of these searches are presented in Fig. 4.13. Note that in the low and medium chirp-mass bins, the known-sky detection efficiency performs worse than that of other sky modes despite the advantage it has of having the lowest FAP of all modes. Parameter error covariance helps the detection efficiency of the other search modes. On the other hand, in the high chirp-mass bin the detection efficiency of the known-sky is better than that of the all-sky mode. Here, the higher FAP of the all-sky mode dominates over any gains arising from Eq. (4.38). Nevertheless, the two sky-patch modes still outperform the known-sky mode in this mass bin as well, by as much as 5%. Therefore, we conclude that the best performance can be expected for a search that employs a sky-patch of the optimal size. More Monte Carlo simulation studies are needed to determine what that size is in different sections of the space of component masses.

To isolate the effect of parameter error covariance on improving signal-template match, we study the combined distribution of the SNRs of the injection triggers in Fig. 4.14 from all three sky-mode searches, without any reference to the distribution of the SNRs of background triggers. There, for every injection the mean of its network SNRs found by the known-sky, sky-patch, and all-sky modes of the search was computed. Next a list of these 3000 mean SNRs was compiled. This is the reference list we compare the SNR distribution of any of the search modes with in Fig. 4.14. In the first plot we find that 253 of the injections had all-sky SNRs greater than 90% of the mean SNRs. The corresponding number of injections (189) was smaller for known-sky SNRs. At the other end of the same plot more known-sky SNRs are less loud than all-sky SNRs: While 552 injections had known-sky SNRs weaker than 90% of the mean SNRs, the corresponding number of injections was 171 for all-sky SNRs. One finds qualitatively similar improvement in the SNR values of the same injections in the sky-patch mode compared to the known-sky mode of the search.

### 4.5.3 Targeted search for GW sources using inaccurate templates: Spin

The CBCNS progenitor of a SGRB can have rapidly spinning components. If it has a highly spinning black hole, the companion neutron star can inspiral closer to it before plunging into it because its LSO is closer than that of a slowly spinning black hole of the same mass. This increases the probability of the neutron star to be ripped apart by the black hole's tidal forces as the two spiral closer to each other. That, in turn, improves the chances of creating an accretion disk with sufficient mass for the GRB engine to fire (see Sec. 4.2.4). This suggests that among CBCNS systems associated with SGRBs there will exist an astrophysical bias toward those with a highly spinning black hole. Current targeted CBC searches do not use spinning gravitational-wave templates, although significant effort is being invested to include them. Matched filtering with non-spinning templates on data that have spinning signals introduces systematic errors due to waveform mismatch. Such a systematic error

leads to reduced SNRs just like the error in component masses does, as discussed in Sec. 4.5.2. If we enable searching in multiple sky positions around the external trigger’s sky position even when its position is known accurately, its GW signal can often be found with a larger SNR from a different sky position. (Note that signal detection rather than accurate parameter estimation is the primary goal here.)

To verify the above claims, we injected 100 non-spinning BNS and NSBH signals to simulated LIGO-Virgo data and ran targeted known-sky and sky-patch searches on them. In these studies the sky-patch used was a set of 21 sky-positions, all with the same RA, and included the true sky position. The remaining twenty sky positions were distributed such that their dec changed in steps of  $2^\circ$  in both sides of the true dec value. The known-sky search used only the true sky-position. We repeated this study with a second set of injections that had the same parameters as the first set but now with a non-zero spin parameter for the binary components. The black hole and neutron star spin parameters of the injected CBC signals were in the ranges (0.70, 0.98) and (0.30, 0.75), respectively. Only non-spinning templates were used in searching both types of injections, which were made quite strong in order to ensure that most of them are found. However, four of the spinning injections were missed in the known-sky search. Three of these were recovered when the search was performed with a sky-patch. Among the remaining injections, which were found in both types of searches (i.e., known-sky and sky-patch), 46 were found with a SNR louder than the SNR of the same injection in the known-sky mode. A similar result is also observed for the same number of non-spinning injections. There, we found that 18 injections in the sky-patch study were found with a SNR louder than the SNR of the same injection in the known-sky study. In Fig. 4.16, the red bars show the gain in SNR of the triggers for non-spinning injections when using the sky-patch instead of the known-sky search. The blue bars show the same for the spinning injections. More spinning injections than non-spinning injections are found with a louder SNR in the sky-patch mode than in the known sky mode. This observation confirms that in the presence of a spin parameter mismatch the parameter error

covariance contributes significantly enough to reduce the SNR loss (and, concomitantly, alter the measured sky-position of the source).

It is important to note that since the same mass template-bank is used in studying the spinning and non-spinning injections, the effect of its discreteness on SNR loss is present in both. Similarly, the mitigation of that effect in a sky-patch search due to sky-position error covariance is also present in both studies. However, since more spinning injections are recovered with a higher SNR in the sky-patch study than the known-sky study, the impact of the sky-position error covariance is more pronounced when there is mismatch in an additional parameter, namely, the spin values of the injections and the templates (which were always non-spinning).

## 4.6 Discussion

Multiple future electromagnetic observatories are being planned that will target transient EM phenomena some of which may potentially be orphaned afterglows. A fraction of these phenomena may be due to compact binary coalescences, involving at least one neutron star. Some studies have argued that if SGRBs are beamed and if some CBCNS systems that generate afterglows do not emit gamma-rays, then a lot many more orphaned afterglows, associated with CBCNS sources, may occur than SGRBs. Coupled GW and EM observations of SGRBs and afterglows, orphaned or not, will unequivocally confirm if the progenitors are indeed CBCNS sources or if there is actually a variety of progenitors. They will also teach us about their galactic or intergalactic environments, the nature of their host galaxies, stellar population synthesis, etc. This exploration critically depends on the EM observatories taking data concurrently with the GW observatories, such as aLIGO, AdV, and KAGRA. Some of the planned EM observatories will have a wide sky coverage and a good cadence to increase their chances of finding orphaned afterglows, which can be ephemeral, dropping in their apparent magnitudes quite rapidly. Owing to their transient nature, it will be helpful

to have GW detectors at multiple sites operate with large duty factors, and GW search codes running with low latency so that they can find CBCNS sources as they coalesce and alert the EM observatories in advance of a prompt EM (and even neutrino) emission or afterglow. However, since GW detectors may not be able to localize every CBCNS or even unmodelled GW burst signal (Abbott et al. (2010)) they detect, e.g., because not enough of them are operating to successfully triangulate the sky position, it will be important to follow-up orphaned afterglows in GW data. We highlight that an orphaned afterglow has not been found yet, and a search pipeline does not exist yet that can use the sky position of such an EM source and search at that specific location but in a time window that can stretch for hours to weeks in the past to detect a GW signal associated with it in archived data. Such a pipeline needs to be developed.

Contrastingly, coherent CBCNS and burst search pipelines for detecting GW counterparts to SGRBs exist and have been run on archived GW data (Abadie et al. (2012a)). Also, fast GW burst searches exist that have been used to alert EM observatories to look for EM counterparts and afterglows, but without any positive identification so far (Abadie et al.). This may change in the advanced detector era. Fast CBC searches are under development that will target detecting their GW signals in advance for the compact binary merger so that they can alert EM observatories to look for afterglows (Cannon et al. (2012)). This development notwithstanding, hunting for GW counterparts of SGRBs in archived GW data will always remain an important exercise. In this regard, in this paper we make the case that searching with a sky-patch with multiple sky positions can improve the GW detection efficiency even when the sky position of the SGRB, or an orphaned afterglow, is known accurately through EM observations.

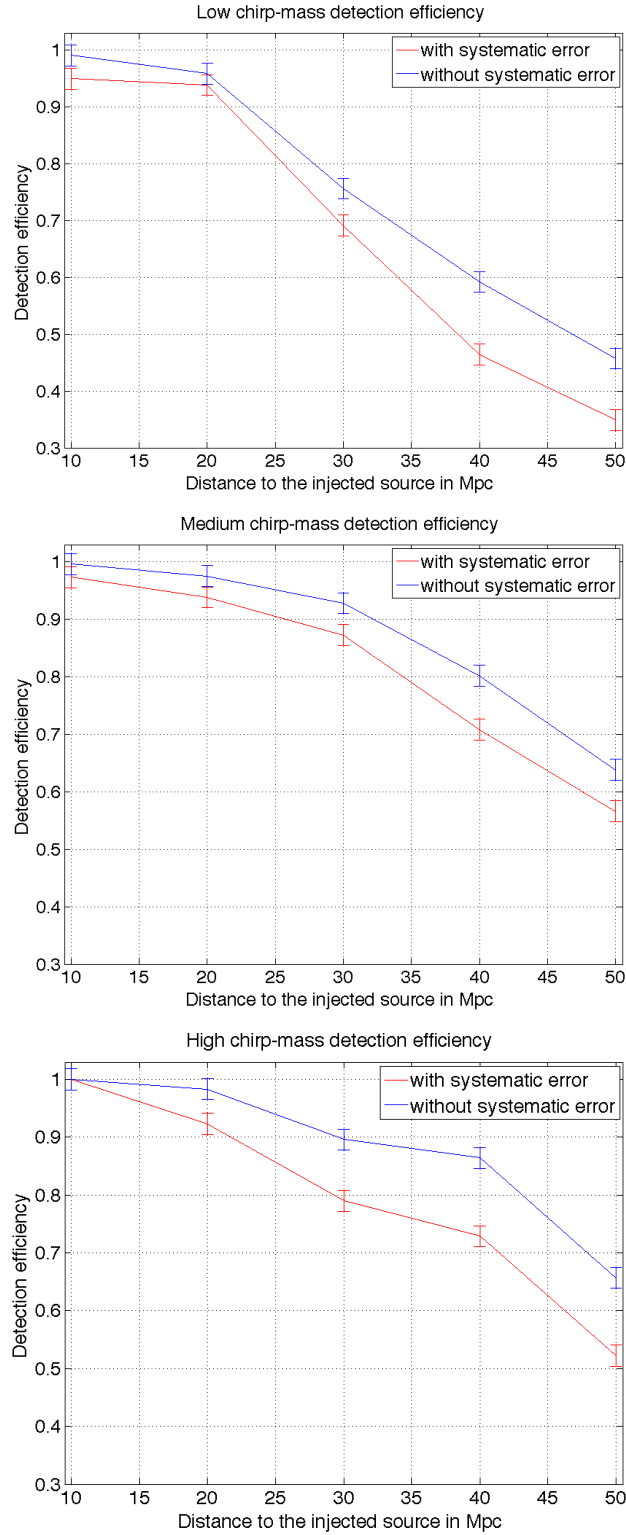


Figure 4.6: Comparison of the detection efficiencies of (from left to right) low chirp-mass, medium chirp-mass and high chirp-mass CBCNS systems with accurately known sky positions (blue or upper curves) and those with a sky-position error of  $20^\circ$  (red or lower curves).

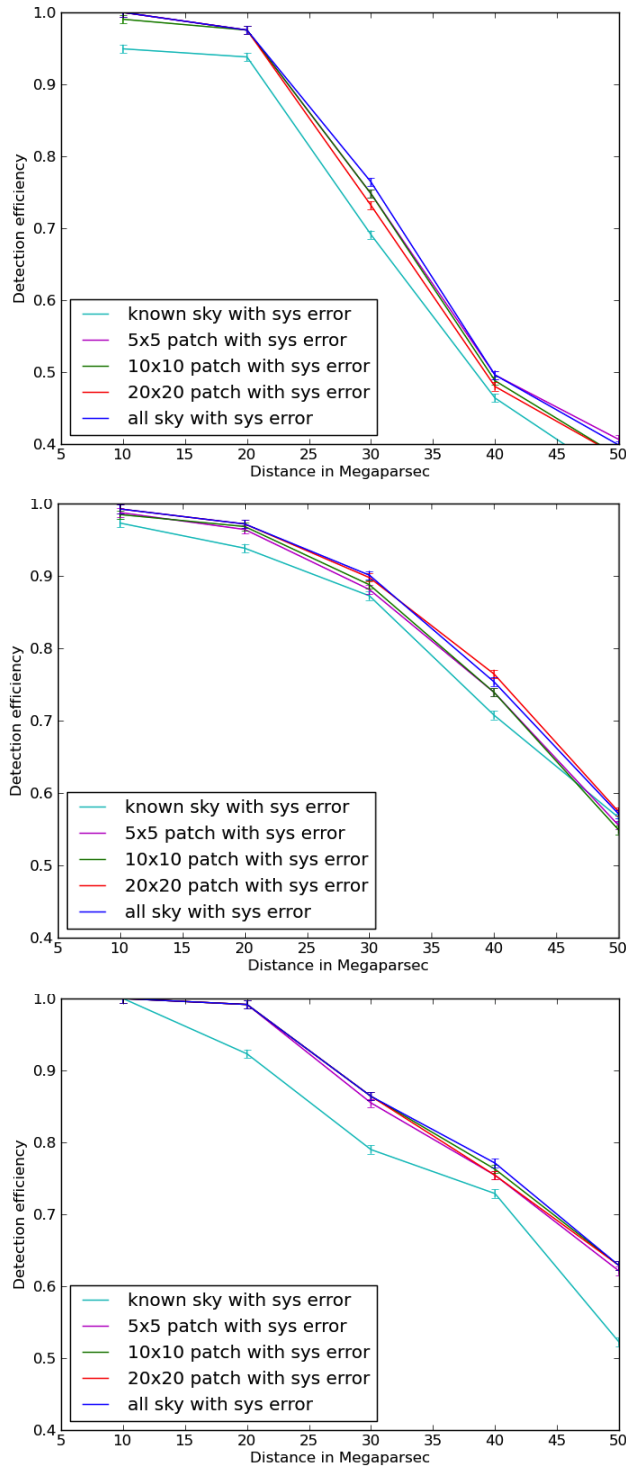


Figure 4.7: Detection efficiency comparison for injections with a sky-position error of  $20^\circ$  (from left to right) in low chirp-mass, medium chirp-mass and high chirp-mass bins.

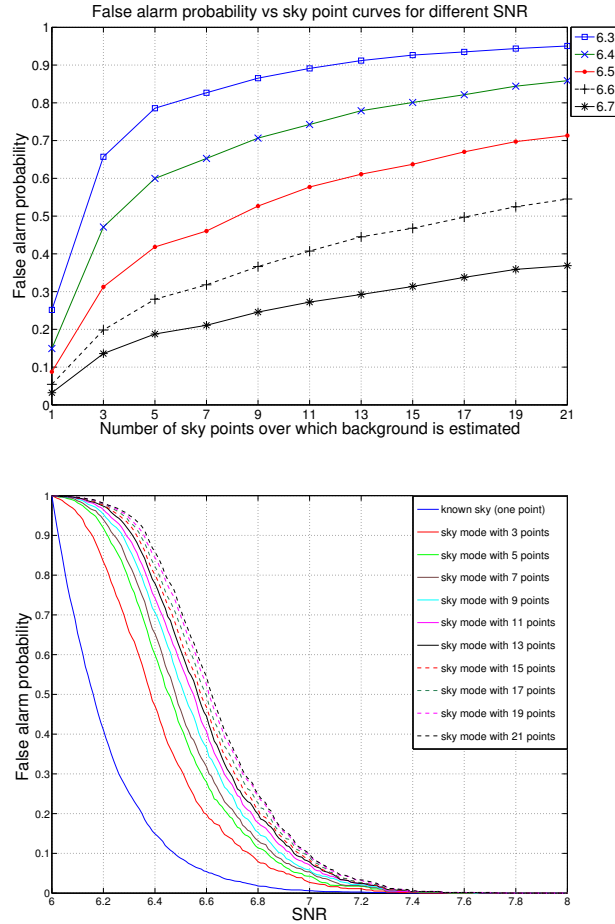


Figure 4.8: **Left:** Plots of the false-alarm probability of a sky-patch search as a function of the number of the sky position templates or points in the patch, for SNR values 6.0 - 7.5. The  $x$ -axis displays the number of sky points in the patch, which includes the true sky-position. An increase in the number of sky points in a search causes a monotonic increase in the false-alarm probability, for any given SNR, and it asymptotes to the all-sky FAP value at that SNR. **Right:** False-alarm probability plotted as a function of SNR for sky-patches with a varying number of sky points. Here the false-alarm probability at a given SNR, plotted on the  $x$ -axis, is defined as the number of background triggers that are found louder than that SNR divided by the total number of background triggers of any SNR found in the search with that sky-patch.

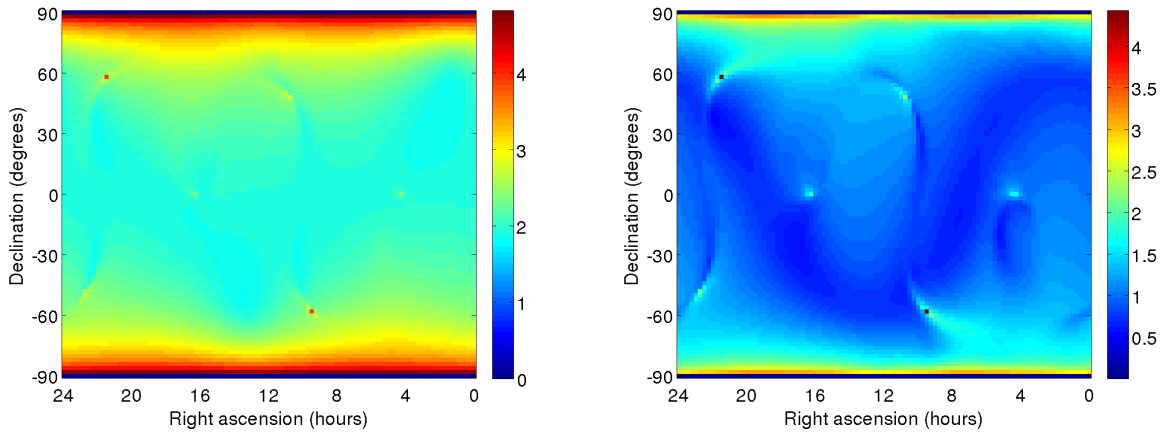


Figure 4.9: **Left plot:** The  $\log_{10}$  of the percentage change in the H1L1V1 network SNR owing to a  $20^\circ$  error in the Declination of the source is mapped as a function of the true source sky position. **Right plot:** Same as the left plot except that here the error in the sky position of the source is taken to be 4 square-degrees of solid angle. For both plots the detector noise PSD is taken to be LIGO-I LIGO Algorithms Library for all three detectors. The source is a non-spinning CBCNS with component masses  $2.5M_\odot$  and  $40M_\odot$ , optimally oriented and located at a distance of 17Mpc.

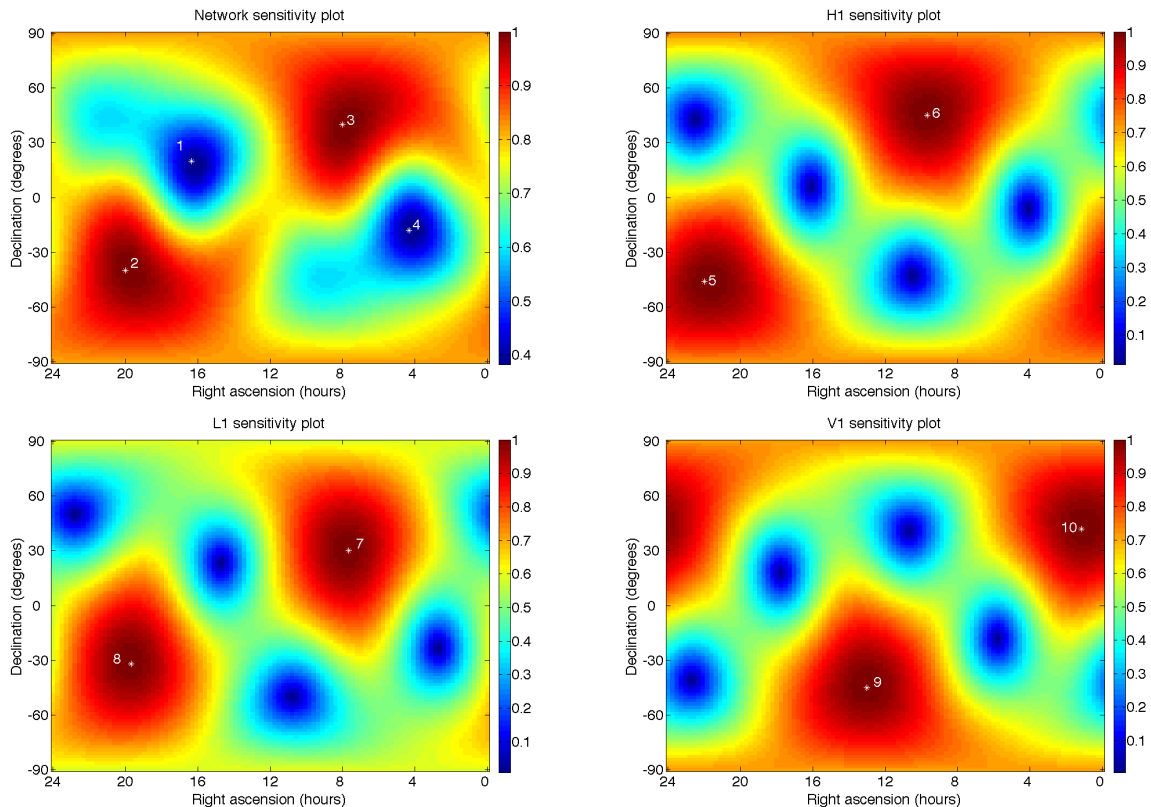


Figure 4.10: **Top left:** Network response across the sky; the quantity  $\sqrt{\sum_I (F_+^{I\ 2} + F_\times^{I\ 2})}$ , normalized to have a maximum value of unity, plotted as a function of the sky for the H1L1V1 network. The four white asterisks in this plot are located at the two most sensitive and two least sensitive sky positions. Their RA and dec, in degrees, are  $(300.0^\circ, -40.0^\circ)$ ,  $(120.0^\circ, 40.0^\circ)$  and  $(245.0^\circ, 20.0^\circ)$ ,  $(65.0^\circ, -18.0^\circ)$ , respectively. These locations were chosen for our study of the variation of detection efficiency across the sky. **Top right:** LIGO-Hanford sensitivity; the two white stars give the locations of greatest H1 response. At these two spots L1 and V1 have a relatively weak response. Thus, injections in these locations provide a good measure of how much the detection efficiency suffers when only one interferometer in the H1L1V1 network has a good response. Their RA and dec (in degrees) are  $(330.0^\circ, -46.0^\circ)$ ,  $(145.0^\circ, 45.0^\circ)$ . **Bottom row:** Same as the top right plot but for L1's best response (bottom left), at  $(115.0^\circ, 30.0^\circ)$  and  $(295.0^\circ, -32.0^\circ)$ , and V1's best response (bottom right), at  $(195.0^\circ, -45.0^\circ)$  and  $(17.0^\circ, 42.0^\circ)$ .

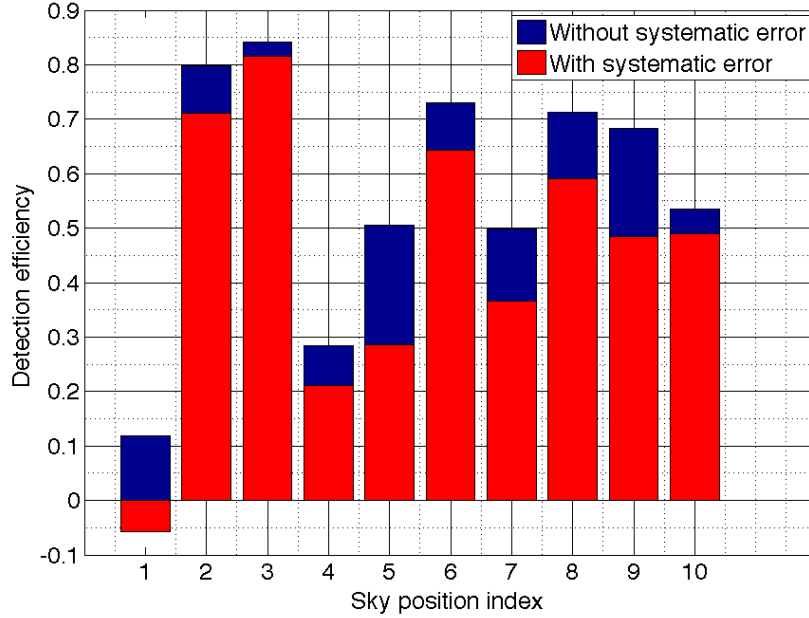


Figure 4.11: The  $y$ -axis above denotes the detection efficiency of injections in the ten sky positions shown in Fig. 4.10. The source is the same as the one used in Fig. 4.9. The ten different sky positions where injections were made to study the variation of detection efficiency as a function of the source sky position are listed on the  $x$ -axis. Their RA and dec (in degrees) are **1**:  $(245.0^\circ, 20.0^\circ)$ , **2**:  $(300.0^\circ, -40.0^\circ)$ , **3**:  $(120.0^\circ, 40.0^\circ)$ , **4**:  $(65.0^\circ, -18.0^\circ)$ , **5**:  $(330.0^\circ, -46.0^\circ)$ , **6**:  $(145.0^\circ, 45.0^\circ)$ , **7**:  $(30.0^\circ, 115.0^\circ)$ , **8**:  $(295.0^\circ, -32^\circ)$ , **9**:  $(195.0^\circ, -45.0^\circ)$ , and **10**:  $(17.0^\circ, 42.0^\circ)$ . The color code of the indices is as follows: Red-colored indices are points where the network response is the highest, as shown in Fig. 4.10. Blue indices are points of lowest network response, and green indices are points where one of the interferometers in the H1L1V1 network has a high response and the other two have a low response. Note that for the first sky position the fractional loss in SNR of the loudest injection is negative. This is because there the SNR of the injection trigger happens to be smaller than that of the loudest background trigger.

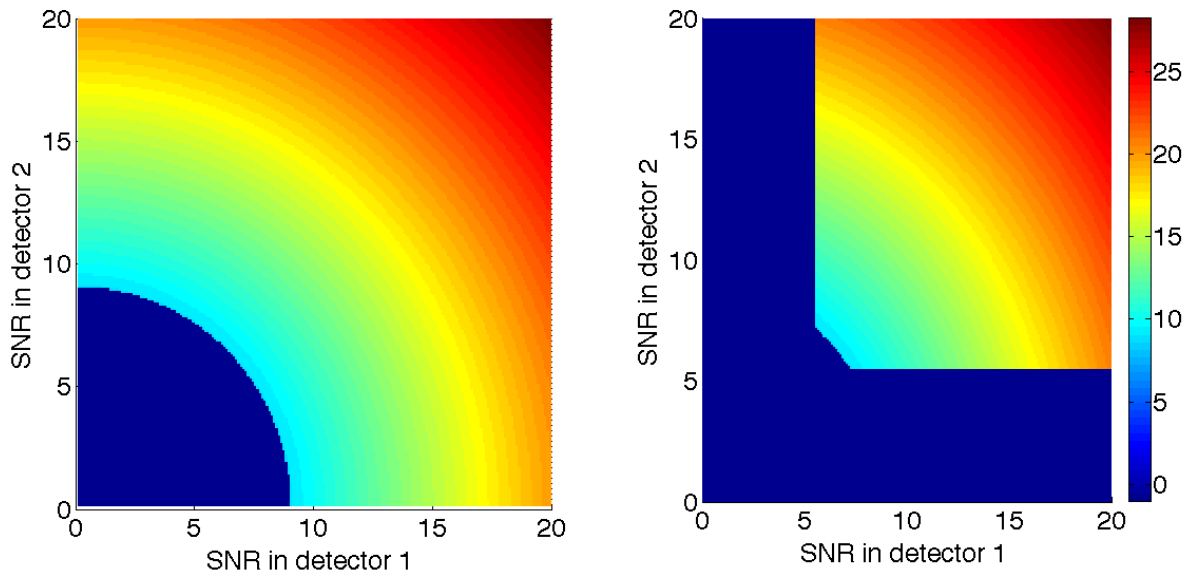


Figure 4.12: The above plots of SNRs of triggers in two detectors show the region where a coincident search with individual detector SNR thresholds of 5.5 will not find any triggers with a network combined SNR, shown in the colorbar, that is greater than 9 but a search with no individual detector thresholds will. Thresholding at an individual detector level rejects all coincidences that have a low SNR in one of the detectors. The three-detector case is easy to understand from this study: If the SNRs of a signal are less than the threshold in two of the three detectors but greater than that in the third, the combined SNR can still have an appreciable value (with a low FAP).

| GRB name   | GRB time (UTC) | RA ( $^{\circ}$ ) | Dec ( $^{\circ}$ ) | Error radius( $^{\circ}$ ) | $T_{90}$ sec        |
|------------|----------------|-------------------|--------------------|----------------------------|---------------------|
| GRB080806A | 14:01:11.2038  | 94.6              | 57.8               | 13.6                       | $2.304 \pm 0.453$   |
| GRB080828B | 04:32:11.2646  | 221.3             | -12.3              | 16.9                       | $3.008 \pm 3.329$   |
| GRB080831A | 01:16:14.7521  | 211.2             | -51.7              | 11.5                       | $0.576 \pm 1.168$   |
| GRB080919B | 18:57:35.1052  | 219.5             | 44.4               | 18.1                       | $0.512 \pm 0.405$   |
| GRB081105B | 14:43:51.2874  | 215.8             | 38.7               | 11.4                       | $1.280 \pm 1.368$   |
| GRB081113A | 05:31:32.8973  | 170.3             | 56.3               | 12.4                       | $0.576 \pm 1.350$   |
| GRB081115A | 21:22:28.1472  | 190.6             | 63.3               | 15.1                       | $0.320 \pm 0.653$   |
| GRB081119A | 04:25:27.0590  | 346.5             | 30.0               | 15.2                       | $0.320 \pm 0.680$   |
| GRB081122B | 14:43:26.2316  | 151.4             | -2.1               | 11.2                       | $0.192 \pm 0.091$   |
| GRB081204B | 12:24:25.7930  | 150.8             | 30.5               | 10.2                       | $0.192 \pm 0.286$   |
| GRB081206B | 14:29:30.6929  | 353.3             | -31.9              | 12.6                       | $7.936 \pm 4.382$   |
| GRB081213A | 04:09:41.6360  | 12.9              | -33.9              | 13.2                       | $0.256 \pm 0.286$   |
| GRB090120A | 15:02:22.7594  | 38.1              | -72.2              | 11.2                       | $1.856 \pm 0.181$   |
| GRB090126C | 05:52:33.7347  | 224.9             | 41.2               | 11.1                       | $0.960 \pm 0.231$   |
| GRB090304A | 05:10:48.1569  | 195.9             | -73.4              | 12.3                       | $2.816 \pm 0.923$   |
| GRB090320C | 01:05:10.5272  | 108.3             | -43.3              | 17.9                       | $2.368 \pm 0.272$   |
| GRB090405A | 15:54:41.3408  | 221.9             | -9.2               | 10.4                       | $0.448 \pm 1.498$   |
| GRB090412A | 01:28:05.2531  | 1.3               | -51.9              | 10.6                       | $0.896 \pm 0.264$   |
| GRB090418C | 19:35:24.9183  | 262.8             | -28.2              | 14.4                       | $0.320 \pm 0.405$   |
| GRB090427B | 15:27:00.8558  | 210               | -45.7              | 11.8                       | $1.024 \pm 0.362$   |
| GRB090616A | 03:45:42.5323  | 103.1             | -3.7               | 10.3                       | $1.152 \pm 1.168$   |
| GRB091006A | 08:38:46.9285  | 243.1             | -31                | 12.8                       | $0.192 \pm 0.091$   |
| GRB091015B | 03:05:42.9372  | 316.1             | -49.5              | 12.7                       | $3.840 \pm 0.590$   |
| GRB091018B | 22:58:20.6027  | 321.8             | -23.1              | 13.1                       | $0.192 \pm 0.286$   |
| GRB091019A | 18:00:40.8812  | 226               | 80.3               | 12.8                       | $0.208 \pm 0.172$   |
| GRB091224A | 08:57:36.5574  | 331.2             | 18.3               | 15.6                       | $0.768 \pm 0.231$   |
| GRB100101A | 00:39:49.3358  | 307.3             | -27                | 17.4                       | $2.816 \pm 0.320$   |
| GRB100126A | 11:03:05.1248  | 338.4             | -18.7              | 18.3                       | $10.624 \pm 12.673$ |
| GRB100204C | 20:36:03.7668  | 91.3              | -20.9              | 16.6                       | $1.920 \pm 2.375$   |
| GRB100208A | 09:15:33.9419  | 260.2             | 27.5               | 29.3                       | $0.192 \pm 0.264$   |
| GRB100326A | 07:03:05.5029  | 131.2             | -28.2              | 12.6                       | $5.632 \pm 2.064$   |
| GRB100411A | 12:22:57.3442  | 210.6             | 47.9               | 31.6                       | $0.512 \pm 0.231$   |
| GRB100516A | 08:50:41.0629  | 274.4             | -8.2               | 18.4                       | $2.112 \pm 1.134$   |
| GRB100516B | 09:30:38.3170  | 297.7             | 18.7               | 13.7                       | $0.640 \pm 0.487$   |
| GRB100530A | 17:41:51.2263  | 289.7             | 31                 | 11.6                       | $3.328 \pm 0.810$   |
| GRB100616A | 18:32:32.8957  | 342.9             | 3.1                | 45.7                       | $0.192 \pm 0.143$   |
| GRB100621C | 12:42:16.4305  | 160.9             | 14.7               | 11.4                       | $1.024 \pm 0.202$   |
| GRB100706A | 16:38:18.9243  | 255.2             | 46.9               | 12.2                       | $0.128 \pm 0.143$   |

Table 4.1: Fermi SGRBs with large sky-position uncertainties that were concurrent with LIGO’s S5 run.

| GRB name   | GPS time (sec) | Error box (square degrees) | Duration of GRB (sec) |
|------------|----------------|----------------------------|-----------------------|
| GRB061001  | 843772482      | $\sim 2000$                | 1.00                  |
| GRB060601B | 833183754      | $\sim 600$                 | 0.50                  |
| GRB070910  | 873480823      | $> 200$                    | 0.38                  |
| GRB070413  | 860531889      | 350                        | 0.19                  |
| GRB070203  | 854579218      | $> 2000$                   | 0.69                  |
| GRB061014  | 844841836      | $> 3000$                   | 1.50                  |
| GRB060916  | 842452428      | $> 3000$                   | 0.13                  |

Table 4.2: Short IPN GRBs with large sky position errors.

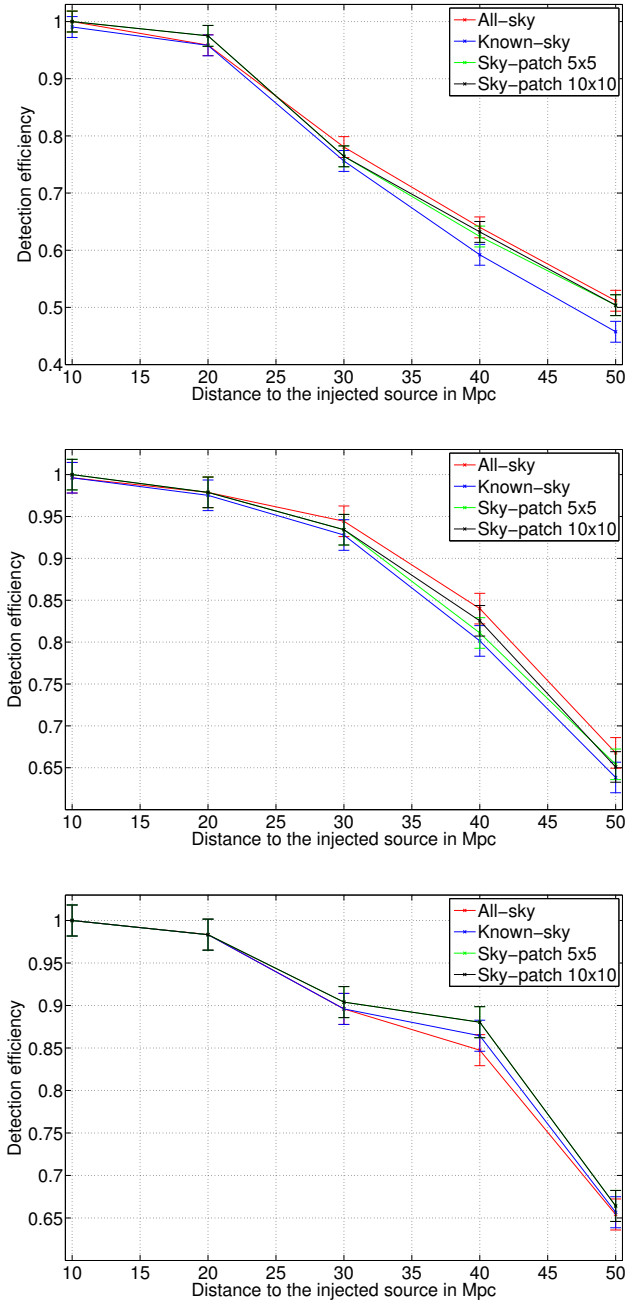


Figure 4.13: Detection efficiency comparison (from left to right) for the low chirp-mass, medium chirp-mass and high chirp-mass bins for four sky modes. Unlike in Fig. 4.7 there is no sky-position error here.

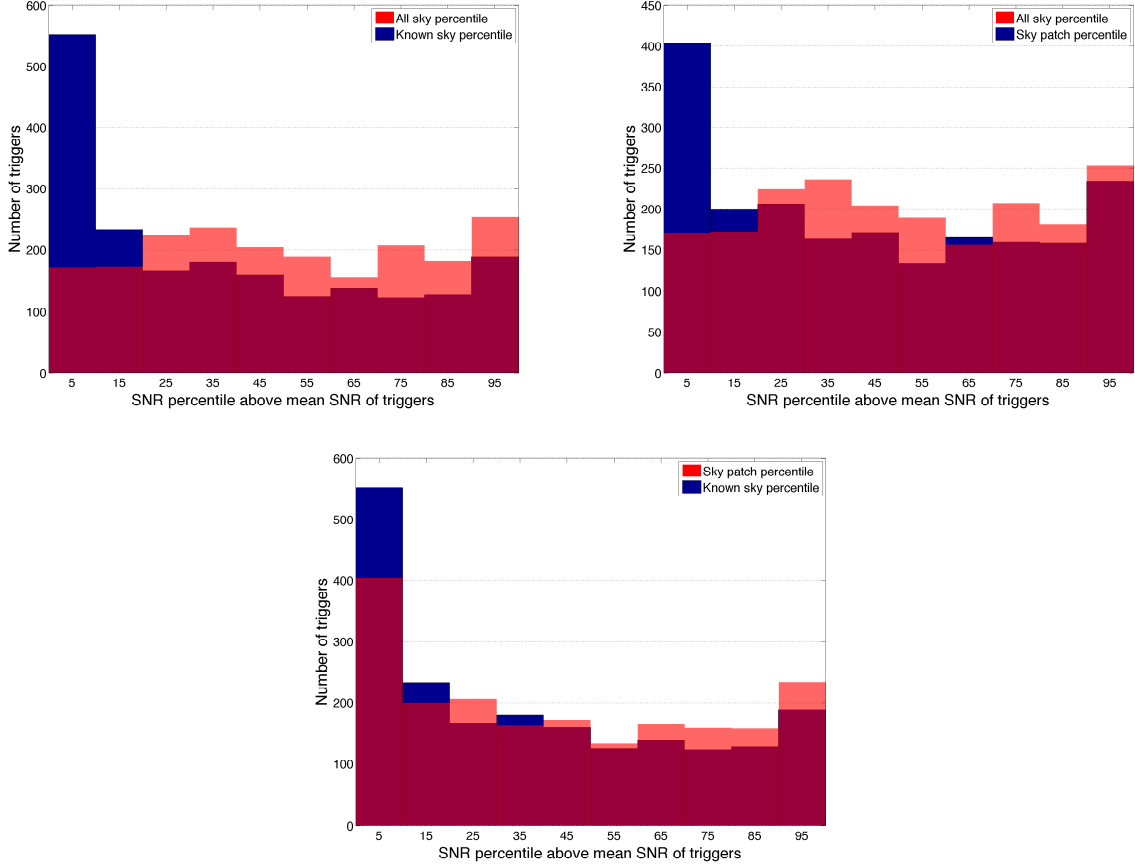


Figure 4.14: In these plots we study the combined distribution of the SNRs of the 3000 injections from all three sky-mode searches. For every injection we compute the mean of its network SNRs found by the known-sky, sky-patch, and all-sky modes of the search. We next compile the list of the 3000 mean SNRs. This is the reference list with which we compare the SNRs of injections from any of the search modes. Pairwise comparisons of distributions of injection SNRs from the different sky-mode searches are shown in these plots. In the first plot we find that 253 of the injections had all-sky SNRs greater than 90% of the mean SNRs. The corresponding number of injections (189) was smaller for known-sky SNRs. At the other end, more known-sky SNRs are less loud than all-sky SNRs: While 552 injections had known-sky SNRs weaker than 90% of the mean SNRs, the corresponding number of injections was 171 for all-sky SNRs. One finds qualitatively similar improvement in the SNR values of the same injections in the sky-patch mode compared to the known-sky mode of the search.

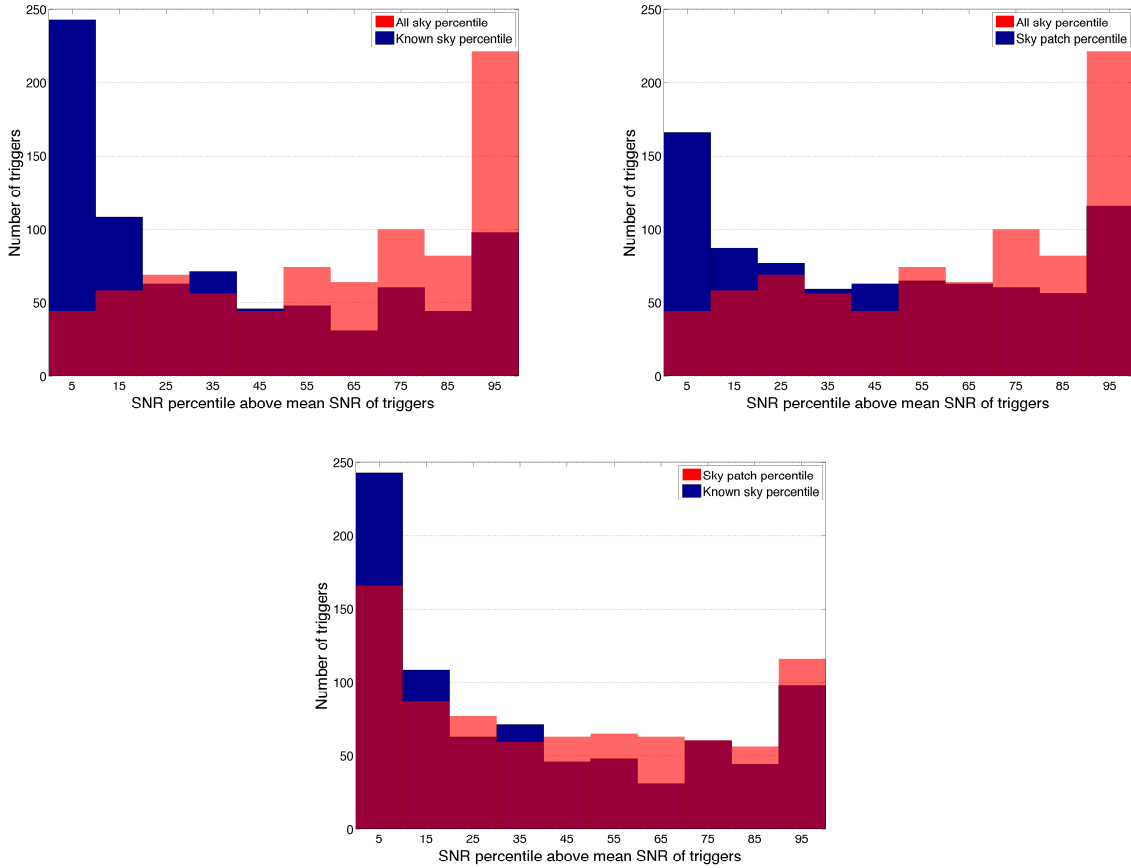


Figure 4.15: Similar plot as in Fig. 4.14 with only those injections were considered whose SNR is less than 20. We note that the performance of the all-sky and sky-patch modes are even better for weaker SNR triggers compared to the known-sky mode in the region where 90% or more triggers were found louder than the mean SNR.

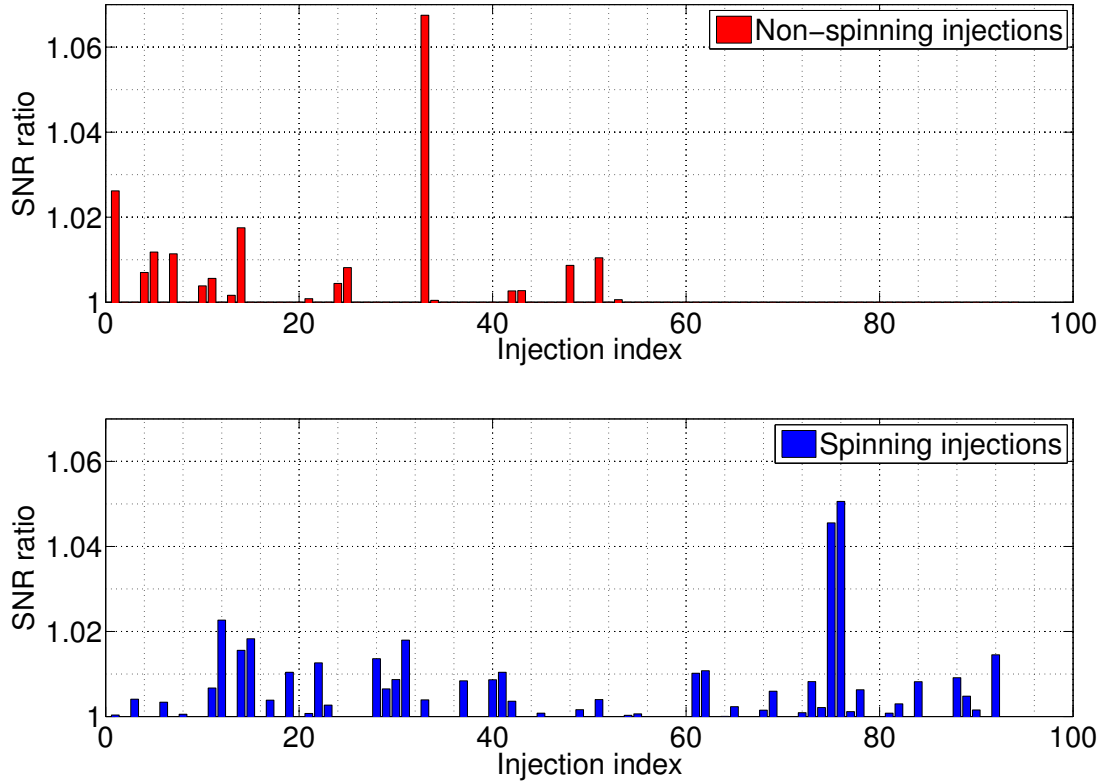


Figure 4.16: Plot of ratio of SNR of the injection trigger when the search was conducted over a patch of 21 points to that of the SNR of the same injection found in a search conducted in one point in the sky. The top plot with red bars is for the case of non-spinning injections, and the bottom plot is the same for the spinning injections. This study was conducted on 100 injections in the low-mass region of the template bank. For the spinning case, the spin was chosen to be very high, i.e., with the spin parameter greater than 0.75, so that the effect of spin is prominent.

# Chapter 5

## Waveform inaccuracy and its effects on parameter estimation and detection

### 5.1 Introduction

In a gamma ray burst (GRB) triggered search of gravitational waves (GW) we have the advantage of knowing *a priori* the sky position and time of occurrence of the event from GRB alerts. But only a fraction of GRBs will be beamed at us and we will miss the prompt emissions from the majority of the potential gamma ray burst sources. On top of that, even for the sources beamed at us, a fraction of the prompt electromagnetic emissions will still be missed because these transient events typically do not last more than 2 seconds. However, the afterglows from these sources will be visible over a much larger angular spread since the beaming angle increases with decreasing Lorentz factor of the jet. And the X-ray afterglows from these sources will be visible up to a day after the prompt emission. Optical afterglows will be visible up to an order of week or more after the prompt emission and radio counterparts will be visible for months or even a year. Thus the sources for which we missed

the prompt emissions, either because they were not beamed at us or because they were too short lived for our space based observatories to point at and detect, we can still search for them by targetting their longer lasting afterglows. Such afterglows, whose prompt emissions went undetected, are called *orphaned afterglows*. However, afterglows tend to be very weak and an afterglow whose location is not betrayed by a strong prompt emission, will indeed be quite hard to detect. Thus, till date no orphaned afterglow has ever been found.

With the advent of second generation gravitational wave detectors, such as advanced LIGO and Virgo, a new opportunity will now be unleashed into the arena of multi-messenger astronomy. A compact binary source that emits gravitational waves can also be a prospective candidate for short duration gamma ray burst. With the information that one receives after the detection of a gravitational wave signal, X-ray, optical and radio telescopes around the world and on near-earth orbits can be alerted. Given the time scales of afterglows, these observatories will have ample time to search for the sources, that were localized in patches of the sky by gravitational wave detection, in great detail without having to scan through the full sky. However, this imposes demands on how precisely certain gravitational wave signal parameters must be measured.

This precision, at the very least, will always be limited by the inherent statistical noise in the measurement process. However, in this chapter we will concern ourselves with the effect of the use of incorrect waveforms in the estimation of parameters. This is because in certain cases this systematic error will dominate over the statistical error. We will also study the effect of waveform inaccuracy on the detection of gravitational wave signal.

A short GRB source must have atleast one of the binary components as a neutron star. However, black holes are much ‘cleaner’ systems, and for the present study whether the system is actually able to emit a jet of gamma ray or not, is irrelevant since the whether a binary system fires a jet or not will depend upon the size of an accretion disk before the merger (see Sec. 2.5.1) and the parameter estimation error due to mismatch of waveform will depend on the mass of the system prior to the formation of the accretion disk. Thus,

we will present the parameter estimation study for binary black hole (BBH) systems. In the detection study we will focus on the effect of using non-spinning templates to detect spin-aligned compact binary sources.

## 5.2 BBH waveforms used for parameter estimation

Just like any compact binary coalescence (CBC) waveform, a gravitational waveform from a binary black hole also consists of three major phases. First is the inspiral phase, when the amplitude and the frequency of the signal increase slowly. This is accurately known through the post-Newtonian (PN) approximation to general relativity. Next is the merger phase, when the amplitude rapidly increases. Numerical relativity has made it possible to compute accurate gravitational waveforms in the merger region. And finally the ringdown phase, when the amplitude decays rapidly (dropping off along a Lorentzian curve), which is well modeled using black hole perturbation theory. In spite of this progress, where our knowledge of the gravitational waveform of compact binary coalescences is not complete. There remain regions of the parameter space that can be astrophysically significant. For instance, our knowledge about the CBC waveforms is limited to fairly low mass ratios and for mass ratio greater than 100 numerical merger waveforms from BBH systems are not available yet. Template banks have been generated for even lower mass ratios ( $< 10$ ). Absence of knowledge of waveforms in different parts of the parameter space leaves us with no choice than to search with less accurate inspiral only waveforms which gives rise to inaccurate modeling of the gravitational waveforms. Our goal in this section and the next is to study the effect of this inaccurate modeling in estimation of parameters that can be determined by a single detector.

To quantitatively assess the effects of inaccurate modeling, however one needs the knowledge of the exact waveforms. Since we do not have the exact waveform over the full duration, we choose as our surrogate waveforms the phenomenological inspiral-merger-ringdown waveforms Ref. Ajith and et. al (2008). These are analytic waveforms that are modeled to

have better than 99% fitting factor with hybrid waveforms constructed from PN and NR waveforms, with mass ratios from 1 to 4. We choose this phenomenological waveform as the exact waveform in the mass ratio range of (1, 8), which is not much wider than their proven range of validity. In order to study the effect of using inaccurate waveforms, we used a bank of TaylorT1 3.5PN templates Ref. Damour et al. (2001). The inspiral phase of the phenomenological inspiral-merger-ringdown (IMR) signals is modeled on the same TaylorT1 approximant. Furthermore, in the low-mass limit, where the merger and ringdown phases are much shorter than the inspiral phase, the errors should tend to vanishingly small values and, thus, provide an important check on the numerical aspects of our simulations. Finally, since the binary black hole signals are not yet known for mass ratios above ten and since signals from CBCs involving neutron stars are affected by uncertainties in the knowledge of their equation of state, inspiral templates are still in use in searches for those signals that involve spin. These motivated us in to the choice of the target and search waveforms.

For modeling the signals, we use the analytical Fourier domain IMR waveforms proposed in Ref. Ajith and et. al (2008).

$$\tilde{h}(f) = A_{\text{eff}}(f)e^{i\psi_{\text{eff}}(f)}, \quad (5.1)$$

where the effective amplitude and the phase are expressed as,

$$A_{\text{eff}}(f) \equiv \frac{M^{5/6}}{d_{\text{eff}} \pi^{2/3}} \sqrt{\frac{5\eta}{24}} f_{\text{merg}}^{-7/6} \begin{cases} (f/f_{\text{merg}})^{-7/6} & \text{if } f < f_{\text{merg}} \\ (f/f_{\text{merg}})^{-2/3} & \text{if } f_{\text{merg}} \leq f < f_{\text{ring}} \\ w \mathcal{L}(f, f_{\text{ring}}, \sigma) & \text{if } f_{\text{ring}} \leq f < f_{\text{cut}}, \end{cases}$$

$$\Psi_{\text{eff}}(f) \equiv 2\pi f t_0 + \varphi_0 + \frac{1}{\eta} \sum_{k=0}^7 (x_k \eta^2 + y_k \eta + z_k) (\pi M f)^{(k-5)/3}. \quad (5.2)$$

In the above expressions,

$$\mathcal{L}(f, f_{\text{ring}}, \sigma) \equiv \left( \frac{1}{2\pi} \right) \frac{\sigma}{(f - f_{\text{ring}})^2 + \sigma^2/4} \quad (5.3)$$

is a Lorentzian function that has a width  $\sigma$ , and that is centered around the frequency  $f_{\text{ring}}$ . The normalization constant,  $w \equiv \frac{\pi\sigma}{2} \left( \frac{f_{\text{ring}}}{f_{\text{merg}}} \right)^{-2/3}$ , is chosen so as to make  $A_{\text{eff}}(f)$  continuous across the “transition” frequency  $f_{\text{ring}}$ . The parameter  $f_{\text{merg}}$  is the frequency at which the power-law changes from  $f^{-7/6}$  to  $f^{-2/3}$ . The *effective distance* to the binary is denoted by  $d_{\text{eff}}$ , which is related to the luminosity distance  $d_L$  by  $d_{\text{eff}} = d_L/C$ . The phenomenological parameters  $f_{\text{merg}}, f_{\text{ring}}, \sigma$  and  $f_{\text{cut}}$  are given in terms of the total mass  $M$  and symmetric mass-ratio  $\eta$  of the binary as

$$\begin{aligned} \pi M f_{\text{merg}} &= a_0 \eta^2 + b_0 \eta + c_0, \\ \pi M f_{\text{ring}} &= a_1 \eta^2 + b_1 \eta + c_1, \\ \pi M \sigma &= a_2 \eta^2 + b_2 \eta + c_2, \\ \pi M f_{\text{cut}} &= a_3 \eta^2 + b_3 \eta + c_3. \end{aligned} \quad (5.4)$$

The coefficients  $a_j, b_j, c_j$ ,  $j = 0 \dots 3$  and  $x_k, y_k, z_k$ ,  $k = 0, 2, 3, 4, 6, 7$  are tabulated in Table I of Ref. Ajith (2008). For component masses  $m_{1,2}$ , the total mass is  $M = m_1 + m_2$  and the symmetric mass-ratio is  $\eta = m_1 m_2 / M^2$ . For the discussion here, it helps to remember that for a mass-ratio of  $m_1/m_2 = 1, 4$ , and  $8$ , one has  $\eta = 0.25, 0.16$ , and  $\sim 0.1$ , respectively.

### 5.3 Parameter measurement errors

Let us define a vector space of time series data of gravitational waves from a detector, which will be the discrete counterpart of the data  $s(t)$ , where  $s(t) = n(t) + h(t)$ ,  $n(t)$  being the noise and  $h(t)$  is the signal. Let us parametrize the gravitational waveforms by a parameters  $\theta^j$ , where  $j$  is the parameter index. The time series corresponding to the exact

signal we denote by  $\mathbf{h}_E(\theta^j)$  and that corresponding to the approximate signal is denoted by  $\mathbf{h}_A(\theta^j)$ . These two waveforms in general will exist in two different manifolds in the same vector space of the data. This is illustrated in Fig. 5.1.

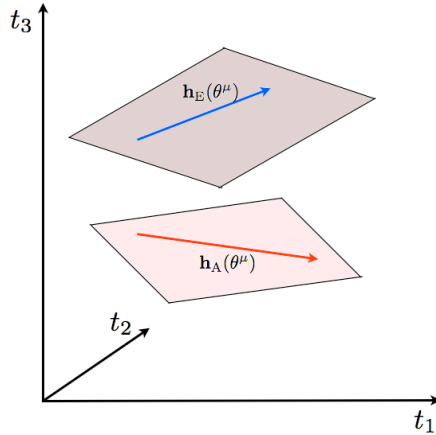


Figure 5.1: In the vector space defined by the data, the exact and the approximate waveforms exist in different manifolds. Here we show it with an example where the data has three time points and hence is three dimensional. These three time points forms the three axes in the figure. Note that in general the two waveforms will exist in different planes, as shown in this example. Thus it is not possible to rotate any one of the waveforms in its own manifold and align it with a waveform in the other manifold.

Note that if the difference between the exact and the approximate waveforms vanishes then the two waveforms exist in the same manifold and one can always align them to each other simply by rotating them within the manifold. This act of rotating the vector in the manifold to match the signal waveform is typically what is done while we maximize the match filter output w.r.t the signal parameters. However, in presence of difference between the approximate and the exact waveforms, one can never match the approximate waveform to the exact one by rotating the former in the manifold of the later. The best one can do is maximize the inner product between these two vectors that exist in two different manifolds. This maximized match between the exact waveform and the approximate waveform is called the *best fit* and the parameters of the approximate waveform for which the match is maximized are called the *best fit parameters*  $\theta_{\text{bf}}$ . Thus the waveform that gives the best match for a given exact signal  $\mathbf{h}_E(\theta_{\text{tr}}^j)$  can be written as  $\mathbf{h}_A(\theta_{\text{bf}}^j)$ . The data vectors will exist in the same

vector space, albeit in a dimension higher than that of the manifolds of approximate or exact waveforms.

$$\begin{aligned}\mathbf{s} &= \mathbf{h}_E(\theta_{\text{tr}}^j) + \mathbf{n} \quad (\text{in presence of signal}), \\ \mathbf{s} &= \mathbf{n} \quad (\text{in absence of signal}).\end{aligned}\tag{5.5}$$

Instead of defining the best fit parameters by the match, one can also define it, following Ref. Cutler and Vallisneri (2007), as those parameters that minimize the distance (measured in the vector space of the data) between the signal (exact waveform) and the template (approximate waveform), namely,

$$\partial_j \|\mathbf{s} - \mathbf{h}_A(\theta)\|^2 \Big|_{\theta_{\text{bf}}} = \partial_j \langle \mathbf{s} - \mathbf{h}_A(\theta_{\text{bf}}) | \mathbf{s} - \mathbf{h}_A(\theta_{\text{bf}}) \rangle \Big|_{\theta_{\text{bf}}} = \langle \partial_j \mathbf{h}_A(\theta_{\text{bf}}) | \mathbf{s} - \mathbf{h}_A(\theta_{\text{bf}}) \rangle = 0. \tag{5.6}$$

where we have dropped the  $j$  index from the  $\theta$ 's for brevity, and  $\partial_j = \partial/\partial\theta^j$ . Let us assume that the true parameter  $\theta_{\text{tr}}^j$  and the best fit parameter  $\theta_{\text{bf}}^j$  are different from each other by an amount  $\Delta\theta^i$ ,

$$\Delta\theta^j = \theta_{\text{bf}}^j - \theta_{\text{tr}}^j. \tag{5.7}$$

Thus in the manifold of the approximate waveforms, the waveform with the true parameters  $\mathbf{h}_A(\theta_{\text{tr}})$  can be expanded around the waveform with the best fit parameters  $\mathbf{h}_A(\theta_{\text{bf}})$  using Taylor expansion. Keeping terms up to first order of  $\Delta\theta^j$ , we get,

$$\mathbf{h}_A(\theta_{\text{bf}}) - \mathbf{h}_A(\theta_{\text{tr}}) \approx \Delta\theta^j \partial_j \mathbf{h}_A(\theta_{\text{bf}}). \tag{5.8}$$

In Fig. 5.2 it is shown how the best fit waveform vector is obtained by essentially dropping a normal on to the manifold of the approximate waveforms from the manifold of the exact waveforms. This by definition would minimize the distance between the signal (exact waveform) and the template (approximate waveform). In this figure we have not considered any noise. In the realistic case the noise will take the data vector out of the manifold of the exact waveforms, but it helps to look at this figure devoid of any noise. In the actual

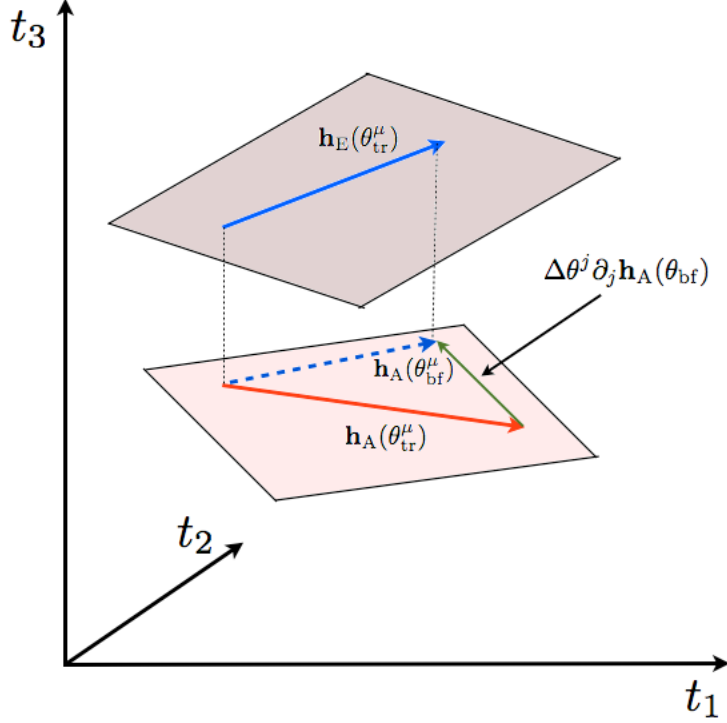


Figure 5.2: For the true parameters the approximate waveform will not give the best fit. This is the systematic error in the parameter that we incur due to the inaccuracy in the templates.

calculation we will keep the noise term in the expressions. We immediately note that for the true parameters the approximate waveform (depicted by the red arrow) will not give the best fit. The loudest signal to noise ratio will be produced by the vector in the approximate waveform manifold with the parameters  $\theta_{\text{bf}}$  (depicted by blue dashed arrow). The difference (depicted by the green arrow in Fig. 5.2) between the best fit approximate waveform vector and the true parameter approximate waveform vector is proportional to the systematic error in the parameter that one incurs due to the inaccuracy in the templates.

The ‘ket’ part of the inner product in Eq. (5.6) can be written after adding and subtracting  $\mathbf{h}_A(\theta_{\text{tr}})$  as follows,

$$\mathbf{s} - \mathbf{h}_A(\theta_{\text{bf}}) = \mathbf{n} + \mathbf{h}_E(\theta_{\text{tr}}) - \mathbf{h}_A(\theta_{\text{tr}}) + \mathbf{h}_A(\theta_{\text{tr}}) - \mathbf{h}_A(\theta_{\text{bf}}), \quad (5.9)$$

Using Eq. 5.8 we get,

$$\mathbf{s} - \mathbf{h}_A(\theta_{\text{bf}}) \approx \mathbf{n} + \mathbf{h}_E(\theta_{\text{tr}}) - \mathbf{h}_A(\theta_{\text{tr}}) - \Delta\theta^i \partial_i \mathbf{h}_A(\theta_{\text{bf}}). \quad (5.10)$$

Substituting this back to Eq. (5.6) we get,

$$\langle \partial_j \mathbf{h}_A(\theta_{\text{bf}}) | \mathbf{s} - \mathbf{h}_A(\theta_{\text{bf}}) \rangle = \langle \partial_j \mathbf{h}_A(\theta_{\text{bf}}) | \mathbf{n} + \mathbf{h}_E(\theta_{\text{tr}}) - \mathbf{h}_A(\theta_{\text{tr}}) - \Delta\theta^i \partial_i \mathbf{h}_A(\theta_{\text{bf}}) \rangle = 0, \quad (5.11)$$

Let us now define the *Fisher information matrix*,

$$\Gamma_{ij}(\theta_{\text{bf}}) = \langle \partial_i \mathbf{h}_A(\theta_{\text{bf}}) | \partial_j \mathbf{h}_A(\theta_{\text{bf}}) \rangle, \quad (5.12)$$

Multiplying Eq. (5.11) on both sides by  $(\Gamma_{ij}(\theta_{\text{bf}}))^{-1}$  and rearranging terms we get,

$$\Delta\theta^i = \left( \Gamma^{-1}(\theta_{\text{bf}}) \right)^{ij} \left\{ \langle \partial_j \mathbf{h}_A(\theta_{\text{bf}}) | \mathbf{n} \rangle + \langle \partial_j \mathbf{h}_A(\theta_{\text{bf}}) | [\mathbf{h}_E(\theta_{\text{tr}}) - \mathbf{h}_A(\theta_{\text{tr}})] \rangle \right\}. \quad (5.13)$$

The first term gives the statistical contribution to the parameter error and the second term gives the parameter error due to the systematic one Ref. Cutler and Vallisneri (2007). Note however that we do not know the true parameters of the signal and the best estimates of the parameters we have are the  $\theta_{\text{bf}}$ . Therefore, to the leading order one can write Eq. (5.13) as,

$$\Delta\theta^i \approx \left( \Gamma^{-1}(\theta_{\text{bf}}) \right)^{ij} \left\{ \langle \partial_j \mathbf{h}_A(\theta_{\text{bf}}) | \mathbf{n} \rangle + \langle \partial_j \mathbf{h}_A(\theta_{\text{bf}}) | [\mathbf{h}_E(\theta_{\text{bf}}) - \mathbf{h}_A(\theta_{\text{bf}})] \rangle \right\}. \quad (5.14)$$

Thus the estimates of the systematic error and the statistical error in the estimation of the parameters are given by,

$$\begin{aligned}\Delta_{\text{sys}}\theta^i &= \left(\Gamma^{-1}(\theta_{\text{bf}})\right)^{ij} \langle \partial_j \mathbf{h}_A(\theta_{\text{bf}}) | [\mathbf{h}_E(\theta_{\text{bf}}) - \mathbf{h}_A(\theta_{\text{bf}})] \rangle, \\ \Delta_{\text{n}}\theta^i &= \left(\Gamma^{-1}(\theta_{\text{bf}})\right)^{ij} \langle \partial_j \mathbf{h}_A(\theta_{\text{bf}}) | \mathbf{n} \rangle,\end{aligned}\tag{5.15}$$

respectively. We note immediately one important difference between the systematic error and the statistical error in parameter estimation. The magnitude of the waveform vectors  $\mathbf{h}_E(\theta_{\text{bf}})$  and  $\mathbf{h}_A(\theta_{\text{bf}})$  corresponds to the amplitude of the signal. Thus, in Eq. (5.15), the  $\Gamma_{ij}(\theta_{\text{bf}})$  term is quadratic in signal strength. Now, the statistical error in estimation of parameters has the following term  $\langle \partial_j \mathbf{h}_A(\theta_{\text{bf}}) | \mathbf{n} \rangle$ , which is linear in signal strength. This implies that,

$$\Delta_{\text{n}}\theta^i \propto \frac{1}{\text{SNR}},\tag{5.16}$$

The  $\Delta_{\text{sys}}\theta^i$  term however depends on  $\langle \partial_j \mathbf{h}_A(\theta_{\text{bf}}) | [\mathbf{h}_E(\theta_{\text{bf}}) - \mathbf{h}_A(\theta_{\text{bf}})] \rangle$  which is quadratic in signal strength, rendering  $\Delta_{\text{sys}}\theta^i$  independent of the signal strength (SNR) to the lowest order. Thus, for stronger signals it is the systematic error term that is going to dominate. However, one must keep in mind that in going from Eq. 5.13 to Eq. 5.14 we made the approximation  $\mathbf{h}_E(\theta_{\text{tr}}) - \mathbf{h}_A(\theta_{\text{tr}}) = \mathbf{h}_E(\theta_{\text{bf}}) - \mathbf{h}_A(\theta_{\text{bf}})$ . Therefore in reality, the error in parameter estimation will depend on the true values of the parameters themselves.

For a non-spinning BBH system nine parameters characterize the waveform. They are the total mass  $M$ , the symmetric mass-ratio  $\eta$ , the sky-position angles  $(\alpha, \delta)$ , the binary's orientation angles  $(\psi, \iota)$ , the luminosity distance  $d_L$ , the initial (or some reference) phase  $\varphi_0$ , and the time of arrival (or some reference time)  $t_0$ . The systematic errors in  $M$  and  $\eta$ , and the fractional loss of SNR, arising from inaccurate waveform modeling was studied and we present the results next.

### 5.3.1 Numerical simulations

For the study that is being presented here, as the exact or target waveform the complete

Inspiral-merger-ringdown (IMR) waveform was chosen, with  $m_{1,2} \in [13, 104]M_{\odot}$  to model the exact (or target) waveform. Thus, the mass-ratio of the target signals ranged from 1 to 8. As the (approximate) template bank we chose 3.5PN TaylorT1 approximant waveforms with mass parameters over-covering the mass-range of the target signals. The choice of the template waveforms is governed by the fact that the inspiral phase of the Phenomenological waveforms (Ajith and et. al (2008)) is modeled after that PN approximant. The templates are modeled with  $M$  and  $\eta$  such that  $m_{1,2} \in [5, 121]M_{\odot}$ , but always with  $\eta \leq 0.25$ , which is the physical upper-bound. For these studies, we used the method and the code described in Ref. Ajith and Bose (2009b). Only one target signal is present in the data at any given time.

In the search of gravitational waves from CBC sources, one uses unit norm templates to find the match with unit norm signals. The choice of unit norm helps us in finding the match of the signal with the template irrespective of the intrinsic strength of the signal. The signal amplitude is measured from the value of the signal-to-noise ratio that we construct by the match between the template and the signal. The measured values of other parameters, specifically the binary's component masses,  $t_0$  and  $\phi_0$ , are those defining the template that yields the *maximum match* with the injected signal. For any given CBC signal and a template bank the fitting factor is the signals match maximized over that template bank. Thus the fractional loss of SNR of a target signal with amplitude  $\beta$  ( $\beta = 1$  for unit norm signals), when searched with a template bank with amplitude  $\alpha$  ( $\alpha = 1$  for unit norm templates) is given by,

$$\text{Fractional loss of SNR} = \frac{\alpha\beta - \alpha\beta \max_{\theta} \langle \mathbf{h}_A(\theta) | \mathbf{h}_E(\theta_{\text{tr}}) \rangle}{\alpha\beta} = 1 - \text{FF}, \quad (5.17)$$

where FF is the fitting factor on that template bank obtained by maximizing the match  $\langle \mathbf{h}_A(\theta) | \mathbf{h}_E(\theta_{\text{tr}}) \rangle$ , which occurs at  $\theta = \theta_{\text{bf}}$ . Here the fitting factor is independent of the CBC signal parameters that cannot be measured by a single detector, namely, the distance and

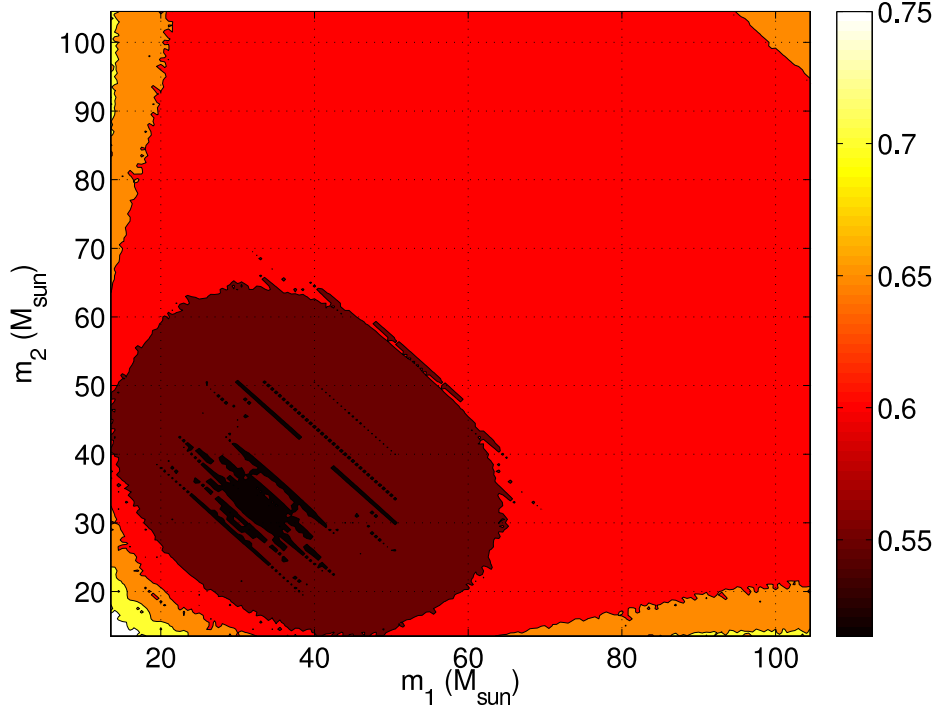


Figure 5.3: The fitting factor obtained from numerical simulations of matched filtering with a bank of 3.5PN TaylorT1 templates of (complete) inspiral-merger-ringdown waveforms as target signals in AdvLIGO PSD. The target waveforms are parameterized by the BBH component masses  $m_1$  and  $m_2$ , each ranging from 13 - 104  $M_\odot$ .

the polarization, inclination, and sky-position angles.

The fitting factor for the above choice of template bank and target signal family is presented in Fig. 5.3, where the maximization over the template parameters  $(t_0, M, \eta)$  was carried out numerically and that over  $\phi_0$  was carried out analytically, as explained above. Recall, that the template bank we used for this study comprised of inspiral waveforms. Thus the reason for the mismatch between signal and template is the difference between the signal and the templates in the merger and the ringdown phase of the coalescence, which for the later case is absent. It implies that, longer the inspiral stage for a binary, better is the match and hence the fitting factor. We know that for inspiraling signal the characteristic time scale for a chirp signal in the detectors sensitivity bucket, also known as the chirp time is given by,

$$\xi = 1390 \left( \frac{\mathcal{M}}{M_\odot} \right)^{-5/3} \frac{f_s}{10 \text{ Hz}} \text{ seconds}, \quad (5.18)$$

where  $\mathcal{M}$  is the *chirp mass* of the system that is defined as,

$$\mathcal{M} = \frac{(m_1 m_2)^{3/5}}{(m_1 + m_2)^{1/5}}, \quad (5.19)$$

Using these we can write,

$$\xi \sim \frac{1}{\eta M^{5/3}}, \quad (5.20)$$

Therefore it is obvious that systems with low  $\eta$  and  $M$  will tend to have longer inspiral durations. Now, we see that the fitting factor in Fig. 5.3 decreases with increase in total mass  $M$ . Moreover, for the same total mass, as the mass ratio gets closer to unity the fitting factor gets worse. This is again because time evolution of an asymmetric mass ratio system and systems with large total mass tends to be longer, thus the longer inspiral signals compensate for the power lost due to the absence of the merger and ringdown part of the signal in the templates.

The implications of these observations are that for a given target signal, the template that gives the best fit match will tend to have lower total mass than the true value since such templates will fit the target signal better due to increase in the template duration, compared to the true total mass templates, i.e.,

$$\langle \mathbf{h}_A(M_{\text{bf}}) | \mathbf{h}_E(M_{\text{tr}}) \rangle > \langle \mathbf{h}_A(M_{\text{tr}}) | \mathbf{h}_E(M_{\text{tr}}) \rangle, \quad \text{for } \frac{M_{\text{bf}} - M_{\text{tr}}}{M_{\text{tr}}} = \frac{\Delta M}{M} < 0. \quad (5.21)$$

This is nicely observed in our results in Fig. 5.4, where the value of  $\Delta M/M$  is consistently negative in the entire mass space over which we have conducted our study. It is also evident in the result that, as we go for higher values of total masses, the error in mass estimation (expectedly) worsens. A diagonal line on this plot from bottom left to top right represents symmetric mass ratio systems. Systems with same total mass will fall on lines that are perpendicular to the diagonal line. As one goes away from the diagonal, along a particular equal total mass line, systems with higher mass ratio are encountered. The result shows that

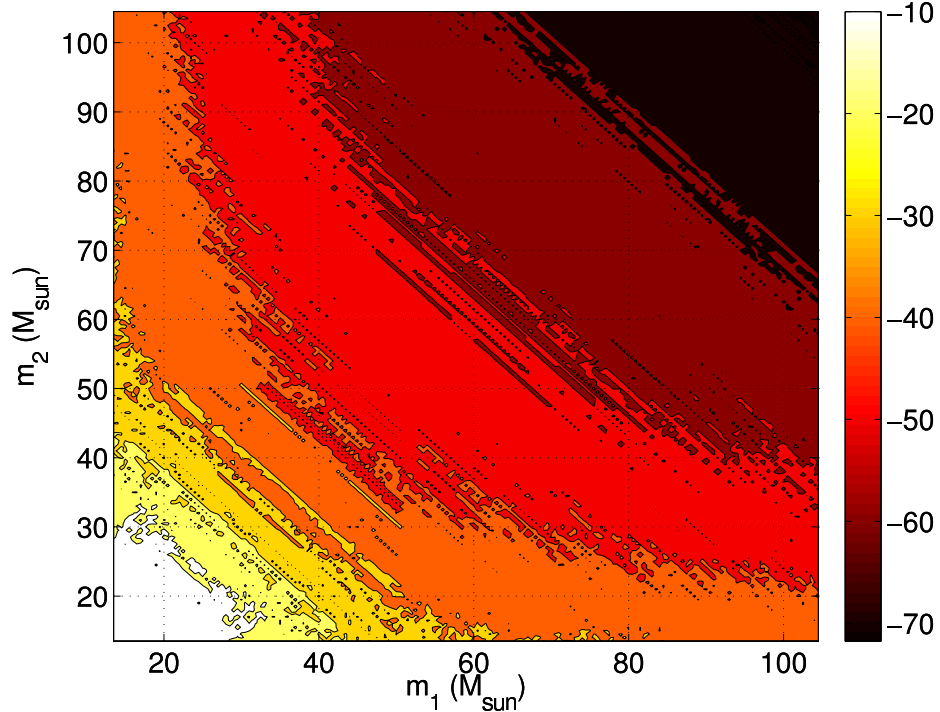


Figure 5.4: The fractional error in total-mass (in %) obtained from numerical simulations of the same template bank and target signals, in AdvLIGO PSD, as shown in Fig. 5.3. Target signals with  $\eta = 0.25$  are represented by points along the equal-mass line (not shown) extending from the left-bottom corner to the top-right corner of the plot.

for asymmetrical mass systems the error in the estimation of the total mass is less compared to the symmetrical mass systems, because the asymmetry in masses is improving the match between the template and the target waveform by increasing the duration of the templates for the same total mass. However, note that this effect is only seen at large total mass values. Tentatively, in this case we start to observe this effect above the total mass of  $40M_{\odot}$ . At lower total masses the error in total mass estimation seems to be immune to the effect of mass ratio of the source involved as is evident also from Fig. 5.5 where we show what is expected analytically. It is only at higher total mass systems that the merger and ringdown part of the waveforms begin to contain significant amount of power, so that the best match template is obtained with an increase in the inspiral waveform's duration by changing both the total mass and the mass ratio from the true values and this explains the hyperbolic bands in Fig. 5.4. For lower total mass systems, the deviation of best fit total mass from the true

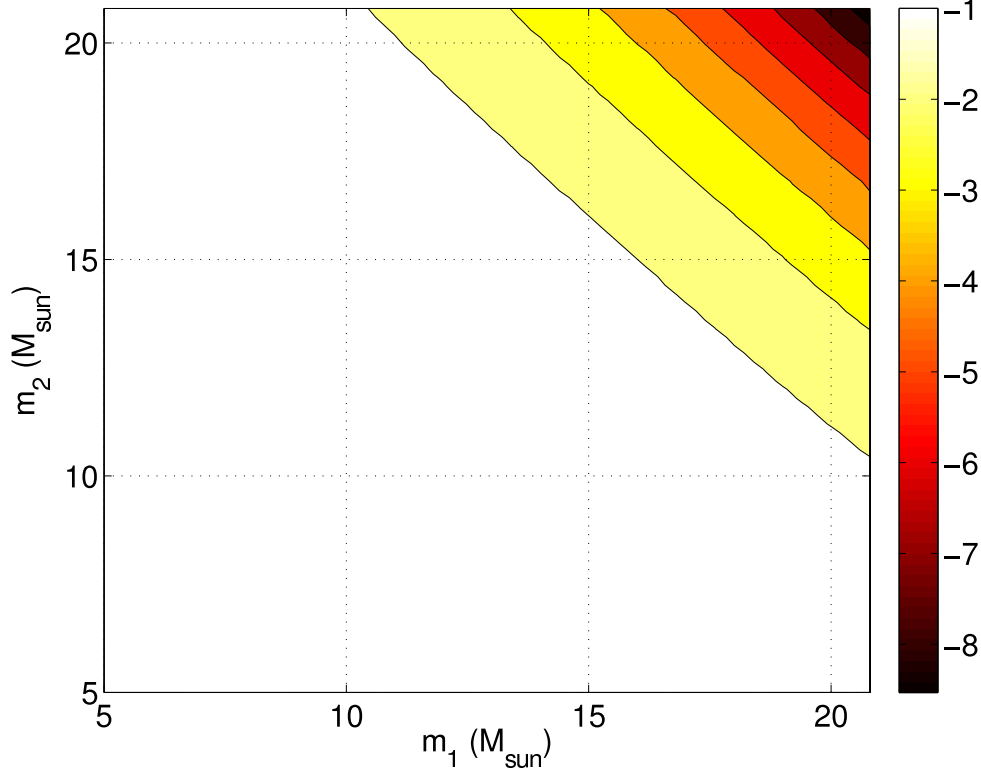


Figure 5.5: The fractional error in total-mass (in %) given by the analytic expression Eq. (5.14) for AdvLIGO PSD. Above,  $m_1$  and  $m_2$  represent the true parameters.

total mass adequately compensates for the absence of the merger and ringdown part of the waveform and this explains the cross-diagonal bands in Fig. 5.4 and Fig. 5.5.

Now suppose the true waveform did not have a merger and ringdown part. In that case any effect of lowering of total mass of the template can be compensated by an increase in the value of  $\eta$ , the symmetric mass ratio. Thus an error in the recovery of the total mass will be correlated to an error in the recovery of  $\eta$ . This correlation can be quantified as follows. From Eq. 5.15 we get,

$$\Delta_{\text{sys}}\theta^i = \left(\Gamma^{-1}(\theta_{\text{bf}})\right)^{ij} \langle \partial_j \mathbf{h}_A(\theta_{\text{bf}}) | [\mathbf{h}_E(\theta_{\text{bf}}) - \mathbf{h}_A(\theta_{\text{bf}})] \rangle, \quad (5.22)$$

For the simplicity of the discussion, if we assume that the correlation of error in the estimation

of  $\eta$  is only non-vanishing with the error in estimation of total mass then,

$$\begin{aligned} \Delta_{\text{sys}}\theta^\eta = & \left(\Gamma^{-1}(\theta_{\text{bf}})\right)^{\eta^\eta} \langle \partial_\eta \mathbf{h}_A(\theta_{\text{bf}}) | [\mathbf{h}_E(\theta_{\text{bf}}) - \mathbf{h}_A(\theta_{\text{bf}})] \rangle \\ & + \left(\Gamma^{-1}(\theta_{\text{bf}})\right)^{\eta^M} \langle \partial_M \mathbf{h}_A(\theta_{\text{bf}}) | [\mathbf{h}_E(\theta_{\text{bf}}) - \mathbf{h}_A(\theta_{\text{bf}})] \rangle, \end{aligned} \quad (5.23)$$

where  $\left(\Gamma^{-1}(\theta_{\text{bf}})\right)^{\eta^M} = \langle \partial_\eta \mathbf{h}_A(\theta_{\text{bf}}) | \partial_M \mathbf{h}_A(\theta_{\text{bf}}) \rangle$ . Thus we note from the second term in the RHS of Eq. 5.23 that any error in estimation of the total mass will affect the error in estimation of the symmetric mass ratio. This result, which we obtained for the above cases, when there is no waveform inaccuracy, must still hold when there is discrepancy between the exact and the approximate waveforms. This is what we observed in our study of the error in symmetric mass ratio in Fig. 5.6. For a target signal that has fairly equal component masses, the inspiral waveform duration of the best fit template increases due to an under estimation of the total mass. This increase in duration is compensating for the absence of the merger and ringdown part in the target waveform. The recovered values of  $\eta$  are fairly accurate as a result of the dominance of the total mass error since the best fit is acquired without any need for altering the  $\eta$  values from the true ones. However, for an asymmetric mass system (for example the lower right hand corner of the plot) the target waveform has most of the power from the inspiral phase, and the power in the merger and ringdown phase is negligible. As a result these waveforms tend to be very similar to the approximate inspiral waveforms. Here, we begin to observe the effect of correlation between the estimation of error of the total mass and the symmetric mass ratio. Due to this correlation, the error in the symmetric mass ratio will be positive or negative depending upon the magnitude of the total mass error. A very large negative total mass error can increase the template duration beyond the optimum match. The best fit  $\eta$  will then deviate towards a higher  $\eta$  value to reduce the template duration, restoring it down to the optimum match. Conversely, if the template size is still smaller than the target waveform for an optimum match for a given negative total mass error, the best fit  $\eta$  value will decrease to maximize the match. This

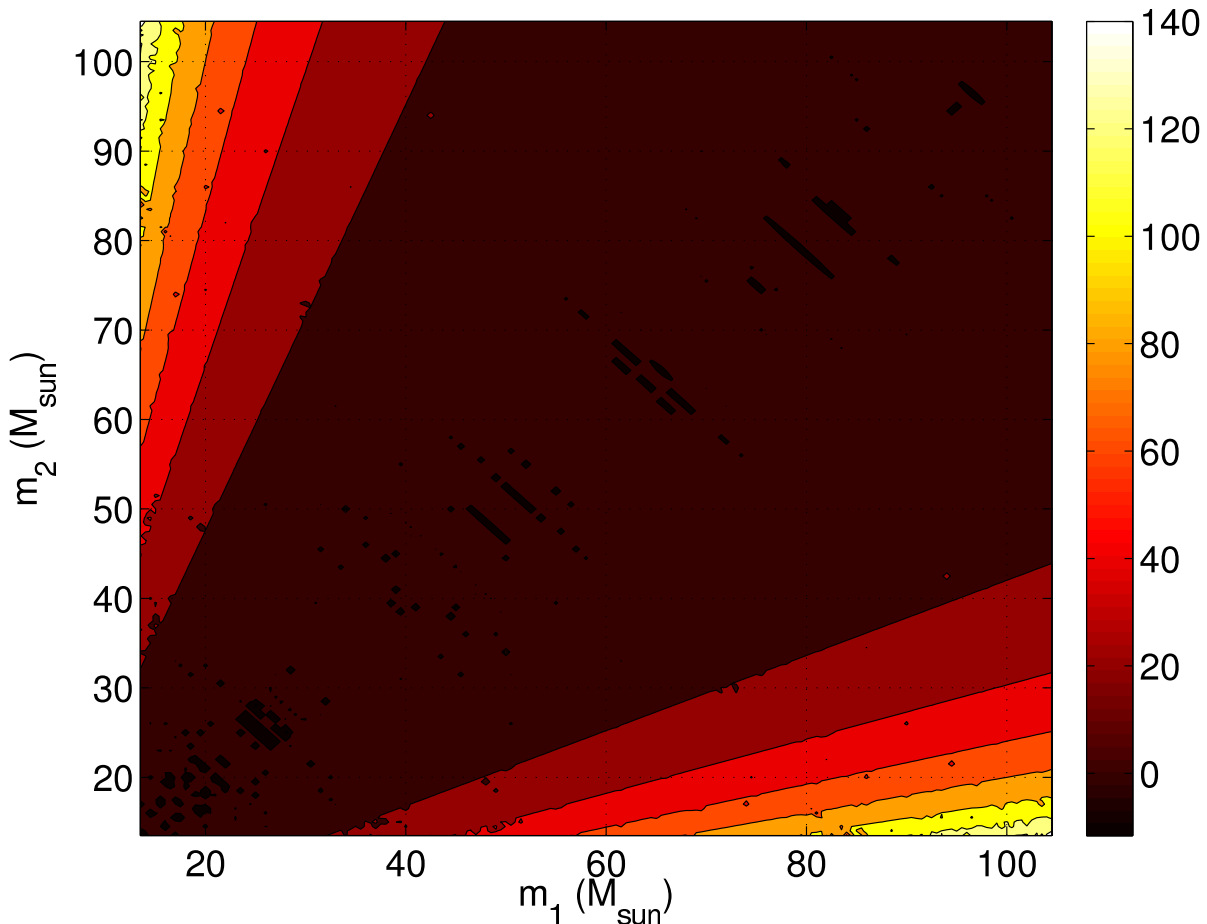


Figure 5.6: The fractional error in the symmetric mass-ratio (in %) obtained from numerical simulations for the same template bank and target signals, in AdvLIGO PSD, as shown in Fig. 5.3.

is being observed in the left plot of Fig. 5.7. Patches of yellow and orange signifies the a positive error in  $\eta$  while patches of dark red signifies a negative error in  $\eta$  in this plot.

### 5.3.2 Analytic results using leading order approximation of the waveform discrepancies

In Eq. (5.14) we found out how the error in estimation of CBC source parameters will depend upon waveform inaccuracies and detector noise. One must keep in mind that in deriving that expression, we dropped higher order terms of  $\Delta\theta^i$ , thus, it should not be expected to be valid at large discrepancies in the waveform model. From the numerical

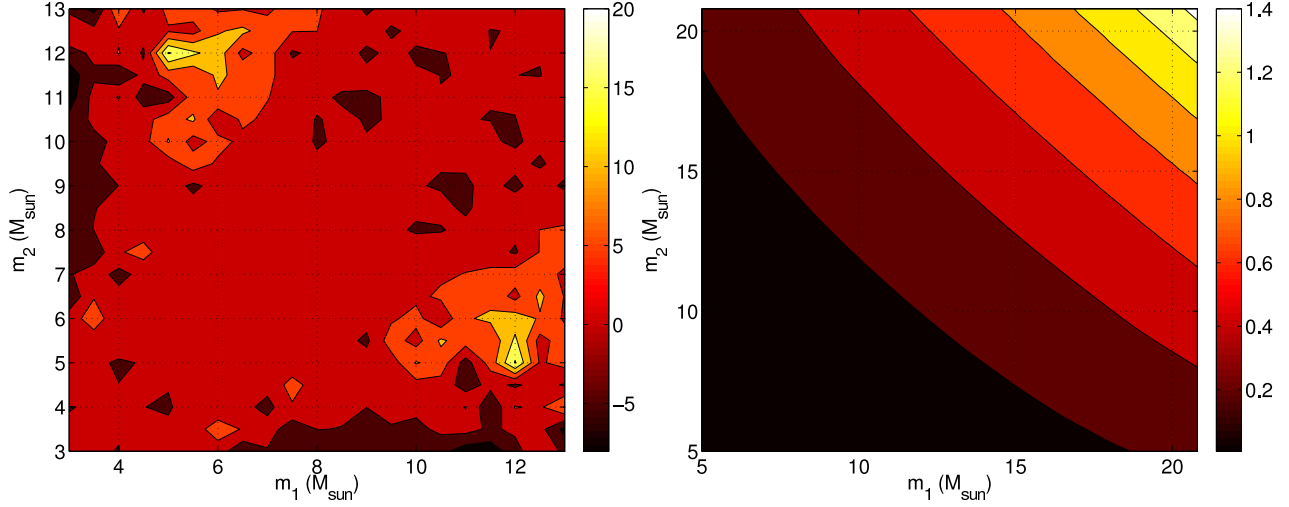


Figure 5.7: The fractional error in the symmetric mass-ratio in AdvLIGO PSD (in %). The figure on the left is obtained from numerical simulations, and that on the right is computed from the analytic expression in Eq. (5.13).

simulations we have observed that the discrepancies between the signal waveform and the template decreases for smaller values of  $M$ . We, therefore, use the analytic approximation in Eq. (5.14) to compute the systematic errors in the parameters in that region, i.e., for  $m_{1,2} \in [5 - 20]M_{\odot}$ . The results for  $\Delta M/M$  are given in Fig. 5.5 and for  $\Delta\eta/\eta$  in Fig. 5.7 (in the right plot). The result of  $\eta$  is especially interesting. As we have discussed in the previous section, the error in  $\eta$  was least in and around the equal mass region for the numerical simulations we performed. Same feature was not obtained in the analytic calculation, as is evident from the Fig. 5.7 (in the right plot). This apparent disagreement can be explained by the fact that in our numerical simulations the templates in the template bank were limited to have  $\eta \leq 0.25$ , since physically a template can not have  $\eta$  greater than that value; no such restriction however is assumed in the derivation of Eq. (5.14). This is why the best fit value of  $\eta$  in the right plot in Fig. 5.7 is larger than 0.25 as one approaches the top-right corner, i.e., where  $m_1 \simeq m_2$  and the target and template waveforms start departing from each other. This also suggests that allowing for templates with unphysical values of  $\eta$  might help mitigate some of the loss in SNR arising from inaccurate waveform modeling (Bose et al. (2008)).

## 5.4 Waveform inaccuracy and its effect on detection of gravitational waves from progenitors of short GRBs

Our focus in the previous sections was on the effect of waveform inaccuracy on parameter estimation, caused by the use of templates that do not have the merger and the ringdown parts. Now we will discuss the other aspect of waveform inaccuracy, namely, detection. For this study we are going to concern ourselves with the use of non-spinning templates for searching of signals from spinning compact binary systems.

In a compact binary system, at least an accretion rate of  $0.1 M_{\odot}$  per second is required for a GRB to be triggered (Kiuchi et al. (2010b)). It was mentioned in the same reference that in order to get that kind of an accretion rate, at least a mass of  $0.01 M_{\odot}$  is required in the accretion disk. For a neutron star - black hole (NSBH) system all of this mass will be obtained from the neutron star (NS) through its tidal disruption by the black hole. How much mass will be available, will depend strongly on the stiffness of the NS equation of state (EOS) and also the amount of tidal force exerted by the black hole (BH). These two factors will determine the extent of tidal disruption of the neutron star. It is the second factor that gets boosted in presence of strong BH spin because the innermost stable circular orbit (ISCO) of a spinning system (especially when the BH spin is aligned to the orbital spin) will be smaller than a non-spinning one (about six times smaller for a maximally spinning BH). This gives the NS an opportunity to sample the space closer to the black-hole before plunging into it. Thus the chance for the formation for an accretion disk capable of creating a fireball energetic enough to launch a GRB increases, making a CBC systems that are highly spinning more likely to be a candidate for a GRB.

However, current search pipelines do not implement spinning template banks for the search of gravitational waves from progenitors of GRBs. This is primarily because spinning searches require a lot of computational power. This prompted us to assess the effects of us-

ing non-spinning templates on spinning signals. It is expected that the use of non-spinning templates in the conventional searches should result in reduced SNR, and consequently detection efficiency due to signal-template mismatch. But the study gets an added dimension when we consider the fact that in a real search the noise is non-stationary. A subset of the non-stationary features in the data that are transients are called glitches. They often trigger the templates in the search pipeline and create false alarm. To deal with these glitches several signal discriminant techniques have been developed. One of the most powerful one being the  $\chi^2$ -test, detail of which is given in Ref. Allen (2005). The performance of the  $\chi^2$ -test depends on the mismatch between the signal and the waveform. The expectation value of  $\chi^2$  is independent of the signal strength when the signal and template do not have any mismatch. However, when the template is inaccurate, then the expected value of  $\chi^2$  depends quadratically on the expected SNR of the signal. Thus, not only the search suffers due to lowering of the signal to noise ratio, but also the performance of the signal discriminants are compromised due to waveform inaccuracies.

To observe this effect happening in an actual search, we injected 3000 spin Taylor 3.5 approximant waveforms as target signals of various spin values and searched for them using TaylorT1 3.5PN templates. We did the same with 3000 weakly spinning injections (  $a \leq 0.01$  ) where  $a$  is the Kerr parameter <sup>1</sup>. For each signal that was recovered we computed the coherent  $\chi^2$  (Harry and Fairhurst (2011)) and the coherent SNR values (Bose et al. (2000); Pai et al. (2001); Bose et al. (2011); Harry and Fairhurst (2011)). A plot of the coherent  $\chi^2$  vs coherent SNR values of the found signals reveals the performance of the  $\chi^2$ -test for different kinds of spinning signals. Since the templates are non-spinning, therefore the weakly spinning signals (in the red pluses) in Fig. 5.8 have better match with the templates and hence, fares better as far as coherent  $\chi^2$  values are concerned than the higher spinning signals.

In order to study the effect of spin on  $\chi^2$  values, we injected a thousand spin aligned binary neutron star (BNS) and NSBH sources each in real S6 LIGO noise and searched for

---

<sup>1</sup> $a = 0$  denotes non-spinning black hole or neutron star and  $a = 1$  for a black hole denotes a maximally spinning black hole. The maximum value of  $a$  for a neutron star in our simulation is chosen to be 0.4.

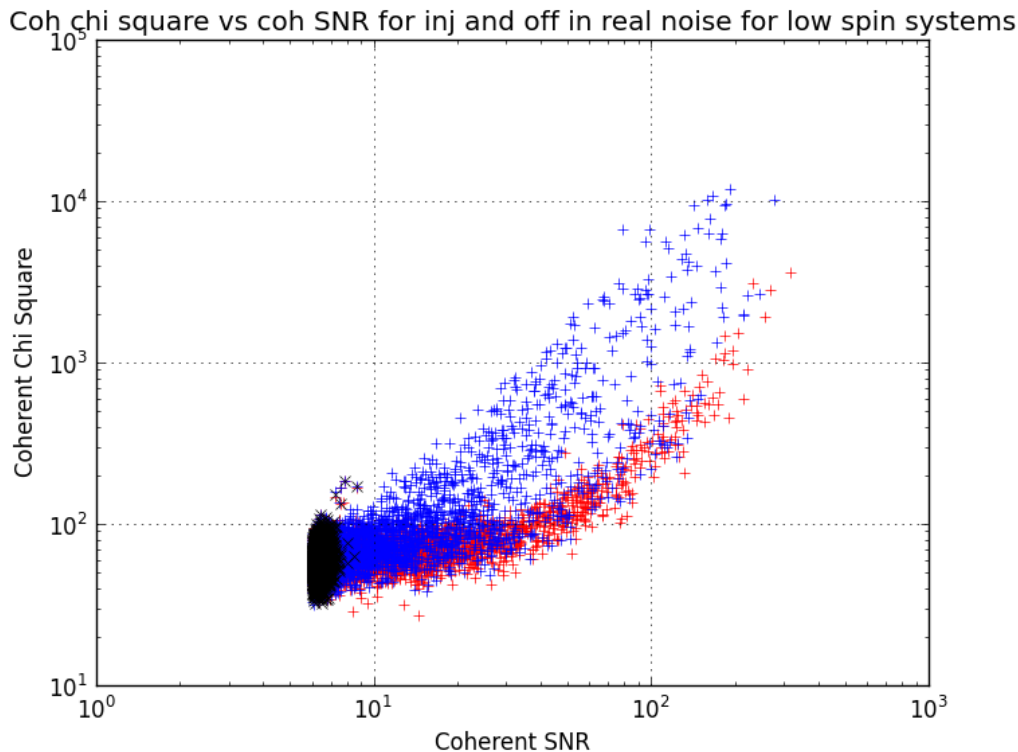


Figure 5.8: Coherent  $\chi^2$  values for weakly spinning sources that were found by searching with non-spinning templates tend to be lower than those for strongly spinning sources. The red pluses are spinning sources that have  $a \leq 0.01$ . The blue pluses have larger spin values. When searched with non-spinning templates, the signal mismatch is increasing the coherent  $\chi^2$  values. The extent of the deterioration is less when the mismatch is lower in the case of low spin system.

them using spin aligned templates<sup>2</sup>. These injections were fairly strong as they were all injected at a distance of (2, 10) megaparsecs. For BNS systems the spins of the neutron stars were in the range  $a \in (0.0, 0.4)$  and for the NSBH systems they were in the range  $a \in (0.0, 0.98)$  for the black hole and neutron star systems were chosen to have spin values in the range  $a \in (0, 0.05)$ <sup>3</sup>. The BNS mass range was  $(1.0, 3.0) M_\odot$  and the mass range for NSBH was  $(3.0, 15.0) M_\odot$ . We further injected 1000 more signals each of BNS and NSBH types that were weaker (injected at a distance of 20 to 40 megaparsecs), and highly spinning (NS Kerr parameter ranging from 0.3 to 0.4 and BH Kerr parameter ranging from 0.9 to

<sup>2</sup>Currently only spin aligned template bank is available (Brown et al. (2012))

<sup>3</sup>Ref. Brown et al. (2012) explains the rationale behind choosing this range of spin for the neutron stars.

0.98). Fig. 5.9 shows that the coherent  $\chi^2$  values becomes smaller upon using the spin aligned template banks. The black crosses in Fig. 5.9 are the background triggers, and the red pluses are the found injections. For a given coherent SNR, we see more injection triggers are to be found with higher (i.e., worse) coherent  $\chi^2$  values when the search is conducted with the inaccurate non-spinning templates.

However, note that the background information available in the Fig. 5.9 which is shown by the black crosses in Fig. 5.9 does not help us to draw much inference about the search. The  $\chi^2$  distribution for the background in the above cases does not look very different than what we expect in a Gaussian noise. To help our understanding about the performance of the  $\chi^2$  test we increased the background information by incorporating additional off-source time in our analysis. To understand how we did that, it will be helpful if we understand how the background estimation is done for a gravitational wave search from progenitors of short GRBs. Conventional search pipeline performing blind search uses time slides to estimate the background. However, the GRB triggered search uses the GRB trigger time as a prior information for gravitational wave search from the GRB progenitors. As a result the background is estimated by looking away from the 6 seconds onsource window around the GRB trigger time Ref. Abadie and et. al (2012a). These are called *offsource* times, which are also 6 seconds long. A total of 340 such offsource times are analyzed. Admittedly, this is a relatively small duration to correctly estimate the background and is reflected in the  $\chi^2$  plots in Fig. 5.9. To address this issue, we looked at times that are a sidereal day away from the GRB time and conducted a similar offsource study there. We call these *additional search* times. By choosing the time a sidereal day away from the actual GRB time we make sure that in our search we are keeping the RA and dec values same. This method is illustrated in the flowchart in Fig. 5.10.

The result of incorporating the additional time in our analysis can be seen in Fig. 5.11. The non Gaussian tail is evident in the plots. The green contours are the contours of constant values of the statistic, called the new-SNR, which is formed by combining the coherent SNR

and the coherent  $\chi^2$  values. The blue curve is the new-SNR contour for detection at zero false alarm probability. The new-SNR is defined in Ref. Harry and Fairhurst (2011) as follows,

$$\rho_{\text{new}} = \begin{cases} \frac{\rho}{\left[ \left( 1 + \left( \frac{\chi^2}{\chi_{\text{dof}}^2} \right)^{4/3} \right) / 2 \right]^{1/4}}, & \text{if } \chi^2 > \chi_{\text{dof}}^2, \\ \rho, & \text{if } \chi^2 \leq \chi_{\text{dof}}^2, \end{cases} \quad (5.24)$$

where  $\rho$  is the coherent SNR, and  $\chi_{\text{dof}}^2$  is the  $\chi^2$  degrees of freedom. The coherent  $\chi^2$  is defined also in Ref. Harry and Fairhurst (2011) as follows,

$$\chi^2 = N \sum_{i=1}^N \sum_{\mu=1}^4 \left( \rho_{\mu}^i - \frac{\rho_{\mu}}{N} \right)^2, \quad (5.25)$$

where  $N$  is the total number of frequency bins,  $\rho_{\mu}$  is obtained by filtering the data with the  $\mu$ th polarization component of the complex waveform given in Eq. 3.50 and  $\rho_{\mu}^i$  is the same evaluated in the  $i$ th bin.

We did the same study for NSBH systems, as shown in Fig. 5.12. Here we note that the background is slightly worse than in the BNS case. The performance of the  $\chi^2$ -test here is lower than the performance in BNS systems most likely because NSBH systems are more massive than BNS systems. Eq. (5.20) shows that the chirp time of a signal decreases with increasing total mass, all else being unchanged. Thus the waveforms of a typical NSBH system has less number of cycle than a BNS system. The  $\chi^2$ -test is performed by dividing the template into  $\chi_{\text{dof}}^2$  equal power bins of frequency and comparing the template power in each bin for a particular signal Ref. Allen (2005). Because of the reduction of the number of cycle in the waveforms, the bin boundaries are smaller for NSBH systems, thus we are unable to reproduce the right expected power in each bin for a given signal as reliably as in the BNS case. This reduces the discriminant power of the test somewhat and that is being reflected in the plots of NSBH system throughout this study.

One thing we note from these two sets of studies is that the green contours of new-NR in

both the cases are not excluding the background triggers efficiently. As a result one needs to define a zero false alarm probability (FAP) blue contour (remember the blue contours are just one of the green contours, whose value of new-SNR, when chosen as threshold, gives detection at zero FAP) that rejects some of the signals. This is more evident when we did this study for the set of weaker injections, the results of which we present in Fig. 5.14.

This choice of statistic is not allowing us to detect many triggers at zero FAP. In the absence of the additional background information it was not possible to recover this, since the choice of new-SNR was primarily based on the limited background information. One should keep in mind though, that the new-SNR is not used as the detection statistic for the GRB trigger search. The detection statistic is obtained after employing cuts, based on null stream (Bose et al. (2011); Harry and Fairhurst (2011)) and single detector SNR values, on the new-SNR. However, in this study we wanted to see the performance of the new\_SNR that depends only on the coherent  $\chi^2$  and coherent SNR. Here we observed that there is room for improvement in the new-SNR itself and those cuts can be further made to improve the final detection statistics. We tested with a modified statistics which we call here test-stat,

$$\rho_{\text{new}} = \begin{cases} \frac{\rho}{\left[ \left( 1 + \left( \frac{\chi^2}{\chi_{\text{dof}}^2} \right)^{15/8} \right) / 2 \right]^{1/4}} & \text{if } \chi^2 > \chi_{\text{dof}}^2 \\ \rho & \text{if } \chi^2 \leq \chi_{\text{dof}}^2 \end{cases} \quad (5.26)$$

Using this statistic we observe an improvement in performance as shown in Fig. 5.16.

Note, however that there is nothing sacrosanct about this choice of the statistics, except that it is based on emperical search. All we did was to look for constant statistic contours that maximize the number of injections that we recover at zero FAP. In a different data set or for other regions of the signal parameter space, some other statistic might perform better than test-stat. However, this study does give us the clue that there is room for improvement in the choice of the statistics that are presently being used for GRB triggered search.

### 5.4.1 Detection efficiency

To study the effect of signal - template mismatch on detection we compared the detection efficiency between the searches using spin-aligned and non-spinning template banks. Firstly, a total of 1000 spin-aligned waveforms were injected in initial LIGO noise psd and then searched for using spin-aligned template bank. The result of this study constituted the case where there is no mismatch between signal and template and thus the exact waveform vector,  $\mathbf{h}_E(\theta_{tr})$  is in the same manifold as the approximate waveform vector  $\mathbf{h}_A(\theta_{bf})$ . Note that the best fit parameters would, in general still turn out to be different from the true parameters due to the statistical contribution to the parameter estimation error given in Eq. (5.15). Next we searched for the same target waveforms using a non-spinning template bank. This time the exact waveform vector,  $\mathbf{h}_E(\theta_{tr})$ , is not in the same manifold as the approximate waveform vector  $\mathbf{h}_A(\theta_{bf})$ . And thus the parameter estimation error will have both statistical and systematic contribution. We show the error in measuring the component masses of these injections in Fig. 5.17.

To study the effect further, we did the same analysis for 1000 weaker injections too. While only 847 out of those injections with non-spinning templates, and 937 were found with the spin-aligned templates.

From the results in Fig. 5.18, we note that the spin-aligned search is able to detect more sources than the search conducted using non-spinning templates. This brings us to detection efficiency, which is defined as follows,

$$\text{Detection efficiency at a given source distance } r = \frac{\text{No. of sources found at distance } r \text{ with a detection statistic } > \text{ loudest background}}{\text{Total number of sources injected at the distance } r}, \quad (5.27)$$

where the loudness of the trigger is defined as the value of the search statistic for that trigger. We present the detection efficiency of these injections in Fig. 5.19. Note that in the BNS case the search based on non-spinning template bank performs consistently worse

than the search conducted with the spin-aligned templates. This is the direct consequence of waveform inaccuracy hampering detection. In the NSBH case the improvement is not that remarkable because the detection statistic used for the detection efficiency study was new-SNR which caused non detection of a lot of sources at zero FAP, as shown in Fig. 5.14.

For the weak injections too we studied the detection efficiency as a function of distance. In the BNS case not a single injection trigger was found with a new-SNR louder than the loudest background. Thus, the detection efficiency in every distance bin became trivially zero. The detection efficiency of NSBH injections is shown in Fig. 5.20.

In order to explore the effect of our detection statistic and  $\chi^2$  statistic for the NSBH search, where the detection efficiency proved inconclusive, we studied the receiver operator characteristic (ROC) plots for the old and the new statistics for searches conducted by both spin-aligned and non-spinning templates. The study of weaker injections is the more interesting one, as we see a marked improvement on switching from new-SNR to test-stat for this case; (see the lower panel in Fig. 5.16 where we see that the test-stat is able to recover more injections than the new-SNR). This is presented in Fig. 5.21 using the ROC curves. Note that the detection probability at the low false alarm probability region is of scientific interest here. At the low FAP region, we see a slight improvement in performance when the accurate templates (red curves) are used instead of the inaccurate non-spinning ones (blue curves). This is reassuring and the effect of signal - template mismatch is manifestly expressed through this plot. However, further improvement is obtained by using the test-stat (solid curves) in the detection probability. Both the spin-aligned and the non-spinning searches is benefited from the use of this modified statistics. As we have discussed before, this modified statistics is not something sacrosanct. This just goes to show that there can be improvements made by incorporating the power of  $\chi^2$  values properly. It is evident that we are not currently making optimum use of the  $\chi^2$  values in constructing the GRB triggered search detection statistics.

## 5.5 Discussion

In the era of multi-messenger astronomy parameter estimation of gravitational waves will be extremely important. Gravitational wave parameters such as masses will determine the length of the chirps. Using detectors at multiple sites, one can construct time delays and with detectors at three or more sites it will be possible to locate the sources in the sky. Since matched filtering requires knowing the family of waveforms *a priori*, a lot of premium is placed on the knowledge of accurate waveforms. Already enormous strides have been made to that end and now, thanks to numerical relativity and analytical work in post-newtonian theory and blackhole perturbation, we have full inspiral-merger-ringdown waveforms. However, these templates are available only for mass ratio less than 10. Thus we still lack a complete CBC template bank with IMR signals. Moreover we also lack a full fledged spinning search, which is essential for detecting gravitational wave counterpart of GRBs. Thus waveforms used in search so far are still susceptible to maladies of waveform inaccuracies. We studied the effect of waveform inaccuracy in parameter estimation and detection. Our numerical results show that the fitting factor can be as low as 60% even for a BBH with  $m_1 = 13M_\odot$  and  $m_2 = 20M_\odot$ . Also, the estimated total-mass for the same pair can be off by as much as 20%. Both of these estimates get worse for some higher-mass combinations. Even the estimation of  $\eta$  suffers a nearly 20% error for this example, and can be worse than 50% for the mass ranges studied here.

We also studied the effect of waveform inaccuracy in detection of signal. We presented the study conducted in analyzing the performance of spin aligned template banks in detecting these signals. As templates we used the non-spinning templates, thus making the search templates inaccurate to the signals that we are searching for. Upon using spin aligned templates to search for spin aligned injections, we observed considerable improvement in detection efficiency. This improvement is owing to the fact that SNR of found injections were reduced due to use of non-spinning templates and also due to the fact that  $\chi^2$  values worsened with signal-template mismatch. Incorporating additional time for more accurate estimation

of the background helped in testing with modified statistics. In our studies we observed the existence of modifications to the “cuts” which tend to remove most of the loudest background triggers. There is room for improvement and tuning of the currently used new-SNR statistics that can help us detect more injections. Receiver operating characteristic curves aided us in comparing performance between use of spinning and non spinning template banks. It also helped us in comparing the performance between existing and modified statistics. In BNS search we observed improvement upon using spinning templates. In NSBH systems detection probability was improved when we employed modified statistics in conjunction with spinning template banks.

Both the sets of studies confirms that accurate waveform modelling is extremely important for both parameter estimation and detection. Fisher information matrix study has revealed that the error in one parameter can affect the error in some of other parameters, specifically there exists error covariance between total mass and symmetric mass ratio, which might be tolerable as far as gravitational wave detection is concerned. However, for electromagnetic follow-up studies, such as the hunt for orphaned afterglows, which will use gravitational wave parameter estimates as priors, such errors can have adverse impact. Gravitational wave detection itself may also be jeopardised if there is too much mismatch between signal and template, an example of which we saw in our study of spin-aligned signal search. Understandably huge emphasis is thus given to waveform modelling and numerical solutions. As faster algorithms of numerical relativity are being developed and as computational power increases, one expects to have better prospects in multi-messenger astronomy in the near future.

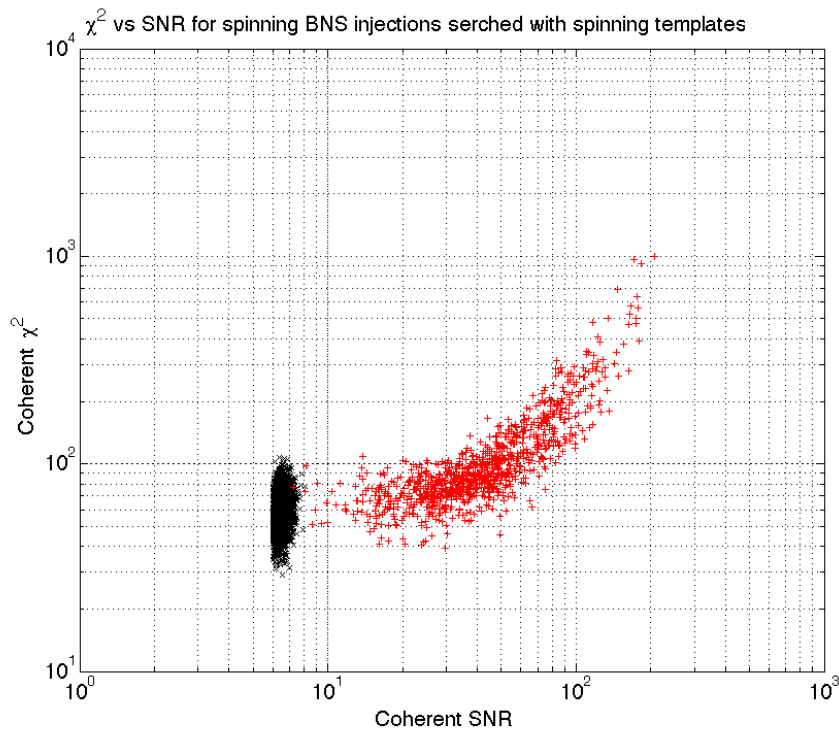
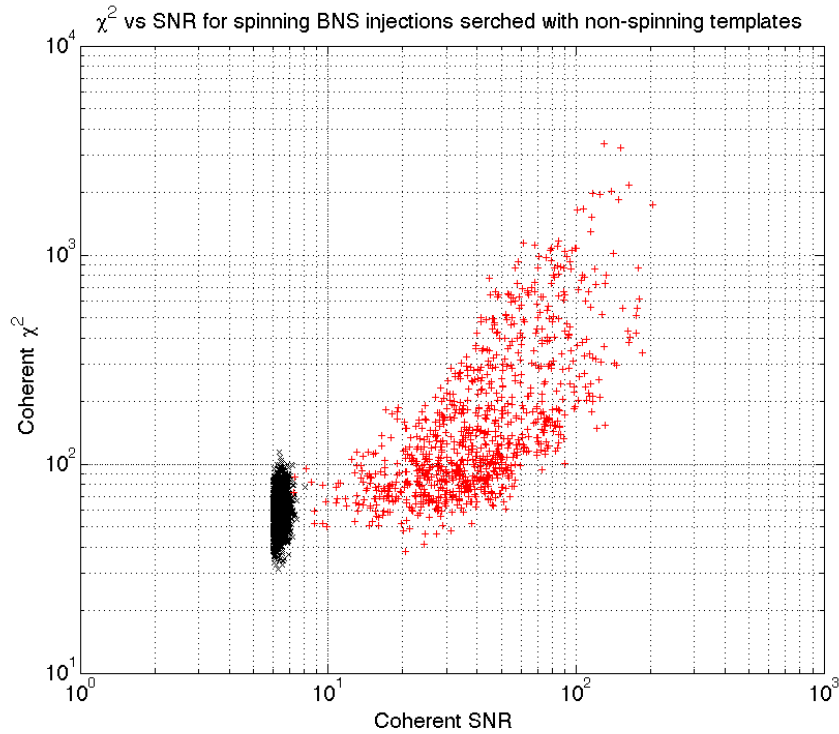


Figure 5.9: Coherent  $\chi^2$  vs coherent SNR plots comparing the spinning and the non-spinning template searches. The black crosses are the background triggers, and the red pluses are the found injection triggers. Both the studies were done on the same set of spin aligned BNS sources. Performance of the non-spinning templates suffers due to the waveform mismatch between them and the injection.

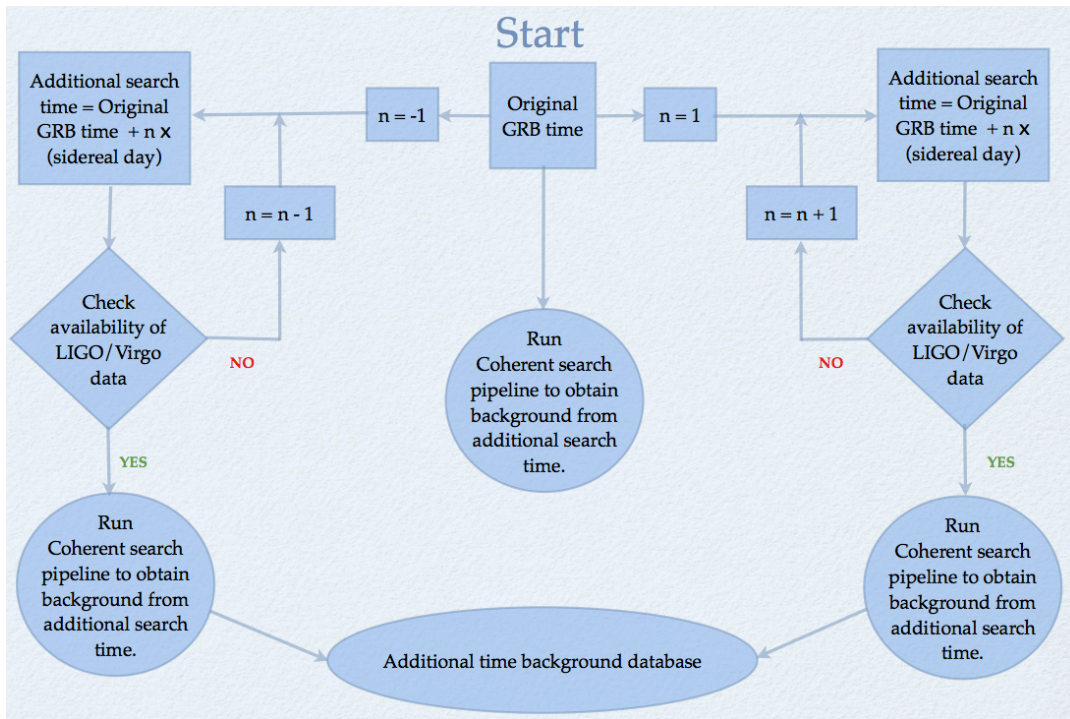


Figure 5.10: Flowchart depicting the method of increasing analysis time for better estimate of the background. Above,  $n$  is an integer.

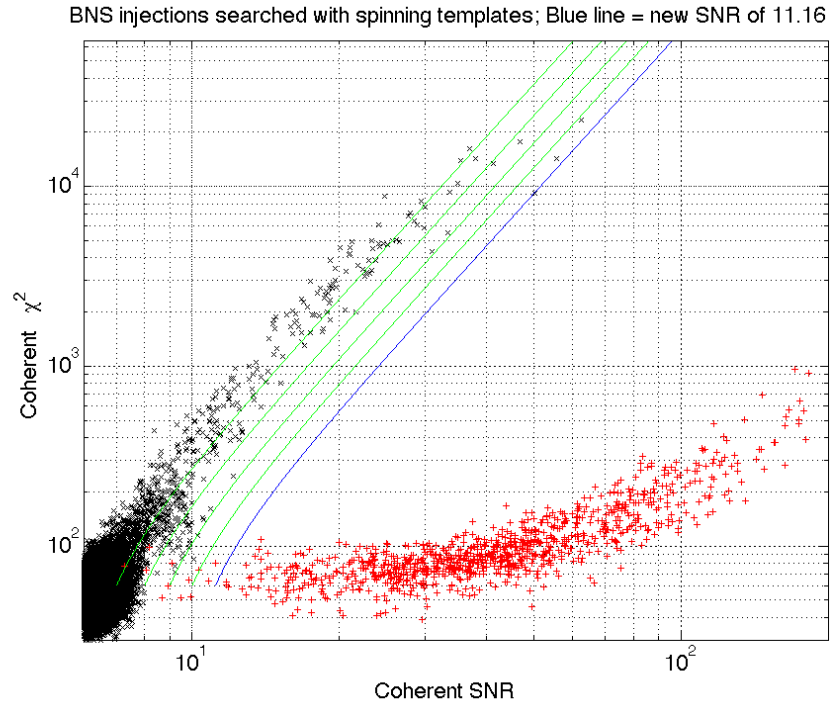
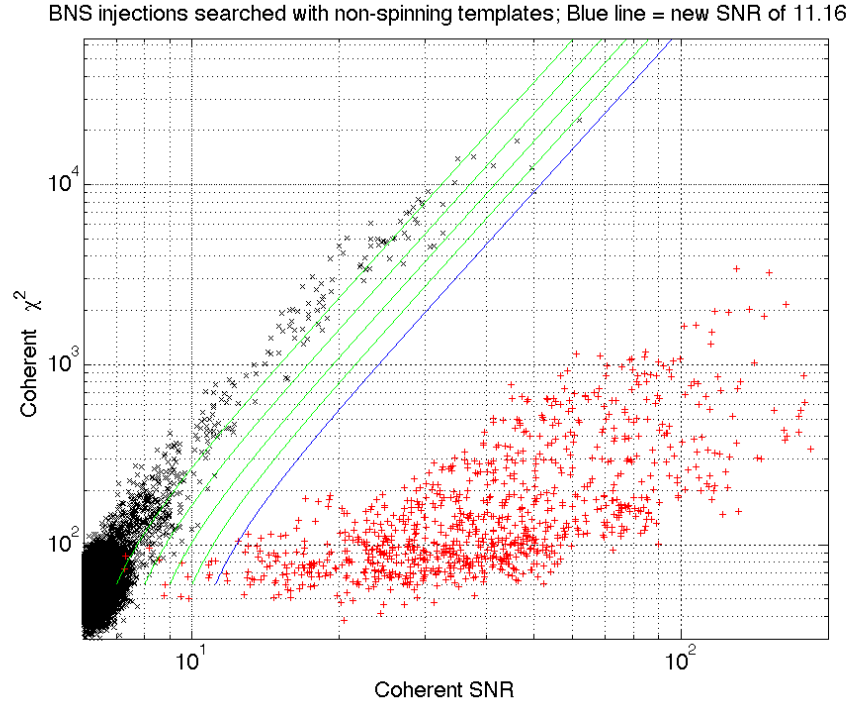
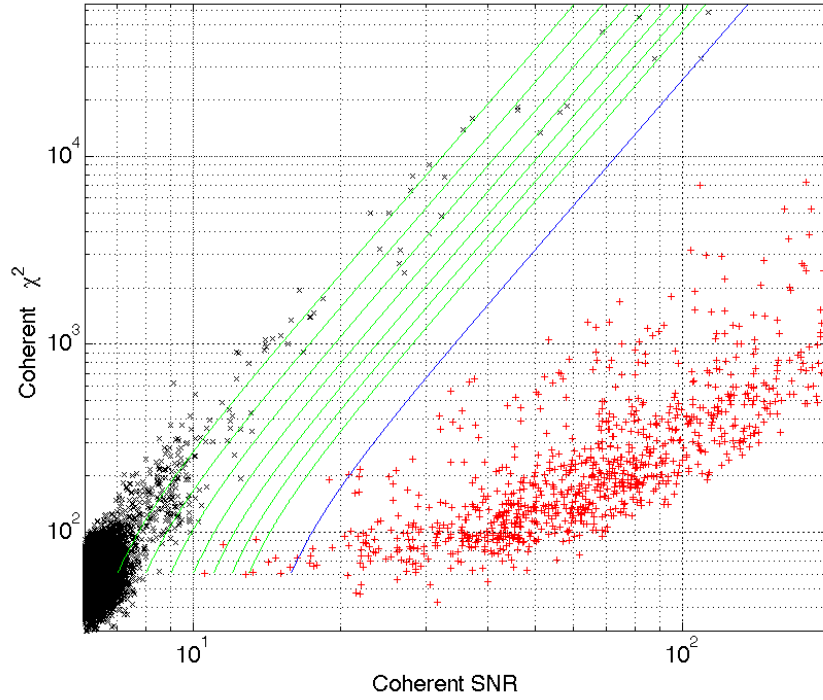


Figure 5.11: Coherent  $\chi^2$  vs coherent SNR plots for spinning BNS injections that were searched with non-spinning templates(left plot) and spinning templates (right plot). The background was estimated using the additional time technique illustrated in Fig. 5.10.

NSBH injections searched with non-spinning templates; Blue line = new SNR of 15.85



NSBH injections searched with spinning templates; Blue line = new SNR of 23.29

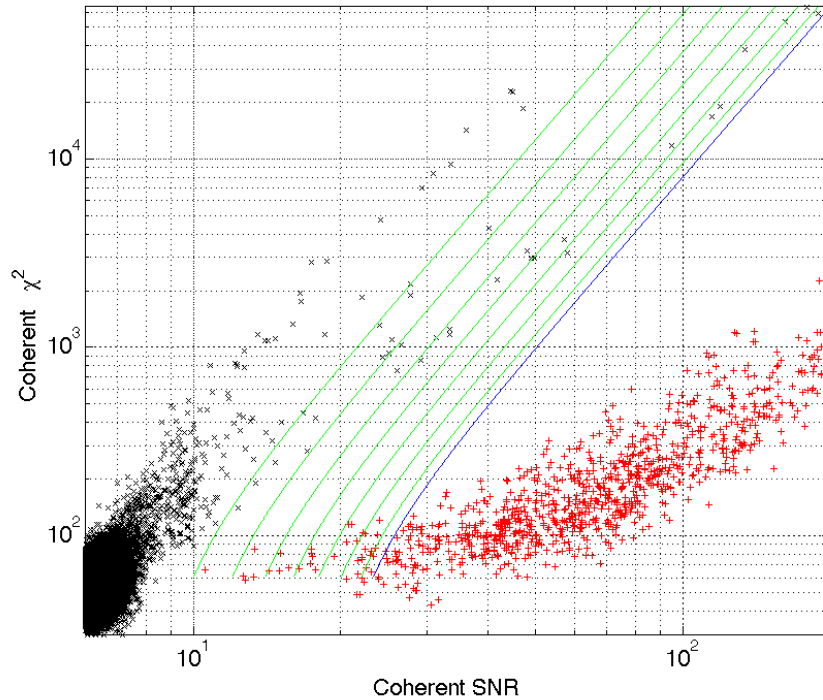
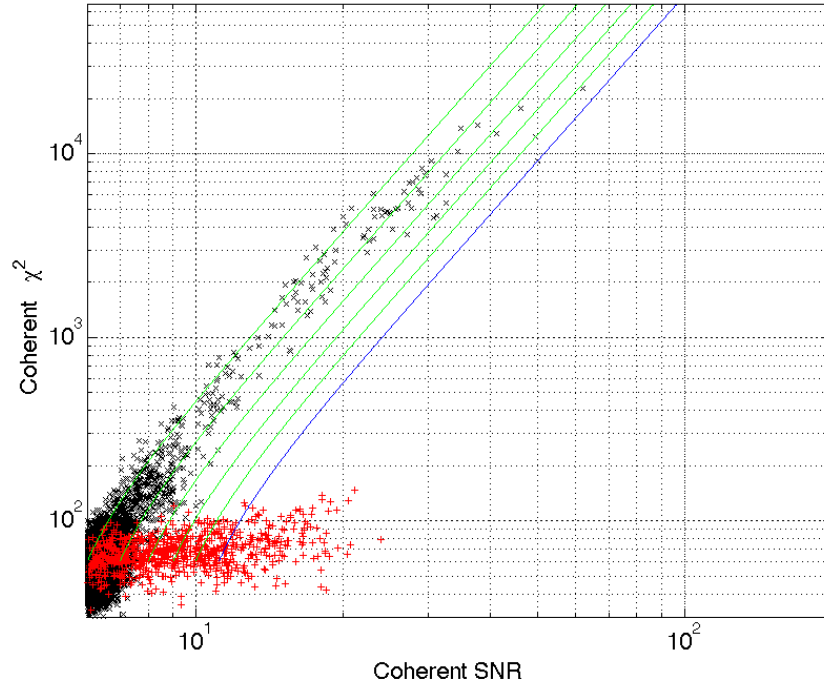


Figure 5.12: Coherent  $\chi^2$  vs coherent SNR plots for spinning NSBH injections that were searched with non-spinning templates (Left) and spinning templates (Right). Background was estimated using the additional time technique illustrated in Fig. 5.10.

Weak BNS injections searched with non-spinning templates; Blue line = new SNR of 11.16



Weak BNS injections searched with spinning templates; Blue line = new SNR of 11.16

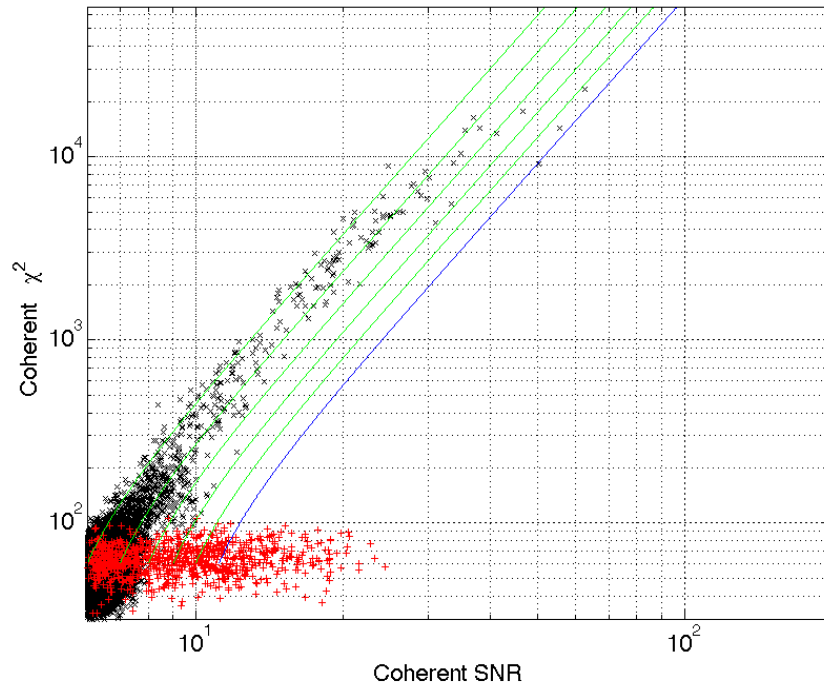
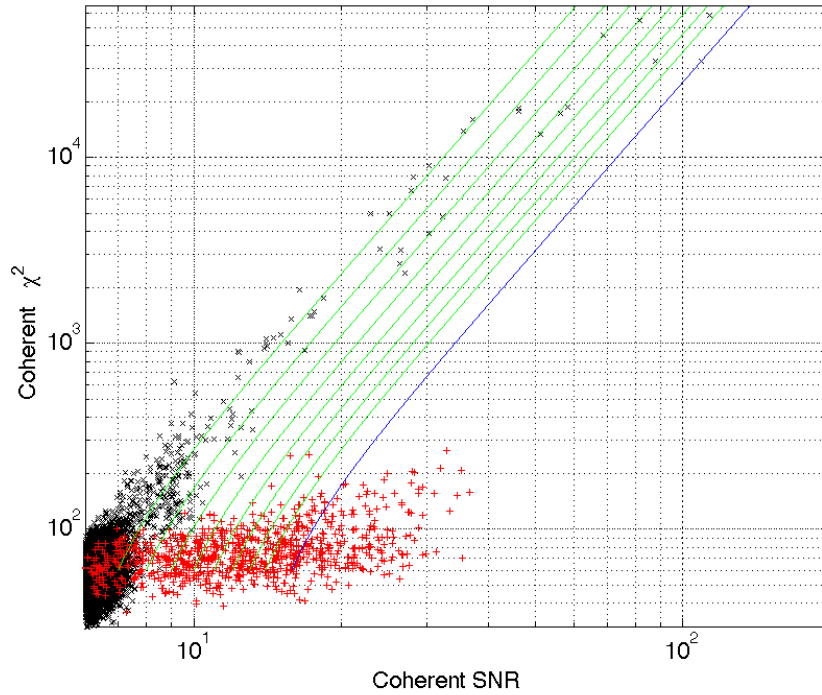


Figure 5.13: Coherent  $\chi^2$  vs coherent SNR plots for weak spinning BNS (top panel) injections that were searched with non-spinning templates (Left) and spinning templates (Right). Note the blue contours of zero-FAP new\_SNR contour in all the four cases misses out majority of the injections.

Weak NSBH injections searched with non-spinning templates; Blue line = new SNR of 15.85



Weak NSBH injections searched with spinning templates; Blue line = new SNR of 23.29

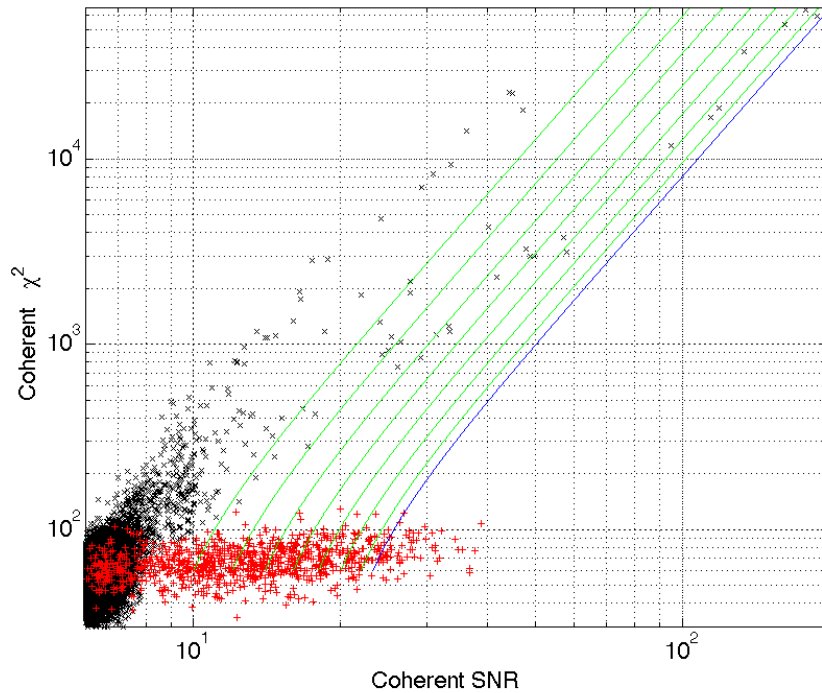


Figure 5.14: Coherent  $\chi^2$  vs coherent SNR plots for weak spinning NSBH (bottom panel) injections that were searched with non-spinning templates (Left) and spinning templates (Right). Note the blue contours of zero-FAP new\_SNR contour in all the four cases misses out majority of the injections.

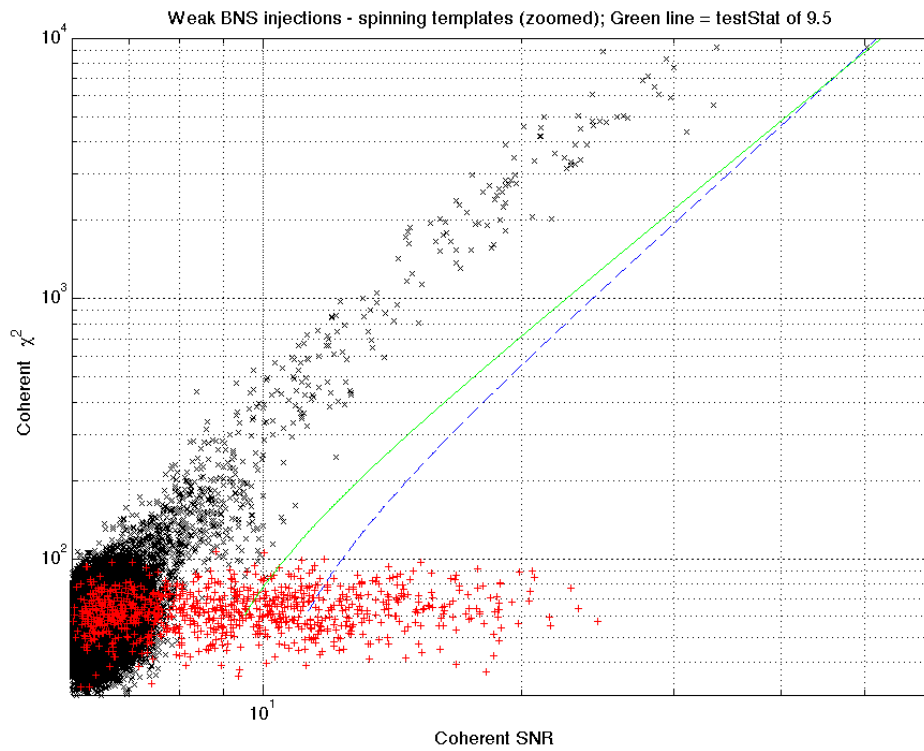
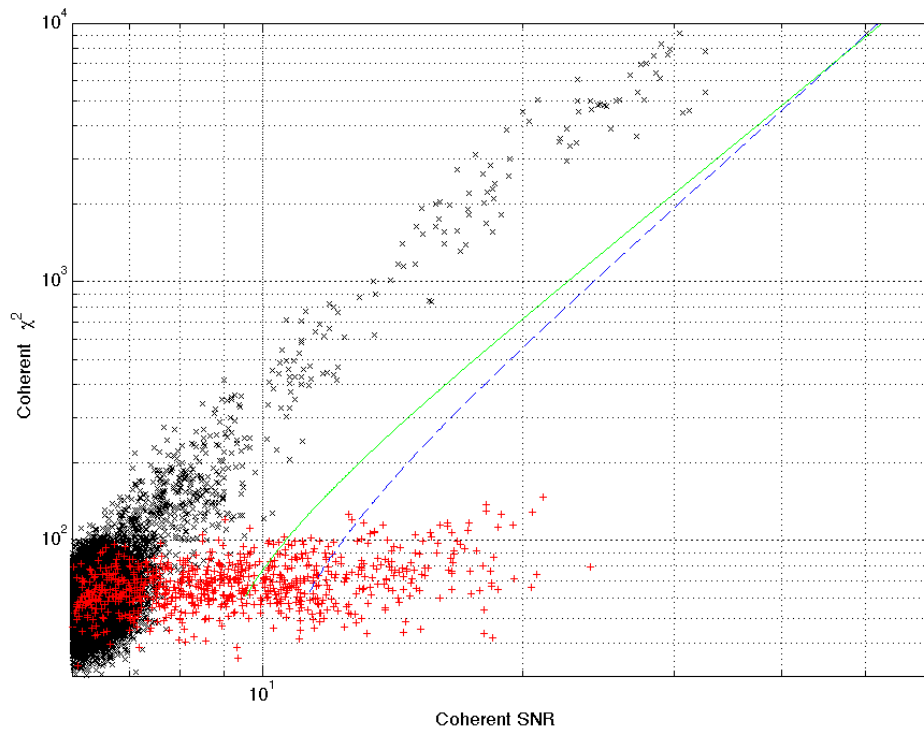


Figure 5.15: Comparison of test\_stat (green contour) with new\_SNR (blue dashed contour) for BNS injections. We note that the test\_stat in these cases are performing better in finding signals with zero FAP.

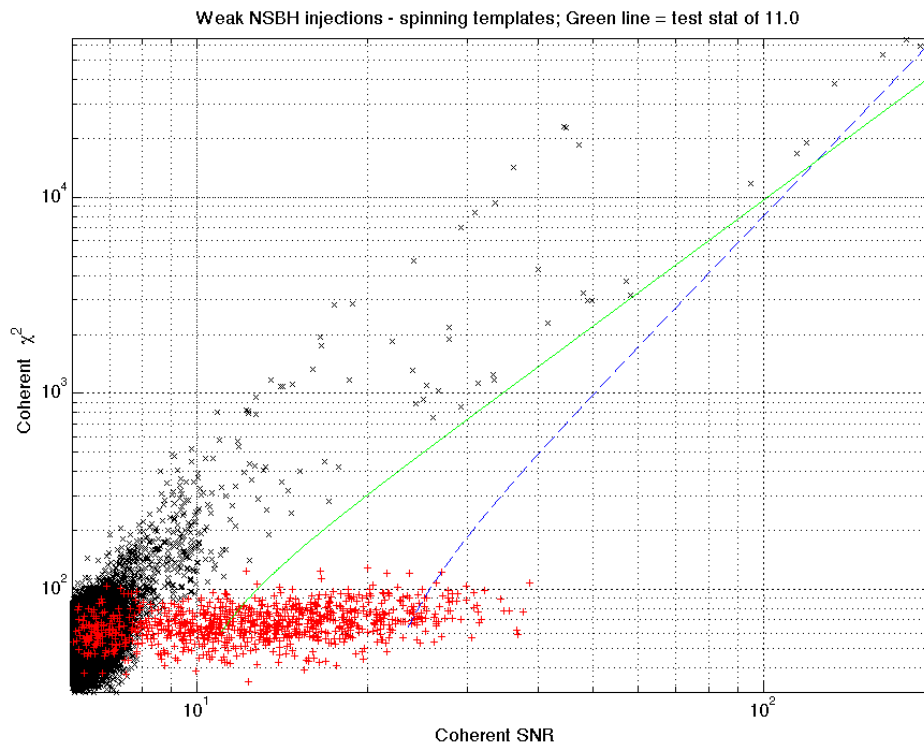
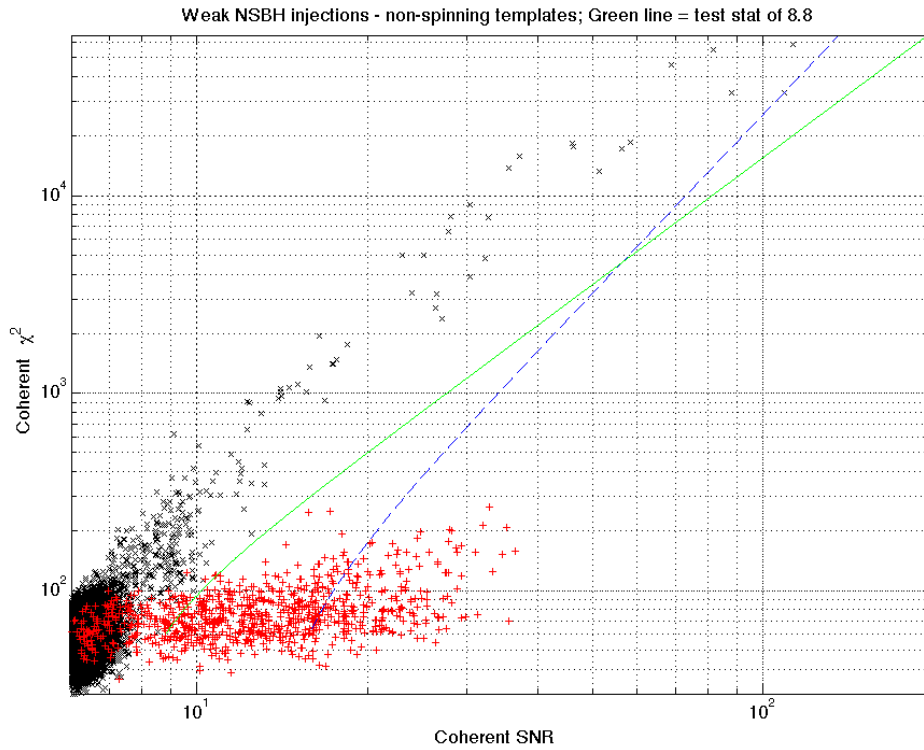


Figure 5.16: Comparison of test-stat (green contour) with new-NR (blue dashed contour) for NSBH injections. We note that the test\_stat in these cases performing better in finding signals with zero FAP.

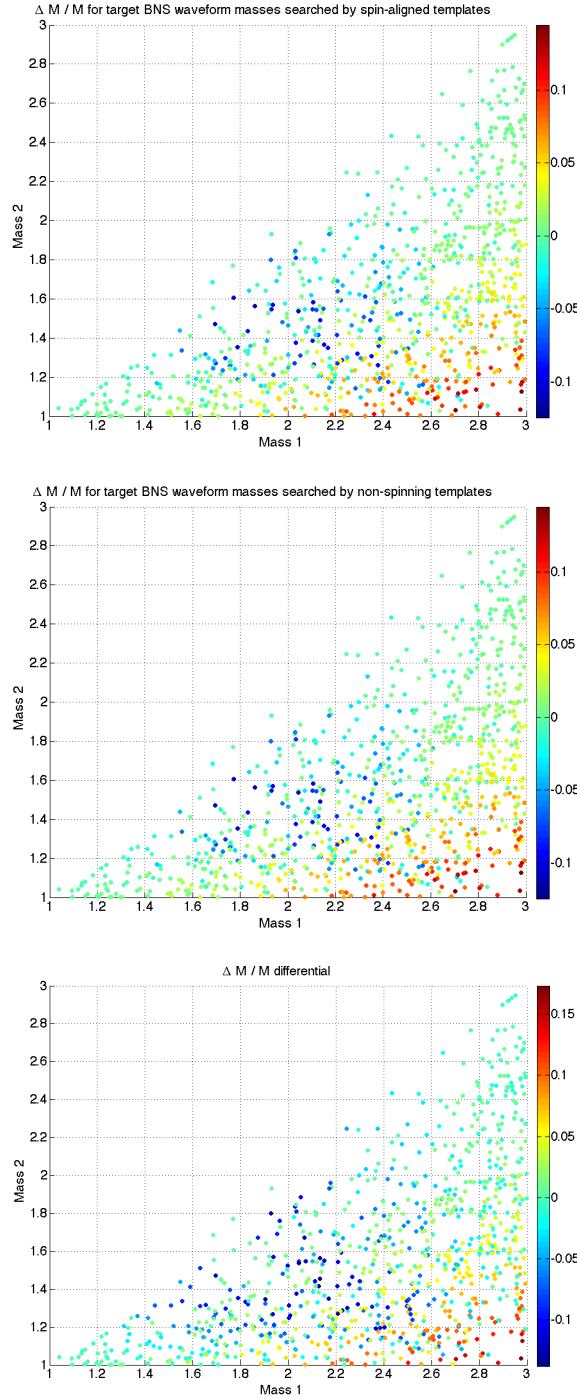


Figure 5.17: The fractional error in estimation of total mass is plotted in the top panel. The one on the top left was obtained when the templates used were spin-aligned and hence the search is devoid of systematic error, the one on the top right was obtained in a search where non-spinning templates were used and therefore, suffers from systematic effect of waveform inaccuracies. The differences are so minute that they are not reflected in the plot colors, so in the lower panel we show the differential of these two sets of errors (error for spin-aligned templates - error for non-spinning templates).

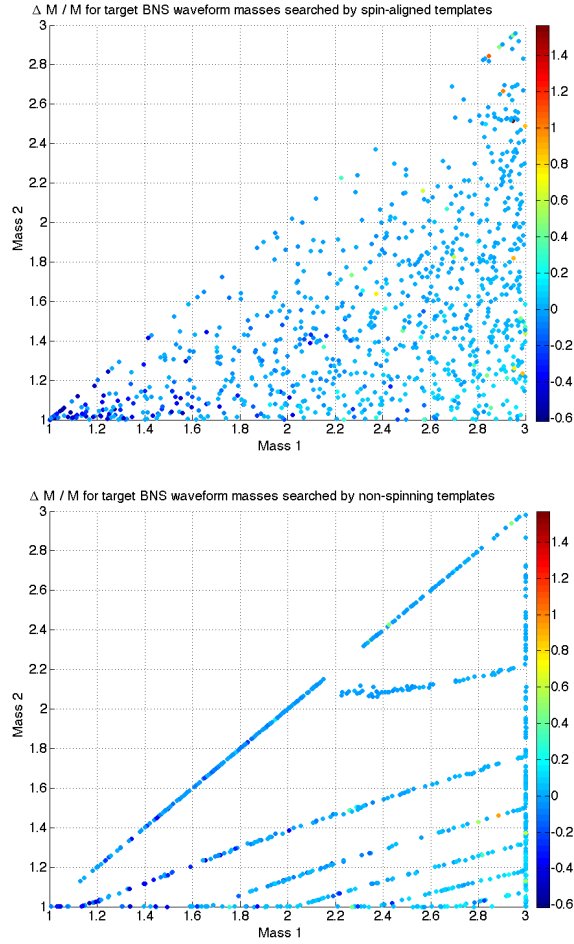


Figure 5.18: The fractional error in estimation of total mass is plotted for weaker BNS injections. The one on the top left was obtained when the templates used were spin-aligned, the one on the right was obtained in a search where non-spinning templates were used. Note that in the later search there was substantial loss of detection. The title of the plots define the color bars.

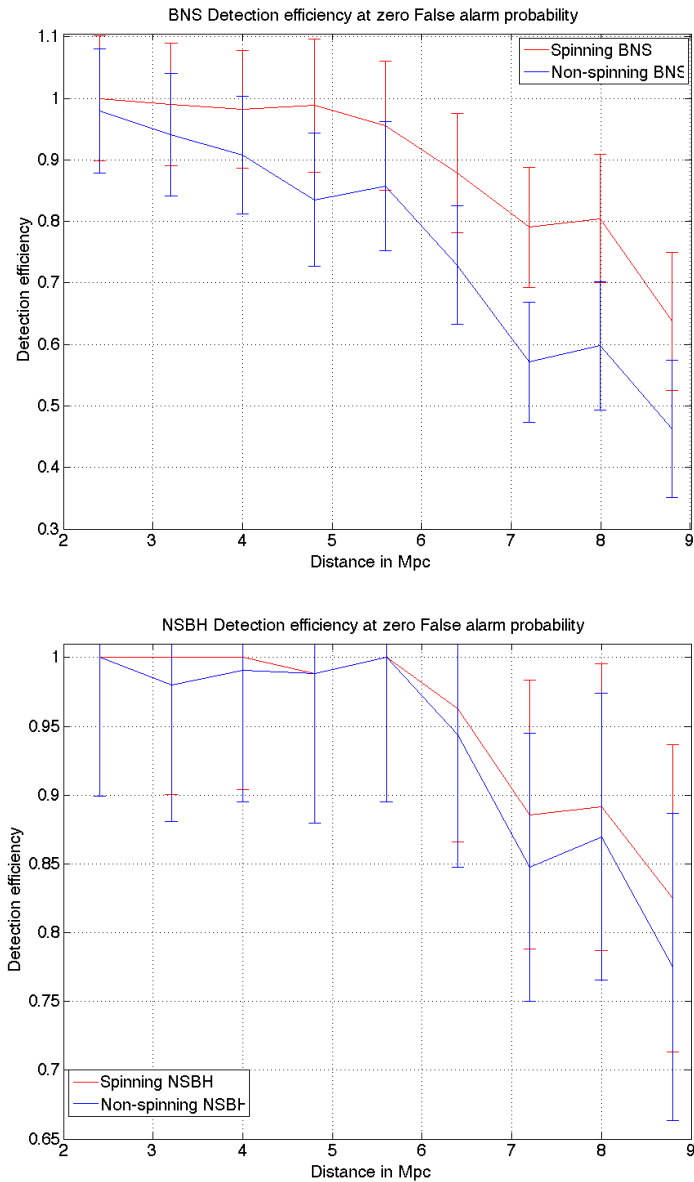


Figure 5.19: Detection efficiency curves for BNS and NSBH sources. Note that in the BNS case the search based on non-spinning template bank performed consistently worse than the search with spin-aligned templates. This is the direct consequence of waveform inaccuracy hurt detectability. In the NSBH case the improvement is not that remarkable because the detection statistics used here is new-SNR which was losing a lot sources as shown in Fig. 5.14.

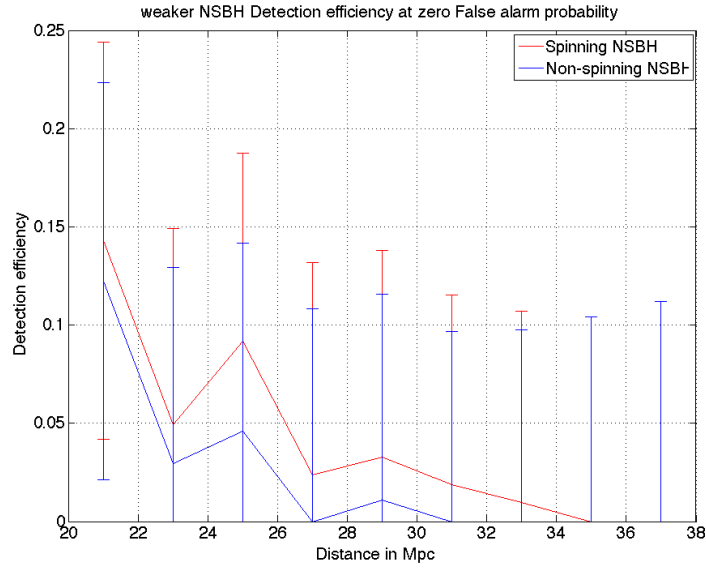


Figure 5.20: Detection efficiency curves for NSBH sources. Here we show the detection efficiency plots for the weaker NSBH sources. Same study for weaker BNS sources gave detection efficiency at all distance bins to be zero as no found injections were louder than the loudest background from that study

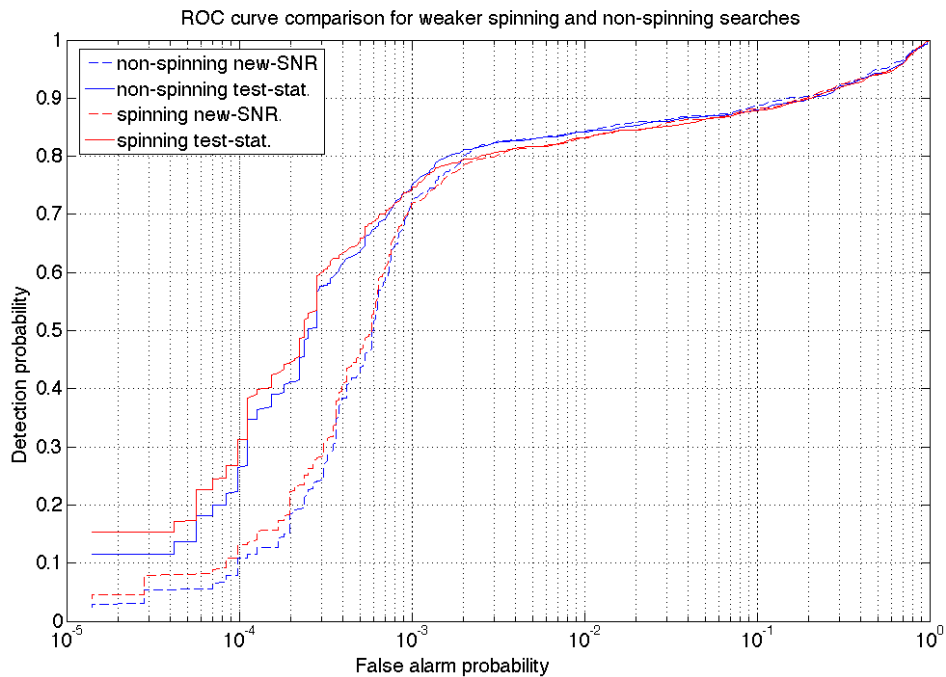


Figure 5.21: ROC curves for weak NSBH systems with high spin, searched with spinning templates (red curves) and non-spinning templates (blue curves). Dashed curves indicate ROC curves with plotted with new-SNR as detection statistic, while solid curves indicate the ROC curves plotted with test-stat as detection statistic.

# Chapter 6

## Conclusion

Compact binary coalescences are among the best suited candidates for the first detection of gravitational waves. Theoretical knowledge of their waveform aids us in the detection of GW from these sources using matched filtering algorithms. Progenitors of short gamma ray bursts are widely considered to be CBC sources with at least one neutron star as a binary component (CBCNS). However there are other competing models for these events. This makes the detection of gravitational waves from such systems an extremely interesting astrophysical problem. A direct detection of gravitational waves in coincidence with electromagnetic detection of a GRB will give the strongest evidence of CBCNS progenitor model for a short GRB. In this thesis we discussed the various avenues of improving detectability of gravitational waves from such systems.

We proposed a new strategy for searching of SGRB progenitors in the sky by constructing patches around the GRB-alert sky positions. We demonstrated that this can improve detection efficiency of the search. We also showed this method is especially useful

- When dealing with sources that are poorly localized (by the GRB observatories) in the sky. For example, GW search from GRBs discovered by the IPN.
- Template waveforms that we use are not accurate. For example, if we are using non-spinning templates to search for spinning astrophysical signals.

We also performed a spin-aligned template search for short GRB progenitors. This is the first time such kind of study is performed in the collaboration and the results we obtained showed as much as  $\sim 40\%$  improvement in detection efficiency.

However, there is scope for a lot of future work to be done. We have established a correlation between error of chirp mass estimation and sky position estimation. This led us into the construction of the sky-patch mode that mitigates the loss of the detection efficiency arising from this error covariance. However, we also observed from our study that there exist correlations between the systematic error in spin and sky position, which we have not explored in much great details. We have studied how much of improvement one obtains when one uses a patch in the sky while using non-spinning templates to search for spinning signal. However, a rigorous study of this effect may allow us to put some bounds on the size of the sky-patch, such that a patch bigger than the sky-patch upper bound will hurt us from increased false alarm probability, and smaller than the sky-patch lower bound will underperform due to parameter error covariance.

Furthermore, we have only explored the search of spin-aligned sources using spin-aligned templates. There is also the scope of studying the effect of using spin-aligned templates to search for gravitational waves from arbitrarily spinning sources. We would like to study the effect of introducing a systematic error in the spin alignment between the injections and the templates. We can analyze the effect of this systematic error on the detection efficiency and chirp mass determination for different values of the offset between the spin axes. Then perform the same study with varying sky patch sizes to empirically understand any relationship that exists between the size of the patch and the systematic error of the spin axis alignment between the templates and the injections. This will enrich our understanding of the parameter error covariance between the systematic error of spin and sky position.

Other than SGRB, we have also discussed about the prospects of using orphaned SGRB afterglows as external triggers. We have only laid down the mathematical foundation of this work in this thesis. We still do not have a pipeline to actually do such a study. In an

orphaned afterglow the time of the prompt emission is not known accurately. For an X-ray afterglow the prompt emission could be hours before the observation of the afterglow. This uncertainty in time could be from days to even of the order of a week for optical afterglows. Thus we need to develop a pipeline that will search at a particular point on the sky (or a sky-patch), but will look back from the afterglow trigger time by about a day (for an X-ray afterglow) to about a week (for an optical afterglow). This will require some modification in the present external trigger pipeline. However some of these new features that we would require have already been developed in our blind hierarchical search pipeline.

# Appendix A

## A brief discussion of Einstein's General relativity

The contents in this appendix are prerequisites for understanding the physics of gravitational waves that a general reader might find useful. While there are numerous books on general relativity (GR) but for the purpose of understanding the origins of gravitational waves (GW) it is possible to avoid a detailed understanding of GR. That is why it might be a good idea to give a brief summary of GR here so that a new reader can understand how the various quantities that we presented *ad hoc* in chapter 2, like the metric, Cristoffel symbols and various curvature tensors, come into existence. Large portion of the general relativistic treatments presented here are heavily influenced from books like *Spacetime and Geometry* by Sean M. Carroll and *Gravitation - Foundation and Frontiers* by T. Padmanabhan. Readers interested in the details of the theory of general relativity can refer to these books.

Some knowledge of special relativity has been assumed in the following discussions.

### A.1 Introduction

Our quantitative understanding of dynamics is pertinent upon the ability to describe a system by four numbers. These four numbers uniquely specifies an ordered set which we call the *spacetime coordinates*. However, the specification of these four numbers is a necessary but

not a sufficient condition for describing dynamics. There are two more important requirements for that. Firstly, and arguably the most fundamental of all, is the geometry of the spacetime. The second requirement is the analytical form of external force. Given that one have all the above requirements satisfied, it is possible to predict the time evolution of the system. However, In this discussion we will confine to dynamics of free particles only. Therefore, we will not discuss the second requirement mentioned above. We begin the discussion with measurement of distance between two points.

## A.2 Distance formula in flat space

From Pythagoras theorem we learn how to calculate the distance between two points. If one lays down a coordinate system, this allows us to label each point in the three dimensional space with an ordered set of three numbers. The values of these numbers depend upon the choice of the origin which is labeled as  $(0, 0, 0)$ . Thus one can label two points  $P_1$  and  $P_2$  as  $(x_{P_1}^1, x_{P_1}^2, x_{P_1}^3)$  and  $(x_{P_2}^1, x_{P_2}^2, x_{P_2}^3)$  using this coordinate system. If we define  $x_{P_2}^i - x_{P_1}^i = dx^i$  where,  $(i = 1, 2, 3)$  then one can express the distance  $ds$  between the two points  $P_1$  and  $P_2$  as

$$ds^2 = (dx^1)^2 + (dx^2)^2 + (dx^3)^2 = \sum_{i=1}^3 (dx^i)^2 = dx_i dx^i. \quad (\text{A.1})$$

In Eq. (A.1) we have introduced the Einstein summation convention where repeating indices are summed over. Thus we can define a quantity  $\mathcal{E}_{ij}$  such that

$$ds^2 = \mathcal{E}_{ij} dx^i dx^j. \quad (\text{A.2})$$

The quantity  $\mathcal{E}_{ij}$  we will call the Euclidean metric (in  $3D$ ), is defined as

$$\mathcal{E} = \begin{pmatrix} 1 & 0 & 0 \\ 0 & 1 & 0 \\ 0 & 0 & 1 \end{pmatrix}. \quad (\text{A.3})$$

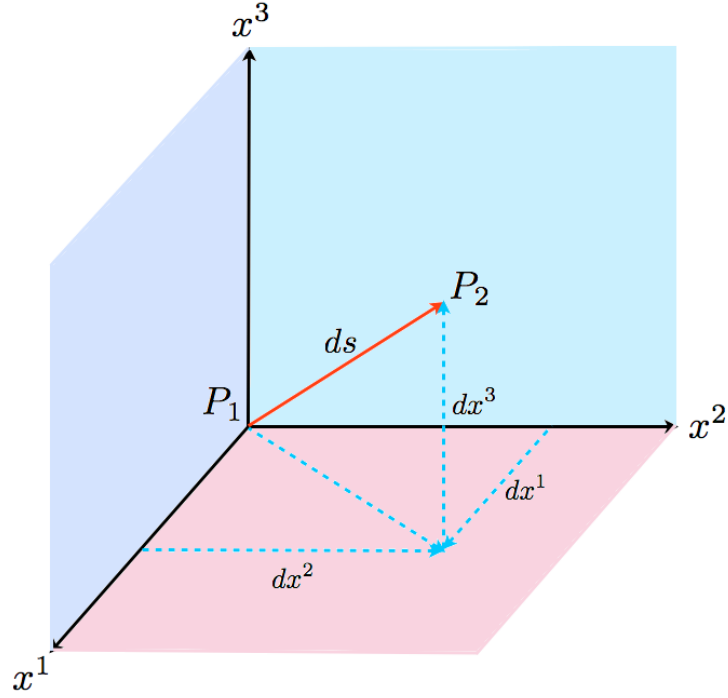


Figure A.1: Distance between two points in three dimensional cartesian coordinate system.

One can transform the coordinate system above to a spherical polar coordinate system using the following transformation equations

$$\begin{aligned}
 x^r &= (x^1)^2 + (x^2)^2 + (x^3)^2, \\
 x^\theta &= \cos^{-1} \left( \frac{x^3}{r} \right), \\
 x^\phi &= \tan^{-1} \left( \frac{x^2}{x^1} \right).
 \end{aligned} \tag{A.4}$$

For the spherical polar coordinate system one write the Euclidean metric as

$$\mathcal{E} = \begin{pmatrix} 1 & 0 & 0 \\ 0 & (x^r)^2 & 0 \\ 0 & 0 & (x^r)^2 \sin^2(x^\theta) \end{pmatrix}. \tag{A.5}$$

One can note that there is coordinate dependence in the metric components. However, we

should keep in mind that we have not changed the geometry of the space itself. We have merely transformed our coordinates and it is this transformation of coordinates that led to this coordinate dependence in the components of the metric.

### A.3 Distance formula in flat spacetime

In special theory of relativity we learned that spacetime interval between two events is an invariant quantity. This quantity is analogous to the distance in the galilean coordinates. We will use the same symbol  $ds$  to denote the spacetime interval

$$ds^2 = -(dx^0)^2 + (dx^1)^2 + (dx^2)^2 + (dx^3)^2, \quad (\text{A.6})$$

where  $x^0 = ct$ . Thus we can write the distance formula again in the condensed form using a metric.

$$\eta = \begin{pmatrix} -1 & 0 & 0 & 0 \\ 0 & 1 & 0 & 0 \\ 0 & 0 & 1 & 0 \\ 0 & 0 & 0 & 1 \end{pmatrix}. \quad (\text{A.7})$$

The quantity  $\eta$ , whose components we will denote as  $\eta_{\mu\nu}$ , is called the Minkowskian metric. Using the Minkowskian metric we can write the distance formula as

$$ds^2 = \eta_{\mu\nu} dx^\mu dx^\nu. \quad (\text{A.8})$$

Since  $ds$  is an invariant quantity, this implies that the proper time  $\tau$ , which is the time elapsed in the frame of the clock, must be given by the following equation

$$d\tau^2 = -\frac{1}{c^2} ds^2 = -\frac{1}{c^2} \eta_{\mu\nu} dx^\mu dx^\nu. \quad (\text{A.9})$$

It would be interesting to see what path a free particle follows in a flat geometry. let us

consider a particle moving from event  $A$  to event  $B$  as shown in the Fig, A.2. The trajectory

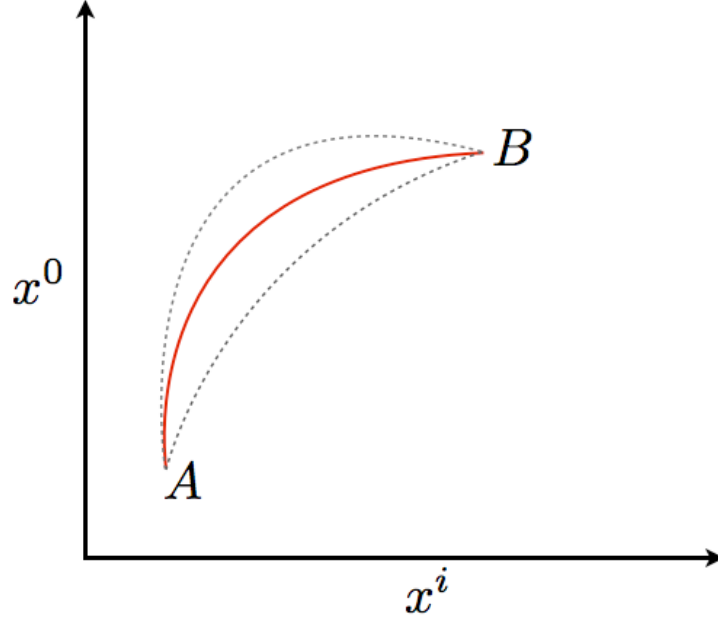


Figure A.2: Path followed by a free particle is given by the path for which the action is an extremum.

the particle follows  $x^\mu(\lambda)$  parametrized by some quantity  $\lambda$  will be given by the path along which a quantity called action will be an extremum. One way to define the action  $S_{AB}$  between paths taken by a particle in going from event  $A$  to event  $B$  is as follows

$$S_{AB} = \int_A^B d\tau = \frac{1}{c} \int_A^B \sqrt{-\eta_{\mu\nu} \frac{dx^\mu}{d\lambda} \frac{dx^\nu}{d\lambda}} d\lambda. \quad (\text{A.10})$$

Comparing the action above with the definition of action in classical mechanics

$$S = \int L(q, \dot{q}, t) dt, \quad (\text{A.11})$$

one can write the Lagrangian of a free particle in flat spacetime as

$$L = L(x^\mu, \dot{x}^\mu, \lambda) = \frac{1}{c} \sqrt{-\eta_{\mu\nu} \frac{dx^\mu}{d\lambda} \frac{dx^\nu}{d\lambda}}. \quad (\text{A.12})$$

One can vary the action in Eq. (A.10) to get the trajectory of the free particle in flat spacetime which is given by the Lagrange's equation of motion

$$\frac{d}{d\lambda} \left( \frac{\partial L(x^\alpha, \dot{x}^\alpha, \lambda)}{\partial \dot{x}^\alpha} \right) - \frac{\partial L(x^\alpha, \dot{x}^\alpha, \lambda)}{\partial x^\alpha} = 0. \quad (\text{A.13})$$

Let us first evaluate the second term in the Lagrange's equation

$$\frac{\partial L(x^\alpha, \dot{x}^\alpha, \lambda)}{\partial x^\alpha} = \frac{\partial}{\partial x^\alpha} \left[ \frac{1}{c} \left( -\eta_{\mu\nu} \frac{dx^\mu}{d\lambda} \frac{dx^\nu}{d\lambda} \right)^{1/2} \right]. \quad (\text{A.14})$$

Note that  $x^\mu$  and  $dx^\mu/d\lambda$  are independent coordinates in the Lagrangian formalism and hence

$$\frac{\partial L(x^\alpha, \dot{x}^\alpha, \lambda)}{\partial x^\alpha} = \frac{1}{2c} \left( -\eta_{\mu\nu} \frac{dx^\mu}{d\lambda} \frac{dx^\nu}{d\lambda} \right)^{-1/2} \left( -\frac{\partial \eta_{\mu\nu}}{\partial x^\alpha} \right) \frac{dx^\mu}{d\lambda} \frac{dx^\nu}{d\lambda} = 0. \quad (\text{A.15})$$

Similarly we calculate the first term in the Lagrange's equation of motion

$$\left( \frac{\partial L(x^\alpha, \dot{x}^\alpha, \lambda)}{\partial \dot{x}^\alpha} \right) = -\frac{1}{2c} \left( -\eta_{\mu\nu} \frac{dx^\mu}{d\lambda} \frac{dx^\nu}{d\lambda} \right)^{-1/2} \left( \eta_{\mu\nu} \delta_\alpha^\mu \frac{dx^\nu}{d\lambda} + \eta_{\mu\nu} \frac{dx^\mu}{d\lambda} \delta_\alpha^\nu \right) = -\frac{1}{c^2} \frac{d\lambda}{d\tau} \eta_{\alpha\mu} \frac{dx^\mu}{d\lambda}, \quad (\text{A.16})$$

where we have used Eq. (A.10) to substitute  $(-\eta_{\mu\nu} \frac{dx^\mu}{d\lambda} \frac{dx^\nu}{d\lambda})^{-1/2}$ . Thus we obtain that

$$\frac{d}{d\lambda} \left( \frac{\partial L(x^\alpha, \dot{x}^\alpha, \lambda)}{\partial \dot{x}^\alpha} \right) = \frac{d}{d\lambda} \left( \eta_{\alpha\mu} \frac{dx^\mu}{d\tau} \right). \quad (\text{A.17})$$

Substituting this back in the Lagrange's equation of motion and multiplying both sides by  $d\lambda/d\tau$  we obtain

$$\frac{d}{d\tau} \left( \eta_{\alpha\mu} \frac{dx^\mu}{d\tau} \right) = \frac{d^2 x^\mu}{d\tau^2} = 0, \quad (\text{A.18})$$

whose solution is given by

$$\boxed{x^\mu = A\tau + B}. \quad (\text{A.19})$$

Thus the trajectory of a free particle in flat spacetime is a straight line. This is also by definition the shortest distance between any two points in the flat spacetime since we extremized

the action to reach to this solution.

## A.4 Distance formula in curved space

We have seen in Eq. A.5 that transformation of coordinates from a cartesian system to a spherical polar system introduces coordinate dependence in the metric components. However, this also implies that one can use a simple transformation to get back the metric in cartesian coordinates. However if the geometry is genuinely curved, then one can not use a transformation of coordinate to convert the metric to a cartesian system. Let us compare the simple cases of the two dimensional polar coordinate and the geometry on the two dimensional surface of a sphere of unit radius.

In the polar coordinate system one can write the distance between two points as

$$ds^2 = dr^2 + r^2 d\theta^2 \tag{A.20}$$

Which explicitly shows coordinate dependence in the metric. However, we can make a coordinate transformation as follows,

$$\begin{aligned} r = \sqrt{x^2 + y^2} &\implies dr = \frac{xdx + ydy}{\sqrt{x^2 + y^2}}, \\ \theta = \tan^{-1} \frac{y}{x} &\implies d\theta = \frac{xdy - ydx}{x^2 + y^2}, \end{aligned} \tag{A.21}$$

Substituting the expressions for  $r$ ,  $dr$  and  $d\theta$  in Eq. A.20 we get back the cartesian distance formula.

$$ds^2 = dx^2 + dy^2 \tag{A.22}$$

Now let us examine the metric on the surface of a sphere. Let us denote a point in this coordinate system by  $(x^\theta, x^\phi)$ . And distance between two points in this coordinate system is given by,

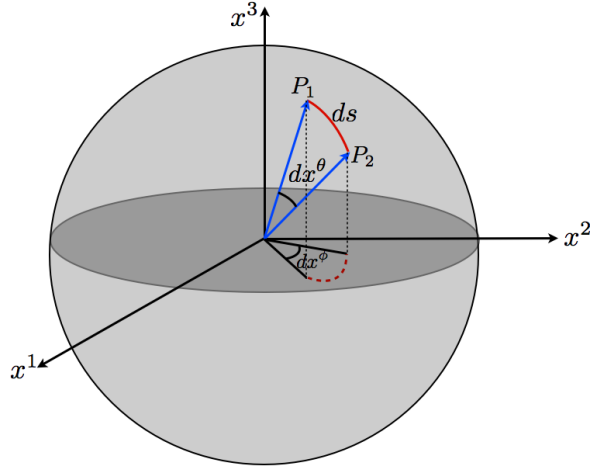


Figure A.3: Distance between two points on the surface of a sphere.

$$ds^2 = (dx^\theta)^2 + \sin^2 x^\theta (dx^\phi)^2 \quad (\text{A.23})$$

Thus the metric  $\mathcal{C}$  on the surface of the sphere can be written as,

$$\mathcal{C} = \begin{pmatrix} 1 & 0 \\ 0 & \sin^2 x^\theta \end{pmatrix}. \quad (\text{A.24})$$

There is no transformation equation, using coordinates alone, that one may use to convert the expression of distance in Eq. A.23 to the one corresponding to a cartesian coordinate system and the coordinate dependence of the metric on the surface of the sphere remains. Thus from the above two example we can conclude that coordinate dependence of the metric component is a necessary but not a sufficient condition for curved geometry.

## A.5 Observer in uniformly accelerated frame moving in flat spacetime

Let us now study the geometry for an observer moving in an accelerated frame (denoted by  $(x, t)$  also known as the *Rindler frame*) through a flat spacetime (denoted by  $(X, T)$ ). For an observer uniformly accelerating along the  $x$ -axis the equation of motion is given by,

$$\frac{d}{dT} \left( \frac{v}{\sqrt{1 - \frac{v^2}{c^2}}} \right) = g, \quad (\text{A.25})$$

If we assume that at  $T = 0$ ,  $v = 0$ , we can find  $v$  from there to be,

$$v = \frac{gT}{\sqrt{1 + \frac{g^2 T^2}{c^2}}}, \quad (\text{A.26})$$

Integrating the above equation and choosing a suitable constant of integration we get,

$$X^2 - c^2 T^2 = \frac{c^4}{g^2}, \quad (\text{A.27})$$

Which is an equation of hyperbola. Now the proper time measure in the frame of the observer is given by,

$$\tau = \int_0^T \sqrt{1 - \frac{v^2}{c^2}} dT', \quad (\text{A.28})$$

Substituting the expression of  $v$  from Eq. A.26, we get,

$$\tau = \frac{c}{g} \int_0^T \frac{d(gT/c)}{\sqrt{1 + (gT/c)^2}}, \quad (\text{A.29})$$

Thus, one gets to the result using the result from the above equation and that from Eq.

A.26 we get the following equations of trajectory under accelerated motion.

$$\begin{aligned} cT &= \frac{c^2}{g} \sinh\left(\frac{g\tau}{c}\right), \\ X &= \frac{c^2}{g} \cosh\left(\frac{g\tau}{c}\right), \end{aligned} \tag{A.30}$$

We know from special relativity that if an observer is traveling along the  $x$ -axis along a trajectory defined by  $X = f(\tau)$ ,  $T = h(\tau)$  then the Lorentz transformation equation connecting the  $(X, T)$  and the  $(x, t)$  frame is of the form,

$$\begin{aligned} X - cT &= f(t - x/c) - ch(t - x/c), \\ X + cT &= f(t + x/c) + ch(t + x/c), \end{aligned} \tag{A.31}$$

Here,  $f(\tau)$  and  $h(\tau)$  are given by A.30. Thus we obtain,

$$\begin{aligned} X - cT &= \frac{c^2}{g} \cosh\left(\frac{g}{c}(t - x/c)\right) - \frac{c^2}{g} \sinh\left(\frac{g}{c}(t - x/c)\right) = \frac{c^2}{g} \exp\left(-\frac{g}{c}(t - x/c)\right), \\ X + cT &= \frac{c^2}{g} \cosh\left(\frac{g}{c}(t + x/c)\right) + \frac{c^2}{g} \sinh\left(\frac{g}{c}(t + x/c)\right) = \frac{c^2}{g} \exp\left(\frac{g}{c}(t + x/c)\right), \end{aligned} \tag{A.32}$$

Thus we obtain the transformation equations between the inertial and the accelerated frame as below,

$$\begin{aligned} X &= \frac{c^2}{g} e^{gx/c^2} \cosh(gt/c), \\ cT &= \frac{c^2}{g} e^{gx/c^2} \sinh(gt/c), \end{aligned} \tag{A.33}$$

From the above transformation equations one obtains,

$$\begin{aligned} d(cT - X) &= e^{(gx/c^2)} e^{(-gt/c)} (cdt - dx), \\ d(cT + X) &= e^{(gx/c^2)} e^{(gt/c)} (cdt + dx) \end{aligned} \tag{A.34}$$

Thus,

$$c^2 dT^2 - dX^2 = d(cT - X)d(cT + X) = e^{2gx/c^2} (c^2 dt^2 - dx^2), \tag{A.35}$$

From this one can construct the line element as,

$$\boxed{ds^2 = -c^2 dT^2 + dX^2 + dY^2 + dZ^2 = -e^{2gx/c^2} dt^2 + e^{2gx/c^2} dx^2 + dy^2 + dz^2}, \quad (\text{A.36})$$

With the metric in the accelerated frame as,

$$g = \begin{pmatrix} -e^{2gx/c^2} & 0 & 0 & 0 \\ 0 & e^{2gx/c^2} & 0 & 0 \\ 0 & 0 & 1 & 0 \\ 0 & 0 & 0 & 1 \end{pmatrix}, \quad (\text{A.37})$$

One can note the coordinate dependence of the metric in the above equation. It is not possible to get rid of this coordinate dependence with a transformation of coordinates. Thus for an accelerated observer the geometry is curved.

## A.6 Principle of equivalence

The general Lagrangian of a particle under an external potential  $V(q, \dot{q}, t)$  can be written as,

$$L(q, \dot{q}, t) = \frac{1}{2}m\dot{q}^2 - eV(q, \dot{q}, t) \quad (\text{A.38})$$

Where  $m$  is the inertial mass of the particle and  $e$  is a generic charge that interacts with the potential  $V(q, \dot{q}, t)$ . For example in electrostatics this  $e$  would be the electrical charge and the potential  $V(q, \dot{q}, t)$  would be the coulombic potential  $V(q)$ . When we construct the Lagrangian of a particle falling freely under uniform gravity we note one interesting property,

$$L(q, \dot{q}) = \frac{1}{2}m\dot{q}^2 - mgq, \quad (\text{A.39})$$

The *charge* for gravitational potential  $V(q) = gh$  is identical to the inertial mass  $m$ . Thus

both the kinetic and potential energy terms contain the same mass  $m$ . No other forces that we know of exhibit this feature and it is unique to gravity. The result is that the Lagrange's equation of motion is free of any mass term and thus devoid of any property of the particle. Thus motion under gravity alone is independent of the particle and depends only on the gravitational potential. This has some far reaching consequences.

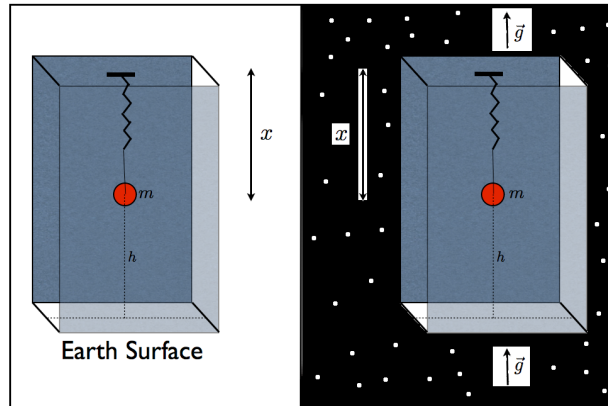


Figure A.4: An accelerated frame in a gravity-less environment is indistinguishable from an inertial frame under gravity.

Imagine two observers in Fig. A.4, one on earth another in space, infinitely away from earth and all other gravitating objects. Both these observers are placed in identical cubicals with opaque walls, ceilings and floors with floor to ceiling height of  $H$ . Both the cubicals have a massless spring of stiffness constant  $\kappa$  attached to the ceiling and a mass  $m$  hanging at the bottom of the spring at a height  $h$  above the floor.

Now for the observer on earth the the Lagrangian is given by,

$$L_{\text{earth}} = \frac{1}{2}m\dot{h}^2 - mgh, \quad (\text{A.40})$$

Since  $H = x + h$ , we can write after solving for the Lagrange's equation of motion,

$$m\ddot{x} = mg, \quad (\text{A.41})$$

If the elongation in the spring due to this force is given by  $\Delta x$ , then

$$\Delta x = \frac{m\ddot{x}}{\kappa} = \frac{mg}{\kappa}, \quad (\text{A.42})$$

For the observer in space, the Lagrangian is given by,

$$L_{\text{space}} = \frac{1}{2}m\dot{h}^2, \quad (\text{A.43})$$

However, if this observer is accelerating in the direction shown in Fig A.4, then the following coordinate transformation gives the position of the mass  $m$  measured in that frame,

$$h' = h - vt - \frac{1}{2}gt^2, \quad (\text{A.44})$$

Using this transformation in the expression of the  $L_{\text{space}}$ , we get,

$$L_{\text{space}} = \frac{1}{2}m(\dot{h}' + v + gt)^2, \quad (\text{A.45})$$

Using this Lagrangian in the Lagrange's equation and the fact that  $H = x' + h'$  and solving for it we get,

$$m\ddot{x}' = mg, \quad (\text{A.46})$$

If the elongation in the spring due to the acceleration of the cubical is given by  $\Delta x'$ , then

$$\Delta x' = \frac{m\ddot{x}'}{\kappa} = \frac{mg}{\kappa} = \Delta x, \quad (\text{A.47})$$

Thus an observer inside either of the two cubicals can not conclude by measuring the elongation of the spring whether the observer's cubical is at rest on earth or moving with acceleration  $g$  in a gravity-free environment. One can devise any dynamical experiment inside the cubical and none will be able to provide the information to the observer whether the

cubical in which the observer is present is accelerating, or is under gravity. But this principle is not confined to dynamical experiments only, the observer can devise *any* experiment that is confined within the walls of the cubical and that experiment will not be able to help the observer tell apart the two frames.

This is known as the *principle of equivalence*. It tells us that it is possible to ‘mimic’ gravity *locally* using acceleration. Conversely, it also means that one can *locally* ‘cancel’ gravity using an accelerated frame. Imagine an observer inside the same cubical over earth surface, only this time the observer is under free fall. The Lagrangian of the mass inside the cubical for an inertial observer is,

$$L_{\text{inertial}} = \frac{1}{2}m\dot{h}^2 - mgh, \quad (\text{A.48})$$

Solving for the Lagrange’s equation of motion using this Lagrangian and using the relation  $H = x + h$ , will get back Eq. A.41. However if we look at the mass from the perspective of an observer in the freely falling frame, the distance of the mass from the floor will be given by,

$$h' = h + vt + \frac{1}{2}gt^2, \quad (\text{A.49})$$

Using this transformation equation, the Lagrangian in the frame of the freely falling observer becomes,

$$L_{\text{freefall}} = \frac{1}{2}m(\dot{h}' - v - gt)^2 - mg\left(h' - vt - \frac{1}{2}gt^2\right), \quad (\text{A.50})$$

Solving for the Lagrange’s equation of motion with this Lagrangian and using the relation  $H = x' + h'$ , we get,

$$m\ddot{x}' = 0, \quad (\text{A.51})$$

Thus, in the frame of the cubical, the observer and the mass will not feel any force as if gravity inside the cubical has been *turned off*. This feature of gravity is a direct consequence of the fact that gravitational *charge* that couples with the gravitational potential is identical

to the inertial mass.

Now, As we have found out in Sec. A.5, that to an accelerated observer the geometry is curved, and principle of equivalence stating that gravity can be replaced locally by an accelerated observer, one can make this statement that gravity can be replaced by curvature in geometry. This is a very profound statement since principle of equivalence states that gravity can *locally* be replaced by an accelerated frame. What this implies in terms of geometry is that a curved spacetime in presence of gravity can always be locally replaced by a Minkowskian spacetime.

## A.7 Metric in curved spacetime, vectors and geodesics

As we have seen in the previous section that the dynamics of a particle in gravitational field can be replaced by motion in curved spacetime, it is worthwhile to spend some time in discussing curved geometry. It was discussed in Sec. A.4 that coordinate dependence in the metric components *can* imply curvature in space. The same is true for spacetime, where a coordinate dependence in the metric components *can* imply curvature in spacetime. Thus we can write the spacetime interval in a general spacetime which could be curved as,

$$ds^2 = g_{\mu\nu} dx^\mu dx^\nu, \quad (\text{A.52})$$

One thing we notice immediately in the above equation is that if we interchange the indices  $\mu \leftrightarrow \nu$ , the commutative property of the product between  $dx^\mu$  and  $dx^\nu$  implies that  $g_{\mu\nu} = g_{\nu\mu}$ . Thus the metric can be chosen to be symmetric. Next we note that if we perform a coordinate transformation  $x^\mu \rightarrow x'^\mu$ ,  $ds^2$  being a scalar should remain independent. Thus, we can write,

$$ds^2 = g_{\mu\nu} \frac{\partial x^\mu}{\partial x'^\alpha} dx'^\alpha \frac{\partial x^\nu}{\partial x'^\beta} dx'^\beta = \left( g_{\mu\nu} \frac{\partial x^\mu}{\partial x'^\alpha} \frac{\partial x^\nu}{\partial x'^\beta} \right) dx'^\alpha dx'^\beta, \quad (\text{A.53})$$

Thus, the metric transforms under coordinate transformation as,

$$\boxed{g'_{\alpha\beta}(x') = g_{\mu\nu}(x) \frac{\partial x^\mu}{\partial x'^\alpha} \frac{\partial x^\nu}{\partial x'^\beta}}, \quad (\text{A.54})$$

Therefore, the *metric is a symmetric tensor of second rank under Lorentz transformation that maps two vectors  $(dx^\mu, dx^\nu)$  to a scalar  $(ds^2)$* . This gives a nice segway to the discussion on vectors. From basic mathematics we know that vectors are defined as quantities that have a magnitude and a direction. Let us define a set of vectors  $V$  that exhibit the following properties,

- Associativity of vector addition :  $\mathbf{a} + (\mathbf{b} + \mathbf{c}) = (\mathbf{a} + \mathbf{b}) + \mathbf{c}$ .
- Commutativity of vector addition :  $\mathbf{a} + \mathbf{b} = \mathbf{b} + \mathbf{a}$ .
- Identity : There exists a vector  $\mathbf{0} \in V$  such that  $\mathbf{0} + \mathbf{a} = \mathbf{a}$ .
- Inverse : For every  $\mathbf{a} \in V$  there exists a vector  $-\mathbf{a} \in V$  such that  $\mathbf{a} + (-\mathbf{a}) = \mathbf{0}$ .
- Distributivity w.r.t scalar multiplication:  $p(\mathbf{a} + \mathbf{b}) = p\mathbf{a} + p\mathbf{b}$  and,  $(p + q)\mathbf{a} = p\mathbf{a} + q\mathbf{a}$ .
- Associativity of scalar multiplication :  $p(q\mathbf{a}) = (pq)\mathbf{a}$ .
- Identity element of scalar multiplication:  $\mathbf{1}\mathbf{v} = \mathbf{v}$ , where  $\mathbf{1}$  denotes the multiplicative identity.

This set  $V$  which satisfies the above requirements is called a *vector space*. Now imagine a point in the manifold of a vector space. The set of all vectors at that point on this manifold forms what is known as the *tangent space*. At each tangent space in this vector space we can define a set of linearly independent vectors. The set of all such vectors in that tangent space constructs what is known as *maximally linearly independent* vectors. This constructs what is known as the *basis vectors*  $\mathbf{e}_\mu$  at that tangent space. For example if we define the tangent space at a point on a two dimensional manifold, then we will be able to construct a

maximally linearly independent set of vectors with two elements  $(\mathbf{e}_x, \mathbf{e}_y)$ . This allows us to define an arbitrary vector on the tangent space using the basis vectors as,

$$\mathbf{A} = A^x \mathbf{e}_x + A^y \mathbf{e}_y, \quad (\text{A.55})$$

Note that the vector is a physical quantity and it exists irrespective of the existence of any coordinate systems. Defining the basis vector on the tangent space simply lets us label the vector at that point. We illustrate this in the Fig. A.5.

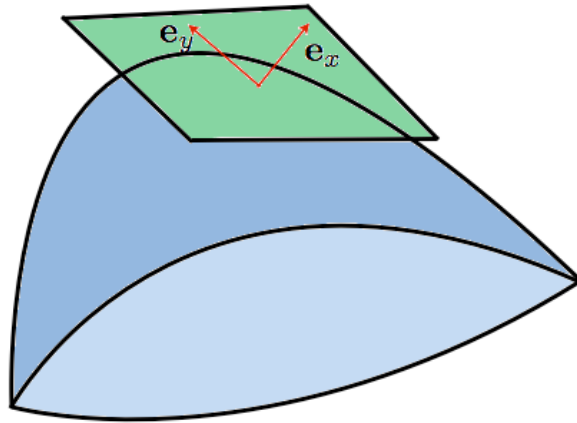


Figure A.5: Definition of basis vectors at the tangent space of a manifold.

The basis vectors  $\mathbf{e}_x$  and  $\mathbf{e}_y$  will be constants if the manifold is flat and the tangent space is identical at every point. The basis vectors in a general spacetime however will change from one tangent space to another which is evident from Fig. A.5. This is a very important point which we will revisit in our discussions of covariant derivatives. In a general  $n$ -dimensional spacetime, a vector can be written as,

$$\mathbf{A} = A^\mu \mathbf{e}_\mu, \quad (\text{A.56})$$

where,  $\mathbf{A} \in V$ . The quantities  $A^\mu$  are the components of vector  $\mathbf{A}$  in the  $\mathbf{e}_\mu$  basis.

Note that  $\mathbf{e}_\mu$  is only defined at the tangent space of a point and it will change from point to point. Now let us define a set of real numbers denoted by  $\mathbb{R}$ . A linear function  $f$  is defined as,

$$f(p\mathbf{a} + q\mathbf{b}) = pf(\mathbf{a}) + qf(\mathbf{b}), \quad (\text{A.57})$$

where,  $p, q \in \mathbb{R}$  and  $\mathbf{a}, \mathbf{b} \in V$ .

Let us now define a linear function  $\alpha$  from  $V$  to  $\mathbb{R}$  such that,  $\alpha : V \mapsto \mathbb{R}$ . Such a linear function acts on a vector  $\mathbf{a}$  and gives a real number  $\alpha(\mathbf{a})$ . This linear function is called a *one form*. For any real function we know that  $(\alpha + \beta)\mathbf{a} = \alpha(\mathbf{a}) + \beta(\mathbf{a})$  and because  $\alpha$  is a linear function we also have,  $\alpha(\mathbf{a} + \mathbf{b}) = \alpha(\mathbf{a}) + \alpha(\mathbf{b})$ . Using these, we get the following properties of a one form,

- Associativity of addition for one forms: If  $\mathbf{a} + (\mathbf{b} + \mathbf{c}) = (\mathbf{a} + \mathbf{b}) + \mathbf{c}$ ,  
then,  $\alpha(\mathbf{a}) + [\alpha(\mathbf{b}) + \alpha(\mathbf{c})] = \alpha[\mathbf{a} + (\mathbf{b} + \mathbf{c})] = \alpha[(\mathbf{a} + \mathbf{b}) + \mathbf{c}]$   
 $\implies \alpha(\mathbf{a}) + [\alpha(\mathbf{b}) + \alpha(\mathbf{c})] = [\alpha(\mathbf{a}) + \alpha(\mathbf{b})] + \alpha(\mathbf{c})$ .
- Commutativity of addition for one forms: If  $\mathbf{a} + \mathbf{b} = \mathbf{b} + \mathbf{a}$ ,  
then,  $\alpha(\mathbf{a}) + \alpha(\mathbf{b}) = \alpha(\mathbf{a} + \mathbf{b}) = \alpha(\mathbf{b} + \mathbf{a}) = \alpha(\mathbf{b}) + \alpha(\mathbf{a})$ .
- Identity for one forms: if  $\mathbf{0} + \mathbf{a} = \mathbf{a}$ ,  
then,  $\alpha(\mathbf{0} + \mathbf{a}) = \alpha(\mathbf{a})$   
 $\implies \alpha(\mathbf{0}) + \alpha(\mathbf{a}) = \alpha(\mathbf{a})$ ,  $\alpha(\mathbf{0})$  being the identity.
- Inverse for one forms: if  $\mathbf{a} + (-\mathbf{a}) = \mathbf{0}$ ,  
then,  $\alpha(\mathbf{a} + (-\mathbf{a})) = \alpha(\mathbf{0}) \implies \alpha(\mathbf{a}) + \alpha(-\mathbf{a}) = \alpha(\mathbf{0})$ , thus there exists an inverse for every one form.

Thus we see that a set of one forms that takes all the vectors in  $V$  to a number in  $\mathbb{R}$ , satisfies the first four properties of a vector space. The next three properties are automatically satisfied due to the fact that  $\alpha$  is a linear function. This space of one forms is called the *dual*

vector space  $V^*$ . To write a one form in the component notation like we did for a vector, we need to define a dual basis vector  $\omega^\mu$  which is defined using the basis vector as follows,

$$\omega^\mu e_\nu = \delta^\mu_\nu, \quad (\text{A.58})$$

Using linear combination of dual basis vectors we write the one form as,

$$\alpha = \alpha_\mu \omega^\mu, \quad (\text{A.59})$$

where,  $\alpha \in V^*$ . The quantities  $\alpha_\mu$  are the components of one form  $\alpha$  in the  $\omega^\mu$  dual basis. Now let us assume a vector  $\mathbf{A}$  whose magnitude is  $A$ . We can construct a one form  $\alpha$  corresponding to this vector in the dual space such that this one form takes the  $\mathbf{A}$  from the vector space  $V$  to a number  $A^2 \in \mathbb{R}$ .

$$A^2 = \alpha \mathbf{A} = A^\mu \alpha_\nu e_\mu \omega^\nu = A^\mu \alpha_\mu, \quad (\text{A.60})$$

Since,

$$A^2 = g_{\mu\nu} A^\mu A^\nu, \quad (\text{A.61})$$

Thus comparing these two equations we get,

$$\alpha_\mu = g_{\mu\nu} A^\nu, \quad (\text{A.62})$$

Which gives the map between the components of the vectors in the vector space  $V$  and the dual space  $V^*$  using the metric.  $\alpha_\mu$  is also called the *covariant* component of the vector  $\mathbf{A}$ . The metric  $g_{\mu\nu}$  can be thus used to lower indices of vectors and higher order tensors to convert them to covariant components.

Finally we can define an analog of a metric in the dual space that takes a one form from the

dual space to a vector in the vector space.

$$A^\mu = g^{\mu\nu} \alpha_\nu, \quad (\text{A.63})$$

Thus we can write,

$$g_{\mu\sigma}(g^{\mu\nu} \alpha_\nu) = \alpha_\sigma = \alpha_\nu \delta^\nu_\sigma, \quad (\text{A.64})$$

Which gives us,

$$g^{\mu\nu} g_{\mu\sigma} = \delta^\nu_\sigma, \quad (\text{A.65})$$

$g^{\mu\nu}$  is sometimes called the *contravariant* metric tensor and is used for raising of indices in tensors.

Now let us derive an expression for the path a free particle follows in a spacetime whose geometry is given by the metric tensor  $g_{\mu\nu}$ . The action for a particle going from an event  $A$  to  $B$  parametrized by a parameter  $\lambda$  is given by,

$$S_{AB} = \int_A^B d\tau = \frac{1}{c} \int_A^B \sqrt{-g_{\mu\nu} \frac{dx^\mu}{d\lambda} \frac{dx^\nu}{d\lambda}} d\lambda, \quad (\text{A.66})$$

Comparing the action above with the definition of action in classical mechanics,

$$S = \int L(q, \dot{q}, t) dt, \quad (\text{A.67})$$

One can write the Lagrangian of a free particle in the geometry defined by the metric  $g_{\mu\nu}$  as,

$$L = L(x^\mu, \dot{x}^\mu, \lambda) = \frac{1}{c} \sqrt{-g_{\mu\nu} \frac{dx^\mu}{d\lambda} \frac{dx^\nu}{d\lambda}}, \quad (\text{A.68})$$

After varying the action we get the Lagrange's equation of motion,

$$\frac{d}{d\lambda} \left( \frac{\partial L(x^\alpha, \dot{x}^\alpha, \lambda)}{\partial \dot{x}^\alpha} \right) - \frac{\partial L(x^\alpha, \dot{x}^\alpha, \lambda)}{\partial x^\alpha} = 0, \quad (\text{A.69})$$

The second term can be calculated from A.15 by simply replacing  $\eta_{\mu\nu}$  with  $g_{\mu\nu}$ .

$$\frac{\partial L(x^\alpha, \dot{x}^\alpha, \lambda)}{\partial x^\alpha} = \frac{1}{2c} \left( -g_{\mu\nu} \frac{dx^\mu}{d\lambda} \frac{dx^\nu}{d\lambda} \right)^{-1/2} \left( -\frac{\partial g_{\mu\nu}}{\partial x^\alpha} \right) \frac{dx^\mu}{d\lambda} \frac{dx^\nu}{d\lambda}. \quad (\text{A.70})$$

Since

$$d\tau = \frac{1}{c} \sqrt{-g_{\mu\nu} dx^\mu dx^\nu}. \quad (\text{A.71})$$

Thus we can write

$$\left( -g_{\mu\nu} \frac{dx^\mu}{d\lambda} \frac{dx^\nu}{d\lambda} \right)^{-1/2} = \frac{1}{c} \frac{d\lambda}{d\tau}. \quad (\text{A.72})$$

Substituting Eq. A.72 in Eq. A.70, we get

$$\frac{\partial L(x^\alpha, \dot{x}^\alpha, \lambda)}{\partial x^\alpha} = -\frac{1}{2c^2} \frac{d\lambda}{d\tau} \frac{\partial g_{\mu\nu}}{\partial x^\alpha} \frac{dx^\mu}{d\lambda} \frac{dx^\nu}{d\lambda}, \quad (\text{A.73})$$

The first term in the Lagrange's equation of motion can be obtained by simply replacing  $\eta_{\mu\nu}$  with  $g_{\mu\nu}$  in Eq. A.16.

$$\left( \frac{\partial L(x^\alpha, \dot{x}^\alpha, \lambda)}{\partial \dot{x}^\alpha} \right) = -\frac{1}{c^2} g_{\alpha\mu} \frac{dx^\mu}{d\tau}. \quad (\text{A.74})$$

Thus the lagrange's equation of motion gives us,

$$\frac{1}{2} \frac{d\lambda}{d\tau} \frac{\partial g_{\mu\nu}}{\partial x^\alpha} \frac{dx^\mu}{d\lambda} \frac{dx^\nu}{d\lambda} = \frac{d}{d\lambda} \left( g_{\alpha\mu} \frac{dx^\mu}{d\tau} \right). \quad (\text{A.75})$$

Multiplying by  $d\lambda/d\tau$  on both sides of the above equation we get,

$$\frac{1}{2} \frac{\partial g_{\mu\nu}}{\partial x^\alpha} \frac{dx^\mu}{d\tau} \frac{dx^\nu}{d\tau} = \frac{d}{d\tau} \left( g_{\alpha\mu} \frac{dx^\mu}{d\tau} \right). \quad (\text{A.76})$$

Note that

$$\frac{d}{d\tau} g_{\alpha\mu} = \frac{\partial g_{\alpha\mu}}{\partial x^\nu} \frac{dx^\nu}{d\tau}, \quad (\text{A.77})$$

Using this in Eq. A.76 we get

$$\frac{1}{2} \frac{\partial g_{\mu\nu}}{\partial x^\alpha} \frac{dx^\mu}{d\tau} \frac{dx^\nu}{d\tau} = g_{\alpha\mu} \frac{d^2 x^\mu}{d\tau^2} + \frac{\partial g_{\alpha\mu}}{\partial x^\nu} \frac{dx^\nu}{d\tau} \frac{dx^\mu}{d\tau}. \quad (\text{A.78})$$

Now we can write

$$\frac{\partial g_{\alpha\mu}}{\partial x^\nu} \frac{dx^\nu}{d\tau} \frac{dx^\mu}{d\tau} = \frac{1}{2} \left[ \frac{\partial g_{\alpha\mu}}{\partial x^\nu} \frac{dx^\nu}{d\tau} \frac{dx^\mu}{d\tau} + \frac{\partial g_{\alpha\mu}}{\partial x^\nu} \frac{dx^\mu}{d\tau} \frac{dx^\nu}{d\tau} \right]. \quad (\text{A.79})$$

Since both  $\mu$  and  $\nu$  are repeatative indices, therefore they can be interchanged ( $\mu \leftrightarrow \nu$ ) in the second term

$$\frac{\partial g_{\alpha\mu}}{\partial x^\nu} \frac{dx^\nu}{d\tau} \frac{dx^\mu}{d\tau} = \frac{1}{2} \left[ \frac{\partial g_{\alpha\mu}}{\partial x^\nu} \frac{dx^\mu}{d\tau} \frac{dx^\nu}{d\tau} + \frac{\partial g_{\alpha\nu}}{\partial x^\mu} \frac{dx^\mu}{d\tau} \frac{dx^\nu}{d\tau} \right]. \quad (\text{A.80})$$

Substituting this result in the second term of right hand side of Eq. A.78 we get

$$\frac{1}{2} \frac{\partial g_{\mu\nu}}{\partial x^\alpha} \frac{dx^\mu}{d\tau} \frac{dx^\nu}{d\tau} = g_{\alpha\mu} \frac{d^2 x^\mu}{d\tau^2} + \frac{1}{2} \left[ \frac{\partial g_{\alpha\mu}}{\partial x^\nu} \frac{dx^\mu}{d\tau} \frac{dx^\nu}{d\tau} + \frac{\partial g_{\alpha\nu}}{\partial x^\mu} \frac{dx^\mu}{d\tau} \frac{dx^\nu}{d\tau} \right]. \quad (\text{A.81})$$

Multiplying both sides by  $g^{\alpha\delta}$  and rearranging terms we get

$$\frac{d^2 x^\delta}{d\tau^2} + \frac{1}{2} g^{\alpha\delta} \left[ \frac{\partial g_{\alpha\mu}}{\partial x^\nu} + \frac{\partial g_{\alpha\nu}}{\partial x^\mu} - \frac{\partial g_{\mu\nu}}{\partial x^\alpha} \right] \frac{dx^\mu}{d\tau} \frac{dx^\nu}{d\tau}. \quad (\text{A.82})$$

Defining

$$\Gamma_{\mu\nu}^\delta = \frac{1}{2} g^{\alpha\delta} \left[ \frac{\partial g_{\alpha\mu}}{\partial x^\nu} + \frac{\partial g_{\alpha\nu}}{\partial x^\mu} - \frac{\partial g_{\mu\nu}}{\partial x^\alpha} \right], \quad (\text{A.83})$$

we get

$$\boxed{\frac{d^2 x^\delta}{d\tau^2} + \Gamma_{\mu\nu}^\delta \frac{dx^\mu}{d\tau} \frac{dx^\nu}{d\tau}}, \quad (\text{A.84})$$

which is the equation of the path taken by a free particle in a geometry defined by the metric  $g_{\mu\nu}$ . This is called the *Geodesic equation* and the path taken by the particle is called the *geodesic*. The quantities  $\Gamma_{\mu\nu}^\delta$  are called the Christoffel symbols. Since the Christoffel

symbols depend on the derivatives of the metric, they vanish when the metric is Minkowskian reducing the geodesic equation to A.18. One important point to note here is that though the Christoffel symbols are written in index notation, they do not form a tensor, and hence they should not be called *components*.

## A.8 Covariant derivatives, parallel transport and curvature tensors

In the previous section we have described the metric of a curved spacetime and the trajectory taken by free particles on it. Next, we would like to quantify curvature itself. But before we do that, it will be a good idea to develop some tools. First of all we will define a modification of the flat space derivative function of a vector. The need for the modification of the derivative of a vector in curved space arises from the fact that the ordinary derivative function of a vector which transforms like a second rank tensor in flat spacetime, does not do so in a curved spacetime. Another way of saying this is to say that the ordinary derivative is not generally covariant. This can be explicitly seen by transforming a vector ordinary derivative from one coordinate system to another. Let us consider a vector  $u^\mu$  and its transformation in another coordinate system  $u'^\mu$ . Therefore one can write

$$\begin{aligned} \frac{\partial u'^\mu}{\partial x'^\nu} &= \frac{\partial x^\alpha}{\partial x'^\nu} \frac{\partial}{\partial x^\alpha} \left( \frac{\partial x'^\mu}{\partial x^\beta} u^\beta \right), \\ &= \left( \frac{\partial x^\alpha}{\partial x'^\nu} \frac{\partial x'^\mu}{\partial x^\beta} \right) \frac{\partial u^\beta}{\partial x^\alpha} + \left[ \left( \frac{\partial x^\alpha}{\partial x'^\nu} \right) \frac{\partial^2 x'^\mu}{\partial x^\alpha \partial x^\beta} \right] u^\beta. \end{aligned} \tag{A.85}$$

If the quantity  $\partial u'^\mu / \partial x'^\nu$  has to transform like a second rank tensor then the second term in the above equation has to vanish. In flat spacetime the double partial derivative this term will vanish owing to the fact that the Lorentz transformations are linear in nature between coordinates. However in a general curved spacetime the second term will generally not be equal to zero. Thus we see that in the curved spacetime the ordinary derivative is

not covariant. This leads one to define a derivative that will transform like a tensor. Let us write the geodesic equation in the following way

$$\frac{du^\delta}{d\tau} + \Gamma_{\mu\nu}^\delta u^\mu u^\nu = 0, \quad (\text{A.86})$$

where,  $u^\mu = \partial x^\mu / \partial \tau$  is the four-velocity vector. Applying chain rule of partial differentiation we get

$$\frac{du^\delta}{d\tau} = \frac{\partial u^\delta}{\partial x^\nu} u^\nu, \quad (\text{A.87})$$

which aid us in writing the geodesic equation as follows

$$\begin{aligned} u^\nu \left[ \frac{\partial u^\delta}{\partial x^\nu} + \Gamma_{\mu\nu}^\delta u^\mu \right] &= 0, \\ u^\nu \nabla_\nu u^\delta &= 0. \end{aligned} \quad (\text{A.88})$$

The quantity  $\nabla_\nu u^\delta$  transforms like a second rank tensor which can be verified in the same way we verified that the ordinary derivative of a vector in general does not transform like a second rank tensor. This newly defined derivative of a vector is called the *covariant derivative*. As we have discussed before (see, discussion above Eq. (A.56)). The basis vectors in a general spacetime will change from one tangent space to another. An act of evaluating a derivative involves finding the difference between the values of a function at two different points. However, since the basis vectors themselves change from one point to another in a generic curved spacetime, upon using the same basis vector for evaluating the value of the function at different locations in the manifold, we incur an error. That is why the ordinary derivative does not transform as a tensor. For the covariant derivative, one makes corrections by introducing the  $\Gamma_{\mu\nu}^\delta u^\mu$  terms. The derivatives of the metric in the Christoffel symbols keep the measure of how the basis vectors are changing from one tangent space to another, thus correcting for the error incurred upon using a single basis for the calculation of the derivative.

Now let us assume a parametrized curve,  $x^\mu(\lambda)$ . Where  $\lambda$  is an arbitrary parameter that

characterizes the curve. In a flat spacetime if we take a vector in a vector field,  $v^\nu(x)$  and translate it parallelly to itself on the curve, then the directional derivative of the vector field at a particular point on that curve vanishes

$$\frac{\partial v^\mu}{\partial x^\nu} \frac{dx^\nu}{d\lambda} = 0. \quad (\text{A.89})$$

Generalizing this to curved spacetime, we simply replace the ordinary derivative with a covariant derivative.

$$\nabla_\nu v^\mu \frac{dx^\nu}{d\lambda} = \frac{dx^\nu}{d\lambda} \frac{\partial v^\mu}{\partial x^\nu} + \frac{dx^\nu}{d\lambda} \Gamma_{\delta\nu}^\mu v^\delta = \frac{dv^\mu}{d\lambda} + \frac{dx^\nu}{d\lambda} \Gamma_{\delta\nu}^\mu v^\delta = 0. \quad (\text{A.90})$$

This equation is called the equation of *parallel transport* in a curved spacetime. Now imagine transporting a vector parallelly to itself from a point (event)  $P_1$  to a point  $P_2$  and then back to  $P_1$  along a closed contour  $\mathcal{C}$  parametrized by  $\lambda$ . In a flat spacetime the vector will preserve its orientation all the way and return to the point  $P_1$  without any change. If we use coordinate system that is curvilinear instead of a cartesian one, we can still define a global cartesian coordinate system and find the basis of the curvilinear coordinate system in terms of the basis of the cartesian coordinates at every point on the curve and define the parallel transport along the closed contour  $\mathcal{C}$ . Changing the coordinate systems at every point of the curve, does not change the orientation of the vector which is a true physical quantity. Thus upon returning to point  $P_1$  the vector will be preserved to its original form. However, if the spacetime is curved, then one can not define a global cartesian coordinate on it. Therefore it is not possible to construct a closed path on the curved spacetimes along which the vector can be parallelly transported and brought back preserving its form. Thus parallel transport gives us an ability to differentiate between a genuinely curved spacetime from a flat spacetime with curvilinear coordinate system, something that we found before that the metric does not provide. In the metric, coordinate dependence was a necessary condition for a spacetime to be curved but was not a sufficient condition. A curvilinear coordinate system can give rise to

a metric that has coordinate dependent terms in its components. The metric of the spherical polar coordinate being a common example. However, using parallel transport over a closed loop if one gets back a vector that is different from the original vector then that definitively indicates that the spacetime is curved. Thus, we can quantify curvature analytically.

Consider the closed contour  $\mathcal{C}$  infinitely small. We would like to calculate the change in a vector  $v^\mu$  after it is transported parallelly around  $\mathcal{C}$  and brought back to point  $P_1$ . Using Eq. (A.90), we can write for the contour  $\mathcal{C}$

$$v^\mu(\lambda) = v_{P_1}^\mu - \int_0^\lambda \Gamma_{\nu\delta}^\mu v^\nu \frac{dx^\delta}{d\lambda} d\lambda. \quad (\text{A.91})$$

Since  $\mathcal{C}$  is infinitesimal, thus we can expand both  $\Gamma_{\nu\delta}^\mu$  and  $v^\nu$  around the point  $P_1$  using Taylor expansions

$$\begin{aligned} \Gamma_{\nu\delta}^\mu(\lambda) &= (\Gamma_{\nu\delta}^\mu)_{P_1} + (\partial_\alpha \Gamma_{\nu\delta}^\mu)_{P_1} [x^\alpha(\lambda) - x_{P_1}^\alpha] + \dots, \\ v^\nu(\lambda) &= v_{P_1}^\nu + \frac{dv^\nu}{dx^\alpha} [x^\alpha(\lambda) - x_{P_1}^\alpha] + \dots, \end{aligned} \quad (\text{A.92})$$

where we have used the notation  $\partial_\alpha = \partial/\partial x^\alpha$ . Using Eq. (A.90) we can write

$$\frac{dv^\nu}{dx^\alpha} = \frac{dv^\nu}{d\lambda} \frac{d\lambda}{dx^\alpha} = -\Gamma_{\gamma\alpha}^\nu v^\gamma. \quad (\text{A.93})$$

Thus we can write the Taylor expansions as

$$\begin{aligned} \Gamma_{\nu\delta}^\mu(\lambda) &\approx (\Gamma_{\nu\delta}^\mu)_{P_1} + (\partial_\alpha \Gamma_{\nu\delta}^\mu)_{P_1} [x^\alpha(\lambda) - x_{P_1}^\alpha], \\ v^\nu(\lambda) &\approx v_{P_1}^\nu - (\Gamma_{\gamma\alpha}^\nu)_{P_1} v_{P_1}^\gamma [x^\alpha(\lambda) - x_{P_1}^\alpha], \end{aligned} \quad (\text{A.94})$$

which, if we insert in Eq. (A.91), gives us

$$\begin{aligned}
v^\mu(\lambda) &= v_{P_1}^\mu - \int_0^\lambda [(\Gamma_{\nu\delta}^\mu)_{P_1} + (\partial_\alpha \Gamma_{\nu\delta}^\mu)_{P_1} (x^\alpha(\lambda) - x_{P_1}^\alpha)] [v_{P_1}^\nu - (\Gamma_{\gamma\alpha}^\nu)_{P_1} v_{P_1}^\gamma (x^\alpha(\lambda) - x_{P_1}^\alpha)] \frac{dx^\delta}{d\lambda}, \\
&= v_{P_1}^\mu - (\Gamma_{\nu\delta}^\mu)_{P_1} v_{P_1}^\nu \int_0^\lambda \frac{dx^\delta}{d\lambda} d\lambda - \\
&\quad \left[ (\partial_\alpha \Gamma_{\nu\delta}^\mu)_{P_1} v_{P_1}^\nu - (\Gamma_{\nu\delta}^\mu)_{P_1} (\Gamma_{\gamma\alpha}^\nu)_{P_1} v_{P_1}^\gamma \right] \int_0^\lambda (x^\alpha(\lambda) - x_{P_1}^\alpha) \frac{dx^\delta}{d\lambda} d\lambda.
\end{aligned} \tag{A.95}$$

Note that the second term vanishes when the integral is evaluated over a closed contour, so does the term involving  $x_{P_1}^\alpha$  in the last term. Thus, defining  $\Delta v^\mu = v^\mu(\lambda) - v_{P_1}^\mu$ , we can write the change in the vector upon parallel transport over a closed loop

$$\Delta v^\mu = - \left[ (\partial_\alpha \Gamma_{\nu\delta}^\mu)_{P_1} v_{P_1}^\nu - (\Gamma_{\nu\delta}^\mu)_{P_1} (\Gamma_{\gamma\alpha}^\nu)_{P_1} v_{P_1}^\gamma \right] \int_0^\lambda x^\alpha dx^\delta. \tag{A.96}$$

Note that the indices  $\gamma$  and  $\nu$  of the second term in the square bracket are repeated and hence are dummy. Thus they can be interchanged  $\gamma \leftrightarrow \nu$ , which gives us

$$\Delta v^\mu = - \left[ (\partial_\alpha \Gamma_{\nu\delta}^\mu)_{P_1} - (\Gamma_{\gamma\delta}^\mu)_{P_1} (\Gamma_{\nu\alpha}^\gamma)_{P_1} \right] v_{P_1}^\nu \int_0^\lambda x^\alpha dx^\delta. \tag{A.97}$$

Now, note that the indices  $\alpha$  and  $\delta$  are dummy indices as well, However if we interchange these two indices  $\alpha \leftrightarrow \delta$ , we note that  $x^\alpha dx^\delta + x^\delta dx^\alpha = d(x^\alpha x^\delta)$  which vanishes upon integrating over a close loop

$$\int_0^\lambda x^\alpha dx^\delta = - \int_0^\lambda x^\delta dx^\alpha, \tag{A.98}$$

from which we can write

$$2\Delta v^\mu = - \left\{ [\partial_\alpha \Gamma_{\nu\delta}^\mu - \Gamma_{\gamma\delta}^\mu \Gamma_{\nu\alpha}^\gamma] - [\partial_\delta \Gamma_{\nu\alpha}^\mu - \Gamma_{\gamma\alpha}^\mu \Gamma_{\nu\delta}^\gamma] \right\}_{P_1} v_{P_1}^\nu \int_0^\lambda x^\alpha dx^\delta. \tag{A.99}$$

Thus we can write the change in the vector upon transporting it parallelly along a closed

loop as

$$\Delta v^\mu = -\frac{1}{2} (\partial_\alpha \Gamma_{\nu\delta}^\mu - \partial_\delta \Gamma_{\nu\alpha}^\mu + \Gamma_{\gamma\alpha}^\mu \Gamma_{\nu\delta}^\gamma - \Gamma_{\gamma\delta}^\mu \Gamma_{\nu\alpha}^\gamma)_{P_1} v_{P_1}^\nu \int_0^\lambda x^\alpha dx^\delta \quad (\text{A.100})$$

Let us define the quantity

$$R_{\nu\alpha\delta}^\mu = \partial_\alpha \Gamma_{\nu\delta}^\mu - \partial_\delta \Gamma_{\nu\alpha}^\mu + \Gamma_{\gamma\alpha}^\mu \Gamma_{\nu\delta}^\gamma - \Gamma_{\gamma\delta}^\mu \Gamma_{\nu\alpha}^\gamma, \quad (\text{A.101})$$

using which we can write

$$\Delta v^\mu = -\frac{1}{2} (R_{\nu\alpha\delta}^\mu)_{P_1} v_{P_1}^\nu \int_0^\lambda x^\alpha dx^\delta. \quad (\text{A.102})$$

If all the components of  $R_{\nu\alpha\delta}^\mu$  are zero then the change in the vector upon a parallel transport around a closed loop zero and a finite value of it results in to a change in the vector when it returns back to the original point. Thus  $R_{\nu\alpha\delta}^\mu$  quantifies the curvature of the spacetime. This is called the *Riemann curvature tensor*.

## A.9 Einstein tensor and Einstein field equations

In the last section we quantified the curvature of spacetime. But from Sec. A.6 we have seen that the dynamics of a particle in gravitational field can be replaced by motion in curved spacetime. Therefore we should be able to relate the curvature defined in the previous section with matter. However matter, represented by the energy momentum stress tensor is a second rank tensor, but the Riemann curvature tensor is a fourth rank tensor. So we must find a second counterpart of the curvature tensor first. This is obtained by contracting the Riemann Curvature tensor using  $g^{\mu\nu}$ . The quantity we get upon contraction is called the *Ricci tensor*.

$$R_{\nu\delta} = g^{\mu\alpha} R_{\mu\nu\alpha\delta}, \quad (\text{A.103})$$

which is symmetric second rank tensor. Contracting once more gives us a scalar called the *Ricci scalar*

$$R = g^{\nu\delta} R_{\nu\delta}, \quad (\text{A.104})$$

Finally from these two new quantities we are in a position to construct the *Einstein tensor*

$$\boxed{G_{\mu\nu} = R_{\mu\nu} - \frac{1}{2}g_{\mu\nu}R}. \quad (\text{A.105})$$

It is this quantity that we will relate to the Energy momentum stress tensor  $T_{\mu\nu}$  using the following equation

$$\boxed{G_{\mu\nu} = \frac{8\pi G}{c^4}T_{\mu\nu}}, \quad (\text{A.106})$$

which is popularly known as the Einstein's field equations.

# Appendix B

## Linearized gravity and gravitational waves

In this appendix we will discuss in details the theory of linearized gravity and how the gravitational wave solutions emerges from it. Before we begin the discussion of gravitational waves we need to understand GR in the weak field limit. Therefore we will begin our discussion with the understanding of gravity in that regime. Much of the work presented here is heavily influenced by Ref. Creighton and Anderson (2011).

### B.1 Linearized gravity

The spacetime curvature in the presence of the massive objects is represented by the metric tensor  $g_{\mu\nu}$ . In the weak field limit we can express the curvature as a mere perturbation on the flat spacetime. This assumption lets us write the metric in weak field regime as

$$g_{\mu\nu} = \eta_{\mu\nu} + h_{\mu\nu}, \tag{B.1}$$

where  $h_{\mu\nu}$  is a small quantity such that we will ignore all terms that are second order and higher in  $h_{\mu\nu}$ . This also implies that lowering and raising of any indices involving terms containing  $h_{\mu\nu}$  will be done by  $\eta_{\mu\nu}$  and not the full metric  $g_{\mu\nu}$ . Thus from Eq. (2.1) we can

write

$$\Gamma_{\alpha\beta}^{\gamma} = \frac{1}{2}\eta^{\gamma\delta} \left( \frac{\partial h_{\beta\delta}}{\partial x^{\alpha}} + \frac{\partial h_{\alpha\delta}}{\partial x^{\beta}} - \frac{\partial h_{\alpha\beta}}{\partial x^{\delta}} \right). \quad (\text{B.2})$$

Knowing the form of the Cristoffel symbols, one can now proceed to calculate the components of the Riemann curvature tensor from Eq. (2.2). Note that the Riemann curvature tensor has four terms two of which are the products of the Cristoffel symbols. These terms we will ignore because they are second order in perturbation. Thus we get

$$\begin{aligned} R_{\alpha\beta\gamma\delta} &= \partial\Gamma_{\delta\alpha\gamma} - \partial\Gamma_{\delta\beta\gamma}, \\ &= \partial_{\beta} [\eta_{\lambda\delta}\Gamma_{\alpha\gamma}^{\lambda}] - \partial_{\alpha} [\eta_{\lambda\delta}\Gamma_{\beta\gamma}^{\lambda}], \\ &= \partial_{\beta} \left[ \eta_{\lambda\delta} \frac{1}{2} \eta^{\lambda\delta} \left( \frac{\partial h_{\alpha\delta}}{\partial x^{\gamma}} + \frac{\partial h_{\gamma\delta}}{\partial x^{\alpha}} - \frac{\partial h_{\alpha\gamma}}{\partial x^{\delta}} \right) \right] - \\ &\quad \partial_{\alpha} \left[ \eta_{\lambda\delta} \frac{1}{2} \eta^{\lambda\delta} \left( \frac{\partial h_{\beta\delta}}{\partial x^{\gamma}} + \frac{\partial h_{\gamma\delta}}{\partial x^{\beta}} - \frac{\partial h_{\beta\gamma}}{\partial x^{\delta}} \right) \right]. \end{aligned} \quad (\text{B.3})$$

From this we get the Riemann curvature tensor in the weak field limit

$$\begin{aligned} R_{\alpha\beta\gamma\delta} &= \frac{1}{2} \left[ \frac{\partial^2 h_{\alpha\delta}}{\partial x^{\beta} \partial x^{\gamma}} + \frac{\partial^2 h_{\gamma\delta}}{\partial x^{\beta} \partial x^{\alpha}} - \frac{\partial^2 h_{\alpha\gamma}}{\partial x^{\beta} \partial x^{\delta}} - \frac{\partial^2 h_{\beta\delta}}{\partial x^{\alpha} \partial x^{\gamma}} - \frac{\partial^2 h_{\gamma\delta}}{\partial x^{\alpha} \partial x^{\beta}} + \frac{\partial^2 h_{\beta\gamma}}{\partial x^{\alpha} \partial x^{\delta}} \right], \\ R_{\alpha\beta\gamma\delta} &= \frac{1}{2} \left[ \frac{\partial^2 h_{\alpha\delta}}{\partial x^{\beta} \partial x^{\gamma}} - \frac{\partial^2 h_{\alpha\gamma}}{\partial x^{\beta} \partial x^{\delta}} - \frac{\partial^2 h_{\beta\delta}}{\partial x^{\alpha} \partial x^{\gamma}} + \frac{\partial^2 h_{\beta\gamma}}{\partial x^{\alpha} \partial x^{\delta}} \right]. \end{aligned} \quad (\text{B.4})$$

The Ricci tensor in the weak field limit is calculated by contracting the above Riemann tensor as follows

$$R_{\alpha\beta} = R_{\alpha\mu\beta}{}^{\mu}. \quad (\text{B.5})$$

In Eq. (B.4) we transform the following indices  $\beta \rightarrow \mu$  and  $\gamma \rightarrow \beta$ . This gives us

$$\begin{aligned} R_{\alpha\beta} &= R_{\alpha\mu\beta\delta}\eta^{\mu\delta} = \frac{1}{2} \left[ \frac{\partial^2 h_{\alpha\delta}}{\partial x^{\mu} \partial x^{\beta}} - \frac{\partial^2 h_{\alpha\beta}}{\partial x^{\mu} \partial x^{\delta}} - \frac{\partial^2 h_{\mu\delta}}{\partial x^{\alpha} \partial x^{\beta}} + \frac{\partial^2 h_{\mu\beta}}{\partial x^{\alpha} \partial x^{\delta}} \right] \eta^{\mu\delta}, \\ &= \frac{1}{2} \left[ \frac{\partial^2 h_{\alpha}{}^{\mu}}{\partial x^{\mu} \partial x^{\beta}} - \eta^{\mu\delta} \frac{\partial^2 h_{\alpha\beta}}{\partial x^{\mu} \partial x^{\delta}} - \frac{\partial^2 h}{\partial x^{\alpha} \partial x^{\beta}} + \frac{\partial^2 h^{\mu}{}_{\beta}}{\partial x^{\alpha} \partial x^{\mu}} \right], \end{aligned} \quad (\text{B.6})$$

where  $h = h_{\mu}^{\mu}$  is the trace of the metric perturbation. From this we can define the Ricci

scalar,  $R = g^{\alpha\beta}R_{\alpha\beta} = \eta^{\alpha\beta}R_{\alpha\beta}$ .

$$\begin{aligned}
R &= \frac{1}{2}\eta^{\alpha\beta} \left[ \frac{\partial^2 h_{\alpha}{}^{\mu}}{\partial x^{\mu}\partial x^{\beta}} - \eta^{\mu\delta} \frac{\partial^2 h_{\alpha\beta}}{\partial x^{\mu}\partial x^{\delta}} - \frac{\partial^2 h}{\partial x^{\alpha}\partial x^{\beta}} + \frac{\partial^2 h^{\mu}{}_{\beta}}{\partial x^{\alpha}\partial x^{\mu}} \right], \\
&= \frac{1}{2} \left[ \frac{\partial^2 h^{\beta\mu}}{\partial x^{\mu}\partial x^{\beta}} - \eta^{\mu\delta} \frac{\partial^2 h}{\partial x^{\mu}\partial x^{\delta}} - \eta^{\alpha\beta} \frac{\partial^2 h}{\partial x^{\alpha}\partial x^{\beta}} + \frac{\partial^2 h^{\mu\alpha}}{\partial x^{\alpha}\partial x^{\mu}} \right].
\end{aligned} \tag{B.7}$$

Now let us make the following transformation of indices.

- In the first term  $\beta \rightarrow \mu$  and  $\mu \rightarrow \nu$ .
- In the second term  $\delta \rightarrow \nu$ .
- In the third term  $\alpha \rightarrow \mu$  and  $\beta \rightarrow \nu$ .
- In the fourth term  $\alpha \rightarrow \nu$ .

Using this transformation we see that the Ricci scalar simplifies to

$$R = \frac{\partial^2 h^{\mu\nu}}{\partial x^{\mu}\partial x^{\nu}} - \eta^{\mu\nu} \frac{\partial^2 h}{\partial x^{\mu}\partial x^{\nu}}, \tag{B.8}$$

and hence the Einstein tensor for weak field can be written as

$$\begin{aligned}
G_{\alpha\beta} &= R_{\alpha\beta} - \frac{1}{2}\eta_{\alpha\beta}R, \\
&= \frac{1}{2} \left[ \frac{\partial^2 h_{\alpha}{}^{\mu}}{\partial x^{\mu}\partial x^{\beta}} - \eta^{\mu\delta} \frac{\partial^2 h_{\alpha\beta}}{\partial x^{\mu}\partial x^{\delta}} - \frac{\partial^2 h}{\partial x^{\alpha}\partial x^{\beta}} + \frac{\partial^2 h^{\mu}{}_{\beta}}{\partial x^{\alpha}\partial x^{\mu}} \right] - \\
&\quad \frac{1}{2}\eta_{\alpha\beta} \left[ \frac{\partial^2 h^{\mu\nu}}{\partial x^{\mu}\partial x^{\nu}} - \eta^{\mu\nu} \frac{\partial^2 h}{\partial x^{\mu}\partial x^{\nu}} \right].
\end{aligned} \tag{B.9}$$

The above form of the Einstein tensor can be expressed in a more convenient and simplified form using some choices of gauges. This is what we will explore next.

## B.2 Transverse traceless gauge

The analytical form of the Einstein tensor that we found in Eq. (B.9) can be simplified after we employ a series of gauge transformations. But before we do that, let us first

introduced the trace-reversed perturbation,  $\bar{h}_{\alpha\beta} = h_{\alpha\beta} - \frac{1}{2}\eta_{\alpha\beta} h$ , where  $h$  is the trace of the metric perturbation. We note that this implies that

$$\begin{aligned}
\frac{\partial^2 h^\mu{}_\beta}{\partial x^\alpha \partial x^\mu} - \frac{1}{2} \frac{\partial^2 h}{\partial x^\alpha \partial x^\beta} &= \frac{\partial^2 \bar{h}^\mu{}_\beta}{\partial x^\alpha \partial x^\mu}, \\
\frac{\partial^2 h_{\alpha}{}^\mu}{\partial x^\mu \partial x^\beta} - \frac{1}{2} \frac{\partial^2 h}{\partial x^\alpha \partial x^\beta} &= \frac{\partial^2 \bar{h}_{\alpha}{}^\mu}{\partial x^\mu \partial x^\beta}, \\
\frac{\partial^2 h^{\mu\nu}}{\partial x^\mu \partial x^\nu} - \frac{1}{2} \eta^{\mu\nu} \frac{\partial^2 h}{\partial x^\mu \partial x^\nu} &= \frac{\partial^2 \bar{h}^{\mu\nu}}{\partial x^\mu \partial x^\nu}, \\
\eta^{\mu\delta} \frac{\partial^2 h_{\alpha\beta}}{\partial x^\mu \partial x^\delta} - \frac{1}{2} \eta_{\alpha\beta} \eta^{\mu\delta} \frac{\partial^2 h}{\partial x^\mu \partial x^\delta} &= \eta^{\mu\delta} \frac{\partial^2 \bar{h}_{\alpha\beta}}{\partial x^\mu \partial x^\delta}.
\end{aligned} \tag{B.10}$$

Using these expressions in Eq. (B.9), we get

$$G_{\alpha\beta} = \frac{1}{2} \left[ \frac{\partial^2 \bar{h}_{\alpha}{}^\mu}{\partial x^\mu \partial x^\beta} + \frac{\partial^2 \bar{h}_{\beta}{}^\mu}{\partial x^\mu \partial x^\alpha} - \eta_{\alpha\beta} \frac{\partial^2 \bar{h}^{\mu\nu}}{\partial x^\mu \partial x^\nu} - \eta^{\mu\nu} \frac{\partial^2 \bar{h}_{\alpha\beta}}{\partial x^\mu \partial x^\nu} \right], \tag{B.11}$$

which we substitute in the Einstein's equations to get

$$\frac{\partial^2 \bar{h}_{\alpha}{}^\mu}{\partial x^\mu \partial x^\beta} + \frac{\partial^2 \bar{h}_{\beta}{}^\mu}{\partial x^\mu \partial x^\alpha} - \eta_{\alpha\beta} \frac{\partial^2 \bar{h}^{\mu\nu}}{\partial x^\mu \partial x^\nu} - \eta^{\mu\nu} \frac{\partial^2 \bar{h}_{\alpha\beta}}{\partial x^\mu \partial x^\nu} = \frac{16\pi G}{c^4} T_{\alpha\beta}. \tag{B.12}$$

The last term in the left hand side of the above equation can be written as the box operator of  $\bar{h}_{\alpha\beta}$ , and applying Lorenz gauge condition ( $\partial^{\bar{h}\mu\alpha}/\partial x^\mu = 0$ ) all the other terms vanishes, thus the Einstein's equations in the weak field regime reduces to

$$\boxed{\square \bar{h}_{\alpha\beta} = -\frac{16\pi G}{c^4} T_{\alpha\beta}}, \tag{B.13}$$

which is the Einstein's field equation in the linearized gravity.

Now we will solve this above equation in free space. The right hand side of the above equation in free space vanishes, thus we are left with

$$\square \bar{h}_{\alpha\beta} = 0. \tag{B.14}$$

One of the solutions of the above equation is the plane wave solution.

$$\bar{h}_{\alpha\beta} = A_{\alpha\beta} e^{ik_\gamma x^\gamma}, \quad (\text{B.15})$$

where we are assuming that the direction of propagation of the wave is given by the vector  $k^\gamma$ , and  $A_{\alpha\beta}$  is the amplitude tensor. Putting this back in the wave equation yields  $k^\gamma k_\gamma = 0$ , which means that the propagation occurs along the null geodesics. Thus the gravitational wave propagates at the speed of light. Using the Lorenz gauge we can also write

$$A^{\alpha\beta} k_\gamma \delta_\alpha^\gamma = A^{\alpha\beta} k_\alpha = 0, \quad (\text{B.16})$$

which implies that the amplitude tensor is orthogonal to the direction of propagation. Thus choosing the Lorenz gauge has enabled us to write the wave equation in such a way that its solutions become transverse. Since the metric for any geometry must be symmetric and the Minkowskian metric  $\eta_{\mu\nu}$  too is symmetric, this implies that the metric perturbation too must be a symmetric tensor. Reversing the trace in order to form the trace reversed perturbation,  $\bar{h}_{\mu\nu}$ , preserves the symmetry of the perturbation metric. The 10 independent components are further reduced by the 4 constraints from the above equation. Thus in the current form the  $\bar{h}_{\alpha\beta}$  has 6 independent components. Furthermore choosing the gauge conditions that the time components of the amplitude terms are zero and that the perturbation is traceless finally helps us to reduce the number of independent components in the amplitude to 2.

Which we write as follows

$$A_{\alpha\beta}^{\text{TT}} = \begin{pmatrix} 0 & 0 & 0 & 0 \\ 0 & h_+ & h_\times & 0 \\ 0 & h_\times & -h_+ & 0 \\ 0 & 0 & 0 & 0 \end{pmatrix}. \quad (\text{B.17})$$

This is the amplitude of the gravitational wave propagating through free space in the transverse traceless gauge (symbolically represented by the superscript TT).

### B.3 Gravitational wave emitted from a source

Now we will find the solution of the linearized Einstein's field equations, given in Eq. (B.13), in the transverse traceless gauge discussed above in presence of the source. This is a second order inhomogeneous differential equation whose solution is given by the Green's function

$$G(r, t) = -\frac{\delta(t - r/c)}{4\pi r}. \quad (\text{B.18})$$

Using the Green's function, the solution of Eq. (B.13) can be obtained to be,

$$\bar{h}^{\alpha\beta} = \frac{4G}{c^4} \int \frac{T^{\alpha\beta}(t - r/c, r')}{r} dV', \quad (\text{B.19})$$

where primed variables are that coordinates measured in the reference frame of the source,  $dV'$  is a volume element in the source, and  $r$  is defined by  $r^2 = \sum_{a=1}^3 (x^a - x'^a)^2$ . In gravitational wave astronomy we are primarily interested in sources that are located far from the observer. In this far field approximation  $r^2 \approx \sum_{a=1}^3 (x^a)^2$ , thus we can write

$$\bar{h}^{\alpha\beta} = \frac{4G}{c^4 r} \int T^{\alpha\beta}(t - r/c, r') dV'. \quad (\text{B.20})$$

In the transverse traceless gauge, we are only interested in the spatial part of the stress energy tensor. The spatial part of  $T^{\alpha\beta}$  can be written as

$$T^{ab} = \frac{1}{2} \frac{\partial^2}{\partial t^2} [x'^a x'^b \rho'(t - r/c, r')]. \quad (\text{B.21})$$

Where  $\rho'(t - r/c, r')$  is the density function of the source measured in the coordinate system of the source. Let us now define a density function  $\rho$  globally as  $\rho(t - r/c, r)$  such that the function will be zero outside the source. Then we can write the stress energy tensor as

$$T^{ab} = \frac{1}{2} \frac{\partial^2}{\partial t^2} [x^a x^b \rho(t - r/c, r)]. \quad (\text{B.22})$$

We can now define a mass quadrupole moment tensor,  $\mathcal{Q}^{ab}$

$$\mathcal{Q}^{ab} = \int x^a x^b \rho(t - r/c, r) dV. \quad (\text{B.23})$$

Using Eqs. (B.20), (B.22) and (B.23) the gravitational waveform can then be written as

$$\boxed{h_{ab}^{\text{TT}}(t) = \frac{2G}{c^4 r} \ddot{\mathcal{Q}}_{ab}^{\text{TT}}(t - r/c)}, \quad (\text{B.24})$$

where we have projected the components of the mass quadrupole moment in the TT gauge.

# Bibliography

The proposal for advanced ligo is available on-line at. URL <http://www.ligo.caltech.edu/advLIGO/>.

Astrosat. URL <http://astrosat.iucaa.in/>.

J. Abadie and et. al. Search for gravitational-wave inspiral signals associated with short gamma-ray bursts during ligo's fifth and virgo's first science run. *The Astrophysical Journal*, 715(2):1453, 2010. URL <http://stacks.iop.org/0004-637X/715/i=2/a=1453>.

J. Abadie and et. al. Search for gravitational waves associated with gamma-ray bursts during ligo science run 6 and virgo science runs 2 and 3. *The Astrophysical Journal*, 760(1):12, 2012a. URL <http://stacks.iop.org/0004-637X/760/i=1/a=12>.

J. Abadie and et. al. Search for gravitational waves associated with gamma-ray bursts during ligo science run 6 and virgo science runs 2 and 3. *The Astrophysical Journal*, 760(1):12, 2012b. URL <http://stacks.iop.org/0004-637X/760/i=1/a=12>.

J. Abadie et al. First low-latency ligo+virgo search for binary inspirals and their electromagnetic counterparts.

J. Abadie et al. Predictions for the Rates of Compact Binary Coalescences Observable by Ground-based Gravitational-wave Detectors. *Class.Quant.Grav.*, 27:173001, 2010a. doi: 10.1088/0264-9381/27/17/173001.

- J. Abadie et al. Search for gravitational-wave inspiral signals associated with short Gamma-Ray Bursts during LIGO's fifth and Virgo's first science run. *Astrophys. J.*, 715:1453–1461, 2010b. doi: 10.1088/0004-637X/715/2/1453.
- J. Abadie et al. Search for gravitational waves from compact binary coalescence in ligo and virgo data from s5 and vsr1. *Phys. Rev. D*, 82:102001, Nov 2010c. doi: 10.1103/PhysRevD.82.102001. URL <http://link.aps.org/doi/10.1103/PhysRevD.82.102001>.
- J. Abadie et al. Search for gravitational waves from binary black hole inspiral, merger, and ringdown. *Phys. Rev. D*, 83:122005, Jun 2011. doi: 10.1103/PhysRevD.83.122005. URL <http://link.aps.org/doi/10.1103/PhysRevD.83.122005>.
- J. Abadie et al. Search for gravitational waves associated with gamma-ray bursts during ligo science run 6 and virgo science runs 2 and 3. *Astrophys.J.*, 760:12, 2012a. doi: 10.1088/0004-637X/760/1/12.
- J. Abadie et al. Search for Gravitational Waves from Low Mass Compact Binary Coalescence in LIGO's Sixth Science Run and Virgo's Science Runs 2 and 3. *Phys.Rev.*, D85:082002, 2012b. doi: 10.1103/PhysRevD.85.082002.
- J. Abadie et al. Search for gravitational waves associated with gamma-ray bursts during ligo science run 6 and virgo science runs 2 and 3. *The Astrophysical Journal*, 760(1):12, 2012c. doi: 10.1088/0004-637X/760/1/12. URL <http://stacks.iop.org/0004-637X/760/i=1/a=12>.
- B. Abbott et al. Search for Gravitational Waves Associated with 39 Gamma- Ray Bursts Using Data from the Second, Third, and Fourth LIGO Runs. *Phys. Rev.*, D77:062004, 2008. doi: 10.1103/PhysRevD.77.062004.
- B P Abbott and et. al. Ligo: the laser interferometer gravitational-wave observatory. *Reports on Progress in Physics*, 72(7):076901, 2009. URL <http://stacks.iop.org/0034-4885/72/i=7/a=076901>.

- B. P. Abbott et al. Search for Gravitational Waves from Low Mass Compact Binary Coalescence in 186 Days of LIGO's fifth Science Run. *Phys. Rev.*, D80:047101, 2009a. doi: 10.1103/PhysRevD.80.047101.
- B. P. Abbott et al. Search for Gravitational Waves from Low Mass Binary Coalescences in the First Year of LIGO's S5 Data. *Phys. Rev.*, D79:122001, 2009b. doi: 10.1103/PhysRevD.79.122001.
- B.P. Abbott et al. Search for gravitational-wave bursts associated with gamma-ray bursts using data from ligo science run 5 and virgo science run 1. *Astrophys.J.*, 715:1438–1452, 2010. doi: 10.1088/0004-637X/715/2/1438.
- Aous A. Abdo et al. Fermi Observations of High-Energy Gamma-Ray Emission from GRB 080916C. *Science*, 323:1688–1693, 2009. doi: 10.1126/science.1169101.
- P Ajith. Gravitational-wave data analysis using binary black-hole waveforms. *Classical and Quantum Gravity*, 25(11):114033, 2008. doi: 10.1088/0264-9381/25/11/114033. URL <http://stacks.iop.org/0264-9381/25/i=11/a=114033>.
- P. Ajith and Sukanta Bose. Estimating the parameters of non-spinning binary black holes using ground-based gravitational-wave detectors: Statistical errors. *Phys. Rev.*, D79:084032, 2009a. doi: 10.1103/PhysRevD.79.084032.
- P. Ajith and Sukanta Bose. Estimating the parameters of nonspinning binary black holes using ground-based gravitational-wave detectors: Statistical errors. *Phys. Rev. D*, 79:084032, Apr 2009b. doi: 10.1103/PhysRevD.79.084032. URL <http://link.aps.org/doi/10.1103/PhysRevD.79.084032>.
- P. Ajith and et. al. Template bank for gravitational waveforms from coalescing binary black holes: Nonspinning binaries. *Phys. Rev. D*, 77:104017, May 2008. doi: 10.1103/PhysRevD.77.104017. URL <http://link.aps.org/doi/10.1103/PhysRevD.77.104017>.

- B. Allen. Ligo calibration accuracy, unpublished. 1996.
- Bruce Allen.  $\chi^2$  time-frequency discriminator for gravitational wave detection. *Phys. Rev. D*, 71:062001, Mar 2005. doi: 10.1103/PhysRevD.71.062001. URL <http://link.aps.org/doi/10.1103/PhysRevD.71.062001>.
- Bruce Allen, Warren G. Anderson, Patrick R. Brady, Duncan A. Brown, and Jolien D. E. Creighton. Findchirp: An algorithm for detection of gravitational waves from inspiraling compact binaries. *Phys. Rev. D*, 85:122006, Jun 2012. doi: 10.1103/PhysRevD.85.122006. URL <http://link.aps.org/doi/10.1103/PhysRevD.85.122006>.
- S. Babak et al. Searching for gravitational waves from binary coalescence. 2012. URL <http://arxiv.org/abs/1208.3491>.
- Imre Bartos, Patrick Brady, and Szabolcs Marka. How Gravitational-wave Observations Can Shape the Gamma-ray Burst Paradigm. 2012.
- Edo Berger, P.A. Price, S.B. Cenko, A. Gal-Yam, A.M. Soderberg, et al. The afterglow and elliptical host galaxy of the short gamma-ray burst GRB 050724. *Nature*, 438:988–990, 2005. doi: 10.1038/nature04238.
- Maria Grazia Bernardini, Raffaella Margutti, Jirong Mao, Elena Zaninoni, and Guido Chincarini. The X-ray light curve of Gamma-ray bursts: clues on the central engine. *Astron.Astrophys.*, 539:A3, 2012.
- S. Bose. Effects of calibration inaccuracies: Applications in gravitational-wave detection and parameter estimation, unpublished. 2005.
- Sukanta Bose, Archana Pai, and Sanjeev Dhurandhar. Detection of gravitational waves from inspiraling, compact binaries using a network of interferometric detectors. *International Journal of Modern Physics D*, 09(03):325–329, 2000. doi: 10.1142/S0218271800000360. URL <http://www.worldscientific.com/doi/abs/10.1142/S0218271800000360>.

- Sukanta Bose, Achamveedu Gopakumar, and Manuel Tessmer. Gravitational wave data analysis implications of TaylorEt inspiral approximants for ground-based detectors: The Non-spinning case. 2008.
- Sukanta Bose, Shaon Ghosh, and P Ajith. Systematic errors in measuring parameters of non-spinning compact binary coalescences with post-newtonian templates. *Classical and Quantum Gravity*, 27(11):114001, 2010. URL <http://stacks.iop.org/0264-9381/27/i=11/a=114001>.
- Sukanta Bose, Thilina Dayanga, Shaon Ghosh, and Dipongkar Talukder. A blind hierarchical coherent search for gravitational-wave signals from coalescing compact binaries in a network of interferometric detectors. *Classical and Quantum Gravity*, 28(13):134009, 2011. URL <http://stacks.iop.org/0264-9381/28/i=13/a=134009>.
- Duncan A. Brown, Ian Harry, Andrew Lundgren, and Alexander H. Nitz. Detecting binary neutron star systems with spin in advanced gravitational-wave detectors. *Phys. Rev. D*, 86:084017, Oct 2012. doi: 10.1103/PhysRevD.86.084017. URL <http://link.aps.org/doi/10.1103/PhysRevD.86.084017>.
- Brown, Duncan. Searching for gravitational radiation from black hole machos in the galactic halo. December 2004.
- Kipp Cannon, Romain Cariou, Adrian Chapman, Mireia Crispin-Ortuzar, Nickolas Fotopoulos, et al. Toward Early-Warning Detection of Gravitational Waves from Compact Binary Coalescence. *Astrophys.J.*, 748:136, 2012. doi: 10.1088/0004-637X/748/2/136.
- Capano, Collin D. Searching for gravitational waves from compact binary coalescence using ligo and virgo data. August 2011.
- J. Creighton and W. Anderson. Gravitational-wave physics and astronomy. 2011.

- Curt Cutler and Michele Vallisneri. Lisa detections of massive black hole inspirals: Parameter extraction errors due to inaccurate template waveforms. *Phys. Rev. D*, 76:104018, Nov 2007. doi: 10.1103/PhysRevD.76.104018. URL <http://link.aps.org/doi/10.1103/PhysRevD.76.104018>.
- Thibault Damour, Bala R. Iyer, and B. S. Sathyaprakash. Comparison of search templates for gravitational waves from binary inspiral. *Phys. Rev. D*, 63:044023, Jan 2001. doi: 10.1103/PhysRevD.63.044023. URL <http://link.aps.org/doi/10.1103/PhysRevD.63.044023>.
- Alexander Dietz, Nickolas Fotopoulos, Leo Singer, and Curt Cutler. Outlook for detection of GW inspirals by GRB-triggered searches in the advanced detector era. 2012. URL <http://arxiv.org/abs/1210.3095>.
- David Eichler, Mario Livio, Tsvi Piran, and David N. Schramm. Nucleosynthesis, Neutrino Bursts and Gamma-Rays from Coalescing Neutron Stars. *Nature*, 340:126–128, 1989. doi: 10.1038/340126a0.
- A. Einstein. Die grundlage der allgemeinen relativittstheorie. *Annalen der Physik*, 354:769–822, 1916. doi: 10.1002/andp.19163540702. URL <http://onlinelibrary.wiley.com/doi/10.1002/andp.19163540702/references>.
- Lee S. Finn. Detection, measurement, and gravitational radiation. *Phys. Rev. D*, 46:5236–5249, Dec 1992. doi: 10.1103/PhysRevD.46.5236. URL <http://link.aps.org/doi/10.1103/PhysRevD.46.5236>.
- Lee Samuel Finn and David F. Chernoff. Observing binary inspiral in gravitational radiation: One interferometer. *Phys.Rev.*, D47:2198–2219, 1993. doi: 10.1103/PhysRevD.47.2198.
- Francois Foucart, M. Brett Deaton, Matthew D. Duez, Lawrence E. Kidder, Ilana MacDonald, et al. Black hole-neutron star mergers at realistic mass ratios: Equation of state and spin orientation effects. 2012.

- N. Gehrels, E. Ramirez-Ruiz, and Derek B. Fox. Gamma-Ray Bursts in the Swift Era. *Ann.Rev.Astron.Astrophys.*, 47:567–617, 2009. doi: 10.1146/annurev.astro.46.060407.145147.
- S. Ghosh and S. Bose. Toward finding gravitational-wave signals from progenitors of short hard gamma-ray bursts and orphaned afterglows. 2013. URL <https://dcc.ligo.org/LIGO-P1200169-v2>.
- S. Ghosh, S. Bose, and I. Harry. Waveform inaccuracy and its effect on detection of gravitational waves from progenitors of GRB. 2013. URL <https://dcc.ligo.org/LIGO-T1300597>.
- B. Grossan, I.H. Park, S. Ahmad, K.B. Ahn, P. Barrillon, et al. A next generation Ultra-Fast Flash Observatory (UFFO-100) for IR/optical observations of the rise phase of gamma-ray bursts. 2012.
- Yekta Gürsel and Massimo Tinto. Near optimal solution to the inverse problem for gravitational-wave bursts. *Phys. Rev. D*, 40:3884–3938, Dec 1989. doi: 10.1103/PhysRevD.40.3884. URL <http://link.aps.org/doi/10.1103/PhysRevD.40.3884>.
- I. W. Harry and S. Fairhurst. Targeted coherent search for gravitational waves from compact binary coalescences. *Phys. Rev. D*, 83:084002, Apr 2011. doi: 10.1103/PhysRevD.83.084002. URL <http://link.aps.org/doi/10.1103/PhysRevD.83.084002>.
- James B. Hartle. *Elements of signal detection and estimation*. Pearson Education, 482 F.I.E Patparganj, Delhi 110092, India, 2003. ISBN 81-297-0094-8.
- Carl W. Helstrom. *Elements of signal detection and estimation*. Prentice-Hall, Inc., Upper Saddle River, NJ, USA, 1995. ISBN 0-13-808940-X.
- K. Hurley. The url of the inter-planetary network is. URL <http://www.ssl.berkeley.edu/ipn3/>.

- Luke Zoltan Kelley, Ilya Mandel, and Enrico Ramirez-Ruiz. Electromagnetic transients as triggers in searches for gravitational waves from compact binary mergers. 2012.
- Drew Keppel. The multi-detector F-statistic metric for short-duration non-precessing inspiral gravitational-wave signals. *Phys.Rev.*, D86:123010, 2012. doi: 10.1103/PhysRevD.86.123010.
- Kenta Kiuchi, Yuichiro Sekiguchi, Masaru Shibata, and Keisuke Taniguchi. Exploring binary-neutron-star-merger scenario of short-gamma-ray bursts by gravitational-wave observation. *Phys. Rev. Lett.*, 104:141101, Apr 2010a. doi: 10.1103/PhysRevLett.104.141101.
- Kenta Kiuchi, Yuichiro Sekiguchi, Masaru Shibata, and Keisuke Taniguchi. Exploring binary-neutron-star-merger scenario of short-gamma-ray bursts by gravitational-wave observation. *Phys. Rev. Lett.*, 104:141101, Apr 2010b. doi: 10.1103/PhysRevLett.104.141101. URL <http://link.aps.org/doi/10.1103/PhysRevLett.104.141101>.
- Ray W. Klebesadel, Ian B. Strong, and Roy A. Olson. Observations of Gamma-Ray Bursts of Cosmic Origin. *Astrophysical Journal*, 182, 1973. doi: 10.1086/181225.
- T. Kruhler, P. Schady, J. Greiner, P. Afonso, E. Bottacini, et al. Photometric redshifts for GRB afterglows from GROND and Swift/UVOT. *Astron.Astrophys.*, 526:A153, 2011. doi: 10.1051/0004-6361/201015327.
- K. Kuroda and LCGT Collaboration. Status of LCGT, April 2010.
- LIGO Algorithms Library. LSC Algorithms Library. URL <https://www.lsc-group.phys.uwm.edu/daswg/projects/lalsuite.html>.
- A. MacFadyen and S.E. Woosley. Collapsars: Gamma-ray bursts and explosions in 'failed supernovae'. *Astrophys.J.*, 524:262, 1999. doi: 10.1086/307790.
- B.D. Metzger and E. Berger. What is the Most Promising Electromagnetic Counterpart of a

- Neutron Star Binary Merger? *Astrophys.J.*, 746:48, 2012. doi: 10.1088/0004-637X/746/1/48.
- Tara Murphy, Shami Chatterjee, David L. Kaplan, Jay Banyer, Martin E. Bell, et al. VAST: An ASKAP Survey for Variables and Slow Transients. 2012. URL <http://arxiv.org/abs/1207.1528>.
- Ehud Nakar. Short-Hard Gamma-Ray Bursts. *Phys.Rept.*, 442:166–236, 2007. doi: 10.1016/j.physrep.2007.02.005.
- Neal Dalal and Kim Griest and Jason Pruet. The Difficulty in Using Orphan Afterglows to Measure Gamma-Ray Burst Beaming. *The Astrophysical Journal*, 564(1):209, 2002. URL {<http://stacks.iop.org/0004-637X/564/i=1/a=209>}.
- Samaya Nissanke, Daniel E. Holz, Scott A. Hughes, Neal Dalal, and Jonathan L. Sievers. Exploring short gamma-ray bursts as gravitational-wave standard sirens. *Astrophys.J.*, 725:496–514, 2010. doi: 10.1088/0004-637X/725/1/496.
- Samaya Nissanke, Mansi Kasliwal, and Alexandra Georgieva. Identifying Elusive Electromagnetic Counterparts to Gravitational Wave Mergers: an end-to-end simulation. 2012.
- M. Nysewander, A.S. Fruchter, and A. Pe’er. A comparison of the afterglows of short- and long-duration gamma-ray bursts. *Astrophys.J.*, 701:824–836, 2009. doi: 10.1088/0004-637X/701/1/824.
- W. S. Paciesas et al. The fermi gbm gamma-ray burst catalog: The first two years. *Astrophys. J.*, 199(1), 2012. doi: 10.1088/0067-0049/199/1/18.
- Archana Pai, Sanjeev Dhurandhar, and Sukanta Bose. Data-analysis strategy for detecting gravitational-wave signals from inspiraling compact binaries with a network of laser-interferometric detectors. *Phys. Rev. D*, 64:042004, Jul 2001. doi: 10.1103/PhysRevD.64.042004. URL <http://link.aps.org/doi/10.1103/PhysRevD.64.042004>.

- T. Piran. Gamma-ray bursts and the fireball model. *Phys.Rept.*, 314:575–667, 1999. doi: 10.1016/S0370-1573(98)00127-6.
- V. Predoi and K. Hurley. Search for gravitational waves associated with the InterPlanetary Network short gamma ray bursts. *Journal of Physics*, 363:012034, 2012. doi: 10.1088/1742-6596/363/1/012034.
- James E. Rhoads. How to tell a jet from a balloon: A Proposed test for beaming in gamma-ray bursts. *Astrophys.J.*, 487:L1, 1997. doi: 10.1086/310876.
- James E. Rhoads. Snapshot identification of gamma-ray burst optical afterglows. 2000.
- James E. Rhoads. Dirty fireballs and orphan afterglows: A Tale of two transients. *Astrophys.J.*, 591:1097–1103, 2003. doi: 10.1086/368125.
- C. A. K. Robinson, B. S. Sathyaprakash, and Anand S. Sengupta. Geometric algorithm for efficient coincident detection of gravitational waves. *Phys. Rev. D*, 78:062002, Sep 2008. doi: 10.1103/PhysRevD.78.062002. URL <http://link.aps.org/doi/10.1103/PhysRevD.78.062002>.
- Peter R. Saulson. Fundamentals of interferometric gravitational wave detectors. 1994.
- Bernard F. Schutz. Networks of gravitational wave detectors and three figures of merit. *Class.Quant.Grav.*, 28:125023, 2011. doi: 10.1088/0264-9381/28/12/125023.
- K. Stobel and M. K. Weigel. On the minimum and maximum mass of neutron stars and the delayed collapse. *A&A*, 367(2):582–587, 2001. doi: 10.1051/0004-6361:20000428.
- Daniel E. Vanden Berk et al. SDSS J124602.54+011318.8: A Highly luminous optical transient at  $Z = 0.385$ . *Astrophys.J.*, 576:673–678, 2002. doi: 10.1086/341887.
- Vedrenne, Gilbert and Atteia, Jean-Luc. *Gamma-Ray Bursts, The brightest explosions in the Universe*. Springer, Praxis, 2009. ISBN 978-3-540-39085-5.

- J. Weber. Evidence for discovery of gravitational radiation. *Phys. Rev. Lett.*, 22:1320–1324, Jun 1969. doi: 10.1103/PhysRevLett.22.1320. URL <http://link.aps.org/doi/10.1103/PhysRevLett.22.1320>.
- J. M. Weisberg, D. J. Nice, and J. H. Taylor. Timing measurements of the relativistic binary pulsar psr b1913+16. *The Astrophysical Journal*, 722(2):1030, 2010. URL <http://stacks.iop.org/0004-637X/722/i=2/a=1030>.
- wikimedia commons. wikimedia: Ligo noise and sensitivity. URL <http://upload.wikimedia.org/wikipedia/commons/0/02/LIG0sensitivity.png>.
- Heng Yu, Paolo Tozzi, Stefano Borgani, Piero Rosati, and Zong-Hong Zhu. Measuring redshift through X-ray spectroscopy of galaxy clusters: results from Chandra data and future prospects. *Astron. Astrophys.*, 529:A65, 2011. doi: 10.1051/0004-6361/201016236.
- Tayyaba Zafar, Darach Watson, Johan P.U. Fynbo, Daniele Malesani, Pall Jakobsson, et al. The extinction curves of star-forming regions from  $z=0.1$  to 6.7 using grb afterglow spectroscopy. *Astron. Astrophys.*, 521:143, 2011. doi: 10.1051/0004-6361/201116663.
- Bing Zhang. Astrophysics: A burst of new ideas. *Nature*, 444:7122, 2006. doi: 10.1038/4441010a. URL <http://www.nature.com/nature/journal/v444/n7122/full/4441010a.html>.
- F. zel, D. Psaltis, R. Narayan, and A. S. Villarreal. On the mass distribution and birth masses of neutron stars. *Astrophys. J.*, 757(1), 2012. doi: 10.1088/0004-637X/757/1/55.